



UNIVERSITÄT  
DES  
SAARLANDES

**Hard (AlTi)N coatings produced by  
high-power impulse magnetron sputtering (HiPIMS)  
with high-temperature resistance - influence of Cr  
and Si additive elements**

Dissertation

zur Erlangung des Grades

des Doktors der Ingenieurwissenschaften

der Naturwissenschaftlich-Technischen Fakultät

der Universität des Saarlandes

Von

Mohamed Riyad ALHAFIAN

Saarbrücken, 2023

**Tag des Kolloquiums:** 11. Januar 2024

**Dekan:** Prof. Dr. Ludger Santen

**Berichterstatter:** Prof. Dr.-Ing. Frank Mücklich  
Prof. Dr. mont. Christian Motz  
Dr. Patrick Choquet

**Akad. Mitglied:** Dr.-Ing. Sarah Fischer

**Vorsitz:** Prof. Dr.-Ing. Dirk Bähre



**Part of the joint**

**European Doctoral Programme in Materials Science and Engineering (DocMASE)**

**in collaboration with**

**Materials Research and Technology (MRT) department**

**at Luxembourg Institute of Science and Technology (LIST), Luxembourg**

This thesis is presented by a compendium of three publications and summary in order to provide a global discussion of the results.



## **Dedicated to**

Family and friends, especially my parents, sister in Syria, my wife, daughter and son.

Syrian children in the shadow of a 12-year conflict

## **Declaration**

I hereby declare that this dissertation is my own result and no further sources of information have been used other than the references cited. Neither this thesis nor any part of it have been submitted to any other university or institution for the application of another degree or qualification. I presented my doctoral studies in the European Doctoral Programme in Advanced Materials Science and Engineering (DocMASE), at two research groups between 2018 and 2023. Functional materials group at Saarland university (Saarbrücken, Germany) (UdS) and Plasma Process and Engineering (PPE) group of the Materials Research and Technology (MRT) department at the Luxembourg Institute of Science and Technology (LIST) (Belvaux, Luxembourg) in strong collaboration with tool solution group of Ceratizit, an Austrian-Luxembourgish based company (Mamer, Luxembourg). In addition, Luxembourg National Research Fund (FNR) supported the work under the CORE PPP project funding for innovation and industry partnerships (C-PPP17/MS/11622578) is gratefully acknowledged.

Mohamed Riyad ALHAFAIN

Saarbrücken, 2023



# Abstract

This thesis presents experimental and theoretical research on nitride coatings, focusing on their morphology, nanostructure and mechanical properties. The chemical composition of the coatings was optimized through a combination of HiPIMS and dcMS processes. Coatings with this co-sputtering configuration demonstrated lower surface roughness and higher tribological properties compared to coatings deposited by CAE. Moreover, the study found that the choice of coating process parameters led to a transition in residual stresses from tensile to compressive, resulting from increased ion impact under higher energetic deposition condition.

The influence of Cr and Si additive elements on the TiAlN systems was also investigated. As-deposited TiAlSiN demonstrated superior hardness 35GPa and Higher  $H^3/E^2$  ratio of 0.171GPa compared to TiAlCrN due to the formation of a nanocrystalline structure resulting from the introduction of Si.

At 950°C, both TiAlCrN and TiAlCrSiN coatings possess multiscale oxide layers, with the oxide thickness increasing regularly over time and its growth kinetics is governed by the inward diffusion of oxygen and outward anionic diffusion of Al, Ti and Cr. TiAlSiN coatings displayed better oxidation resistance than the previous coating systems. A protective oxide layer is composed of mixed oxide  $Al_2O_3$  near the surface and  $TiO_2$  near the nitride, thanks to the presence of Si which limits the diffusion of Ti to the surface and hinders the formation of near-surface  $TiO_2$ .

## Zusammenfassung

Diese Arbeit präsentiert experimentelle und theoretische Forschung zu Nitrid-Beschichtungen und konzentriert sich auf deren Morphologie, Nanostruktur und mechanische Eigenschaften. Die chemische Zusammensetzung der Beschichtungen wurde durch eine Kombination von HiPIMS- und dcMS-Verfahren optimiert. Beschichtungen mit dieser Co-Sputter-Konfiguration zeigten im Vergleich zu Beschichtungen, die mittels CAE abgeschieden wurden, eine geringere Oberflächenrauheit und bessere tribologische Eigenschaften. Darüber hinaus ergab die Studie, dass die Wahl der Beschichtungsprozessparameter zu einem Übergang von Zug- zu Druckspannungen führte, der auf erhöhten Ionenstößen unter Bedingungen höherer Energieeinspeisung beruhte.

Der Einfluss der Zusatzelemente Cr und Si auf die TiAlN-Systeme wurde ebenfalls untersucht. TiAlSiN im abgeschiedenen Zustand zeigte eine überlegene Härte von 35 GPa und ein höheres  $H^3/E^2$ -Verhältnis von 0,171 GPa im Vergleich zu TiAlCrN aufgrund der Bildung einer nanokristallinen Struktur, die auf die Einführung von Si zurückzuführen ist.

Bei 950°C besitzen sowohl TiAlCrN- als auch TiAlCrSiN-Beschichtungen mehrskalige Oxidschichten, wobei die Oxiddicke im Laufe der Zeit regelmäßig zunimmt und ihre Wachstumskinetik durch die einwärts gerichtete Diffusion von Sauerstoff und die auswärts gerichtete anionische Diffusion von Al, Ti und Cr gesteuert wird. TiAlSiN-Beschichtungen zeigten eine bessere Oxidationsbeständigkeit als die vorherigen Beschichtungssysteme. Eine schützende Oxidschicht besteht aus einer gemischten  $Al_2O_3$ -Oxidzone in der Nähe der Oberfläche und  $TiO_2$  in der Nähe des Nitrids, dank der Anwesenheit von Si, das die Diffusion von Ti zur Oberfläche begrenzt und die Bildung von  $TiO_2$  in der Nähe der Oberfläche behindert.

## **Included papers and my contributions.**

Research carried out during the course of study has up to date resulted in the following publications:

### Paper I

**Comparison on the structural, mechanical and tribological properties of TiAlN coatings deposited by HiPIMS and Cathodic Arc Evaporation.**

M-R. Alhafian, J-B. Chemin, Y. Fleming, L. Bourgeois, M. Penoy, R. Useldinger, F. Soldera, F. Mücklich and P. Choquet

### **Surface and Coatings Technology**

### Paper II

**Study of the oxidation mechanism at high temperature of nanofiber textured AlTiCrN coatings produced by physical vapor deposition using high-resolution characterization techniques**

M-R. Alhafian, J-B. Chemin, N. Valle, B.El Adib, M.Penoy, L. Bourgeois, J.Ghanbaja, J. Barrirero, F. Soldera, F. Mücklich and P. Choquet

### **Corrosion Science**

### Paper III

**Influence of Si addition on the phase structure and oxidation behavior of PVD AlTiN and AlTiCrN coatings using high-resolution characterization techniques**

M-R. Alhafian, N. Valle, J-B. Chemin, L. Bourgeois, M. Penoy, R. Useldinger, J. Ghanbaja, F. Mücklich, and P. Choquet

### **Journal of Alloys and Compounds**

In the papers listed above, I, Mohamed Riyad Alhafian, carried out the major part in planning, coating deposition, and characterization using various methods such as OES, SEM-EDX, XRD, Nanoindentation, and tribological testing. Additionally, I contributed to the analysis and discussion of results involving TEM, SIMS, and APT. Moreover, I was responsible for writing the original manuscripts, editing them, and handling their submission.

## Acknowledgment

I would like to express my deepest gratitude to Professor Frank Mücklich, my supervisor at UdS for his invaluable contributions to my academic journey and for giving me the opportunity of being part of his research group and to work on an exciting research project. I have learned so much during this study.

I wish to thank my supervisor Dr. Patrick Choquet, my supervisor at LIST. His insightful feedback, challenging questions, and thought-provoking discussions have pushed me to expand my horizons and strive for higher achievements. Thank you for all the guidance and support, and for the opportunity of researching in a very interesting field. I have learned a lot from you, on professional and personal levels.

I would furthermore like to thank Prof. Dr. Christian Motz for his kind acceptance to read my thesis and to be my jury member.

My special gratitude goes to Dr.-Ing. Flavio Soldera the general manager of the European Doctoral Programme in Advanced Materials Science and Engineering (DocMASE) for his valuable input and useful discussions.

Dr. Laurent Bourgeois, Dr. Ralph Useldinger and Marianne Penoy. Special thanks to all of you, without your collaboration, this thesis would not have been possible. Thank you all for all the interesting discussions and support along with this thesis and of course all the samples.

I would like to acknowledge my co-supervisors who have substantially contributed to the progress in my work, specifically Dr. Nathalie Valle, Dr. Yves Fleming and Jean-Baptiste Chemin. Thank you for your great help, inspiring discussions and friendship.

I would also like to thank my colleagues and all the technicians' members. I have been truly fortunate to have the chance to work with so many talented individuals. I wish to express my gratitude to Plasma Process and Engineering (PPE) group who have shared with me the fluctuation of these years. Thank you for being there whenever I needed your help.

I would like to thank my family and friends who are spread all over the world and who gave me the strength and support to finish this project. Last but not least, I wish to thank my wife for her unconditional love and motivation that enabled me to finish this thesis.







# Table of contents

Part of the joint .....	I
Dedicated to .....	II
Declaration .....	III
Abstract .....	V
Zusammenfassung .....	VI
Included papers and my contributions .....	VII
Acknowledgment .....	VIII
List of tables .....	1
List of figures .....	2
Acronyms and symbols .....	5
<b>1 Introduction to the field .....</b>	<b>7</b>
<b>2 State of the art.....</b>	<b>12</b>
2.1 Synthesis and film deposition .....	12
2.1.1 Magnetron sputtering .....	13
2.1.2 High-Power Impulse Magnetron Sputtering .....	15
2.1.3 Comparing coating approaches of HiPIMS and dcMS techniques.....	17
2.2 Hard nitride coating system.....	21
2.2.1 Ti-Al-N .....	21
2.2.2 Ti-Al-Cr-N .....	25
2.2.3 Ti-Al-Cr-Si-N .....	27
2.3 Hard nitride coating system at high temperature .....	29
2.3.1 Ti-Al-N .....	29
2.3.2 Ti-Al-Cr-N .....	31

2.3.3	Ti-Al-Cr-Si-N .....	33
<b>3</b>	<b>Experimental procedure .....</b>	<b>35</b>
3.1.	Targets.....	35
3.2.	Substrates .....	36
3.3.	Coating deposition.....	37
<b>4</b>	<b>Characterization methodology .....</b>	<b>39</b>
4.1	Process characterization by optical emission spectroscopy.....	39
4.2	Scanning electron microscopy and x-ray emission spectroscopy .....	41
4.3	X-ray diffraction .....	42
4.4	Transmission electron microscopy .....	44
4.5	Secondary ion mass spectrometry.....	45
4.6	Atom probe tomography .....	46
4.7	Profilometer: .....	47
4.8	Nanoindentation.....	48
4.9	Scratch test.....	50
4.10	Ball-on-disk tribological test.....	51
4.11	Thermogravimetric analysis.....	52
<b>5</b>	<b>Question section .....</b>	<b>54</b>
<b>6</b>	<b>Summary of results.....</b>	<b>56</b>
<b>7</b>	<b>Included papers.....</b>	<b>65</b>
7.1	Paper I .....	66
7.2	Paper II.....	84
7.3	Paper III.....	104
<b>8</b>	<b>Perspectives and outlook.....</b>	<b>119</b>
<b>9</b>	<b>Appendix.....</b>	<b>121</b>
9.1	Stoichiometric curve .....	121
9.2	Energetics of adhesion .....	124

9.2.1	Plasma ion etching .....	125
9.2.2	An intermediate layer.....	126
9.3	Impact of substrate temperature .....	128
9.4	Coatings thermal response .....	129
9.4.1	Isotherm and temperature sweep tests by TGA .....	129
9.4.2	Study Ti/Al ratio effect by SIMS.....	131
<b>10</b>	<b>References.....</b>	<b>134</b>
	<b>Curriculum Vitae .....</b>	<b>147</b>

## List of tables

Table 2.1 Typical dcMS and HiPIMS selected parameters. Reproduced from [9, 11 & 12].

Table 2.1. Hardness, Young's modulus, and  $H^3/E^2$  factor values for different TiAlN-based coatings.

Table 3.1 Typical values of selected physical and mechanical properties of cemented tungsten carbide.

## List of figures

**Fig. 1.1** Side view of the chip formation on a TiAlN cutting insert (left) and temperature distribution inside the cutting insert during chip formation (right). Modified from [3].

**Fig. 1.2** Graphical abstract of the thesis arranged as a cumulative dissertation of papers: I, II and III.

**Fig. 2.1** Schematic drawing of a magnetron-sputtering source in the side view presented the magnetic field distribution of the magnetron and the possible transport of electrons, the principle of ions generated in plasma and accelerated towards a target sputter material, which condenses at the substrates.

**Fig. 2.2** Schematic drawing of a typical HiPIMS pulse (right) and an example of waveforms traces from the HiPIMS discharge operated at duty cycle 5.5%, time-on 110  $\mu\text{s}$ , time-off 1890  $\mu\text{s}$ , peak power density 0.5 Kw/cm<sup>2</sup> (left).

**Fig. 2.3** Different deposition rate for several target materials prepared by dcMS and HiPIMS coatings using the same conditions. dcMS deposition rate is plotted as bars (left axis) and the deposition rate of HiPIMS over dcMS is plotted as scattered points (right axis). Modified from [25]

**Fig. 2.4** Schematic drawing of the structural development of the TiN system with increasing Al addition. Modified from [50].

**Fig. 3.1** Schematic drawing of the experimental vacuum chamber and both systems of rectangular/circular targets.

**Fig. 3.2** Cemented tungsten carbide composite microstructure and schematic drawing of the binding phase between the hard material particles. Modified from [114].

**Fig. 3.3** Picture of the PVD sputtering device at LIST and schematic illustration of the reactor particles and the deposition system used to synthesize the films.

**Fig. 4.1** Experimental set-up for OES spectrum, the optic fiber is between the target and substrate holder  $d_1=d_2=TSD/2$ , where (TSD) is target substrate distance.

**Fig. 4.2** Overview of typical key materials characterization techniques and its resolution, reproduced from [119].

**Fig. 4.3** Experimental setup for local electrode atom probe tomography with a 2D detector.

**Fig. 4.4** KLA Tencor P6 with dongle and computer representation. Modified from [130].

**Fig. 4.5** Schematic drawing of an indentation with a pyramidal indenter under the load  $F$ . The elastoplastic behavior of the coatings causes an indentation depth of  $h_{\max}$  under  $F_{\max}$ , where the indenter is only in contact with the material for the depth  $h_c$ . After unloading the residual imprint has the depth  $h_r$  due to elastic recovery (right), the corresponding load-displacement curve with the loading and unloading segment (left). The elastic contribution to the maximum displacement is indicated with  $h_e$ . Reproduced from [131 & 132].

**Fig. 4.6** Schematic representation of nano-scratch systems instrument and Rockwell diamond stylus indenter. Modified from [133 & 134].

**Fig. 4.7** Standard Anton Paar tribometer setup and mounting of the instrument for performing the ball-on-disc test (right), a close configuration of ball-on-disc (Left). Modified from [139 & 140].

**Fig. 4.8** Overview of thermogravimetric methods of analysis. Reproduced from [142].

**Fig. 9.1** Hysteresis curves for the reactive sputtering discharge of dcMS above TiAl cathode in  $N_2/Ar$  mixture. The transition region between the metallic and poisoned target, the two-stage of cathode charge are highlighted (left). The full reactive mode (poisoning) target by dcMS requires a higher amount of  $N_2$  flow than HiPIMS for same applied power density, as well as increasing duty cycles, increase the required  $N_2$  flow for poisoning (middle). Using optical emission spectrum to define the required  $N_2$  flow for poisoning target is more precise than using gas pressure (right).

**Fig. 9.2** Top-view image of the crack propagation on the coating's surface on WC-Co substrate (A1). The cross-section image of the vertical and branching crack propagation between the coating columns on WC-Co substrate (A2). Top-view image of the scales

coatings formed on Si substrate resulting from weakly adhesion (B1) and cross-section (B2).

**Fig. 9.3** Top-view images in the scanning electron microscope (SEM) and the 3D maps view by Atomic Force Microscopy (AFM) for the WC-Co substrates after different biases exposure time. Where  $S_q$  and  $S_a$  are root mean square height and arithmetical mean height, respectively.

**Fig. 9.4** Schematic representation of TiAlN coating with the different intermediate layers, the binocular images of scratch test track at starting and near ending test, as well as the electron microscopy images of near ending test.

**Fig. 9.5** Change of deposition rate at different substrate temperatures.

**Fig. 9.6** In-situ measurements of the mass change of one uncoated blank alumina as a reference signal and three coated one by  $Al_{51}Ti_{49}N$ ,  $Al_{45}Ti_{29}Cr_{26}N$  and  $Al_{55}Ti_{33}Si_{12}N$  during heating from room temperature until 1100 °C (left), and the derivative relative mass change of its (right).

**Fig. 9.7** In-situ measurements of the weight change of  $Al_{51}Ti_{49}N$ ,  $Al_{37}Ti_{36}Cr_{27}N$  at 900 °C (left) and  $Al_{51}Ti_{35}Si_{14}N$ ,  $Al_{43}Ti_{31}Cr_{26}N$  at 950 °C (right).

**Fig. 9.8** SEM top-view image of the oxide crystal growth on the  $Al_{37}Ti_{35}Cr_{28}N$ ,  $Al_{43}Ti_{33}Cr_{24}N$  and  $Al_{48}Ti_{30}Cr_{22}N$ . SIMS analysis of the oxidized samples  $Al_{37}Ti_{35}Cr_{28}N$  presenting the two oxides regions, as well as the comparative SIMS analysis of the oxidation part of the three coatings using the N intensity as a baseline.



## Acronyms and symbols

PVD: Physical Vapor Deposition.

HiPIMS: High Power Impulse Magnetron Sputtering.

dcMS: direct current Magnetron Sputtering.

HPPMS: High Power Pulsed Magnetron Sputtering.

CAE: Cathodic Arc Evaporation.

Y: Sputter yield.

dc: direct current.

$B_v$ : negative substrate Bias Voltage.

$V_p$ : plasma potential.

PM: Powder Metallurgical.

$R_t$ : Rectangular target.

$C_t$ : Circular target.

TSD: Target Substrate Distance.

TiAlN: Titanium Aluminium Nitride.

c-(Ti, Al)N coating: cubic titanium aluminium nitride coating.

WC-Co: Cemented tungsten carbide.

WC: Tungsten carbide.

hcp / B4: Hexagonal close-packed.

fcc: face-centred cubic.

B1: Rock salt structure.

w: Wurtzite structure.

$\nu$ : Poisson's ratio.

E: Young's modulus.

O<sub>2</sub>: Oxygen.

Al<sub>2</sub>O<sub>3</sub>: Aluminium Oxide / Alumina.

N<sub>2</sub>: Nitrogen.

FIB: Focused Ion Beam.

TGA: Thermo Gravimetric Analysis.

APT: Atom Probe Tomography.

OES: Optical Emission Spectroscopy.

SEM: Scanning Electron Microscopy.

FE-SEM: Emission Scanning Electron Microscope.

EDS: Energy-Dispersive X-ray Spectrometer.

SE: Secondary Electrons.

TEM: Transmission Electron Microscopy.

PIPS: Precise Ion Polishing System.

XRD: X-ray diffractometry.

D-SIMS: Dynamic Secondary Ion Mass Spectrometry.

FWHM: Full Width at Half Maxima.

## 1 Introduction to the field

The machining industry is looking to reduce environmental risks as much as possible by using as little lubricant as feasible. Additionally, environment-friendly recycling of the coolants or even avoiding the usage of coolant came to high importance. Consequently, during cutting activities, the tools are exposed to increased surface temperature and subsequently a reduced life span. Coated surfaces have become indispensable for a vast number of applications where specific surface properties of the materials are needed. The coatings have to withstand a large range of working conditions without delamination from the underlying material. For instance, using coatings for cutting tools is possible by combining the properties of both coatings and bulk in order to reach higher toughness, hardness, wear resistance and oxidation resistance for high-temperature applications such as dry high-speed machining. Coated cutting tools with protective hard thin films have lifetimes up to 10 times higher than tools without any protective coating [1]. For users, this means improved productivity and reduced costs of industrial machining.

During machining, the estimated temperatures facing the edges of cutting tools are in the range of 750 – 850 °C, where the chemical wear due to the formation of soft oxides with poor adherence dominates over the abrasive wear. These temperatures upgrade to ~950 °C in the dry machining environment (Figure 1.1), hence the temperature may reach above 1000 °C at the edge of a cutting tool during metal machining and high stresses ~700 MPa during material removal [2].

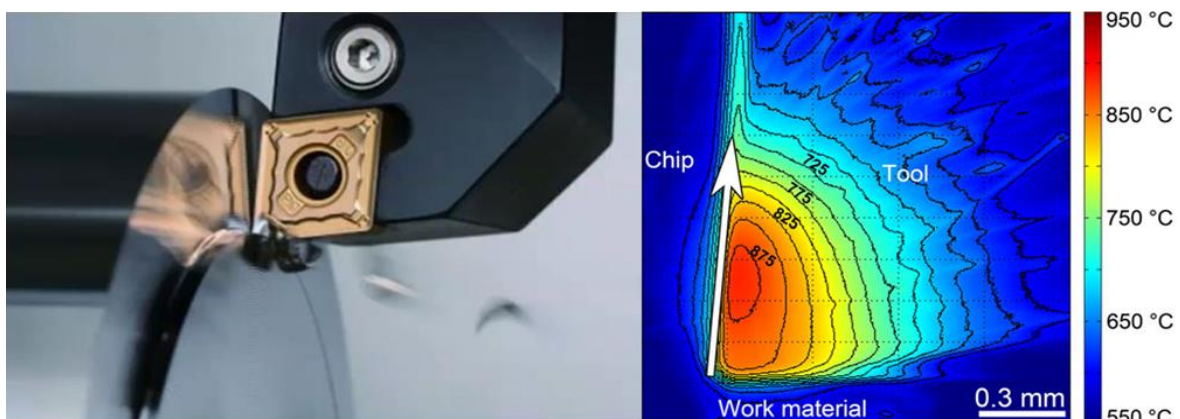


Fig. 1.1 Side view of the chip formation on a TiAlN cutting insert (left) and temperature distribution inside the cutting insert during chip formation (right). Modified from [3].

The abrasive wear resistance and the hardness of TiN and CrN coatings are low in comparison to other transition metal nitrides and therefore not suited to protect the cutting tools used for metal machining. Adding Al to these coatings is one way to improve the mechanical properties and thermal stability [4]. For instance, forming a ternary system of c-(Ti, Al)N coating for the cutting tool will extend its lifetime. In this way, manufacturing will benefit from the presence of protective coatings where both material and machining costs necessary for the tool fabrication can be significantly diminished, as well as the downtime required for the tool replacement.

This thesis focuses on the development of an innovative nitride-based hard coating with outstanding properties, including remarkable hardness exceeding 35 GPa, thermal stability up to 950 °C, and excellent oxidation resistance. The study investigates the relationship between deposition process parameters of hard (Ti, Al)N coatings and various film properties such as synthesis, microstructure, morphology, and micro-mechanical characteristics.

Three coating processes, namely Cathodic Arc Evaporation (CAE), direct current Magnetron Sputtering (dcMS), and High Power Impulse Magnetron Sputtering (HiPIMS), are examined to identify the optimal coating process. After achieving the best mechanical and tribological properties, the focus shifts towards enhancing thermal stability. This is accomplished by incorporating additive elements, namely Al, Cr, and Si, into the coating. Oxidation experiments are conducted with different coating compositions to validate the chemical composition and determine the required ratios of Al/Cr, Al/Si, and Al/(Cr+Si) needed to maintain the desired (fcc) structure.

The study involves characterizations at multiple scales, including macro, micro, and nano levels. Furthermore, experiments aim to refine grains, increase hardness, elastic modulus, and wear resistance. The study also investigates oxidation mechanisms. The findings reveal that both mechanical and oxidation behaviors are influenced by the coating composition, deposition method, and their parameters. These factors impact crucial aspects such as crystallinity, composition, surface roughness, grain size, and orientation.

The study is divided into two main parts. The first part sets out to identify the research that was already carried out, introduce the fundamental concepts, present the characterization techniques employed, and describe the experimental setup. Further, work to enhance the understanding of thermal stability and the mechanical properties of ternary (Ti, Al)N HiPIMS

coating under different process parameters is presented. It concludes with the study of the additions of Al, Cr or Si to these ternary coating systems followed by two different compositions of quaternary nitrides coating (Ti, Al, Cr)N and (Ti, Al, Si)N. It ends with a study on quinary (Ti, Al, Cr, Si)N coating. The fundamental mechanisms that yield the good properties of (Ti, Al, Cr, Si)N were not understood at the beginning of this work.

The high-temperature mechanical properties, thermal response, microstructure and phase evolution of this quaternary and quinary system have been characterized and is presented in the second part of this thesis. The research result is presented in three scientific publications I, II and III, which are briefly described below:

**In Paper I**, a large range of Ti<sub>50</sub>Al<sub>50</sub>N HiPIMS coating process parameters was studied. The aim was to understand the effect of different coating conditions on the growth of TiAlN films and to better tune the coating properties of the film deposited by HiPIMS in comparison with a Cathodic Arc Evaporation (CAE) deposition process with regard to their tribological performances. Regarding the mechanical properties of the coating, it has been found that both CAE and HiPIMS produce TiAlN coatings with compressive stresses. The evolution of stress can lead to very high values superior to -5000 MPa by controlling the energetic deposition conditions such as the applied duty cycle, bias and power.

However, no direct correlation was found between the values of hardness and the level of compressive stress for TiAlN HiPIMS coating, which is not the case with Arc coatings. Both coatings have the hardness range of 30 - 35 GPa. An improvement of tribological coating properties was achieved by TiAlN HiPIMS coating since the Young's modulus can easily be tuned by changing the HiPIMS deposition conditions, which is an advantage as it is known that tribological coating properties are linked to the ratio of both H/E (Hardness/Young's modulus) and  $H^3/E^2$  (plastic deformation).

**In Paper II**, the influence of Cr additions on the structure, mechanical properties and oxidation resistance of different Al<sub>x</sub>Ti<sub>y</sub>Cr<sub>z</sub>N HiPIMS coatings were studied. The stability of the nitride layer until 950 °C was reported. Furthermore, the oxidation resistance and the oxide scale characterization of different Ti/Al ratios and Cr content was detailed discussed.

Regarding the oxidation behavior at 950 °C, different oxidation durations were carried out using sequential steps of <sup>18</sup>O<sub>2</sub> with <sup>16</sup>O<sub>2</sub>, then the oxide part was analysed by Secondary Ion

Mass Spectrometry and Atom Probe Tomography. From all this data, an oxidation mechanism was proposed, and the oxide part consisted of a double oxide layer. The TiO<sub>2</sub>-rutile at the upper surface is followed by (CrAl)<sub>2</sub>O<sub>3</sub> underneath. The Cr content decreases the outward diffusion of Ti to the surface. Also, increasing the Al content in the coatings reduces dramatically the total oxide thickness. In the (CrAl)<sub>2</sub>O<sub>3</sub> layer, the Cr concentration was increasing through the layer from the upper part to the interface between oxide and nitride. Hence the Al<sub>2</sub>O<sub>3</sub> is the main oxide present in the upper part of this layer followed by the (CrAl)<sub>2</sub>O<sub>3</sub> oxide present in the bottom part of this layer with small TiO<sub>2</sub> islands.

**In Paper III**, the effects of Si additions on both of the TiAlN and TiAlCrN coatings with a Si content between 0 to 5 at.% were studied. It was noticed that the Full Width at Half Maxima (FWHM) increased with improving Si addition for TiAlSiN coatings whereas TiAlCrSiN coatings show reverse behavior. The highest value of H/E ratio was 0.09 for both coatings' alloys.

At 950 °C, the oxidation mechanisms and the kinetics of the oxide growth for various durations were determined using sequential steps of <sup>18</sup>O<sub>2</sub> with <sup>16</sup>O<sub>2</sub> of these two coatings with different Si contents. By combining the investigations of the X-ray Diffraction (XRD), the Transmission Electron Microscopy (TEM), the Dynamic Secondary Ion Mass Spectrometry (D-SIMS) and the Atom Probe Tomography (APT) of the different oxidized coatings, a complete study of the different oxide layers was achieved. At 950 °C, the oxidized coatings of TiAlSiN show better oxidation resistance than oxidized coatings of TiAlCrSiN. A bi-layered oxide, with Al<sub>2</sub>O<sub>3</sub> outward and TiO<sub>2</sub> underneath was formed at the oxidized coatings of TiAlSiN. While the oxidized coatings of TiAlCrSiN show a triple-layer oxide with TiO<sub>2</sub> outward and Al<sub>2</sub>O<sub>3</sub> underneath followed by a mixed oxide region of (CrAl)<sub>2</sub>O<sub>3</sub> and small TiO<sub>2</sub> islands and an amorphous SiN<sub>x</sub> surrounding the oxide.

A graphical abstract of the thesis is presented in figure 1.2. More details of the papers' scope and interrelation is given in section 7.

A detailed review of the coating deposition processes and their impact on hardness, wear resistance, oxidation resistance, and thermal stability can be found in Section 6. Section 6 also explores the mechanisms involved in the oxidation processes.

## Hard AlTiN coatings produced by HiPIMS with high-temperature resistance - influence of Cr and Si additive elements

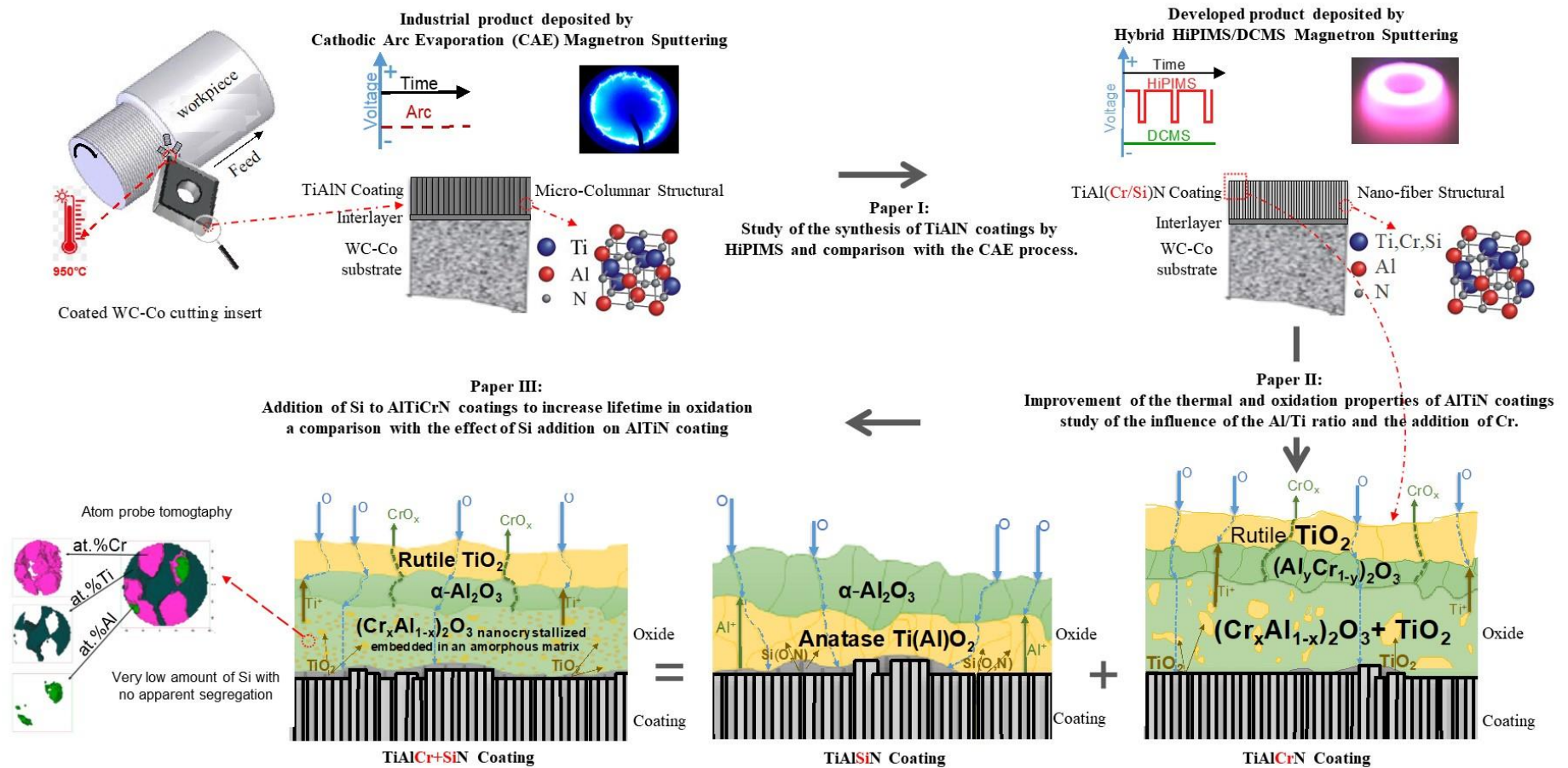


Fig. 1.2 Graphical abstract of the thesis arranged as a cumulative dissertation of papers: I, II and III.

## 2 State of the art

Titanium nitride is a hard material, often used by PVD coating on tungsten carbide to improve the substrate surface properties. This section will present an outline of the deposition technologies relating to nitride hard coating, as well as the evolution of hard coatings alloy based on TiN.

### 2.1 Synthesis and film deposition

Over more than a century ago, it was known that ions bombarding a surface can lead to particles being knocked out of this surface and condensing on a nearby surface, so-called substrates that usually face the material's source [5]. In 1902, Edison et al. reported the first commercial application of thin film deposition [6]. There are numerous techniques to prepare thin films. Film applications and properties define the suited technique to prepare it, such as shape and dimensions of the substrate, film thickness, interfacial adhesion, level of acceptable impurities in the film, surface roughness and electrical conductivity of the deposited material and the substrate, etc. Moreover, depositing the same material with different techniques will have different properties.

The Physical Vapor Deposition (PVD) is the most flexible technique that allows one to deposit a large number of materials, including those with a high melting point, metal alloys and even dielectrics. PVD is used to classify a group of vacuum-assisted processes for thin-film deposition. The film growth is influenced by an evaporation film of precursors (mostly neutral atoms or ions). The latter are produced either by thermalizing (e.g., laser ablation, electron beam and arc discharge), or produced by ion bombardment-induced sputtering of the solid-state source material, so-called target. The target atoms are released from the surface by physical bombardment by energetic ions. These ions can be created from a plasma discharge maintained directly above the sputtered target (e.g., magnetron sputtering), where the target serves as the driving cathode, and the substrate holder that faces the target, as well as all the walls of the surrounding deposition chamber, act as the anode. The target can consist of either metals, alloys or compounds. In the case of a reactive deposition process, condensation involves the reaction of the condensing material with a reactive gaseous species (e.g., N<sub>2</sub>, O<sub>2</sub>, CH<sub>4</sub>) in order to create the compound.



### 2.1.1 Magnetron sputtering

In sputter coating, the material from the target (cathode) is ejected by ion bombardment (e.g. Ar ion) and momentum is transferred from the atom ion or cluster towards the substrate (anode).

The fundamental operations are occurring as a result of a collisional cascade initiated at the cathode surface by incident energetic projectile particles. These particles are usually gas ions that are accelerated by the strong electric field of the plasma sheath adjacent to the cathode. In principle, when two particles collide, one or both particles may change their momentum or their energy, neutral particles can become ionised, and vice versa. The incident ion first impacts the cathode surface or near-surface atoms of it and conveys some of its energy to the surrounding atoms. If this energy is high enough to break the atomic bonds and to dislodge some of the impacted atoms, one or more of these atoms may be removed from the cathode surface. Reactive gases can be used regarding their high chemical reaction which occurs on the exposed cathode surface, where the reactive gas binds with the sputtered material and forms a compound.

We should consider collisions/ interactions between all these species since the glow discharge contains electrons, different types of ions, neutral atoms and molecules as well as photons [9]. These reactions are vital for the formation of the desired coatings. A simplified magnetron configuration, similar to the one used in this study, can be seen in figure 2.1 with the most important collisions.

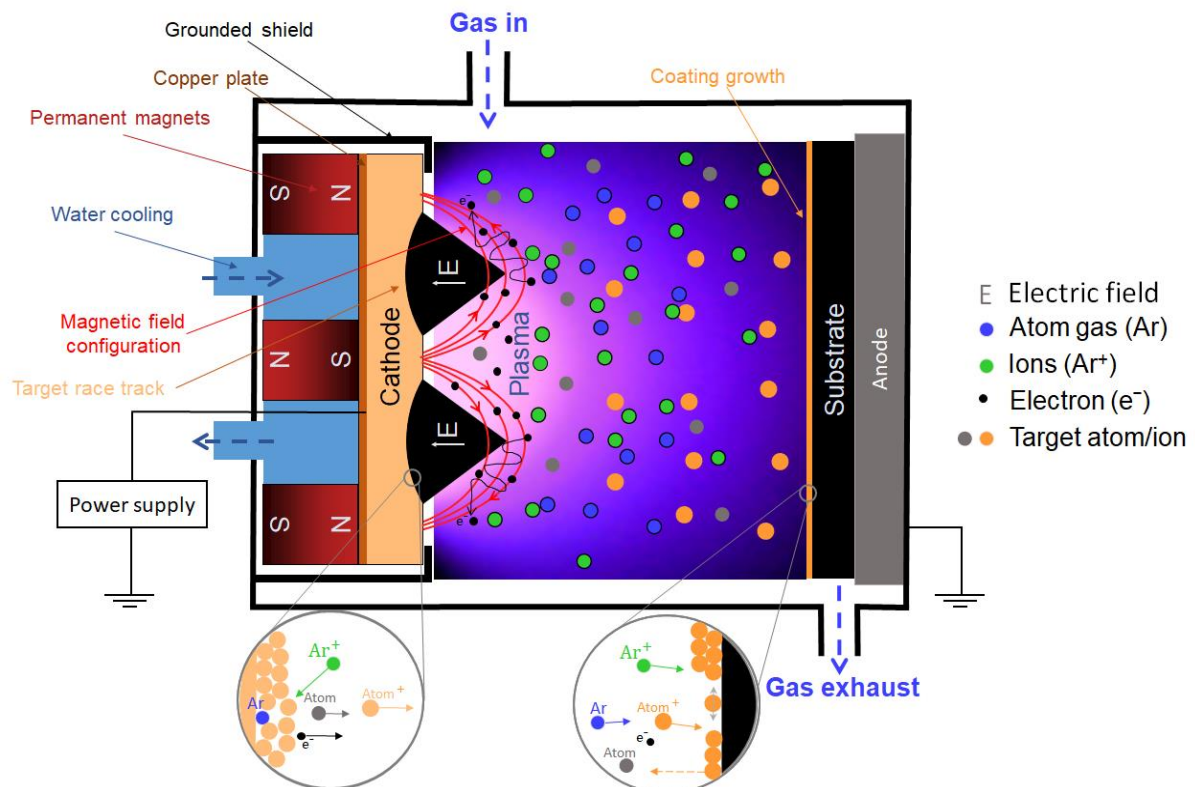


Fig. 2.1 Schematic drawing of a magnetron-sputtering source in the side view presented the magnetic field distribution of the magnetron and the possible transport of electrons, the principle of ions generated in plasma and accelerated towards a target sputter material, which condenses at the substrates.

The magnetic field in the sputtering system is used to extend the lifetime of the electrons escaping from the cathode. Consequently, the electrons readily follow the magnetic field lines where the ions generated are hardly affected by the magnetic field due to their relatively high mass. Therefore, only electrons can be entrapped in the magnetic field while the ions can more or less freely move across the magnetic field lines. For instance, the exothermic reactions of both ions and excited species upon their collisions with the other species significantly contribute to the chemistry in the discharge and to the reactions on the treated surfaces/ growing films.

In addition, the applied power (Watt per square centimetre) has a major influence on the ion density, degree of ionisation species, and ion energies. Hence the applied power has a strong effect on coating growth and film properties. Further advances in the magnetron sputtering technique are one of the subjects of this work.

## 2.1.2 High-Power Impulse Magnetron Sputtering

In 1999, Kouznetsov et al. introduced a promising technology called high power pulsed magnetron sputtering (HPPMS) which is known today as HiPIMS [7]. HiPIMS discharge is a rapidly developing deposition technique based on high-power unipolar pulses that are applied to a target at a low duty cycle (ratio of pulse on-time over off-time), usually 0.5 – 5 %. It is thus possible to stay below the power limit for target overheating while at the same time achieving high-density plasmas with peak power densities on target in the 0.4 - 10 kW/cm<sup>2</sup> range and highly ionised flux of the sputtered material. These ionised atoms have much higher energies than sputtered atoms in conventional magnetron sputtering and result in very dense and stable films [8]. Typically, with a voltage value in the range of 500 - 2000 V. The consequent power densities of HiPIMS can exceed the ones used in dcMS by up to two orders of magnitude, which generates peak current densities on target of up to 3 - 5 A/cm<sup>2</sup> [9]. Table 2.1 compares some of the operational parameters for HiPIMS to those obtained in conventional dcMS discharges. The biggest difference between them lies in the power supply. The power is delivered in pulses to the plasma and is often quenched during the cycle, hence the need for a power supply that can store the energy and release it in a short interval for HiPIMS. Therefore, the principle of operation is rather simple and consists of a large capacitor to store the energy, a charging circuit to replenish the capacitor in the discharge time-off and a fast-high current switch. The pulse has a square shape and is 20 - 500  $\mu$ s long, with a low repetition frequency of usually 50 – 5000 Hz. Anders et al. define HiPIMS from other pulsed magnetron processes as a pulsed magnetron sputtering technique where the peak power during the pulse exceeds the time-averaged power by typically two orders of magnitude [10].

Table 2.1 Typical dcMS and HiPIMS selected parameters. Reproduced from [9, 11 & 12]

Parameter	dcMS	HiPIMS
Discharge voltage (V)	300 - 700	500 - 2000
Maximum power density (kW/cm <sup>2</sup> )	Up to 0.05	0.4 - 10
Maximum current density (mA/cm <sup>2</sup> )	4 - 60	500 - 5000
Duty cycle (%)	100	0.5 - 5

Electron density ( $\text{m}^{-3}$ )	$10^{15} - 10^{17}$	$10^{18} - 10^{19}$
Electron temperature (eV)	1 - 5	1 - 5
Ionized density fraction of the sputtered material (%)	<1	$\geq 50$
Ion energy (average for metal ions) (eV)	5	20

Recent research in HiPIMS has improved the ability to fabricate highly dense coatings exhibiting superior material with functional characteristics. Hence HiPIMS has led to a significantly improved film homogeneity and decreased surface roughness, even for complex-shaped substrates [13 - 15]. Matej et al. reported that HiPIMS could provide rich metal-ion fluxes to the substrate, which enables the discharge operation in a self-sputtering mode [16]. Self-sputtering mode is considered as a powerful tool for adhesion pre-treatment for protective coating preparation, due to its ability to clean surfaces and prepare nanoparticle-free interface, which provides the best conditions for local epitaxial growth over large surface areas. The high metal ion content in the bombarding flux modifies the interface to include a metal implantation zone that promotes a strong bond between the substrate and the subsequently deposited coating [17].

However, the ionisation rate is raised usually under extreme sputtering conditions such as very high instantaneous power or low pressure. The flux of ionised sputtered particles is generally considered largely beneficial to the film growth as the ions can significantly increase the ad-atom mobility on the substrate and help grow films far away from thermal equilibrium. It also becomes possible to control the metallic ion bombardment by biasing the substrates, leading to an improvement of the film density and adhesion [18 & 19].

Figure 2.2 shows the discharge voltage and current traces taken from a HiPIMS discharge. This configuration exhibits a rather rectangular voltage pulse and slow growth of the discharge current during the pulse. The discharge pulse starts with applying a voltage to the target. Respecting the target voltage, the discharge current builds up with a well-defined delay, which is due to the time needed to create ionisation avalanches until the full electrical breakdown is achieved. The discharge ignition is also accompanied by strongly negative plasma potentials as well as high axial electric fields, which indicates a strongly expanded sheath. The evolution of the plasma potential  $V_p$  is sensitive to the distance between target-substrate, the applied pressure and power density [20 & 21]. The ignition stage of the

HiPIMS discharge is followed by a change of the gas composition in front of the target, where a rarefaction of the working gas in front of the target during magnetron sputtering is caused by momentum transfer between the highly-directed sputtered particles and the working gas atoms [22]. This effect is pronounced due to the enormous discharge current and high sputtering rates associated. However, if a large fraction of multiply charged ions can be produced, secondary electron emission can be sustained, the discharge can be operated in a self-sustained sputtering mode without the presence of working gas [23].

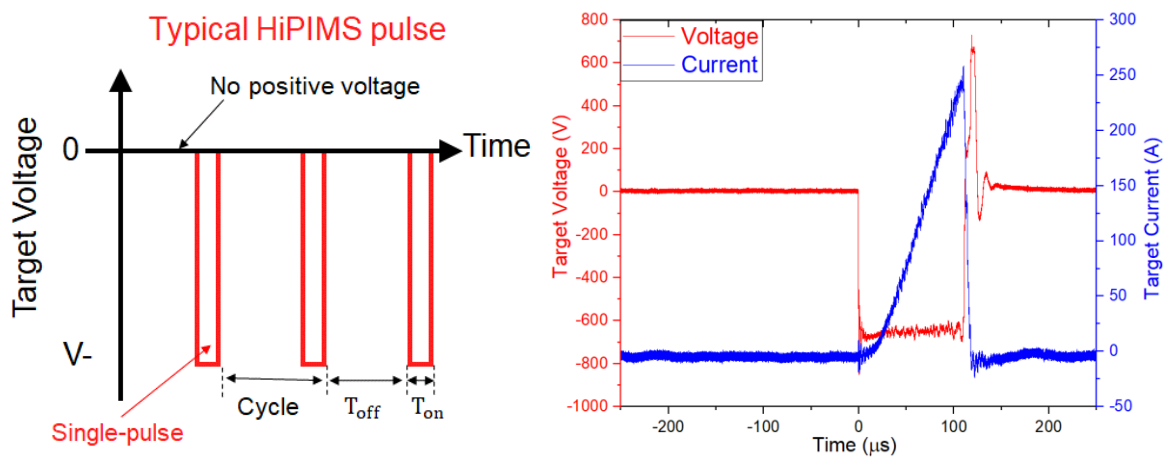


Fig. 2.2 Schematic drawing of a typical HiPIMS pulse (right) and an example of waveforms traces from the HiPIMS discharge operated at duty cycle 5.5%, time-on 110  $\mu\text{s}$ , time-off 1890  $\mu\text{s}$ , peak power density 0.5 Kw/cm<sup>2</sup> (left)

A common way to define the strength of the pulse is to define the pulse energy. The pulse energy can be obtained by measuring the voltage and current (as in figure 2.2 right) and multiplying the two traces. The result is the discharge power as a function of time. The integration of this curve then gives the pulse energy.

### 2.1.3 Comparing coating approaches of HiPIMS and dcMS techniques

The main advantage of HiPIMS compared to dcMS is the high ionisation rate of sputtered material even if both discharges are operated at the same average power. Figure 2.3 shows the different deposition rate for several target materials prepared by dcMS and HiPIMS coatings using the same conditions.

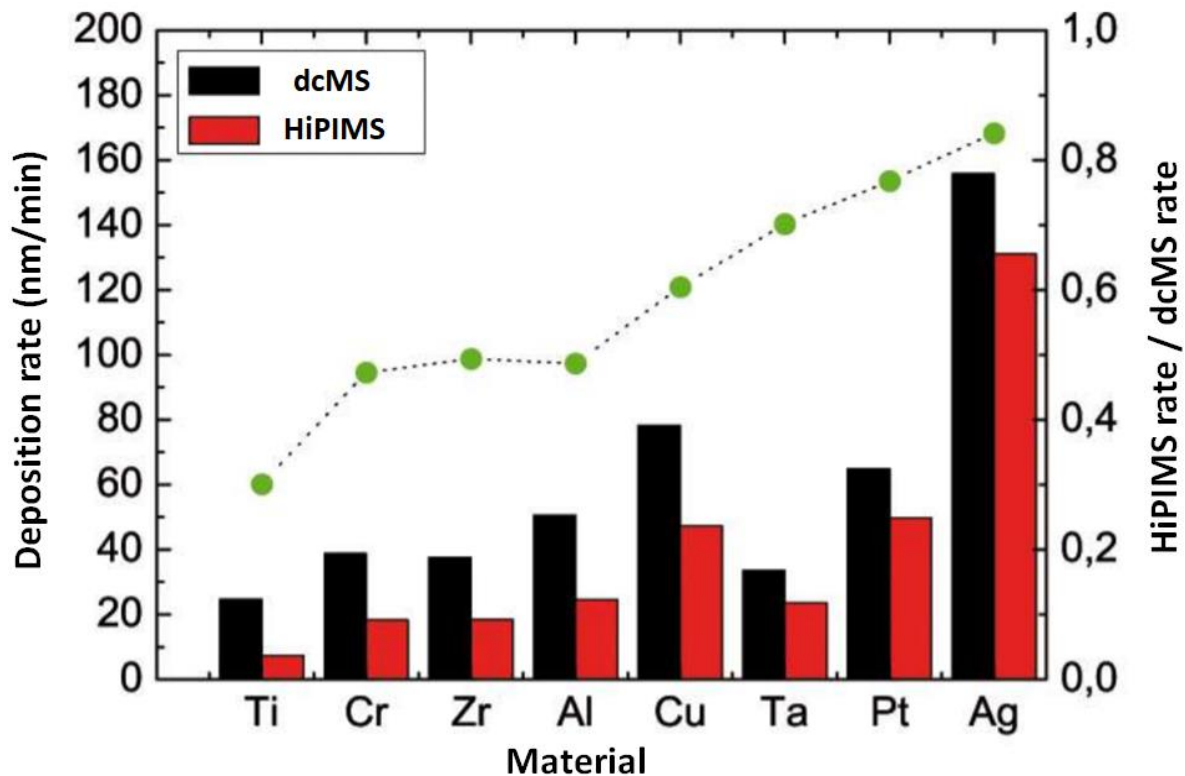


Fig. 2.3 Different deposition rate for several target materials prepared by dcMS and HiPIMS coatings using the same conditions. The deposition rate of HiPIMS over dcMS is plotted as scattered points (right axis) and dcMS deposition rate is plotted as bars (left axis). Modified from [25]

The flux of ionised (sputtered) particles was found to be beneficial for the film growth. Moreover, the ionisation of the sputtered flux yields the deposition rate, as the ionised particles have to overcome the plasma potential barrier towards the substrate. The sputter yield  $Y$  is defined as the mean number of atoms removed from the target surface for each incident ion. The deposition rate is proportional to the sputtering yield. It is good to have a maximal sputter yield since this means a higher deposition rate of sputtered material [25 & 26].

Since the movement of the charged species is subject to magnetic fields, the transport of the ionised fraction of the sputtered material is largely affected by the magnetic field configuration of the deposition system. In general, the sputter yield depends on the energy of the incoming projectile ion, the ion incident angle in relation to the target normal, the bombarding ion mass, and the target material [27]. By modifying the magnetic field between the target and substrates and thus the trajectory of the incoming ion, deposition rate of HiPIMS can be increased [28]. Several studies were conducted to investigate the origin of the

apparently lower deposition rates and to overcome this disadvantage of depositing films with HiPIMS. Among these studies an improvement in the deposition rates was noted by using multiple targets arrangements and co-deposition HiPIMS/dcMS configurations.

Based on such a configuration, it is now possible to superimpose signals or to connect the DC power supply in parallel with the HiPIMS power supply to multiple targets. The main advantage of such a parallel combination of dcMS and HiPIMS is a preionization of the discharge plasma before the HiPIMS pulse ignition [29]. The second advantage is a higher deposition rate compared to arc evaporation technology. Lately, different hybrid HiPIMS depositions techniques were applied. For example, integrating the HiPIMS with DC, RF, MF or pulsed power. This effort is aiming to obtain the specific morphology and microstructure of the thin film. Greczynski et al. used a hybrid HiPIMS/dcMS configuration to do co-sputtering from two metal targets, Al and Ti. He reported that the TiAlN coating produced by Al-HiPIMS/Ti-dcMS has higher hardness and relatively lower compressive stress than the coating produced by Ti-HiPIMS/Al-dcMS [30]. Luo et al. reported that the TiN coatings deposited by hybrid HiPIMS + dcMS are slightly harder with a significant decrease in the residual compressive stress than TiN coatings deposited by dcMS alone [31]. Holtzer et al. studied the enhancement of deposition rate yielding to higher flux toward the substrate at lower pressures as well as the change of NbSi films from columnar structure deposited by HiPIMS to amorphous deposited by hybrid RF + HiPIMS using dual co-sputtering systems with one Si target connected to RF and the other Nb target connected to HiPIMS [32].

Hybrid HiPIMS is not only a conventional process with its power quenched into only a fraction of ionization time of sputtered particles but it shows a couple of unique features, including strong rarefaction of the working gas, better stability of deposition process and suppression of arcing. Furthermore, the magnetron sputtering of the hybrid-HiPIMS systems can operate at a lower pressure than conventional HiPIMS systems [33 - 35]. The aim of this new system is to combine several different coating properties in one high-performance coating system in order to decrease the defect density and to improve the surface roughness compared to the classic cathodic Arc technology. One disadvantage can be that, by comparison with the Arc process, magnetron HiPIMS is considered a slow deposition process. However, newly developed hybrid generators enable the use of a DC power supply with superimposed HiPIMS pulses. This increases the number of sputtered particles, hence the deposition rate, while keeping the advantages of this innovative technology. In this study,

we utilized a co-deposition approach, combining HiPIMS for one target and dcMS for the other. This process enabled precise control over the concentration of additive elements, specifically Si and Cr, within the (AlTi)N HiPIMS coating by adjusting the applied current of dcMS.



## 2.2 Hard nitride coating system

### 2.2.1 Ti-Al-N

Since the 1980s (Ti, Al)N system replaced the use of (Ti)N systems for industrial protective coating of cutting tools. The (Ti)N system belongs to the transition metal nitrides with NaCl-type B1 structure, which are described as two face-centred cubic (fcc) crystal structures with one-unit cell shifted half an a-axis towards the other. One (fcc) lattice is occupied by N atoms and the other by Ti atoms. One main characteristic of the (Ti)N system is that it can accommodate a large quantity of nitrogen deficiency via nitrogen vacancies in the N lattice [36], making the (Ti)N system stable over a large compositional range ( $0.64 \leq N \leq 41.2$ ) [37]. TiN films exhibit high hardness ( $31 \pm 4$  GPa), good thermal conductivity (10 – 12 W/mK), relatively low friction coefficient against steel ball (0.5 – 0.63), good corrosion resistance and reasonable coating adhesion [38 - 40]. They show a limitation of oxidation resistance where the onset of oxidizing is at  $\sim 550$  °C, forming rutile ( $\text{TiO}_2$ ) [41]. On the other hand, (Al)N system has a hexagonal (wurtzite) structure. This phase does not accommodate any excess nitrogen or aluminium in thermodynamic equilibrium. Therefore, alloying aluminium to the (Ti)N system improves the mechanical properties of (Ti, Al)N coatings system at elevated temperatures compared to poor oxidation resistance of the (Ti)N system. (Ti, Al)N coatings deposited by PVD, exhibit a hardness of  $\sim 30$  GPa, low thermal conductivity (4.5 – 5.5 W/mK) and good wear resistance [39, 42 & 43].

Different studies have covered the effects of nitrogen on the growth morphology and mechanical properties of TiAlN thin film coatings. They reported that decreasing  $\text{N}_2$  flow rate for  $\text{Ti}_{1-x}\text{Al}_x\text{N}_y$  films present two phases c-AlN and w-AlN where the Al is ( $0.52 < x \leq 0.59$ ) [44]. The impact of nitrogen vacancies at elevated temperature shows a substantial improvement of the thermal stability by reducing the nitrogen content for alloys with Al of ( $x = 0.48$  and  $0.60$ ). Alloys with  $x = 0.28$  presented nucleation and growth of Al-Ti clusters inside the grains and w-AlN formation at grain boundaries and N deficiency from ( $y = 0.92$  to  $0.75$ ) [2]. Additionally, they reported that the film deposited at the higher  $\text{N}_2$  flow rates has denser and finer grained morphology compared with that deposited at lower rate. This morphological change is very important for the oxidation resistance since oxygen can diffuse through the column and grain boundaries [45]. A reduction of N in TiAlN increases the driving force for the formation of a metallic c-AlTi mixture.

It is worth mentioning that both N and Al concentrations play a significant role in the mechanical and thermal properties. In addition, the nitrogen partial pressure applied during the process affects the Al content and the microstructure of the coating. In this thesis, the N concentration was kept stable at  $y=1$ . The impact of varying nitrogen concentration is beyond the scope of this thesis but should be taken into consideration for future studies.

The mechanical properties and the oxidation resistance increase with higher Al content as long as a cubic crystal structure can be maintained. Al addition forms a metastable solid solution  $c\text{-(Ti}_{1-x}\text{Al}_x\text{)N}_y$  coating obtainable in a wide compositional range of Al metal fraction. When Al fraction is  $x < 0.67$  and the N to metal ratio is  $0.37 \leq y \leq 1$ , the structure is similar to that of (Ti)N system where two (fcc) sub-lattices are interpenetrated. One (fcc) lattice is randomly occupied by Ti or Al atoms, and the other by N atoms. This is the miscibility gap of the quasi-binary isostructural (B1) TiN-AlN phase (Figure 2.4). It has been reported by several authors that the maximum mixing enthalpy within the spinodal region ( $x \approx 0.67$ ) will tend to phase separate into coherent  $c\text{-AlN}$ ,  $c\text{-TiN}$  via spinodal decomposition instead of the thermodynamically stable phases  $w\text{-AlN}$  and  $c\text{-TiN}$ . Further increasing Al content yields a dual-phase (fcc) and hexagonal (hcp) crystal structure. After that, when  $x \approx 0.8$ , the system will lead to an overall decreased energy. Therefore, no nucleation site is required to initiate the segregation of TiN and AlN. Also, the structure will change from (fcc) B<sub>1</sub> to (hcp) B<sub>4</sub>, which is explained by the electronic structure mismatch between TiN and AlN, stronger in the Al-rich side [46 & 47]

Spinodal decomposition is a mechanism where an initial phase separates into two phases without a nucleation barrier. The main advantage of spinodal decomposition is the formation of nanometre-sized  $c\text{-AlN}$  and  $c\text{-TiN}$  domains. The difference in elastic properties and lattice parameters between the different domains leads to coherency stress and because of this high micro-stress level, propagation of dislocations is obstructed and results in an increase in hardness (Koehler-type hardening), resulting in age hardening [2]. In other words, the mixing enthalpy of  $c\text{-(TiAl)N}$  is positive and contains a spinodal region, which is an unstable system. It is therefore expected to transform into a more stable form upon exposure to high temperatures which is the mechanisms behind the age hardening [48]. According to Zhou et al. [49], the increase in hardness can be explained because of bonding characteristics. With the addition of Al the interatomic distance decreases (as compared to the consideration of the

lattice parameter). This leads to an increasing bulk modulus and consequently to a distinct increase in hardness [46].

In general, the system is stable if its energy is minimized. If the system in a given environment has enough time it will eventually transform into its most stable form. The energy of a system may have several different local minima corresponding to different phases. The relative energies of different phases will only determine the magnitude of the forces that may drive a transformation. This energy is named Gibbs free energy. For example, if the system is not in its global minimum, there is a driving force for lowering the energy and when the temperature is increased, the atoms have higher kinetic energy and thus have a higher chance to rearrange into a more stable phase. The most stable phase will always prevail, but the temperature will control at which rate the decomposition occurs. A phase transformation describes the change in a system from an initial state to a new one. The driving force for this is the minimization of the system's Gibbs free energy. In alloys, different elements are mixed together, and more than one phase can be stable for the same condition. Therefore, Gibbs free energy becomes composition, temperature and pressure dependent [1].

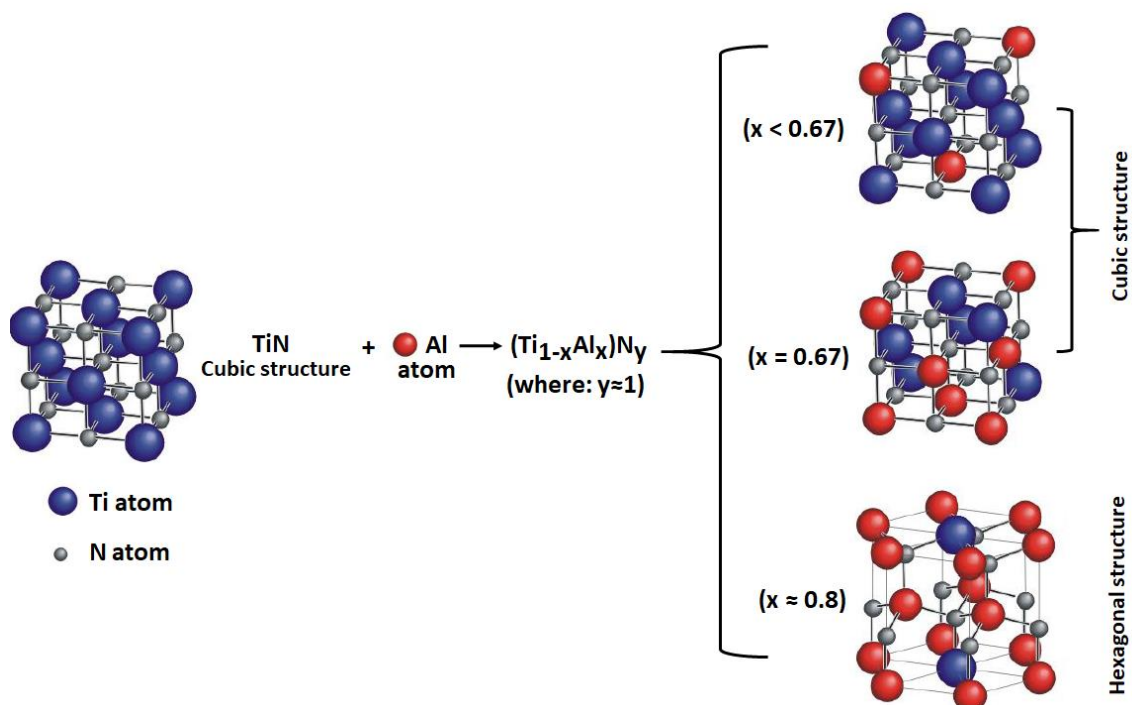


Fig. 2.4. Schematic drawing of the structural development of the TiN system with increasing Al addition. Modified from [50].

McIntyre et al. reported on a thermodynamically metastable system of  $\text{Ti}_{0.5}\text{Al}_{0.5}\text{N}$  coating before showing a phase separation or precipitation of AlN phase at 1.5 h of annealing at 900 °C [51]. Another author reported on the stability of arc  $\text{Ti}_{0.33}\text{Al}_{0.67}\text{N}$  coating for 2 h annealing at 900 °C [52].

In the HiPIMS coatings, vacancies and dislocations are very high. This yields high hardness of the coatings in their as-deposited state due to the coating's non-equilibrium state. When the temperature is increased, the number of vacancies and dislocations is lowered and the hardness decreases. This process is referred to as recovery. The recovery is an irreversible process. As mentioned above, c-AlN is a metastable phase with a small volume mismatch with c-TiN in comparison to w-AlN. A difference in volume of 22.5 % between c-AlN and w-AlN exists [53 & 54].

## 2.2.2 Ti-Al-Cr-N

In recent years, attempts to increase the service life of (Ti, Al)N coated cutting tools and to decrease the cost of production have become a key factor in hard coatings research for elevated temperatures applications. Some of the approaches are adding a third metal element like Cr, Si, Y or Ta to the system in order to modify the coating properties [55 - 58].

Adding Cr to the (Al)N system delays its transformation from fcc into wurtzite phase due to the fact that the Cr is participating in generating better thermal stability and ageing of the fcc-AlN phase after the spinodal decomposition. Consequently, Cr improves the oxidation resistance and the tribological performance of AlN coatings [59].

At the working temperatures of cutting tools (650 - 950 °C), the mechanical properties of the TiAlN coatings benefit from phase transformation. Due to the unstable nature of the (Ti, Al)N system, this improvement upon high-temperature exposure is known as age hardening. In contrast, (Cr,Al)N coatings do not demonstrate the age hardening to the same extent as in (Ti,Al)N system, which means Cr addition to (Ti,Al)N leads to lower hardness [60 - 62].

Yamamoto et al. found that the  $(\text{Ti}_x, \text{Cr}_y, \text{Al}_z)\text{N}$  coatings with  $(x:y ; 1:2)$  and  $(z \sim 0.7)$  revealed a drastic change of hardness upon the phase change from hexagonal (B4) to cubic (B1) structure under approximately 50 V of changing bias [63].

Forsèn et al. published that the  $(\text{Ti}_x, \text{Cr}_y, \text{Al}_{60})\text{N}$  coatings with  $(x < 10)$  should not decompose spinodally, in contrast to  $(x > 30)$ . Therefore, going from low to high Ti content (from  $x < 10$  to  $x > 30$  at.%) consorts with the transition of the decomposition process from nucleation and growth to spinodal decomposition. The homogeneous distribution of Ti atoms in the TiAlN coating remained the obstructing Al diffusion and thereby slowing down the growth of wurtzite AlN phase. Because of this, the hardness is retained at higher temperatures compared to pure (Cr, Al)N coatings [64].

Luo et al. reported a decrease in energy when Cr content decreases in the  $(\text{Ti}_x, \text{Cr}_y, \text{Al}_z)\text{N}$  coating. The decrease in energy can be identified as a spinodal region in the mixing enthalpy of TiCrAlN, e.g. c-TiAlCrN coatings can be deposited when the  $(y+z \sim 65$  at.%) unless the Al and Cr concentration is increased where h-AlN will form and the hardness decreases. The hardness is strongly related to dislocation movement. Dislocation movements can be altered

if nanometre-sized coherent regions with different composition and elastic constants are formed in the material. Spinodal decomposition is one mechanism to form such regions [65].

In short, (Ti, Cr, Al)N contains two important properties, which originate from two different coatings, CrAlN and TiAlN, in order to have both oxidation resistance at elevated temperatures and improved hardness.

Adding Cr to TiAlN affects the diffusion, namely altering the driving force for spinodal decomposition and its kinetics. The migration mechanism during the decomposition is substitutional, and the diffusion mechanism is on the metal sub-lattice. The presence of Cr obstructs the segregation of Ti and Al because of its relatively favourable miscibility and large atomic size [66].

In the (Ti, Al, Cr)N system, the most immiscible component is c-AlN with the largest gap versus c-TiN. The system becomes more stable with increasing Cr content because the ternary c-TiCrN is less stable for all compositions, while the binary c-TiN, c-CrN and c-AlN are the most stable components in the system. Therefore, there is a driving force for the transformation of c-AlN into its stable form h-AlN, as well as for the transformation of c-CrN into one of two stable forms hexagonal  $\beta$ -Cr<sub>2</sub>N or bcc-Cr, which appear at high temperatures [65].

The different lattice parameters of binary c-TiN, c-CrN and c-AlN components lead to increased strain energy which is associated with the coherent segregation of the elements during the spinodal decomposition of c-AlTiCrN. This strain energy increases the force required for a dislocation to pass the domains with different compositions. Therefore, the movement of the dislocations is obstructed, and the material becomes harder. The hardening effect is stable as long as the domains remain coherent. When the domain size is increasing, the strain becomes too large during the coarsening and above some critical size, misfit dislocations are introduced hence reducing the strain. The material is then over-aged and results in a lower hardness [67 - 69].

### 2.2.3 Ti-Al-Cr-Si-N

The influence of doping elements is a very important factor in tailoring the properties of TiAlN-based coatings. It has been found that the addition of Cr or/and Si can improve both thermal stability and mechanical properties of the quaternary nitride coating.

Linqing He et al. published that the doping of Si into (CrAl)N system positively affects the thermal properties and demotes mechanical properties as a result of forming a wurtzite AlN phase [70]. Siwawut et al. tested the cutting performance and mechanical properties of TiAlSiN and CrTiAlSiN coatings deposited by Arc on WC substrate in the dry milling of cast iron using 140-300 m/min cutting speed. TiAlSiN shows the highest hardness (21 GPa) and Young's modulus value compared to CrTiAlSiN [71]. Kulkarni et al. studied the cutting forces of AlTiN, AlTiCrN coated cutting tools in dry turning of stainless steel using 140-320 m/min cutting speed. The AlTiCrN coating exhibited the lowest cutting force values and smoothest surface compared to AlTiN [72].

Chowdhury et al. reported the mechanical properties of TiAlCrSiYN/TiAlCrN multilayered coating for different layer thicknesses. They conclude that the hardness is in good relation with the layer thickness and the best hardness is for the thinner interlayer thickness of 300 nm [73]. Zhang et al. did a comparison study between AlTiN monolayered and AlTiN/AlCrSiN nano multilayered coating. They conclude that the coating with multilayered 8.3 nm thickness has the best hardness and Young's modulus 37.5 GPa and 486.9 GPa, respectively [74].

Kim et al. studied a multilayered structure of TiCrAlSiN deposited on steel using a cathodic arc deposition method at a bias voltage of -200 V and pressure of 4 Pa. These coatings showed good mechanical properties with super hardness (~43 GPa) and Young's modulus ~560 (GPa) [75].

Table 2.1 summarises the best mechanical properties of different development regarding monolayered, multilayered and nanolayered TiAlN-based coatings reported by different research groups.

Table 2.1. The hardness, Young's modulus and,  $H^3/E^2$  factor values for different TiAlN-based coatings

Coating	Hardness	Young's modulus	$H^3/E^2$
	(GPa)	(GPa)	(GPa)
monolayer-TiAlN [76 - 78]	29.2 - 34.9	482 - 511	0.10 - 0.16
monolayer-AlTiN [79]	20.0 - 24.3	337 - 358	0.07 - 0.11
monolayer-TiAlSiN [71]	25.2 - 29.8	266 - 289	0.22 - 0.31
monolayer-CrTiAlSiN [71]	24.0 - 27.1	200 - 275	0.34 - 0.26
multilayer- TiAlSiN [80]	32.2 - 37.5	400 - 415	0.20 - 0.30
multilayer-TiAlN [81 & 82]	29.0 - 37.1	370 - 462	0.17 - 0.23
multilayer- TiAlN/CrN [83 & 84]	37.0 - 41.1	420 - 475	0.28 - 0.30
nanomultilayer- TiSiN/TiAlN [85]	33.0 - 39.0	550 - 570	0.11 - 0.18
nanomultilayer- AlTiN/AlCrSiN [74]	31.0 - 38.5	410 - 450	0.17 - 0.28

The research trends for TiAlN-based coatings are intensively focused on the development of novel nanocomposite and/or nano-layered coating to improve the coating properties. Therefore, a high number of papers have been published on this topic, rather than focusing on the alloy of monolayered coating alone. The (Ti, Al, Cr, Si)N system shows promising results in terms of mechanical properties and thermal stability however, the amount of research made on them is still quite sparse. Therefore in this thesis, we gave this quinary monolayered coating high attention.



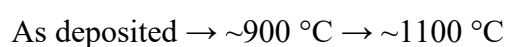
## 2.3 Hard nitride coating system at high temperature

### 2.3.1 Ti-Al-N

At high temperatures, atoms diffusion is one of the fundamental mechanisms of phase transformation that occurs via thermal activation. Diffusion is based on the Brownian motion of particles e.g. the movement of atoms, and it is induced by a gradient of the chemical potential of the components. Generally, two types of diffusion can appear, downhill where the atoms move to eliminate concentration gradients, and uphill where the movement is towards the high concentration regions [86]. At high temperatures, understanding the oxidation mechanism of the coating is related to understanding the outward diffusion of metal atoms and inward diffusion of O<sub>2</sub>. e.g. the study of oxidation mechanism at ~500 °C for TiN coating shows a rutile TiO<sub>2</sub>, which has been proved with spallation of the oxide layer due to the difference in molar volume. The diffusion of O<sub>2</sub> through TiO<sub>2</sub> is the main mechanism of oxide growth.

Under specific circumstances, e.g. coated cutting tools exposed to elevated temperatures during metal machining operations, spinodal decomposition can take place. The formation of c-AlN is energetically favourable as an intermediate step during the phase transformation of c-(Ti, Al)N into the stable phases c-TiN and w-AlN following two-phase transformation path [87].

Therefore, Al-rich TiAlN coatings are widely used for high temperature applications. It is known that annealing of TiAlN coatings at atmospheric pressure in flowing Ar in order to avoid oxidation can be the result of age hardness improvements at ~ 900 °C. Further annealing of TiAlN coatings at ~1100 °C leads to coarsening of the domains, the formation of w-AlN, and degradation of mechanical properties, especially hardness. The hardness decreases because of the segregation of the Ti and Al atoms, while maintaining one single crystal structure.



At above 700 °C, the initial oxidation reaction path for medium to high Al content was found to be similar for all alloys with the formation of a bi-layered oxide scale with a dense

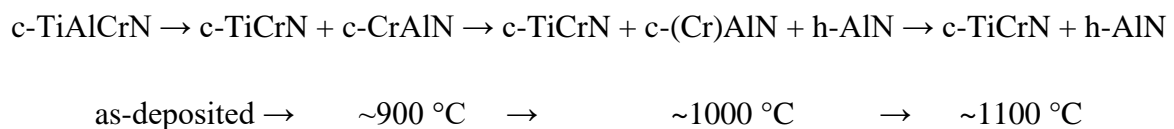
protective  $\text{Al}_2\text{O}_3$  outer-layer formed, which is responsible for the good oxidation resistance followed with porous  $\text{TiO}_2$  sub-layer [88]. The oxide layer at the surface acts as a barrier for the oxygen atoms to diffusion further into the coating and thus improving its thermal stability [89]. Furthermore, it exhibits low thermal conductivity and prevents direct contact of the coating and the wearing material. Therefore, the  $\text{Al}_2\text{O}_3$  layer also reduces adhesive wear [90].

At high temperatures of  $\sim 950$  °C, spinodal decomposition occurs very fast and the onset of the coarsening process begins almost instantaneously. During the coarsening process, the energy is reduced by lowering the surface to volume ratio of the c-AlN and c-TiN domains. When the domain interface becomes small in comparison to the domain size, the coherency stress is relaxed by the formation of dislocations. This is accompanied by a transformation of the c-AlN into the more stable w-AlN phase. These events lead to a dramatic decrease in hardness [91]. However, following those treatments with a longer oxidation duration at temperatures above 950 °C, the protecting  $\text{Al}_2\text{O}_3$  layer is not existent anymore and the coating will be fully oxidized forming a brittle outer-layer of rutile  $\text{TiO}_2$ . This is due to the fast Ti ion diffusion to the surface that affects the performance of the protecting Al oxide layer [92].

### 2.3.2 Ti-Al-Cr-N

Many investigations have shown that Cr addition to TiAlN coating exhibits an improvement of oxidation resistance.

Forsén et al. published that (Ti, Cr, Al)N system with ( $\text{Cr} \geq 17 \text{ at.}\%$ ) after annealing shows a lower driving force, extends the time duration of the spinodal decomposition and delays the coarsening process [93]. The coarsening process is driven by the minimization of the gradient energy which is rate controlled by the diffusion. It means that due to the smaller c-TiCrN and c-AlN domain sizes in the c-TiCrAlN coatings the diffusion is expected to be obstructed, resulting in a slower coarsening rate. The coherency is maintained up to higher temperatures suppressing the transformation of c-AlN to h-AlN. The decomposition route can be expressed according to the following equation [1].



According to oxidation resistance studies of TiCrAlN coatings at low temperatures, the oxidation reactions occur at a significantly slower rate than it for TiAlN due to the presence of chromium, and the activation energies are generally large; hence, a protective layer of chromium and aluminium oxide was formed at the coating surface preventing diffusion of oxygen deeper into the coating. Crystalline or amorphous  $\alpha\text{-(CrAl)}_2\text{O}_3$  is known to be a good oxygen diffusion barrier [94].

For elevated temperatures, the oxidation process deteriorates the metallic properties in a much shorter time and the activation energies are low. Oxides remain at surfaces of metals and form a continuous oxide layer. If CrTiAlN coating was Al-rich, a protective  $\text{Al}_2\text{O}_3$  layer were formed. This oxide barrier that separates the reactants and thereby delays the transport of the reactants through it. On the other side, Ti-rich TiCrAlN coatings negatively affected the oxidation process caused by the promotion of porous  $\text{TiO}_2$  surface layer against a more protective  $\text{Al}_2\text{O}_3$  [95 - 98].

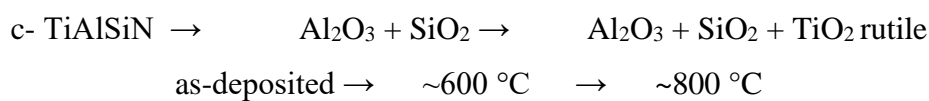
However, with a lower heating rate providing more time for inward diffusion of oxygen, it becomes clear that the oxidation resistance is worsened with increasing Ti content. The

reason behind this can be explained by the fact that the  $\alpha$ -(CrAl)<sub>2</sub>O<sub>3</sub> is suppressed against TiO<sub>2</sub> [99].

In summary, the thermal stability, oxidation resistance and mechanical stability depend on the content of Cr/Al and Ti ratio in (Ti, Al, Cr)N system. Improved thermal stability and the retained hardness above 1000 °C can be explained by an intermediate metastable c-AlCrN and c-TiCrN. These two intermediate ternary phases are formed in the decomposition route of the annealed coatings prior to the final stage. In the end, both h-AlN and c-TiCrN phases are formed [60 - 63 & 100 - 104]. The oxidation evolution of (Ti, Al, Cr)N system at 950 °C is addressed in detail in this thesis (see paper II).

### 2.3.3 Ti-Al-Cr-Si-N

Si is an important element that significantly improves the mechanical properties, thermal stability and oxidation resistance of hard-based nitride coatings. For example, the (Ti, Al, Si)N system has a better microhardness in comparison to the (Ti, Al)N system. Improving microhardness is a result of decreasing the crystallite size by doping Si in the AlTiN matrix [105]. Also, presenting the Si<sub>3</sub>N<sub>4</sub> phase of (Ti, Al, Si)N gets converted to SiO<sub>2</sub> phase at elevated temperature which ultimately causes an effective increase in the thermal stability of the coating. The development of oxidation produced during the sliding process at different temperatures is summarised in the following equation [106].



Recently, the (Al, Cr)N system with Si doping has been focused on by several research groups due to their high hardness and high temperature oxidation resistance. AlCrSiN coating showed an onset temperature of oxidation of 1100 °C, and the oxidation rate was determined to be very slow, consisting the oxide growth of AlCr<sub>2</sub>O<sub>3</sub> and SiO<sub>2</sub> [107].

Chang, Yin-Yu, et al. have investigated the oxidation resistance of CrAlSiN coatings with a low content of Si (3 at.%) at 800 °C in air for 2h [108]. They revealed that the diffusion of oxygen displaced the metal elements and nitrogen. Therefore, a very thin mixed oxide layer near the surface at the initial oxidation stage was formed. This mixed layer includes Cr<sub>2</sub>O<sub>3</sub>, Al<sub>2</sub>O<sub>3</sub>, and SiO<sub>2</sub>. After this thin mixed oxide layer was formed, oxygen continued to diffuse inwardly through this oxide layer to reach the coating/oxide interface. During the oxidation process, nitrogen was released into the environment through the diffusion path through the mixed oxide layer. The formation of both SiO<sub>2</sub> and Al<sub>2</sub>O<sub>3</sub> that originated from the silicon nitride inhibited not only further oxygen diffusion into the coating but also outward diffusion of Cr resulting in an improvement of the coating oxidation resistance.

The same research group studied the oxidation resistance of Cr<sub>0.40</sub>Ti<sub>0.22</sub>Al<sub>0.36</sub>Si<sub>0.02</sub>N with columnar microstructure after annealing at 900 °C in air for 2h. The result is Ti, Cr, and Al oxides formed throughout the 0.2 μm-thick oxide layer [109]. During the oxidation process, N diffuses significantly faster than the metal atom [110], therefore N was released and did not

remain bound or trapped in the oxide layer. In contrast, Ti, Cr, and Al diffused outward and oxygen diffused inward to form rod-like surface oxides.

However, Gibbs free energies ( $\Delta G^\circ$ ) for  $\text{Al}_2\text{O}_3$ ,  $\text{Cr}_2\text{O}_3$ ,  $\text{TiO}_2$  and  $\text{SiO}_2$  at this temperature were  $-1336$ ,  $-845$ ,  $-753$  and  $-725$  kJ/mol, respectively. That explained preferential growth of  $\text{Al}_2\text{O}_3$  layer. Interestingly,  $\text{TiO}_2$  has a coefficient of thermal expansion of  $10.5 \times 10^{-6}/\text{K}$ , which is larger than that of  $\text{Al}_2\text{O}_3$  ( $8.4 \times 10^{-6}/\text{K}$ ) and  $\text{Cr}_2\text{O}_3$  ( $7 \times 10^{-6}/\text{K}$ ). Hence, Ti diffused faster than Al and Cr towards the surface through the column boundaries and cracks of the  $\text{Al}_2\text{O}_3$ - $\text{Cr}_2\text{O}_3$  mixed layer to react with oxygen and formed  $\text{TiO}_2$  oxides on the top surface [111].

The growth stress during oxidation and the thermal stress caused by different thermal expansion coefficients between the film and oxides prevented the formation of perfect oxide scales and lead to cracks in the mixed oxide layer.

However, the oxidation behavior of the monolayered TiCrAlSiN coatings have not yet been adequately studied to date. Therefore, the purpose of this thesis is to investigate its oxidation behavior at high temperature (see paper III).

### 3 Experimental procedure

#### 3.1. Targets

In sputter deposition, there are different possibilities to achieve multi-component thin films. The first is to use different pure element targets, the second is to use compound targets. The third method is both at the same time, which means a co-deposition system. Alloy targets can be made by various processing techniques such as casting and powder metallurgical techniques [64]. To achieve different compositions of coatings during this thesis, targets with different metal ratios (Ti:Al) were selected. Ratios selected were 50:50, 45:55 and 40:60 with one or two deposition techniques. A schematic drawing of the coating chamber is presented in Fig. 3.1. Different target compositions were also used e.g.  $\text{Ti}_{100\%}$ ,  $\text{Cr}_{100\%}$ ,  $\text{Si}_{99.999\%}$ . Hence, different compositions of the targets will also influence the deposition parameters such as ion charge distributions and surface mobility.

Rectangular and circular targets produced by powder metallurgical (PM) techniques were used to control the architecture and alloys of the coatings. The deposition configuration consists of three circular targets ( $\text{Ø } 101.6 \times 6.35$  mm) mounted next to each other, or two rectangular targets ( $400 \times 125 \times 8$  mm) mounted facing at each other in the vacuum chamber. A rotating substrate holder can move to be faced by the different targets.

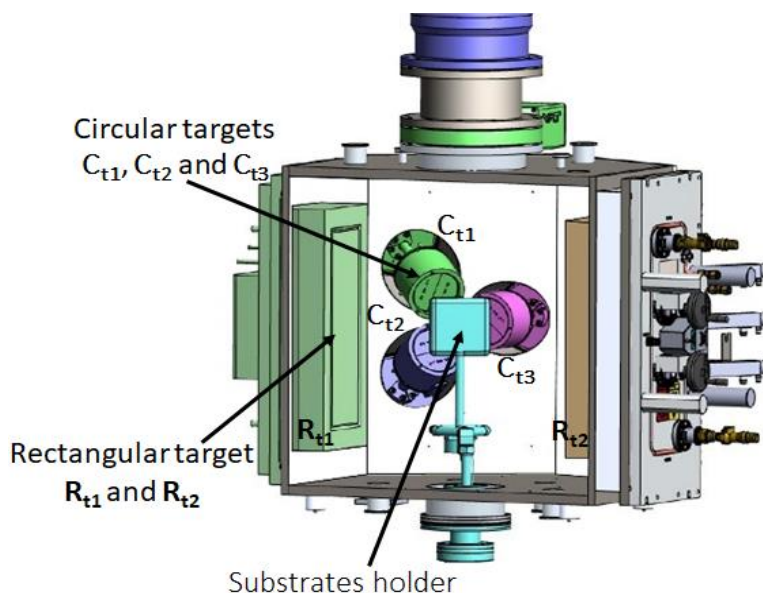


Fig. 3.1 Schematic drawing of the experimental vacuum chamber and both systems of rectangular/circular targets.

### 3.2. Substrates

The substrates coated within the present work were conventional cemented tungsten carbide (WC-Co) plane disc and mirror-polished silicon wafers (Si) with  $(100 \pm 0.5^\circ)$  orientation and P-boron type of doping. The coated silicon samples were used to determine the morphology and the thickness of the coating, while for all other investigations the coated WC-Co substrates were used.

Generally, the hexagonal close-packed (hcp) tungsten mono-carbide (WC) and metals like (Fe, Ni, Co) are sintered in the presence of liquid phase later on to produce a solid dense body (Figure 3.2), [112]. In this study, mixture powder of (WC-9%Co) and other elements like ((Ti, Ta, Nb) C) are mainly used to produce high-performance coated cutting tools, with  $14.55 \text{ g/cm}^3$  density for submicron grain average. Table 3.1. presents the main mechanical properties and thermal conductivity for WC-Co that have shown an excellent hot hardness and wear resistance due to its chemical composition. These substrate properties can be optimised depending on the application. For example, toughness and hardness can be adjusted to different machining needs, hence defining the correct percentages of stainless steels or cast iron in the mixture powder is needed for the final product [113].

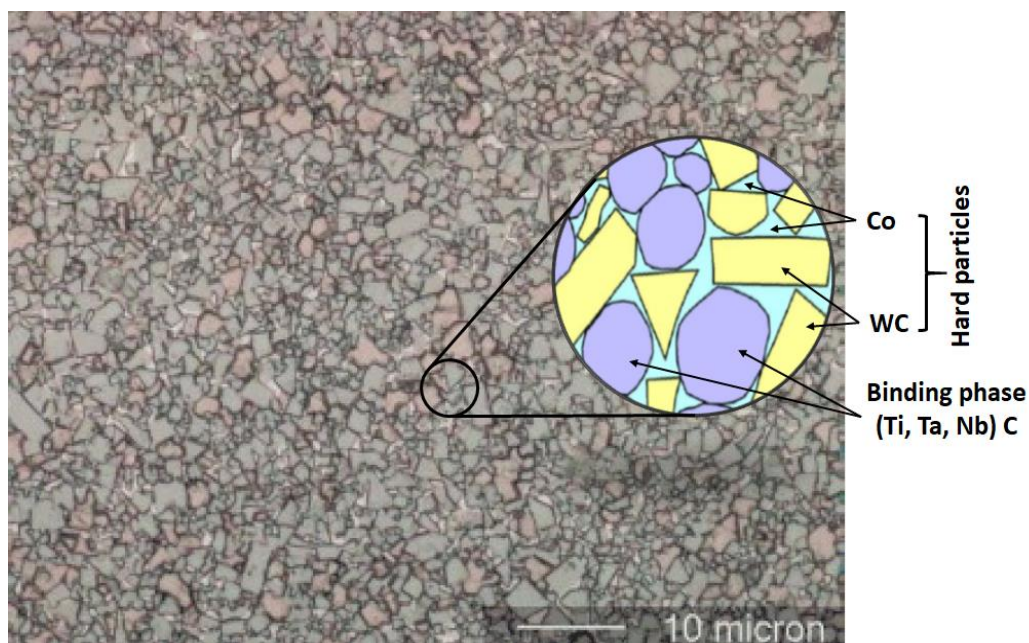


Fig. 3.2 Cemented tungsten carbide composite microstructure and schematic drawing of the binding phase between the hard material particles. Modified from [114]



In summary, most properties of cemented carbides can be described in a good way by relating them to the excellent weight percent of both Co and WC grain size in the composite. Moreover, adjusting the binder content and average WC grain size is an important factor for the unique properties of the WC-Co system [115 - 117].

Table 3.1 Typical values of selected physical and mechanical properties of cemented tungsten carbide

Average grain		Submicron
Density (ISO 3369)	<b>(g/cm<sup>3</sup>)</b>	14.55
Hardness (ISO 3878)	<b>(HV10)</b>	1610
Compressive strength	<b>(MPa)</b>	6600
Young's modulus	<b>(GPa)</b>	590
Fracture toughness (SEVNB)	<b>(MPa.m<sup>1/2</sup>)</b>	11
Thermal conductivity	<b>(Wm<sup>-1</sup>K<sup>-1</sup>)</b>	90

### 3.3. Coating deposition

All the coatings deposited in this study have been fabricated using a semi-industrial PVD coating machine designed and assembled at the Luxembourg Institute of Science and Technology (LIST). This machine can connect to the HiPIMS, dcMS or Hybrid HiPIMS power supply (Figure 3.3). Prior to deposition, all substrates were ultrasonically cleaned in ethanol for five minutes each. Then they were mounted on the substrate holder. Before deposition in the reactor, a dry primary pump and a turbo pump were used in order to have the cleanest atmosphere (best vacuum) possible and avoid contamination and to reach the process pressure. During the deposition, the Papillon valve was used to control the working pressure. A flowmeter was used to regulate and supply the reactor with the process gas atmosphere of Ar and N<sub>2</sub> at a fixed total gas pressure. Three microwave antennas provided by HEF group are present in the reactor and used for the etching and cleaning process, where the substrates were cleaned through a heating step and subsequently by Ar<sup>+</sup> ion etching. There, the substrate is bombarded by the Ar<sup>+</sup> ions from the ignited plasma, where the substrate carousel acts as the cathode by a negative bias polarisation. After substrate ion etching, the actual deposition process was started.

Several parts of the reactor connect to the cooling system. A heating system connected to the substrate and the chamber, and regulated by two PID controllers, allows us to deposit from room temperature to 550 °C. Three power supplies were plugged to cathodes and the substrate holder to generate different plasma-power and apply different biases, which leads to control the kinetic energy of the ions arriving at the substrate in order to change the microstructure of the thin film.

The sources for depositions in the PVD2 are three circular cathodes with diameter of four inches installed on the backside of the reactor, and two 500 cm<sup>2</sup> rectangular cathodes placed equally on the left and right sides of the reactor's walls (refer to figure 3.1). LabVIEW software was used to control the parameters of all previously discussed parts.

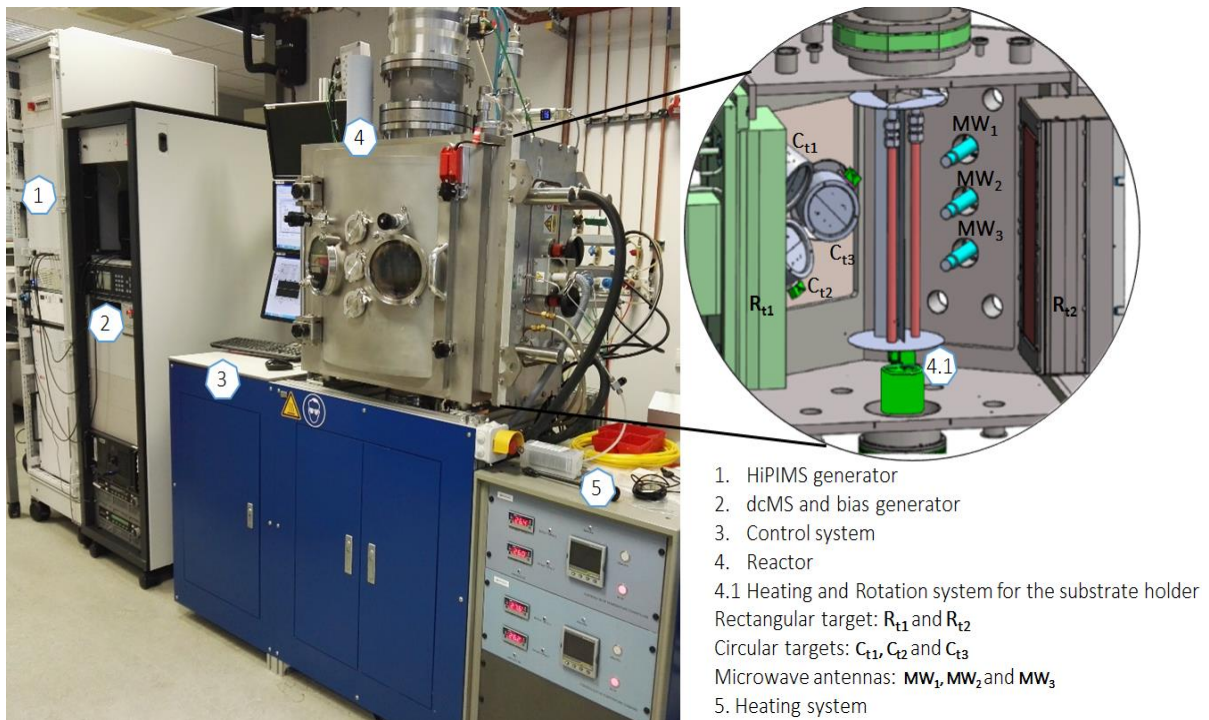


Fig. 3.3 Picture of the PVD sputtering device at LIST and schematic illustration of the reactor particles and the deposition system used to synthesize the films.

## 4 Characterization methodology

This chapter introduces the experimental methods for determining the elemental composition, plasma monitoring and the techniques that has been applied for characterizing the deposited films or the process of deposition. The characterization of thin films is an essential task combining the material, the limited dimensions of the film and pre-requirements of the characterization technique, e.g. the amount of material available for analysis, the substrate used, the sample preparation, structural analysis and the difficulty of quantitative chemical analysis.

Therefore, it is important to specify characterization techniques and to choose the appropriate combinations to cover different scales and information about the coated films. The techniques used during this study are presented below with a description of the setup and parameters used. The focus was on microstructure and hardness characterization of as-deposited and on oxidation characterization of as-annealed thin films.

### 4.1 Process characterization by optical emission spectroscopy

Optical emission spectroscopy (OES) is a reliable technique suitable for analysis and monitoring of physical and chemical processes of the plasma-induced emission, i.e. the energy levels and their difference which are characteristic for each species present in the plasma. OES allows fast and easy qualitative discharge monitoring, which can be performed in both times- and space-resolved mode. It is mostly used for the identification or quantification of various gas-phase species present in the plasma, based on the detection of the radiation originating from the de-excitation transitions of bound electrons in ions, atoms or molecules, each electron transition between the higher-lying and lower-lying energy levels results in emitting photons of a characteristic wavelength.

The interpretation of the quantitative information by OES can be difficult because of the indirect relation between the excited species' concentration and the detected radiation intensity. Moreover, the observed bands are composed of a large number of emission peaks or lines which originate from numerous electronic transitions in between various vibrational and rotational energy levels that are superimposed to the molecular electronic states. However, the emitted photon has a well-defined energy (wavelength) that is equivalent to the energy difference of the higher-lying and lower-lying energy level of the excited electron. A

large number of such emitted photons can be detected as emission lines or peaks, thus can be used to define the radiating species by comparing the experimentally obtained spectral bands with the tabulated values in the reference list.

OES can observe wavelengths typically range between 200 nm and 1000 nm. The experimental setup consists of a SpectraPro 2750 spectrometer (PI Acton), which diffracts the light coupled into it and a detector that measures the intensity of the light and the wavelength, using an optical resolution of 0.35 nm for qualitative analysis of the ion and excited neutral densities in the HiPIMS and dcMS plasma at the different working pressures, (More details will be given in Appendix chapter 9.1). Spectra were collected from emissions from the entire region in front of the target; the measured intensity provides information on the density of the particles in the excited state, as schematically shown in figure 4.1.

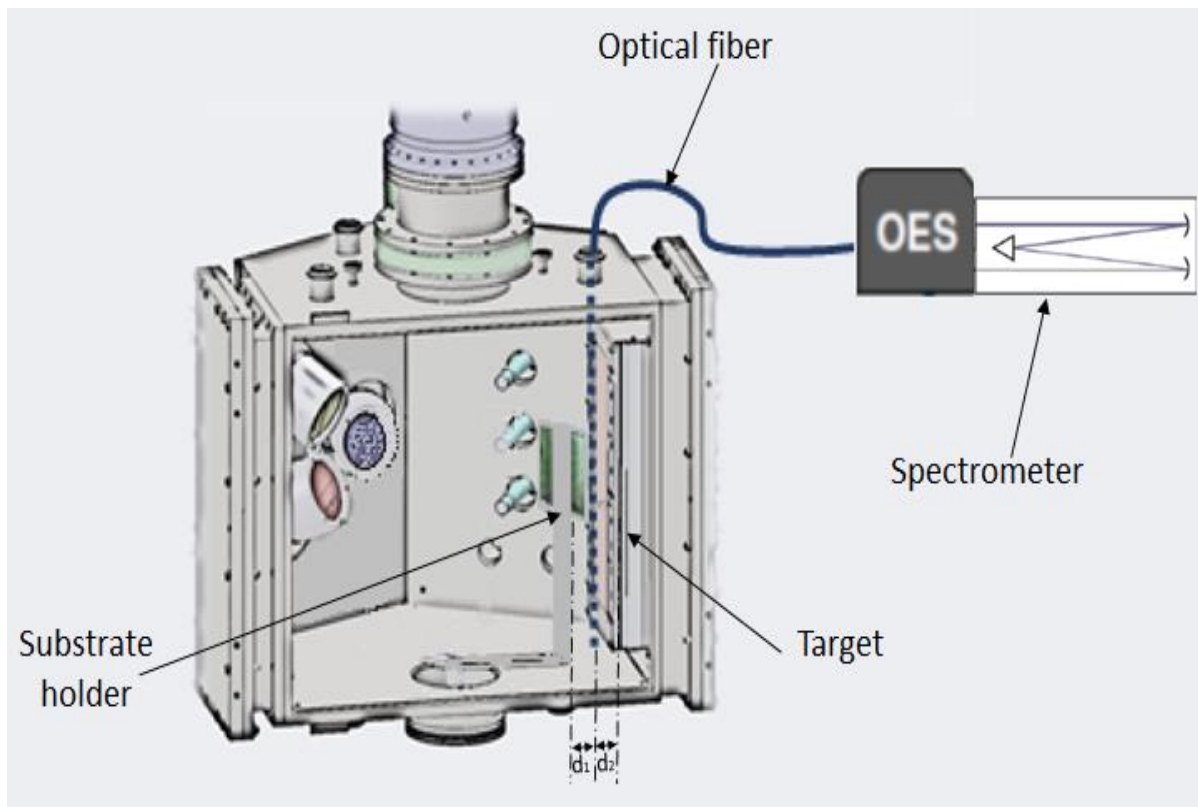


Fig. 4.1. Experimental set-up for OES spectrum, the optic fiber is between the target and substrate holder  $d_1=d_2=TSD/2$ , where (TSD) is target substrate distance.

## 4.2 Scanning electron microscopy and x-ray emission spectroscopy

It is known that the smallest distance that can be resolved is proportional to the wavelength of the radiation. Therefore, the resolution of light optical microscopes is limited by the wavelength of visible light radiation (~400 - 700 nm) [118]. When electrons are accelerated to (200 kV) the wavelength of the electron radiation is ( $\sim 10^{-2}$  nm), which achieves an improvement of around five orders of magnitude compared to a light optical microscope. Wavelength and the volume's size where significant interaction occurs are the main resolution criteria. The variants of different microscopes are presented in figure 4.2.

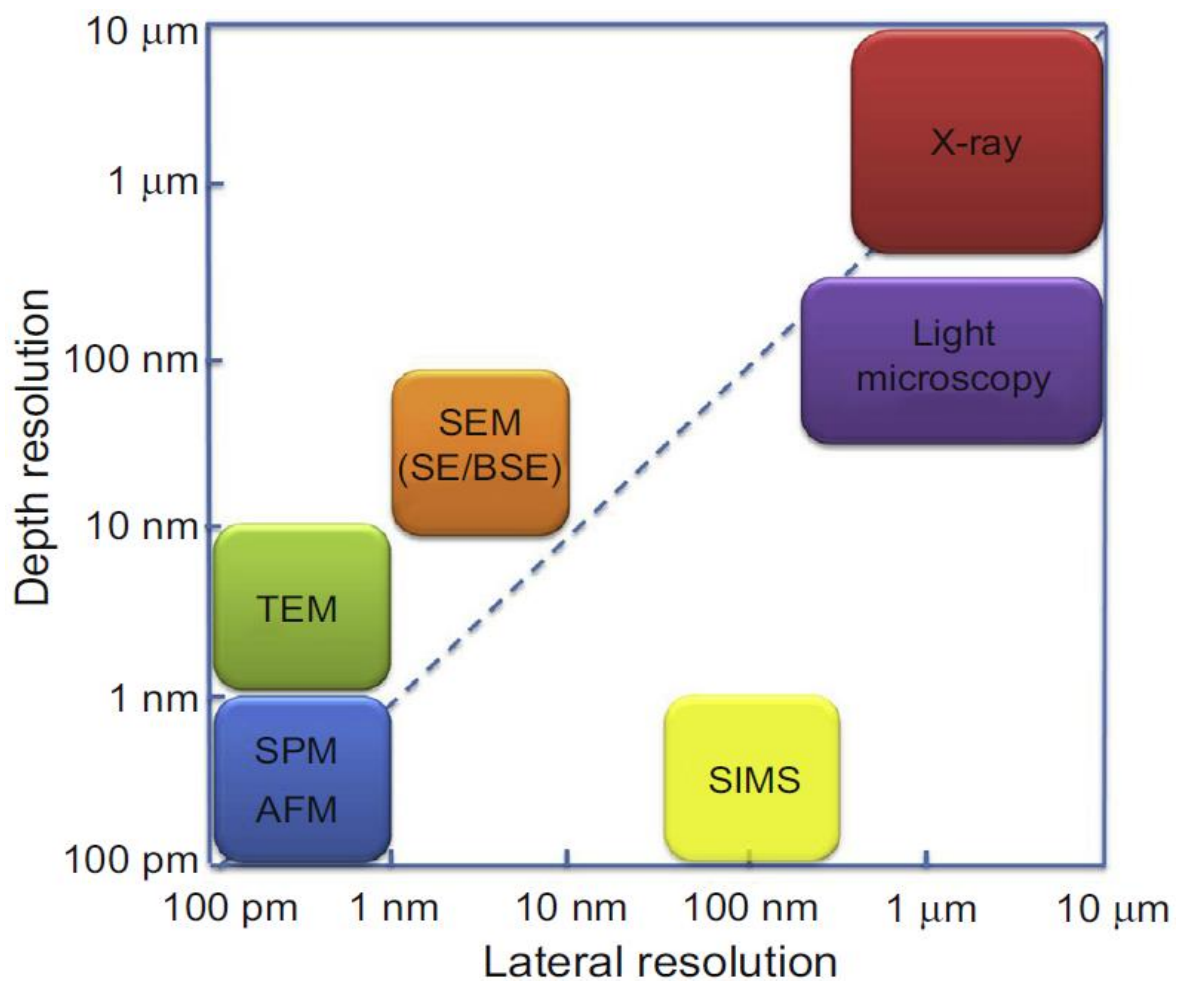


Fig. 4.2 Overview of typical key materials characterization techniques and its resolution, reproduced from [119]

SEM is one of the popular techniques for characterizing thin film surface, where the specimen is scanned by a focused electron beam of highly energetic electrons usually varied between a few and several tens of keV and created by an electron gun. A system of

electromagnetic lenses is used to focus the electron beam on the specimens, which can achieve an image with nanometre resolution. The electrons bombarding the specimen are partly recoiled and partly absorbed within the subsurface region; this will generate backscattered electrons, x-ray photons and secondary electrons (SE). The emission of SE is necessary to carry the topographic information of the surface, where the contrasts in the SEM images are due to shadowing effects.

In addition, the emitted backscattered and x-ray photons carry information about the composition of the surface elements. Each element has a unique atomic structure allowing a unique set of peaks on its X-ray emission spectrum. It is collected by the respective energy-dispersive detector positioned in the sample vicinity, hence can be used to perform chemical analysis with capabilities to detect the elements present in concentrations  $> 1\%$  by mass.

Hitachi SU-70 field-emission scanning electron microscope (FE-SEM) equipped with an Oxford XMax<sup>N</sup> 20 mm<sup>2</sup> energy-dispersive X-ray emission spectrometer (EDS) (with an error of 1.0 at.%) was used to determine the elemental composition, the morphology and the microstructure of the coatings, the thickness and the surface of the films.

The as-deposited and oxidized coatings on Si wafer substrates were used for SEM cross-section observations. This was done to determine the coating growth morphology, oxide structure, coating/oxide thickness, and grain size.

In the case of the coating on the WC substrate, SEM was used for surface morphology imaging and inspection of topography, defects, and particles. Furthermore, it was used to inspect the wear track and identify damages such as cohesive fracture and coating delamination.

### 4.3 X-ray diffraction

X-ray diffraction (XRD) is a sensitive non-destructive characterization technique commonly applied for a deduction of the atomic distribution within the studied material, from which the crystalline structure, the lattice spacing, and the residual stress level can be determined. Thus, the analysis of the obtained diffraction pattern can be used to determine the composition,

physical properties and phase analyses. Furthermore, it is possible to estimate e.g. the crystallite (grain) size, the lattice strain and the coating preferred orientation (texture).

Evaluation of the coating's stress has crucial importance for the coating stability and for its adhesion to the underlying substrate since the internal stress is a sum of the thermally induced stress due to the difference in thermal expansion coefficients between the substrate and the film, and of the intrinsic microstructural stress originating in growth defects. The phase transformation, recrystallization or other processes at elevated temperatures may also induce stress. The principle of XRD is correlated to Bragg's law, focusing the light in the X-ray wavelength region is ( $\sim 10$ - $0.1$  nm) [118].

The incident radiation into the sample will be backscattered spherically in all directions by the sample atoms. If the atoms are arranged in a periodic fashion, as in a crystalline lattice, the diffracted X-rays will generate sharp interference maxima, which reflect the symmetry of the lattice atoms. If there is some kind of periodicity among the atoms in the sample, the scattered radiation will interfere constructively in some directions. The constructive interference can be measured by focusing the scattered light on an X-ray detector. Constructive interference will occur when the path length difference between scattered light from different interatomic planes corresponds to a multiple of the wavelength of the x-ray source.

When applying this technique, the lattice parameter or the interatomic distances in the sample can be extracted since the wavelength and the geometry are known variables. By measuring the distance between the atoms in a sample the crystal structure and the phases present in the sample can be determined.

In the present work, all coatings were analysed at room temperature either as-deposited or after annealing using Bruker D8 Discover diffractometer in parallel beam configuration using a Cu K $\alpha$  radiation with a power of 1600 W 40 kV; 40 mA. The residual stress measurements were performed on the 422 diffraction peak using the classical single  $\{hkl\} \sin^2\psi$  method. The elastic constants used to convert the strain measurements to stress are Young's modulus and Poisson's ratio where  $E = 450$  GPa and  $\nu = 0.177$ . Pole figure measurements were performed in the main reflections 111, 200 and 220 of the structure of the coating with a resolution of five degrees for  $\psi$  and  $\phi$ . Both of Bragg-Brentano as well as in grazing incidence configuration were used. In Bragg-Brentano, a range of the incident angle  $\theta$  was



selected. The sample was irradiated with an X-ray incident at an angle  $\theta$  to the surface of the sample and the diffracted beam intensity is detected at an angle  $2\theta$  with respect to the incident beam. In grazing incidence mode, the incident angle  $\theta$  was adjusted to a constant small value and only the diffraction angle  $2\theta$  passes through the selected angle range. Thus, only information about the near-surface area is provided.

## 4.4 Transmission electron microscopy

Nowadays, the most advanced transmission electron microscopes can achieve Angstrom-level resolution. Transmission electron microscopy (TEM) is a microscope that operates on a different principle from SEM. In TEM, a focused electron beam interacts with the sample. During the interaction of the electrons with the sample, there is a transmission, absorption, reflection and scattering, which are the contrast mechanisms of different TEM patterns' results. The magnification range in SEM is typically around 10 to 500 times, while in TEM, it is higher, ranging from 2000 to 1 million times. Additionally, the resolution range in SEM is approximately between 4 and 0.5 nm, whereas in TEM, it reaches higher resolution levels, typically between 0.2 and 0.1 nm. Therefore, the SEM is designed to examine material surfaces whereas TEM is designed to examine the internal structure of the sample. In scanning mode, TEM is sometimes called STEM [120]. Since the mean free path of electrons in solid materials is very short, the thicker the sample, the longer the electron path and the projected image generated. The electrons transmitted through the material will contain information from any overlapping features. The sample has to be thin enough to allow transmission of electrons and to provide structural information, where the maximum thickness is 200  $\mu\text{m}$ . Sample preparation is not trivial. Good preparation is essential to benefit from the high theoretical resolution that the microscope may have [119].

In this study, different TEM patterns are used to get information about the samples microstructure and crystal structure, e.g. bright-field imaging, dark-field imaging, high resolution transmission electron microscopy, lattice imaging, selected area diffraction, the X-ray spectroscopy or electron energy loss spectroscopy [121].

TEM imaging was performed in a JEOL JEM 2011 at an acceleration voltage of 200 kV. Scanning TEM (STEM) analysis was carried out using JEM - ARM 200F Cold FEG



TEM/STEM (JEOL) operating at 200 kV and equipped with a spherical aberration (Cs) probe and image. The point resolution was 0.12 nm in TEM mode and 0.078 nm in STEM mode. TEM samples were produced by Focused Ion Beam (FIB) technique: Helios Nanolab 600 dual beam focused ion beam instrument. The lift-out technique was used, and the thinning of the sample was done starting with 30 kV and successive steps reducing the ion current down to 50 nA. The final cleaning step was done with 5 kV and 16 nA to minimize possible artefacts.

## 4.5 Secondary ion mass spectrometry

Secondary ion mass spectrometry (SIMS) is a widely employed solid materials characterization technique for surface chemical analysis. As the name implies, in this technique the sample is bombarded in vacuum by a high energetic primary ion beam, usually  $\text{Ar}^+$ ,  $\text{Ga}^+$  or  $\text{Cs}^+$ . This bombardment causes sputtering of the surface and ejections of small particles which can be electrons, neutral species (atoms or molecules), or atomic and cluster ions. Following the bombardment, the emission of secondary ions of a metal surface are subsequently accelerated towards a mass spectrometer. The secondary ions provide information on the elemental, molecular, and isotopic composition of a material's surface. Therefore, they are separated according to their mass-to-charge ratio and counted. The measured secondary ions number is converted to concentrations and compared with known standards [126].

The weaknesses of SIMS are that the method is destructive to the surface and analysis can be complex because the measured signal represents fragments of the film and the mass of these fragments often changes with the energy of the sputtering ions.

The SIMS measurements carried out in this thesis concern the different oxide layers formed on the surface of the thin film coatings after different oxidation processes. For that, a different type of analysis called chemical depth profile was obtained by SIMS in a CAMECA SC-Ultra under a low energy  $\text{Cs}^+$  bombardment (1 keV), 40 nA/ 20 nA. The size of the analysed area was limited to a diameter of 8  $\mu\text{m}$  centred in a (150 $\times$ 150)  $\mu\text{m}^2$  scanned area. The different elements of interest were measured as  $\text{MCs}_x^+$  (M = Al, Ti, Cr, Si, O or N and

x=1 or 2) cluster ions. The analysis of oxidized samples was assisted with an electron gun for charge compensation.

Depth profiling can be useful in determining stratification of coatings or diffusion of atoms into a part underneath a surface and can be achieved by profilometer to evaluate the sputter-depth after the SIMS measurement.

## 4.6 Atom probe tomography

APT is a powerful material analysis technique that gives chemical composition and spatial information with a near-atomic scale (around 0.04 nm resolution in depth and 0.2 - 0.5 nm laterally). [122 & 123] APT offers both a 3D imaging and composition measurements at the near-atomic resolution.

The working principle of APT is as follows: First, the solid material to be studied was prepared in the shape of the needle with an end radius between 50 -100 nm. Then the needle was subject to ultrahigh vacuum  $10^{-11}$  mbar at cryogenic temperatures ( $> 15$  K) to hold the atoms in their place. Second, the needle was biased at a high voltage between 1-15 kV. As a result, the sharpness of the tip and the high voltage induced an electrostatic field at 10 - 15 V/nm. Third, through a laser or high voltage pulse applied to the specimen, the atoms at the surface of the tip are ionized; hence, the ion at the time is removed from the surface by field evaporation and accelerates toward a 2D position sensitive time of flight detector. Finally, that allows to simultaneously measure the X, Y, Z position of the ion impact and the atom time of flight. These two pieces of information with specialised software based on an algorithm protocol allow to create a 3D reconstruction of the sample with up to 80% detection efficiency [124]. The experimental setup for APT is shown in figure 4.3.

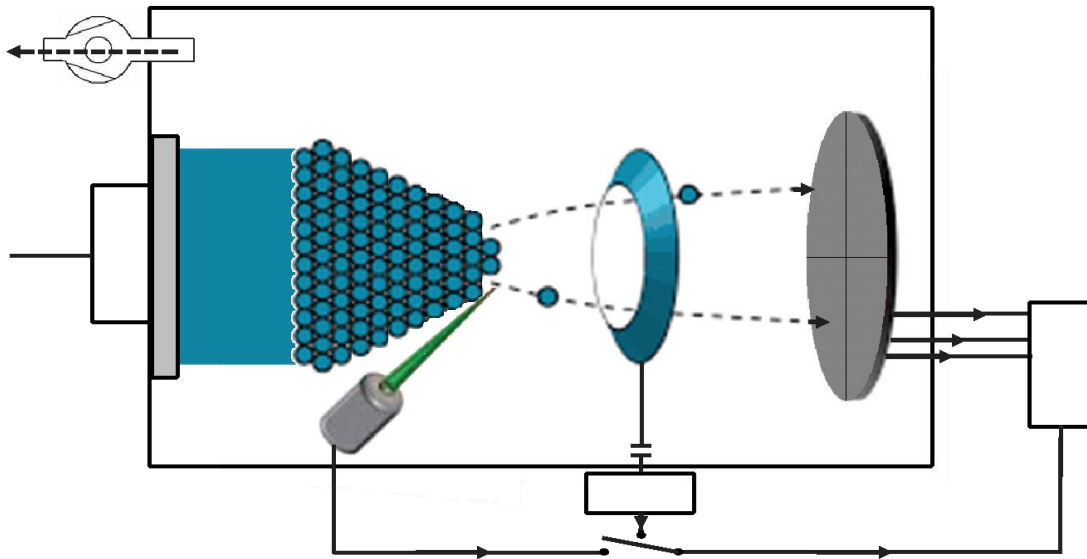


Fig. 4.3 Experimental setup for local electrode atom probe tomography with a 2D detector.

APT samples in this thesis were prepared in a dual-beam focused ion beam/scanning electron microscopy workstation (FIB/SEM) Helios NanoLab 600™ (FEI), following the standard lift-out preparation detailed in [125]. A final cleaning step at 2kV was performed to minimize Ga damage during the thinning of the specimens. The APT measurements were performed using a LEAP™ 3000XR (CAMECA) in laser pulsed mode at a repetition rate of 200 kHz, a laser pulse energies of 0.5 – 0.7 nJ, a pressure lower than  $133 \times 10^{-12}$  mbar, and at cryostat temperature of about 50- 60 K. The evaporation rate of the specimen was 5 atoms per 1000 pulses. Data reconstruction was carried out with the software package IVAS™ (version 3.6.14, Cameca) using voltage mode with an evaporation field of 35 V/nm, k-factor ( $k_f$ ) of 4 and image compression factor of 1.5.

#### 4.7 Profilometer:

KLA Tencor P-6 surface profilometer was used to do high-resolution 2D and 3D analysis of the surface roughness and topography. The P-6 is equipped with a 2  $\mu\text{m}$  radii tip for the measurement application. All the analyses were averaged over two runs by setting the multi-scan average option to two. Profilometry setting in most of the cases was with a scan speed of (10 -20)  $\mu\text{m}/\text{sec}$ , sampling rate of (100/200) Hz, applied stylus force 2 mg, vertical range/resolution of 13  $\mu\text{m}/0.078 \text{ \AA}$  and Lateral resolution: 0.025 $\mu\text{m}$  (2D), 0.5 $\mu\text{m}$  (3D). A picture of a KLA Tencor P-6 profilometer is shown in figure 4.4.



Fig. 4.4 KLA Tencor P6 with dongle and computer representation. Modified from [130].

## 4.8 Nanoindentation

The wide applications of hard coatings require a better understanding and controlling of their surface mechanical properties. Hardness is one of these properties that is defined as the resistance of a material against plastic deformation caused by the penetration of harder material. It is based on the measurement of the vertical position of the indenting stylus during its displacement into and from the examined sample, caused by the variable load applied upon [127]. Using nanoindentation tests allows evaluating the hardness ( $H$ ) and Young's modulus ( $E$ ) of thin film coatings. To achieve accurate results, it is important to calibrate the nanoindentation apparatus before each experiment. Furthermore, the size of the indenter, as well as its penetration depth has a precisely defined geometry (i.e., the stylus is not worn by excessive use) [128]. Due to surface roughness, it is important to avoid the surface topography effects (i.e. the areas containing the macroparticles). These residues (macroparticles) from the deposition process impose defects in the lattice and will affect the mechanical properties in their vicinity. Therefore, the proper use and interpretation of the depth-sensing nanoindentation analysis requires particular caution and expertise.

In this study, all hardness measurements of thin films coatings on WC-Co substrates were performed with an Anton Paar – CSM Nanoindentation tester NHT3 using a Berkovich diamond tip which indents into the film while continuously observing the load. The tip has a known contact area versus its penetration depth. The tip leaves a plastic deformation not deeper than 10% of the coating thickness, therefore we assumed that the deformation is independent of the substrate and the hardness of the coating determined as the force divided by the cross-sectional area of the tip, where the load-displacement curve was generated during the indentation. The samples, i.e. as-deposited coatings, were prepared by mechanically grinding and polishing leading to the removal of a thickness of (0.2-0.3  $\mu\text{m}$ ). The indentation sites are then carefully chosen using an optical microscope to avoid the micrometre-sized particles. The average hardness values were obtained using the Oliver and Pharr method [129], average hardness  $\pm 1$  standard deviation was extracted from approximately 20 indents on each sample with the removal of maximum 4-7 test points using a maximum load of  $F=30$  mN, leading to a penetration depth of about 0,2-0,3  $\mu\text{m}$ . The classical test of hardness is presented in figure 4.5 where the load  $F$  to the projected contact area  $A$  is clarified as well as the nano-indentation, load-displacement curves.

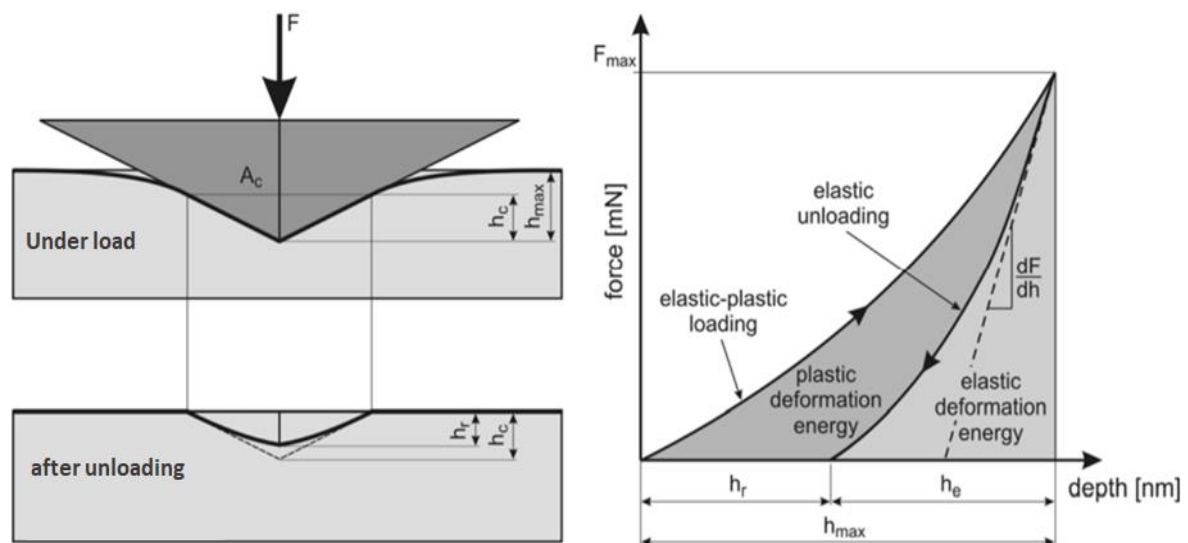


Fig. 4.5 Schematic drawing of an indentation with a pyramidal indenter under the load  $F$ . the elasto-plastic behavior of the coatings causes an indentation depth of  $h_{\text{max}}$  under  $F_{\text{max}}$ , where the indenter is only in contact with the material for the depth  $h_c$ . After unloading the residual imprint has the depth  $h_r$  due to elastic recovery (right), the corresponding load-displacement curve with the loading and unloading segment (left). The elastic contribution to the maximum displacement is indicated with  $h_e$ .

Reproduced from [130 & 131]

## 4.9 Scratch test

Further development of the indentation systems instrument has provided additional tribological measurements such as nano-scratch. In the nano-scratch test, the stage of the instrumented indentation system is required to move the rigidly mounted sample laterally, whilst the indenter is subjected to the normal force. During a test, an increasing force range (1 to 100 N) normal to the surface under test is applied to the stylus (Rockwell with diamond tip  $n^{\circ}1425$ ) so as to promote adhesive and/or cohesive failure of the coating-substrate system.

The general principle on which the scratch method is based relies upon the fact that different materials show different resistances to deformation upon scratching and hence, different modes of deformation. The data obtained provides several surface properties such as the scratch hardness, the fracture toughness, the abrasion resistance and the identification of the various deformation modes that are specific to the material being examined [132]. A schematic drawing of a typical scratch tester arrangement is shown in figure 4.6.

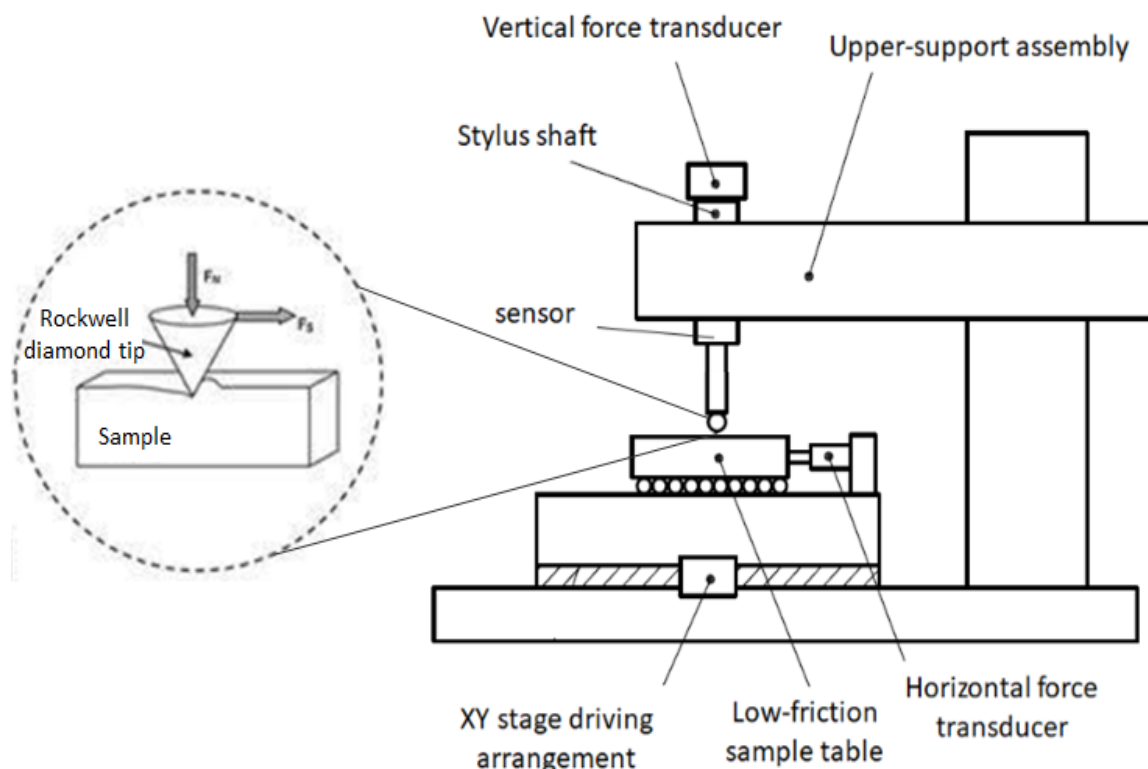


Fig. 4.6 Schematic representation of nano-scratch systems instrument and Rockwell diamond stylus indenter. Modified from [133 & 134]

The surface after scratching as well as the failure events are detected by direct microscopic and SEM technique in order to subsequently assess the deformation modes. Both the scratch depth and width were used to evaluate the scratch hardness of the coatings. In addition, the geometry of these scratches provided a characterization of the damage processes, such as the material removal and the debris generation mechanisms, as well as the wear and the mechanical dissipation properties of the coatings and the adhesion characteristics of coatings.

The normal force at which failure occurs is called the critical normal force  $L_c$ . The driving forces for the failure of the coating-substrate system in the scratch test are a combination of elastic-plastic indentation stresses, frictional stresses and the residual internal stress present in the coating. The nano-scratch test in this study used to investigate coating adhesion through analysis of the force at which the coating delaminates in a ramped force scratch, and finally scratch resistance. Nano-scratch hardness is a further measurement that can be obtained from the nano-scratch test giving a quantitative measurement of the resistance of a material to a laterally applied force or sliding contact [135].

#### 4.10 Ball-on-disk tribological test

Ball-on-disk test was used to define the wear of the coatings. The wear is defined as the damage or removal of a material due to sliding contact to a solid surface; hence it involves progressive loss of material. This loss takes place due to relative motion between that surface and contacting substances [137]. The bonding between the two materials can be strong enough to cause detaching of fragments, mostly from the softer material, and subsequent re-attachment on the other material during sliding testing [138].

The wear resistance of coatings in this thesis was obtained by CSM high-temperature ball-on-disc in a dry atmosphere onto cemented tungsten carbide disks (WC-Co) ( $\varnothing$  30×4 mm). Considering that, the friction coefficient ( $\mu$ ) is the ratio of the friction force ( $F_f$ ) and the applied normal load ( $F_N$ ), where  $F_f = \mu \times F_N$ . As  $\mu$  is independent of the sliding velocity and the normal load but the real contact area influences it, the 2 N load was chosen to ensure sufficient coating lifetime while preventing artefacts in the friction curves that could arise from sample roughness. The sliding speed was (2.6 m/min) for all tests and radius of the wear track were kept constant at (7 mm) against a steel ball and (10 mm) against alumina ball at



room temperature and 850 °C, respectively. The ball diameter is 6 mm. The alumina ball was chosen because of its higher wear resistance compared to the deposited coatings, and shows nearly no wear at elevated temperature. The dry sliding tests were performed for 800 laps (the distance of 35 m). Figure 4.7 shows a schematic image of the CSM tribometer.

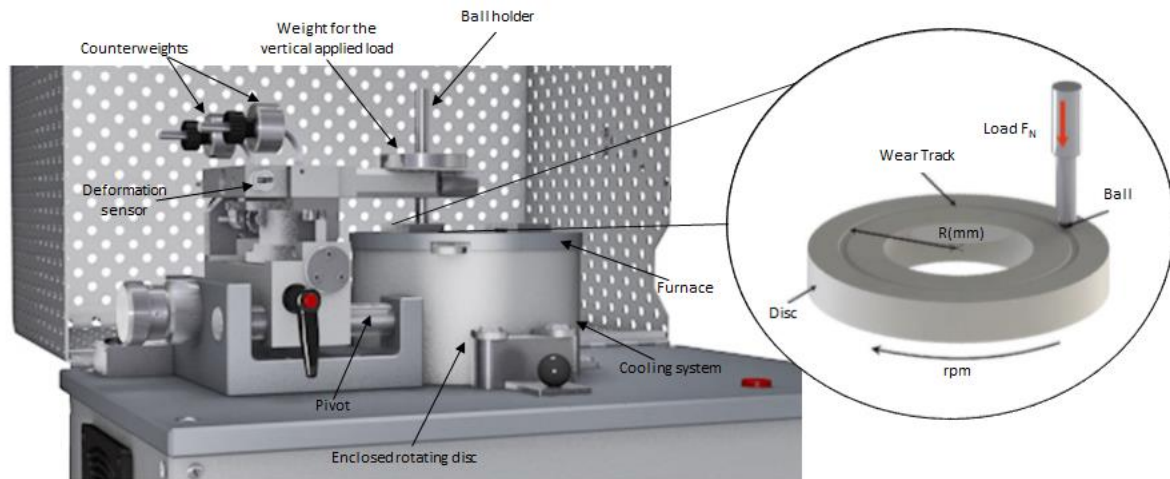


Fig. 4.7 Standard Anton Paar tribometer setup and mounting of the instrument for performing the ball-on-disc test (right), a close configuration of ball-on-disc (Left). Modified from [139 & 140]

The wear-scar diameter on the ball was measured by optical microscopy, while the wear-track depth profile was assessed by the means of a mechanical stylus profilometer, which is highly suitable for the evaluation of the surface topography. This technique consists of measuring the mechanical movement of a stylus in a vertical direction as it is moved horizontally (scanned) on the sample's surface. The position of the stylus, terminated by a diamond needle, is monitored by the piezoelectric sensor [141].

#### 4.11 Thermogravimetric analysis

Thermogravimetric analysis (TGA) is used to accurately measure the sample mass versus temperature (typically at least 10  $\mu\text{g}$ ) in a controlled atmosphere. For example, the sample's mass can change during heating, due to losing humidity (vapour emission, weight loss) or oxidizing (fixation of gas from the atmosphere, weight gain). TGA traces the mass change, which appears as steps or consist of peaks; one can deal with derivatives of TGA with respect to time or temperature.



Figure 4.8 shows the schematic diagram of the TGA principle. It consists of placing a sample into a pan connected to a microbalance set to zero. Then, the sample is heated according to a controlled thermal cycle (gas flow, heating rate and so on). The atmosphere can be either an inert atmosphere, such as nitrogen or helium, or a reactive atmosphere for instance air or oxygen. During the analyses, weight changes are continuously recorded as a function of elapsed time or increasing temperature. Thus, the TGA curve corresponds to the TGA signal, converted to percent weight change (wt%) on the Y-axis versus the reference material temperature ( $T$  °C) on the X-axis.

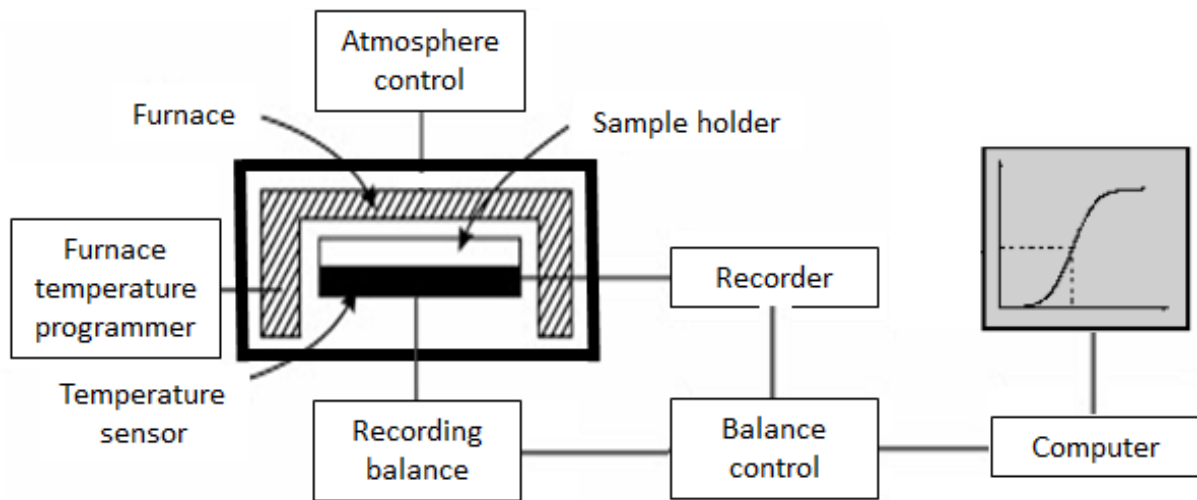


Fig. 4.8 Overview of thermogravimetric methods of analysis. Reproduced from [142]

## 5 Question section

The thesis investigates the structure transformation and optimises the chemical composition of hard nitride coating produced by PVD and its stability at high temperatures. Furthermore, it correlates the high tribo-chemistry and tribo-oxidation surface using high-resolution characterization techniques with the performance obtained on WC-Co cutting tools during high-speed machining.

Overall, this dissertation addresses the following questions:

- What are the benefits and limitations of PVD coating methods used to deposit hard nitride coating, specifically dcMS, HiPIMS, and CAE?
- How does choosing the correct discharge parameters affect the coating structure, mechanical properties, and tribological properties in the three PVD deposition systems?
- Is it possible to develop unique properties for coatings by a co-deposition process using a combination of HiPIMS and dcMS?
- How does varying the Ti/Al ratios influence the structural, mechanical, and tribological properties of TiAlN hard coatings?
- How can Al/Cr, Al/Si, and Al/(Cr+Si) ratios affect crystallographic phase and stability of nitride coatings?
- What is the relationship between microstructure and micromechanical properties of these nitride coatings with different Ti/Al ratios, Cr and/or Si additive elements?
- How can the addition of Cr to TiAlN coatings affect the thermal stability, considering the Ti/Al ratio?
- What is the significance of Si addition in relation to the thermal stability of TiAlN and TiAlCrN coatings?
- How does oxidation occur and what mechanisms are involved?
- What was the effect of the coating alloys on the oxide growth kinetics?

All of these questions were addressed by employing the most advanced analytical techniques at the micrometric and nanometric scales to determine the microstructural and structural properties of the coating as-deposited and after several oxidation times at 950 °C.

Due to these analytical techniques, the thesis presents information on the thermal stability and mechanical properties of TiAlCrN, TiAlSiN, and TiAlCrSiN coatings at high temperature, 950 °C. It also provides data to understand the root causes for improving the oxidation resistance of the c-TiAlN solid phase by alloying Cr or a combination of Cr and Si.

The result of this study is new functional coatings for industrial applications in the field of dry high-speed machining, significant to the steel or stainless steel milling or even for the tuning of refractory materials, with an increase of 30% in the lifetime of the coated cutting inserts with a better performance at higher temperatures (>850 °C).

## 6 Summary of results

This chapter offers a brief recapitulation of the most important results obtained during the presented work and highlights the main contributions to the field.

One of the primary objectives in this work was to gain an in-depth understanding of the PVD processes operated within dcMS and HiPIMS discharges. In order to achieve this goal, we have studied the impact of the main sputtering parameters during the deposition of TiAlN coatings. The study included the effect of ( $N_2$  flow, substrate temperature, pressure, duty cycle, applied power density, substrate bias and interlayer) on the deposition rates, coatings thickness, thin-film morphology, structure and texture orientation as well as, mechanical properties (e.g. residual stress, hardness and wear). Furthermore, the methodology included a comparative study of a same coating obtained with an industrial CAE process.

Summary:

- The  $N_2$  flow significantly influences the growth of the coating structure during the deposition process. Coatings produced without  $N_2$  flow exhibit a laminate structure. In cases where the nitrogen content constitutes less than 50 at.% of the total coating content, the development of a columnar structure is minimal, even when employing the full target poisoning mode.

The study determined the gas ratio that optimizes the coating composition for achieving stoichiometry while maintaining a columnar structure. Transitioning the target to the fully reactive mode (poisoning target) using dcMS requires a higher  $N_2$  flow compared to HiPIMS, even when applying the same power density and different duty cycles (refer to appendix 9.1). This discrepancy can be attributed to the utilization of short unipolar power pulses on the target. These pulses provide more time for the  $N_2$  gas to react and cover the target surface during the time-off periods. This phenomenon also explains the varying  $N_2$  flow requirements for different duty cycles.

- The main impact of pressure was on the kinetic-molecular structure between the target and substrate. The pressure exerted by gas in a chamber result from collisions between the gas molecules and the walls of the chamber, where the number of collisions decreases with decreasing pressure (for more details see the paper I). Depending on the working pressure, the mean free path of atoms between the target and the substrate will change. At low

pressures, the dominant transport mechanism for sputtered particles is ballistic, with collisional transport playing a significant role. In contrast, at high pressures, diffusive transport becomes the dominant mode both before and after their thermalization. Additionally, for the highest pressures (i.e. for the less energetic species), a backscattering effect of the sputtered atoms to the target can also be considered. It is worth mentioning that a direct correlation between the evolution of the main free path estimation and the deposition rate has been identified. This correlation shows a continuous decrease when pressure is increased, with no change in slope. The working pressure also influences the level of in-situ residual stress for these nitride coatings. The stress level changes from tensile stress at high pressure to compressive stresses at lower pressures. Furthermore, the (FWHM) of the peak slightly decreases with increasing working pressure, which can be linked to the evolution of grain size. It can be proposed that the decrease in working pressure leads to an extension of the grain size, resulting in compressive stress in the coating.

- The nucleation and growth mechanisms are also governed by the surface mobility of the film-forming species (adatoms), which in turn depends on the energy, flux and direction of the incident species. For HiPIMS, the decrease in duty cycle can be compensated by an increase in pulse power energy and an increase of the ionization of the Ti and Al sputtered atoms when the duty cycle was decreased. The deposition rates increase when the duty cycle decreases, hence increasing the applied power density (for more details see the paper I). The understanding of these effects could be explained by the dynamics discharges of HiPIMS, where the duty cycle represents the ratio between time-on and time-off.

- Since the ion to neutral ratio is the key parameter determining the evolution of the film texture, applying a negative substrate bias allows an intense ion bombardment of the growing film, resulting in an improvement of the coating hardness of  $30 < B_v > 120$  (for more details see the paper I). Applying bias increases the average kinetic energy of the ionic energetic species and significantly modifies the nucleation mechanism, which affects the film properties. By tuning the negative bias voltage applied onto the substrate during the peak power, more  $Al^{n+}$  and  $Ti^{n+}$  ions participate in the growing mechanism of the film, providing additional kinetic energy and momentum transfer that alter the film-forming conditions. Increasing the negative substrate bias voltage may cause resputtering of the film due to argon ion substrate bombardment, where Ar atoms are implanted in the film, leading to the

generation of lattice defects and potential high residual stresses. This also results in a small decrease in the coating's crystallization with a higher bias voltage of -70 V.

- The properties of thin films are often affected by the properties of the underlying material (intermediate layer) between the WC-Co substrate and the thin film coatings. The study covered three different cases: coating without an intermediate layer, with a gradient intermediate layer from TiAl to TiAlN, and with TiN intermediate layer. The intermediate layer does not have a clear effect on the coatings' morphology, texture, or main plane orientation. However, the intermediate layer effect was evident in the scratch test where the coating with TiN intermediate layer has the best adhesion (see the appendix 9.2). The coating with an intermediate layer deposited by dcMS has better adhesion than the one deposited by HiPIMS, which could be explained by the effect of flux and the ions distribution energy on the substrate actually contributing to film growth, which is greater in HiPIMS than dcMS.

- TiAlN coatings' stress level achieved by HiPIMS coatings successfully matches the stress level induced by Arc, despite the ability to adjust residual stresses from tensile (in dcMS mode) to compressive stresses (in HiPIMS mode) through process parameter adjustments. This comprehensive comparative study holds significant importance for coating manufacturers aiming to optimize their specific deposition processes. The micromechanical properties of the coatings are significantly influenced by HiPIMS process parameters. Notably, increasing the compressive stress of the coatings improves cutting performance and enhances their mechanical properties, aligning with the requirements of coating technology. While the stress level decreases in TiAlSiN coatings with increasing Si addition, no evolution was observed in TiAlCrN and TiAlCrSiN coatings. This stress evolution is attributed to the reduction in crystallinity density of TiAlN coatings with Si addition. However, this structural phenomenon is not visible when Cr is added with or without Si to quaternary TiAlCrN or quinary TiAlCrSiN coatings (for more details see papers II and III).

- The comparison between CAE and HiPIMS for the TiAlN coating composition showed that both coating processes result in high-density coatings without any voids. They exhibit similar fine fibrous structure and grain size. These finer fibrous structures can be attributed to the fact that both coatings were grown using relatively high-energy species. In the case of the TiAlSiN coatings, the addition of Si resulted in the refinement of the fibrous structure. Furthermore, the introduction of Si led to an increase in the crystalline cell and a decrease in the grain size. On the other hand, when Cr is present in the coatings, the opposite effect

occurs. This situation could explain why the amorphization mechanism's retardant effect has been observed due to the addition of Si when chromium is present in the coating composition.

- Arc deposition has the advantage of high deposition rates with a large ratio of ionized vapor. However, its disadvantage is the negative effect of microscopic droplets on the coating topography. On the other hand, HiPIMS offers enhanced ionization sputtering and provides better control of thin film growth morphology. This leads to minimized surface defect generation, increased coating density, smoother surface coating, improved surface roughness, and high tribological properties compared to the classic CAE technology.

Additionally, CAE coatings have slightly lower Al content than HiPIMS coatings. This difference in Al content could be attributed to the formation of droplets at the coating surface in CAE, as these droplets are generally reported to be richer in Ti.

Moreover, in HiPIMS the top-view micrographs of the films have shown that the coating deposited with the highest applied power exhibits the smoothest surface. However, increasing the applied power in HiPIMS does not significantly alter the film morphology and structure.

In the same coating installation, the deposition rate range in HiPIMS is lower than that in dcMS. Nevertheless, in HiPIMS the average deposition rate increases as the power increases.

The HiPIMS/dcMS co-deposition configuration has the potential to achieve a high kinetic solid-solubility limit for adding elements in the fcc structure. This is achieved by carefully selecting the HiPIMS composition target and this for dcMS. As a result, the co-deposition configuration demonstrates a higher deposition rate range compared to CAE technology.

- The  $Ti_{50}Al_{50}N$  coating has an fcc structure with preferred orientation textures of (200) and (111) for CAE and HiPIMS, respectively. The nature of the substrate or the gradient (adhesion layer) in this  $Ti_{50}Al_{50}N$  coating does not appear to cause any change during growth. The ratio between these two crystallographic orientations was not significantly modified. No correlation was found between the residual stress and the development of a preferred orientation.

The study demonstrated that the initial fibrous growth already has a main orientation. The gradient of nitrogen content with thickness does not affect this selective fibrous growth mechanism, as low levels of stress were detected in this first stage of deposition. Similar conclusions were achieved for all HiPIMS coating alloys:  $TiAlN$ ,  $TiAlCrN$ ,  $TiAlSiN$  and  $TiAlCrSiN$ , which exhibited a preferred orientation texture of (111).

To explain this structural difference, our hypothesis is that the growth-oriented coating with a main preferred orientation of (111) for HiPIMS can be attributed to two factors. First, the high deposition rate with energetic ions/clusters during the plasma pulses, and second, the alternative free time during the plasma pulses off, allowing for film relaxation and increased surface mobility of sputtered particles.

The presence of Cr has allowed for better stability of the crystallinity structure when adding Si. In the TiAlSiN coating structure, Al atoms substitute the Ti atoms in the TiN lattice, and Si atoms are present with nitride atoms either through incorporation as a substitutional solid solution into the TiAlN lattice or via the formation of a separate amorphous Si<sub>3</sub>N<sub>4</sub> phase surrounding a nano-crystalline TiAlN (for more details, refer to papers II and III).

- The influence of elasticity, in combination with hardness, is considered a reliable indicator of wear resistance. The toughness/resistance to plastic deformation ( $H^3/E^2$ ) and the elastic strain (H/E) prior to plastic deformation are more important than extremely high hardness. Higher H/E ratios of a coating indicate its ability to resist mechanical degradation and failure in tribo-contact events. This is because the contact area remains elastic at higher stresses during an external impact. Additionally, a high value of the  $H^3/E^2$  ratio could be associated with the increased ability of the coating to absorb energy during deformation up to fracture. All coatings exhibit high wear resistance with a 0.1 H/E ratio, regardless of the stress level.

- A study was conducted to clarify the effect of two coating technologies, CAE and HiPIMS, on the friction coefficient. The measurements were obtained using a ball-on-disc tribological test. The wear rate between the CAE and HiPIMS TiAlN coatings was found to be quite similar, regardless of the level of compressive stresses. It was observed that there were different friction coefficients between the two types of coatings. The friction coefficient showed a strong correlation with adhesive wear. In the case of the CAE coating, this was linked to higher roughness due to the presence of particles on top of the coating.

- TiAlN coatings with fcc structure show an efficient resistance against oxidation up to 850 °C. This resistance is achieved by forming a protective  $\alpha$ -Al<sub>2</sub>O<sub>3</sub> outer-layer and a porous TiO<sub>2</sub> sub-layer, contributing to enhanced thermal stability up to 950 °C. First, an optimisation of the TiAlN chemical composition was done by defining the best Ti/Al ratio, second, by the incremental alloying of Cr to TiAlN, third, by additional doping by Si. A variety of TiAlCrN, TiAlSiN and TiAlCrSiN coatings were used to understand the mechanical properties and



oxidation resistance of the coating at elevated temperatures of up to 950 °C. The result confirmed when the TiAlN cubic structure decomposes into equilibrium phase cubic TiN and hexagonal AlN the mechanical properties (hardness) drastically decrease. Similarly, when the Si and/or Cr present in the coatings the cubic structure decomposes into c-TiN and h-Al(Cr/Si)N with the same behavior. The oxidation-resistance was improved when the Al content exceeded 26 at. % and reached 31 at. %. Beyond this range, the coatings exhibited a hexagonal structured (refer to appendix 9.4.2 for more details). Furthermore, the addition of Cr to TiAlN coatings provided excellent oxidation resistance while increasing the onset oxidation temperature by approximately 50 °C (more information can be found in paper II). The addition of Si to TiAlN coatings hindered the kinetic growth of oxidation (for additional details, please refer to appendix 9.4).

- The evolution of the structure during the annealing process of the HiPIMS coating alloys TiAlCrN, TiAlSiN, and TiAlCrSiN revealed that all coatings maintained the fcc micrometric fibrous structure with elongated fibers along the growth direction at 950 °C, after a 60-minute annealing duration. No segregation or coarsening was observed, even at the coating-substrate interface. Despite the duration and temperature of the annealing step, there was no evidence of spinodal decomposition or further precipitation of h-AlN. Furthermore, no indication of structural phase separation between the aluminum and titanium phases was highlighted. Therefore, it can be considered that the incorporation of Si and Cr atoms into these nitride alloys significantly delays phase separation during their use at high temperatures. High-resolution TEM investigation found that the size of the coating's fiber texture at 950 °C had increased compared to the as-deposited state, and the presence of an oxide scale on top of the nitride coatings was detected.

- Description of the oxide layers at 950 °C and their kinetic growth:

- First, in the case of the TiAlN coating, the coating does not show oxidation resistance above 800 °C primarily due to the quality of the oxide scales. A rutile TiO<sub>2</sub> layer forms with a relatively large number of porosities. This is caused by the fast diffusion of Ti ions to the surface, which affects the performance of the protective Al<sub>2</sub>O<sub>3</sub> layer, rendering it ineffective.
- Second, in the oxidized TiAlCrN coating at 950 °C, the oxide structure consists of a tetragonal TiO<sub>2</sub>-rutile region at the outermost layer, followed by an aluminum-chromium-based oxide containing Ti oxide-rich islands. The Cr concentration decreases

from the inner to the outer zone. Since Ti is not miscible in the mixed  $(AlCr)_2O_3$ , it forms islands with larger grain sizes compared to the mixed Al-Cr oxide matrix. D-SIMS depth profiles reveal that each oxide layer continues to grow throughout the oxidation period. Furthermore, the thickness of these oxide layers decreases with a higher addition of Cr content and with an increase of Ti/Al ratio in the coating without changing the layers that composed the oxide (for more details, refer to paper II).

- Third, the TiAlCrSiN oxidized coatings exhibit a similar oxide scale description to TiAlCrN coatings. The oxide scale morphology consists of a pure  $TiO_2$ -rutile layer at the external surface, followed by an Al-rich oxide layer. Internally, there is a mixed oxide region of  $(CrAl)_2O_3$  with small islands of  $TiO_2$ . However, the description of the third oxide region differs from the inner oxide region reported for oxidized TiAlCrN coatings without Si. In this case, the oxide scale is entirely composed of small crystallized grains surrounded by other amorphous grains. This particular oxide scale morphology has been correlated to the detection of Si and N elements which could delayed the total crystallization mechanism of this mixed oxide layer. The elemental compositions associated with these regions do not indicate a significant concentration of Si or possible segregation of Si at grain boundaries. TEM observations reveal that the internal oxide region is partially crystallized with particle grain sizes of approximately 5 nm, surrounded by an amorphous area. Electron diffraction analyses confirm that this mixed oxide region contains nano-sized or sub-nanosized  $(CrAl)_2O_3$  grains mixed with  $TiO_2$ -rutile grains. For this last coating composition, there is a consistent increase in the oxide scale thickness over time (for more details, refer to paper III).
- Finally, the TiAlSiN oxidized coating exhibits a bilayer oxide structure. The outer layer is rich in aluminum, consisting of  $\alpha-Al_2O_3$  corundum, while the inner layer is rich in titanium, composed of  $TiO_2$ -anatase. Additionally, Si and N are detected in the inner oxide layer. After TiAlSiN oxidized coating develops a double oxide layer of  $Al_2O_3/TiO_2$  on its surface. Unlike the other coatings, there is no regular increase in oxide thickness over time, which contributes to its high oxidation resistance.

- To summarize, the formation and growth of oxides at 950 °C are influenced by several factors, including the properties of the metal oxides, the partial pressure of the reaction gas, and the presence of defects in the crystal structure. These factors have an impact on diffusion phenomena. In order to gain a better understanding of the oxidation process and its kinetics,

isotopic oxidation experiments were conducted using D-SIMS. These experiments were carried out at 950 °C in different atmospheres, with varying durations based on whether  $^{16}\text{O}_2$  or  $^{18}\text{O}_2$  was used.

- First, at 950 °C, the addition of Cr to the TiAlN coating delays the diffusion of Ti to the surface. This delay leads to an improvement in oxidation by promoting the growth of an inner protective crystalline  $(\text{CrAl})_2\text{O}_3$  layer.

The presence of  $^{18}\text{O}$  in the outer  $\text{TiO}_2$ -rutile layer indicates the contribution of outward oxygen diffusion to the oxide-coating interface during oxide growth. The enrichment of  $^{18}\text{O}$  at the nitride/oxide interface suggests the inward diffusion of oxygen during the transport process, while outward cationic diffusion with titanium and inward anionic diffusion with oxygen continue. These diffusion processes lead to the formation of a thicker  $\text{TiO}_2$  layer.

As a result, a relatively high oxygen pressure can be observed at the interface between the mixed chromium oxide and the titanium oxide. This leads to two reactions: the formation of a chromium-rich oxide scale and the production of volatile chromium oxide species. Consequently, a chromium depletion zone is formed, and a very high aluminum oxide layer is generated just below the titanium oxide scale.

The APT results in the mixed aluminum-chromium oxide scale depict grain boundary segregations, confirming the outward diffusion of titanium for the development of  $\text{TiO}_2$  and driving the oxidation kinetics of the coating at the oxide-nitride interface.

- Secondly, the inclusion of Si in the TiAlCrN coating leads to the formation of oxidation layers that are similar to those observed in standard TiAlCrN coatings. These oxidation layers exhibit a regular increase in thickness, and their kinetic growth is primarily governed by inward oxygen diffusion over time. The main oxidation mechanism occurs at the interface of the nitride coating. Moreover, the development of the two oxide layers, namely the outer Ti oxide layer and the inner aluminum-chromium oxide layer, requires anionic diffusion of Al and Ti. This observation suggests that the growth kinetics of these layers are slower than the growth kinetics of the oxide layer in the TiAlCrN oxidized coating, due to decreasing oxide grain size when Cr and Si are present.
- Finally, at 950 °C, the addition of Si to TiAlN coatings leads to the formation of a bi-layer oxide consisting of nanometer-sized  $\text{TiO}_2$ -anatase crystallites beneath the dense

Al<sub>2</sub>O<sub>3</sub> protective oxide. Over time, this bi-layer oxide limits the kinetic growth of the oxide and acts as a barrier against internal oxidation phenomena.

The high oxidation resistance of this coating was confirmed by the absence of a high concentration of <sup>18</sup>O at the oxide-nitride interface, suggesting a weak internal oxidation mechanism. The presence of <sup>18</sup>O on the external surface indicates minimal external alumina oxide growth. This explains the low inward cationic diffusion of oxygen.

The presence of Al in the TiO<sub>2</sub>-anatase layer acts as a doping process, stabilizing the anatase phase at high temperatures. Additionally, the presence of Si and N in the TiO<sub>2</sub> layer delays oxygen diffusion at the oxide/nitride interface, minimizing oxygen partial pressure at grain boundaries, and delaying the anatase-rutile transformation.

The presence of these two elements (Si and N) in the internal oxide layer indicates the possibility of other silicon-rich phases, such as Si<sub>3</sub>N<sub>4</sub> (with SiO<sub>2</sub>), surrounding the titanium oxide grains. These silicon-rich phases further delay internal oxygen diffusion and facilitate the bulk oxide diffusion of Al and Ti, which is a low kinetic process.

Analyzing D-SIMS depth profiles at 950 °C for different durations indicates a minimal increase in sputtering time. This finding suggests the development of a dense and compact oxide layer during the initial 16 minutes of oxidation, significantly reducing oxygen diffusion at the oxide/nitride interface and subsequently hindering the oxide growth mechanism.

## 7 Included papers

### Paper I

#### **Comparison on the structural, mechanical and tribological properties of TiAlN coatings deposited by HiPIMS and Cathodic Arc Evaporation**

- A. Supplementary information:
- B. Supplementary information:
  - B 1 Stress measurement:
  - B 2 Texture coefficient:

### Paper II

#### **Study of the oxidation mechanism at high temperature of nanofiber textured AlTiCrN coatings produced by physical vapor deposition using high-resolution characterization techniques**

- A Supplementary material about APT
  - A 1 APT sample preparation
  - A 2 Determination of compositions by APT

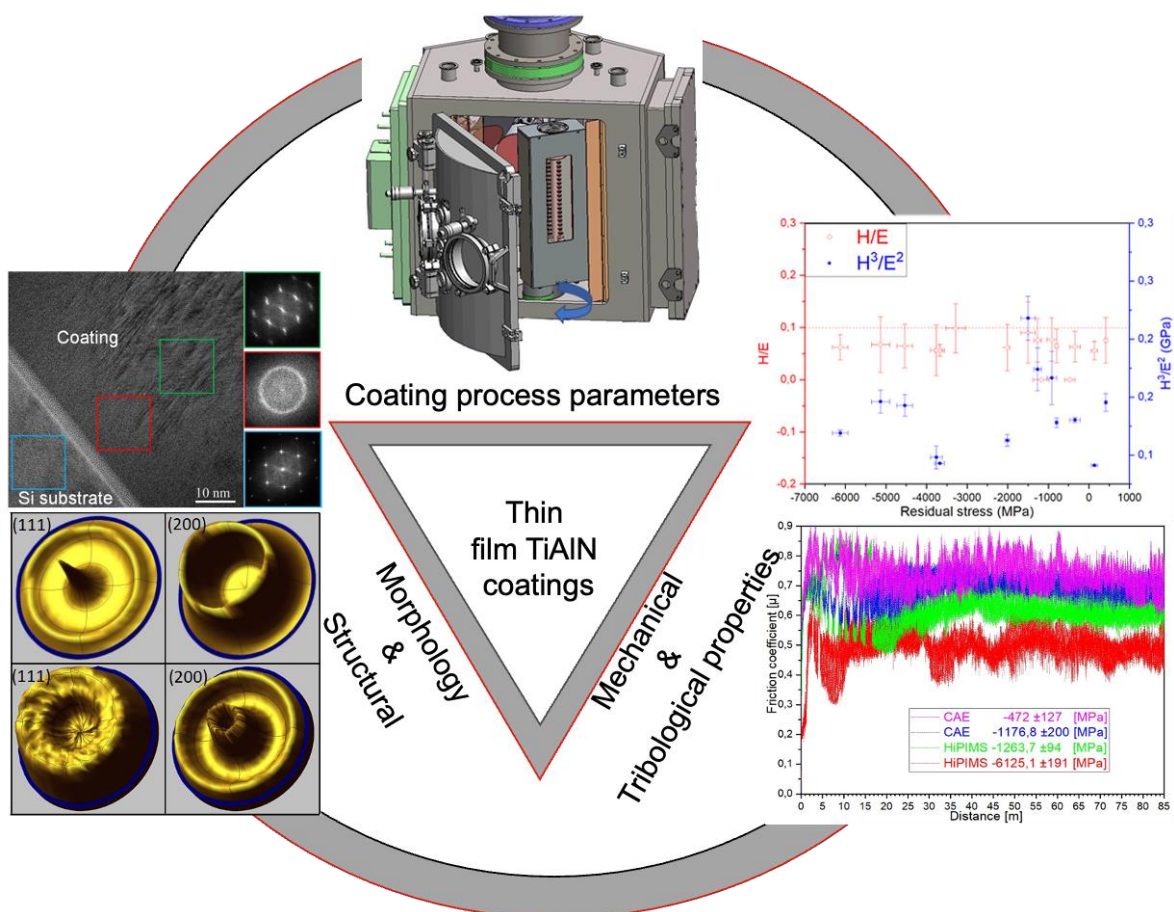
### Paper III.

#### **Influence of Si addition on the phase structure and oxidation behavior of PVD AlTiN and AlTiCrN coatings using high-resolution characterization techniques**

7.1 Paper I

**Comparison on the structural, mechanical and tribological properties of TiAlN coatings deposited by HiPIMS and Cathodic Arc Evaporation.**

M-R. Alhafian, J-B. Chemin, Y. Fleming, L. Bourgeois, M. Penoy, R. Useldinger, F. Soldera, F. Mücklich and P. Choquet





Contents lists available at ScienceDirect

Surface &amp; Coatings Technology

journal homepage: [www.elsevier.com/locate/surfcoat](http://www.elsevier.com/locate/surfcoat)

## Comparison on the structural, mechanical and tribological properties of TiAlN coatings deposited by HiPIMS and Cathodic Arc Evaporation

M.-R. Alhafian<sup>a,\*</sup>, J.-B. Chemin<sup>a</sup>, Y. Fleming<sup>a</sup>, L. Bourgeois<sup>b</sup>, M. Penoy<sup>b</sup>, R. Useldinger<sup>b</sup>,  
F. Soldera<sup>c</sup>, F. Mücklich<sup>c</sup>, P. Choquet<sup>a,\*</sup>

<sup>a</sup> Luxembourg Institute of Science and Technology, 41 rue du Brill, L-4422 Belvaux, Luxembourg

<sup>b</sup> Ceratit Luxembourg S.à.r.l., 101 route de Holzem, L-8232 Mamer, Luxembourg

<sup>c</sup> Saarland University, Chair of Functional Materials, Campus D3.3, Saarbrücken 66123, Germany

### ARTICLE INFO

#### Keywords:

High-Power Impulse Magnetron Sputtering (HiPIMS)  
Cathodic Arc Evaporation (CAE)  
Titanium-aluminium-nitride TiAlN-coatings  
X-ray diffraction (XRD)  
Transmission Electron Microscopy (TEM)  
Ball-on-disc tests

### ABSTRACT

TiAlN single layer coatings deposited by High-Power Impulse Magnetron Sputtering (HiPIMS) on carbide and Si-wafers substrates were performed. They were characterized in order to study the effects of different process parameters on the film stoichiometry, microstructure and morphology and finally their mechanical and tribological properties were investigated. For comparison, the properties of the same composition  $Ti_{50}Al_{50}N$  coatings produced by Cathodic Arc Evaporation (CAE) were also studied. Only the most influential process parameters, which are the effects of duty cycle, pressure, power and bias for the HiPIMS process are here discussed. High-resolution TEM images were used to investigate the microstructure of CAE and HiPIMS coatings and the observations indicate that both processes produced high density  $Ti_{50}Al_{50}N$  coatings with a fine fibrous structure, and a similar grain size. XRD analyses showed that TiAlN coatings deposited by CAE and by HiPIMS have a single-phase cubic structure with respectively the (200) and (111) reflection peaks as a preferred orientation. Furthermore, the residual stresses determined by XRD for the HiPIMS coated samples show that it can be possible to tune them from tensile (+500 MPa) to high compressive stresses (-4000 MPa) by adjusting the process parameters. Independently of their intrinsic stress level, the HiPIMS coatings show similar hardness and the values obtained are in the same range of CAE coatings (30–35 GPa) with same composition and thickness. However, during ball-on-disc tests in dry condition using a steel ball against the coated carbide substrate, the behaviour of similar  $Ti_{50}Al_{50}N$  as deposited coatings produced by these two processes was different. Lower friction coefficients (-30%) but, higher abrasion kinetic of the steel ball as counterpart during pin-on-disk test (+50%) were recorded for the  $Ti_{50}Al_{50}N$  HiPIMS coatings. In conclusion, it is proposed that, for HiPIMS coatings with high compressive stresses (<-5000 MPa), having also low surface roughness and (111) main texture orientation, high tribological properties can be achieved.

### 1. Introduction

The mechanical and friction properties of binary titanium nitride (TiN) coatings obtained by Physical Vapor Deposition (PVD) can cover a large spectrum of cutting performance needs. However, due to this material's low oxidation resistance – the oxidation onset point is around 600 °C – more efforts were needed to make this type of material more resistant to oxidation. By adding other elements such as aluminium (Al) to the films, these ternary coatings can improve their thermal behaviour and consequently, their in-service life [1,2]. The ternary titanium-aluminium-nitride (TiAlN) coatings have been studied due to their

outstanding mechanical and physical properties, such as thermal stability, wear properties and corrosion resistance [3,4]. The focus for this type of coatings on commercial cutting tools is now to improve its sustainability in the machining process under a completely dry environment [5].

Cathodic Arc Evaporation (CAE) deposition of TiAlN coatings on cemented carbides is currently one of the main used technique in the industrial applications compared to direct current Magnetron Sputtering (dcMS) and High-Power Impulse Magnetron Sputtering (HiPIMS) techniques. It has the advantage of having high deposition rates with a large ratio of ionized vapor [6]. However, the main disadvantage of CAE is the

\* Corresponding authors at: Luxembourg Institute of Science and Technology (LIST), 41, rue du Brill, L-4422 Belvaux, Luxembourg.  
E-mail addresses: [mohamed.alhafian@list.lu](mailto:mohamed.alhafian@list.lu), [r.alhafian@gmail.com](mailto:r.alhafian@gmail.com) (M.-R. Alhafian), [patrick.choquet@list.lu](mailto:patrick.choquet@list.lu) (P. Choquet).

<https://doi.org/10.1016/j.surfcoat.2021.127529>

Received 9 June 2021; Received in revised form 15 July 2021; Accepted 17 July 2021

Available online 21 July 2021

0257-8972/© 2021 Published by Elsevier B.V.



M.-R. Alhafian et al.

negative effect of microscopic droplets on the coating topography [7,8].

Since Mozgrin et al. published the first HiPIMS coating deposition in 1993 [9], HiPIMS has gained more and more substantial interest amongst industrialists as a future technique for coating applications. Over the last years, hard nitride coatings were deposited by HiPIMS and proposed to the market as an alternative to similar CAE coatings. On the other side, academic works have also reported interests for the mechanical properties of titanium nitride-based coatings synthesized by HiPIMS. It is difficult here to give an extensive view of the works already published, but some of them can be given as illustration. Firstly, it is claimed that this process leads to smoother surface coatings and it offers a better control of thin film growth morphology compared to CAE [6,10,11]. Alami et al. reported the enhanced ionization sputtering and thus an increased coating density of TiN HiPIMS coatings [12]. The improvement of the quality and the uniformity of TiAlN coatings deposited by HiPIMS were proposed by Shimizu et al. [13]. Hardness enhancements using HiPIMS were reported by Guillaumot et al. for AlN coatings [14]. However, as far as the authors know, a direct comparison between the same titanium nitride coatings processed by HiPIMS on the one hand and CAE on the other hand, and deposited on the same substrates and at the same substrate temperature was not really considered. Therefore, in this present work, we report the effect of different Ti<sub>50</sub>Al<sub>50</sub>N HiPIMS deposition conditions on the mechanical properties of the coating like the intrinsic stress, the hardness and the wear resistance in comparison to CAE coatings. The comparison covers the effect of pressure and bias, as well as the duty cycle on the time-dependent discharge characteristics and on the film chemistry and microstructure.

## 2. Experimental and characterization

A set of Ti<sub>50</sub>Al<sub>50</sub>N single layer coatings were deposited on mirror-polished silicon wafers (Si) with a crystal orientation of  $100 \pm 0.5^\circ$  and on polished cemented tungsten carbide (WC-Co) plane discs, produced from a mixed powder of (WC-9%Co) and other carbide elements like (Ti, Ta, Nb) C with  $14.55 \text{ g/cm}^3$  density. Before depositing the coatings, both substrates were cleaned in an ultrasonic bath using ethanol for 5 min. The coatings were carried out by dcMS or HiPIMS technique inside a PVD coater machine (Fig. 1) specifically designed and assembled in the Luxembourg Institute of Science and Technology (LIST), to upscale and to further implement the process from the laboratory to the industrial scale. The same composition CAE-TiAlN coatings were deposited with an Oerlikon Balzers RCS industrial CAE without filtering system in pure N<sub>2</sub> atmosphere at a pressure of  $3.2 \times 10^{-2}$  mbar. The bias voltage was fixed at  $-40 \text{ V}$  and the substrate temperature was at  $450^\circ \text{C}$ . By HiPIMS, a 500 Hz pulse frequency was used and three average powers density 4, 6 and  $8 \text{ W/cm}^2$  besides three duty-cycles 2.5%, 3.5% and 5.5% were applied. The power was supplied to the target by using a MELEC SIPP 2000 generator. Prior to the coating step, the chamber was pumped down to  $10^{-6}$  mbar thanks to a turbo-molecular pump. Before depositing the coatings, a gradient interlayer of TiAl/TiAlN (from metallic to nitride coatings) with a thickness of  $\approx 0.5 \mu\text{m}$  was deposited by dcMS to improve the coating adhesion. The thicknesses of the coatings were in the range of 3.0–3.5  $\mu\text{m}$ . The target was prepared by a powder metallurgical process with a composition of Ti<sub>0.50</sub>Al<sub>0.50</sub> at.% and its surface is  $500 \text{ cm}^2$ . The depositions were carried out in static mode and the distance between the substrate holder and the target was 85 mm. A mix of nitrogen (N<sub>2</sub>) gas and argon (Ar) gas in (99.998% purity) was used and the pressure was regulated between  $2 \times 10^{-3}$  and  $1 \times 10^{-2}$  mbar by a butterfly valve. Bias voltages were applied on the substrates during the coating time, and 6 different values were

Surface & Coatings Technology 423 (2021) 127529

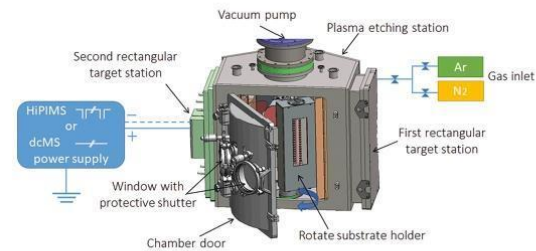


Fig. 1. Schematic drawing of PVD coater machine, targets magnetron and substrate holder rotation.

chosen between 0 to  $-160 \text{ V}$ . During the deposition, the substrate temperature was measured by using a thermocouple and the heating system was stabilized before and during the deposition. The nitrogen flow rates for each duty cycle conditions were adjusted to reach stoichiometric nitride coatings, while the argon flow rate was held constant at 50 sccm. The voltage and the current intensity on the target were monitored as a function of time by using a Teledyne Lecroy HDO4054 oscilloscope [15]. The target voltage evolution as a function of the ratio of nitrogen content has been measured in order to generate the hysteresis curve between metallic and reactive sputtering mode and to deduce the optimum gas ratio to get stoichiometric coating composition. Plasma emissive species in the discharge were identified using an Acton SP 2750 optical emission spectroscopy (Princeton Instruments). Here, the optical fiber probe was mounted within the chamber in order to detect the space-resolved discharge. The optical signal was recorded during all time-on/off for every duty cycle with a minimum overlap of 1 nm and a final resolution 0.023 units/points (more details in supplementary information Fig. A.1).

The determination of the thin film's crystalline phases and the structural properties were assessed by X-ray diffraction (XRD). The measurements were carried out using a Bruker D8 Discover diffractometer in parallel beam configuration using a Cu K $\alpha$  radiation with a power of 1600 W (40 kV; 40 mA). The texture analyses were performed on an Empyrean XRD (PANalytical, Almelo, Netherlands) operated in Bragg-Brentano geometry in point focus configuration using a Cu K $\alpha$  radiation at 45 kV and 40 mA. The residual stress measurements and the stress-free lattice  $a_0$  were performed using the classical single  $\{hkl\}$   $\sin^2\psi$  method on the (200) reflection plane of the Ti<sub>0.45</sub>Al<sub>0.55</sub>N phase. This choice was made because of the strong texture of the coatings, which in some cases induced a relatively large error on the stress values. More details of the method are described in the supplementary information [40–50]. For the determination of the residual stresses, each E-modulus was measured by nano-indentation test and the method is reported later. For determining the coating's texture, pole figure measurements were carried out on the (111) and (200) Ti<sub>1-x</sub>Al<sub>x</sub>N reflections to get information on the distribution of the specific crystal orientation over all possible sample orientations. During the whole measurement, the sample was rotated in steps of  $5^\circ$  starting from  $\Phi = 2.5^\circ$  to  $357.5^\circ$ . The sample was tilted up to an angle  $\Psi$  of  $85^\circ$  with a step of  $5^\circ$ . The FWHM calculated on the (422) reflection peak measured in Grazing Incidence (GI)-XRD with an incident angle  $\omega$  fixed to  $2^\circ$ , and the crystallite size was calculated using Scherrer's equation.

The elemental composition and morphology of the thin film coating were investigated using Field-Emission Scanning Electron Microscope (FE-SEM) (Hitachi SU-70, Japan) equipped with an Oxford X-Max<sup>N</sup> 20



**Table 1**  
Summarizes the main deposition conditions, the compositions determined by EDX and the main structure data obtained by XRD.

Mode	T <sub>substrate</sub> °C	Bias V	Texture coefficient			Lattice a <sub>0</sub> Å	FWHM determined on (422) (°)	Composition (at.%)		
			(111)	(200)	(220)			Al	Ti	N
CAE-TiAlN <sup>a</sup>	450	-40	0.882	1.424	0.206	4.1827	2.0884	22	28	50
HiPIMS-TiAlN <sup>a</sup>	400	0	3.758	0.049	0.138	4.1790	2.3364	26	24	50

<sup>a</sup> The coating has been deposited on the WC-Co substrate.

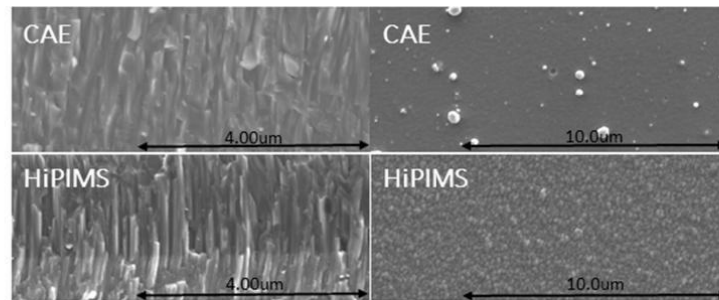


Fig. 2. Cross-sectional and top-view images of the TiAlN films deposited by CAE and HiPIMS.

mm<sup>2</sup> Energy Dispersive X-ray Spectrometer (EDS) (error of 1 at.%) [16]. The coatings on Si wafers substrates have been used for the SEM cross-section observations to determine the structure morphology and the coating thickness. Furthermore, high-resolution TEM observation was used to examine the grain size, crystal structure and diffraction patterns. The samples were prepared by Focused Ion Beam (FIB) technique: Helios Nanolab 600 dual beam focused ion beam instrument. The lift-out technique was used and the thinning of the sample was done starting with 30 kV and successive steps reducing the ion current down to 50 nA. The final cleaning step was done with 5 kV and 16 nA to minimize possible artifacts. TEM was conducted with a JEOL JEM 2011

instruments and performed at 200 keV beam energy, with an objective aperture of radius 0.5 Å<sup>-1</sup> in reciprocal space, to exclude high angle diffuse scattering and improve contrast.

The nanoindentation tests were performed at room temperature by using Anton Paar-CSM NHT3 with a Berkovich diamond tip to evaluate the instrumented hardness (H<sub>IT</sub>) and instrumented E-modulus (E<sub>IT</sub>) [17]. Before doing this test, the samples were polished, removing ≈0.3 µm of the coating, in order to avoid the influence of the different surface roughness arising on the coatings deposited in different conditions. The applied load was 20 mN leading to a penetration depth of about 0.2 µm in a 5 × 5 indentation matrix. The Poisson ratio was assumed to be  $\nu =$

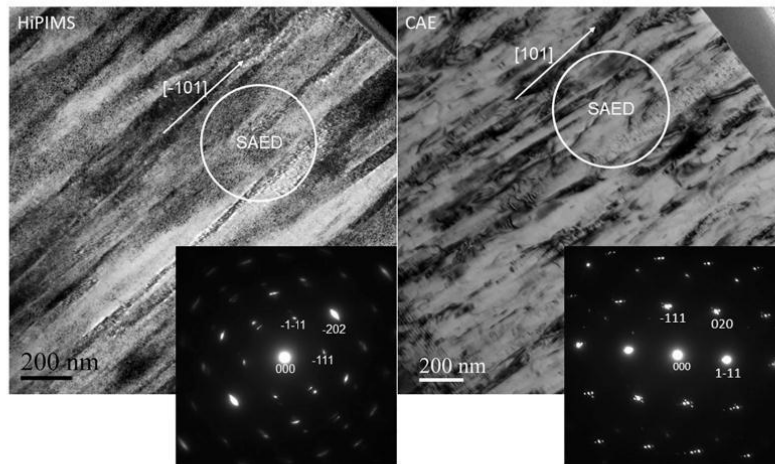


Fig. 3. Transmission Electron Microscopy-high-angle annular bright-field (STEM-HAA-BF) cross-sectional overview image of the TiAlN HiPIMS (left) and CAE (right) coating, SAED pattern in the coating region presenting the main texture orientation.

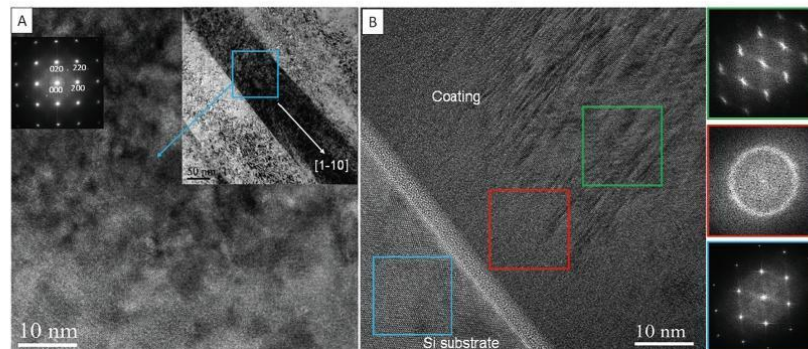


Fig. 4. HRTEM micrograph of TiAlN HiPIMS coating. (A) image of the grain distribution inside a fiber of the coating, (B) image of the interface between the Si substrate and the TiAlN interlayer with corresponding Fast Fourier Transform (FFT) patterns for each zone.

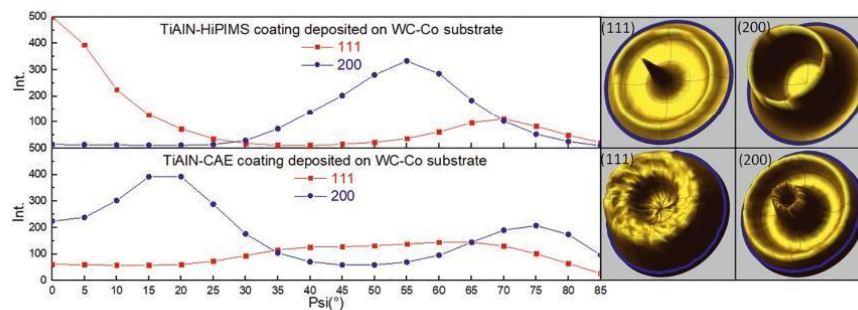


Fig. 5. Fiber texture and pole figures of (111) and (200) crystal direction for the same TiAlN coating deposited on Si wafer and WC-Co substrates by HiPIMS and CAE.

0.177 [18]. The tribological behaviour of the coatings was investigated by dry-sliding test at room temperature by using an Anton Paar TRB<sup>3</sup> tribometer. The normal load, sliding speed, and radius of the wear track were kept constant at 2 N, 10 cm/s, and 7 mm, respectively. This 2 N load is the best compromise between a sufficiently lasting coating lifetime and a lack of friction measurement artifacts due to the roughness of the samples. The test was undertaken in ambient atmosphere against a steel ball Ø 6 mm. The dry-sliding test was performed for 2000 laps. After the tribo-test, the wear scar on the ball was observed using an optical microscopy, while the wear-track depth profile was assessed by the means of a mechanical profilometer using the KLA Tencor P-17 benchtop stylus profiler system [19].

### 3. Results and discussion

Table 1 summarizes the main deposition conditions for the two processes and data for the TiAlN coatings with the composition determined by EDX and the structural information by XRD. In both types of coatings, the nitrogen is close to stoichiometry ( $\pm 2$  at.%), while the Al content is slightly lower by CAE coatings than by HiPIMS. This latter feature could be the effect of the droplet formation at the coating surface generally observed in Arc discharge as these droplets are generally

reported to be richer in Ti [20,21].

The SEM cross-sectional views of the films deposited by CAE and HiPIMS show a similar micro-columnar structure. However as observed on the top views (Fig. 2), the surface topographies are different with impingement of micro-particles with a diameter between 1 and 0.1  $\mu\text{m}$  for the CAE coating.

The HiPIMS coatings displayed a similar structural morphology of the coatings, independently of the nature of the substrates (WC-Co or Si-wafer). To observe the film's structure at highest resolution, TEM images were performed (cf Fig. 3). For both deposition process, a very high coating density can be observed and no voids can be detected at grain boundaries all across the coating thickness. The width of the columns is around 100 nm and quite constant from the interlayer to the external surface, for both CAE and HiPIMS deposition modes. These finer columnar structures can be linked to the fact that all films were grown essentially with relatively high energetic species. Electron diffraction studies showed that the  $\text{Ti}_{50}\text{Al}_{50}\text{N}$  coatings deposited by CAE and HiPIMS are crystalline with B1 NaCl-type crystal structure. Selected Area Electron Diffraction patterns (SAED) done in different regions for each film and complemented with bright field images show that both CAE and HiPIMS deposition process give coatings with a main texture orientation. This effect will be discussed in a next section of this article.

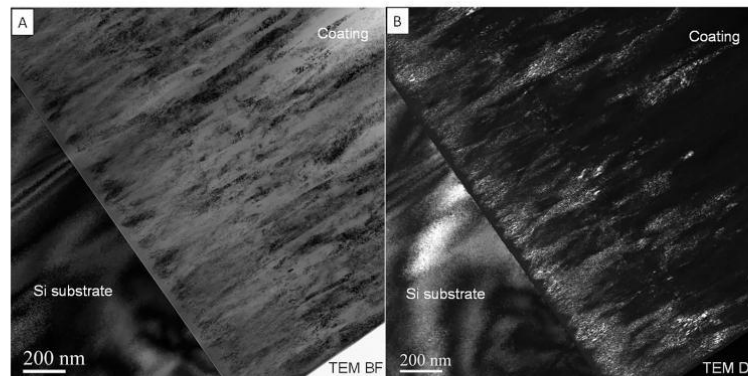


Fig. 6. TEM observations of a cross section for a TiAlN HiPIMS coating. Images at the interface between the Si substrate and the coating, bright field image (A) and dark field image (B).

High Resolution Transmission Electron Microscopy (HRTEM) analyses has also been carried out on these coatings. Fig. 4a shows the grains distribution inside the column for the TiAlN HiPIMS coating. The grain size can be estimated to be below 10 nm, which is in good agreement with estimations deduced from XRD analyses, and most of these grains inside the column have the same crystallographic orientation. At the interface between the adhesion layer and the coating, the first part of the TiAlN coating with an estimated thickness of 10 nm shows an amorphous structure Fig. 4b. Compared to same composition coatings deposited by magnetron sputtering, this amorphous zone is much thinner when the TiAlN is deposited by HiPIMS. This quick structural organization of the nitride coating is certainly associated to the deposition of more energetic species by HiPIMS. On the Si-wafer substrate, this interface is clear and no common interphase between  $\text{SiO}_x$  and titanium nitride phases have been observed.

Furthermore, to get information on the orientation distribution, pole-figure measurements were performed in a Schultz arrangement [22,23]. Fig. 5 shows the effect of the process on the two preferred orientations (111) and (200) for the  $\text{Ti}_{50}\text{Al}_{50}\text{N}$  coatings on WC-Co. For the HiPIMS coating, the (111) pole figure has its maximum intensities at  $\psi$  values around 0–5 and 65–75°, whereas the (200) pole figure with minor intensity comparatively to (111), has maximum intensities at  $\psi$  values around 50–60°. Contrary to the HiPIMS coatings, the CAE coatings present (200) maximum intensities at  $\psi$  values around 15–20 and 70–80° where the maximum intensities of (111) was very low (less than half of (200)). There is a clear difference between the two types of coatings where the preferred orientation changes from close to (111) at HiPIMS to (200) at CAE. All films presented in this study are either (111) or (200) fiber textured and are rotationally symmetric. Hence, an equal-biaxial stress state is present. The nature of the substrate or the gradient (adhesion layer) in the TiAlN coatings does not seem to produce any change during the growth, as the ratio between these two crystallographic orientations was not significantly modified (not reported here).

The development of texture in PVD coating was explained by different authors as a competition between the coating's surface energy and residual stress energy. For instance, Falub et al. discussed the transition from a (200) as a preferred orientation to a (111) for TiAlN CAE-coatings and they have correlated this transition to the apparent

residual stress during the film's growth considering that the film with higher residual stress has a (111) preferred orientation during its growth [22]. Moreover, Alling et al. explained the orientation difference between the monolithic TiN CAE-coatings as a result of increasing the kinetic energy of the incoming ions hence increase the probability of surface diffusion out of the (100) plane. He concluded that compressive stress development and (002) preferential growth are both kinetically driven processes but exhibit distinct dependence with the substrate fluxes [24]. More recently, Abadías et al. observed a correlation between the residual stress and the development of a preferred orientation in TiN thin film coatings. They mention that TiN coatings with tensile or near-zero residual stress have a (111) preferred orientation due to the presence of attractive forces at the grain boundary and/or void formation. In case of a (200) preferred orientation, the latter is due to incorporation of point defects in the film induced by the bombardment of energetic species (atomic peening). While the inclination angle of diffracting planes for the third texture orientation (220) is decreased with the increase of the residual stress in the coating [25]. In our study, the (111) and (220 - at the highest bias voltage) textures are the main preferred orientations observed for HiPIMS coatings whereas the (200) preferred orientation is obtained for CAE coatings.

Fig. 6a shows the bright field TEM observations of the interlayer for the HiPIMS  $\text{Ti}_{50}\text{Al}_{50}\text{N}$  coating. With the dark field image of this area (Fig. 6b), it can be clearly shown that even the first columns of this layer have already a main orientation and the gradient of nitrogen content with the thickness does not affect this selective columnar growth mechanism. This statement will not support the principle of residual stresses which can drive a preferential growth orientation of the column as low level of stresses are detected in the first stage of deposition. For these  $\text{Ti}_{50}\text{Al}_{50}\text{N}$  coatings deposited by HiPIMS, it would more support the hypothesis that the growth-oriented coating with the main preferred orientation (111) can be linked to: first the high deposition rate with energetic ions/clusters during the plasma pulse on, and second the alternative free time during the pulse off, which leaves for the film time for relaxation, hence more time for surface mobility of sputtered particles.

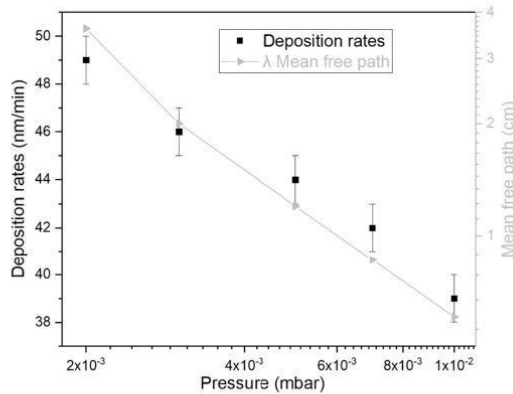


Fig. 7. The mean free path of the sputtered atoms at each pressure and the related deposition rates.

3.1. Influence of HiPIMS process parameters on the micro-mechanical properties of the coatings

It is known that the level of the internal stresses of the coating plays a dominant role in the lifetime of WC-Co coated cutting tools. Bouzakis et al. reported an improvement in cutting performance as a result of improving coatings mechanical properties by increasing their compressive stress [26,27]. Other authors have also reported that the coated inserts with low compressive stresses or with tensile stresses in the substrate-film interface are more subject to cohesive tool damages during cutting processes [28]. In this context, the evolution of coating residual stresses with respect to different deposition parameters need to be studied. The main results will now be discussed throughout the coming section.

3.1.1. Effect of the pressure impact

Depending on the working pressure, the mean free path of atoms between the target and the substrate will change. Therefore, to understand the influence of the pressure, the properties of five HiPIMS films deposited under a range of working pressure from  $2 \times 10^{-3}$  to  $10 \times 10^{-3}$  mbar were studied. Considering a distance of 85 mm (between target surface and substrate) at the lowest pressure, it will result in a higher probability of a straight trajectory with none or 2–3 collisions. At the highest pressure, it can be predicted that more than 10 collisions are possible for the sputtered atoms. If no clear dependence can be observed for the final chemical composition of the film, some other differences linked to the microstructure and the in-situ mechanical properties have been seen. These observations can be discussed based on the effective thermalizing collision theory. Depending on the working pressure, the collisional transport of sputtered particles at low pressures can be a dominant ballistic transport whereas at high pressures, diffusive transport (is dominant) before and after their thermalization. Also, for the highest

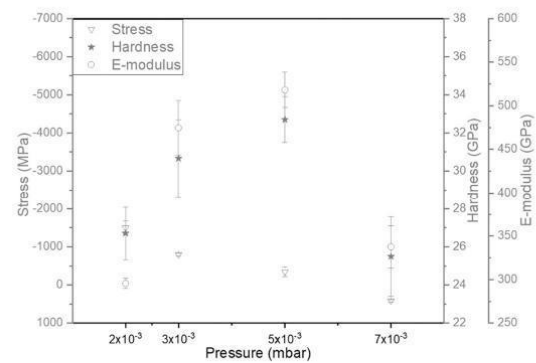


Fig. 8. The effect of different pressures on the evolution of internal compressive stresses, E-modulus and hardness.

pressures (i.e. for the less energetic species), it can also be considered a backscattering effect of the sputtered atoms to the target.

The mean free path at each pressure and the deposition rates in relation with the working pressure are reported in Fig. 7. In this range of pressure variation, a direct correlation between the evolution of the mean free path estimation and the deposition rate has been identified with a continuous decrease when pressure is increased and with no slope change. The Table 2 reports the chemical and structural data of the coatings depending on the deposition pressure and the electrical working conditions of the target. A continuous decrease of the peak target voltage (–10%) with increasing pressures is here recorded, and an increase of the peak current is observed, which could be associated to an increase of the secondary electron emission and consequently, to a higher probability of the ionization of sputtered atoms [29]. The chemical compositions of the coatings with nitrogen contents flow are not sensitive to the different working pressures, but a texture modification is observed for the higher pressures, which can indicate a change of the growth mechanism of the coating. The morphology of the films shows the same structure independently of the working pressure. The (111) diffraction peak position at the pressure of  $2 \times 10^{-3}$  mbar is in good agreement with the PDF card number 04-015-2554 for the chemical formula of  $Ti_{0.45}Al_{0.55}N$ , while a small shift toward the higher angles is observed when increasing the working pressure. The inclusion of argon atoms at the higher pressures can be considered to explain this behaviour, this Ar-entrapment was detected by EDX measurements.

The working pressure has also an influence on the level of the in-situ residual stress for these nitride coatings (Fig. 8). The stress level has changed from tensile stresses at high pressure  $7 \times 10^{-3}$  mbar to compressive stresses for the lower pressure. The measured stresses at  $10 \times 10^{-3}$  mbar is not reported as small cracks were observed on the coating's surface during the SEM observations. Furthermore, the FWHM of the (422) peak slightly decreased from  $2.336^\circ$  to  $0.506^\circ$  with increasing the working pressure from  $2 \times 10^{-3}$  to  $10 \times 10^{-3}$  mbar, respectively. If we consider that the evolution of this parameter can be

Table 2

Summarizes the main deposition conditions, the compositions determined by EDX, the change in orientation of the TiAlN coatings for different applied pressure and both of the FWHM and the lattice parameters  $a_0$ .

Pressure mbar	Peak target voltage V	High peak target current A	Texture coefficient			Lattice $a_0$ Å	FWHM determined on (422) (°)	Composition (at.%)		
			(111)	(200)	(220)			Al	Ti	N
$2 \times 10^{-3}$	622	156	3.76	0.05	0.14	4.179	2.336	26.5	22.6	51
$3 \times 10^{-3}$	610	159	1.89	0.06	2.06	4.171	1.822	25	24.8	50
$5 \times 10^{-3}$	608	171	3.64	0.14	0.08	4.169	1.383	26.3	22.7	51
$7 \times 10^{-3}$	571	172	1.48	0.07	2.49	4.166	0.607	26.5	23.5	50
$1 \times 10^{-2}$	553	177	0.94	0.04	3.12	4.163	0.506	26	24	49



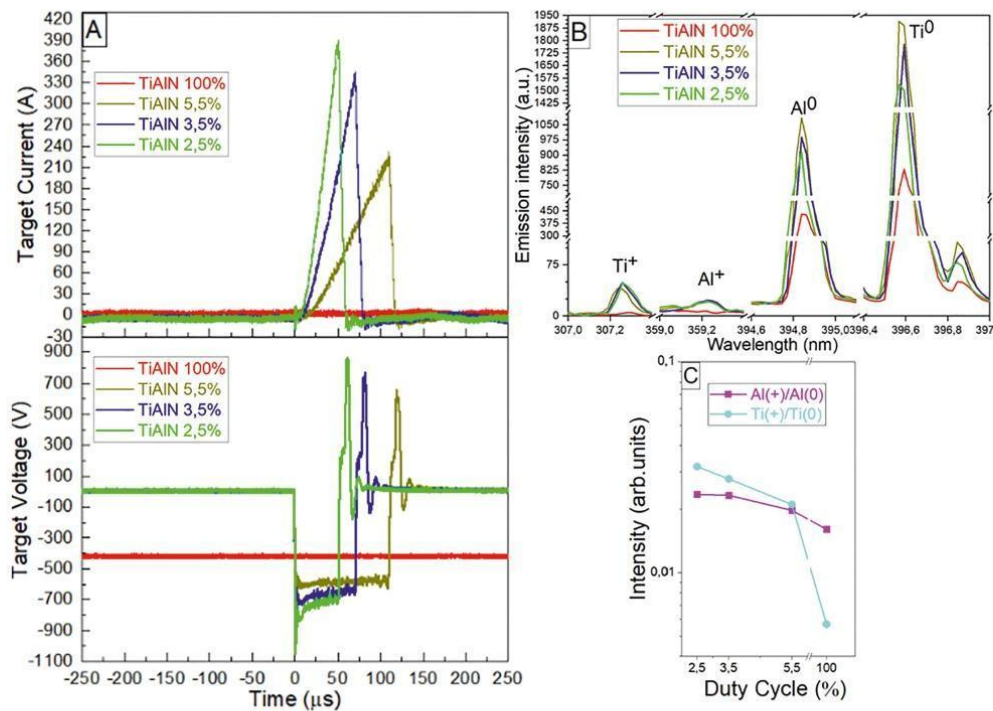


Fig. 9. The changing electrical signal of target voltage and target current over time evolution during dcMS and during the on/off time of duty-cycles represented as a graph on (A). The optical emission spectrum during TiAlN alloy sputtering in mixed Ar/N<sub>2</sub> atmosphere (B), the intensity of Ti and Al ionization emission during the sputtering time in mixed Ar/N<sub>2</sub> atmosphere at different pulsing (C).

linked to grain size evolution, it can be proposed that the decrease of the working pressure follows to an extension of the grain size, which can generate compressive stress in the coating, a statement also reported by other authors [30–32]. The change of the working pressure has also an effect on the mechanical properties of the coating as seen from the hardness and E-modulus measurements.

### 3.1.2. Effect of duty cycle impact

The nucleation and growth mechanisms are also governed by the surface mobility of the film-forming species (adatoms), which in turn depends on the energy, the flux and the direction of the incident species. In this section, the pressure of  $2 \times 10^{-3}$  mbar was selected for all process conditions and the depositions were performed at constant parameters except for the On/Off-sputtering time, covering three different duty cycles: 2.5%, 3.5% and 5.5%. These three values have allowed the possibility of varying the amplitude of the peak power density from  $\approx 87$ ,  $\approx 127$  to  $\approx 180$  W/cm<sup>2</sup> for the same average power of 4 W/cm<sup>2</sup> and a frequency of 500 Hz, as shown in Fig. 9a.

In order to deposit the same coating stoichiometry, the ratio of

nitrogen to argon flow rates was chosen in such a way, that it corresponds to the limit of the target poisoning state. In Table 3, the Al content relating to the different duty cycles is below 50 at.% as compared to the original Al target content (Ti<sub>0.5</sub>Al<sub>0.5</sub>). Fig. 9b and c show the intensity of Ti and Al ionization emission for the different pulsing times measured by Optical Emission Spectroscopy (OES). The ratio of emission for Ti<sup>+</sup>/Ti<sup>0</sup> was found to be generally higher than Al<sup>+</sup>/Al<sup>0</sup> for each HiPIMS cycle. Furthermore, a significant difference between the emission of Ti<sup>+</sup> and Ti<sup>0</sup> species was recorded as a function of the duty cycle. These results can be correlated to the estimations of the deposition rate for high pulse plasma deposition conditions. The range of deposition rate in our HiPIMS installation, independently of the duty cycle conditions, is  $\approx 0.80$ – $0.85$  nm/s which is lower than the deposition rate in dcMS  $\approx 1.6$  nm/s in the same coater installation. For the HiPIMS tested conditions, the decrease of the duty cycle can be compensated by an increase of the pulse power energy and consequently the deposition rate can be kept constant. So, the main difference during these deposition conditions was an increase of the ionization of the Ti and Al sputtered atoms when the duty cycle was decreased from 5.5% to 2.5%.

Table 3

The change in orientation of the TiAlN coatings for dcMS and HiPIMS, the lattice parameters a<sub>0</sub>, The FWHM of the (422) peak and the compositions determined by EDX.

Duty cycle %	Texture coefficient			Lattice a <sub>0</sub> Å	FWHM determined on (422) (°)	Composition (at.%)		
	(111)	(200)	(220)			Al	Ti	N
2.5	3.74	0.11	0.03	4.186	1.8525	24	26	50
3.5	3.88	0.03	0.04	4.208	2.7063	25	26	49
5.5	3.76	0.05	0.14	4.179	2.3364	25.5	23.7	50.8
dcMS	3.51	0.16	0.15	4.153	1.4323	28	24	48

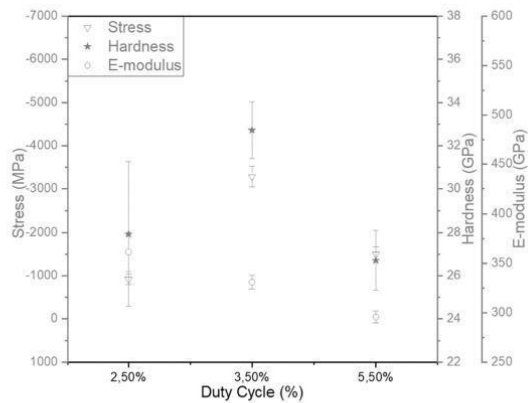


Fig. 10. The effect of different duty cycles in the evolution of the internal compressive stresses, E-modulus and Hardness.

The XRD patterns were carried out for TiAlN coatings at 5.5%, 3.5% and 2.5% duty cycles, the lattice parameters, the FWHM determined on (422) and the main orientation are presented in Table 3. All these coatings have a polycrystalline single-phase cubic structure with a strong (111) preferred orientation and at least two more visible reflections (200) and (220). The lattice-parameter 4.15 Å for magnetron dcMS TiAlN film was slightly increased for HiPIMS TiAlN films with duty cycles of 5.5%, 3.5% and 2.5%. The reported stress values indicated that all TiAlN coatings have changed from tensile stress in dcMS mode to compressive stress in HiPIMS with values between -1000 to -3000 MPa (Fig. 10). The E-modulus decreases as the duty cycle increases and the hardness of the coatings is higher when the stress is also higher and vice-versa, with small deviations from 33 to 27 GPa.

3.1.3. Effect of power impact

In order to provide an overall view of the effect of the energy density during a pulse, three TiAlN coatings at respectively 4, 6 and 8 W/cm<sup>2</sup> average power, have been synthesized and characterized in Table 4. Following the discussion in the previous sections, the pressure of 2 × 10<sup>-3</sup> mbar and the duty cycle of 5.5% were chosen. The three applied average powers were varied by keeping the same frequency and just adjusting the applied power. The chemical compositions of the three thin films are similar. The average deposition rate increases from ~49 to ~74 and ~76 nm/min when the average power increases from 4 to 6 and to 8 W/cm<sup>2</sup>. Increasing the applied power does not change significantly the film morphology and structure. In addition, the top-view micrographs of the films have shown that the coating deposited with the highest applied power has the smoothest surface.

As determined by XRD, the lattice parameters, the FWHM determined on (422) and the level of compressive stresses changed with increasing power. However, the (200) peak intensities are higher at a

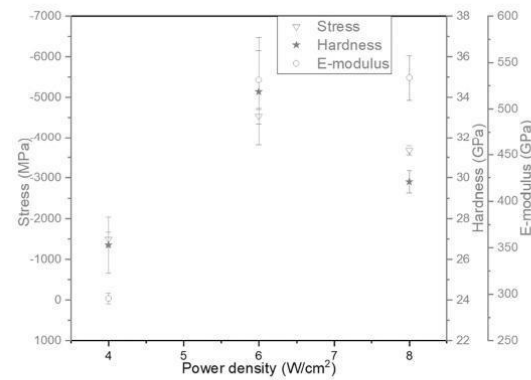


Fig. 11. The effect of peak power density in the evolution of internal compressive stresses, E-modulus and Hardness.

power of 8 W/cm<sup>2</sup>. The results presented in Fig. 11 are showing the relation between the mechanical properties, compressive stresses and power density. The E-modulus is getting higher with increasing stress, whereas the hardness is showing a maximum at 6 W/cm<sup>2</sup>, and is following also the residual stress level variation.

3.1.4. Effect of bias

Thanks to the application of a bias voltage on the substrate holder during the deposition, it is possible to increase the average kinetic energy of the ionic energetic species and to significantly modify the nucleation mechanism, which affects the film properties [33–35]. In this section, the following continuous substrate negative bias values of 15, 35, 50, 70, 160 V were applied during the HiPIMS coating deposition. The pressure of 2 × 10<sup>-3</sup> mbar, the duty cycle of 5.5% and the average power of 8 W/cm<sup>2</sup> were selected for all performed depositions. From the SEM cross-section observations, independently of the bias values, a fine fibrous structure characterizes the microstructure of all the coatings. The highest bias voltage leads to a small decrease in the deposition rate as presented in Table 5, but no modification of the coating composition is recorded. By tuning the negative bias voltage applied onto to the substrate during peak power, more Al<sup>+</sup> and Ti<sup>+</sup> ions have participated in the growing mechanism of the film, hence additional kinetic energy and momentum transfer change the film-forming conditions. However, in this case, these possible beneficial effects are counterbalanced by a continuous Argon ion substrate bombardment. This may cause a re-sputtering of the film and Ar atoms implantation in the film for the higher bias voltages, leading to a generation of lattice defects and possible high residual stresses [36,37]. Depending on the applied bias voltage, XRD patterns present a small angular shift of the diffraction peaks in 2θ as well as a change of the peaks' broadening. This change can be attributed to a small decrease of the coating crystallization with increasing the negative substrate bias voltage to -70 V. The level of

Table 4

The change in orientation of the TiAlN coatings for three applied power density HiPIMS coatings, the lattice parameters a<sub>0</sub>, the FWHM of the (422) peak, the compositions determined by EDX, the gas flow ratio and the deposition rate.

Applied power density W/cm <sup>2</sup>	Gas flow rate ratio N <sub>2</sub> /Ar	Deposition rate nm/min	Texture coefficient			Lattice a <sub>0</sub> Å	FWHM determined on (422) (°)	Composition (at.%)		
			(111)	(200)	(220)			Al	Ti	N
4	0.2	49 ± 1	3.76	0.05	0.14	4.179	2.3364	25.5	23.7	50.8
6	0.28	74 ± 1	3.83	0.01	0.16	4.193	2.3938	26	26	48
8	0.32	76 ± 1	3.70	0.09	0.09	4.190	2.1361	26	25	49

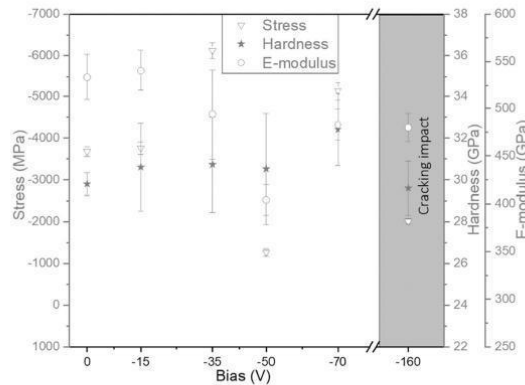


Fig. 12. The effect of different bias in the evolution of internal compressive stresses, E-modulus and Hardness.

Table 5

The change in orientation of the TiAlN coatings for different applied bias in HiPIMS coatings, the lattice parameters  $a_0$ , the FWHM of the (422) peak, the deposition rate and the compositions determined by EDX.

Bias V	Deposition rate nm/min	Texture coefficient			Lattice $a_0$ Å	FWHM determined on (422) (°)	Composition (at.%)		
		(111)	(200)	(220)			Al	Ti	N
-160 ± 5	68 ± 1	1.93	0.54	0.99	4.200	2.1765	26	25	49
-70 ± 5	77 ± 1	2.43	0.06	1.52	4.222	3.4594	25	26	49
-50 ± 5	76 ± 1	3.77	0.01	0.22	4.190	1.9378	26	26	48
-35 ± 5	75 ± 1	3.22	0.04	0.72	4.198	2.6605	24	28	48
-15 ± 5	75 ± 1	3.91	0.02	0.06	4.190	2.3119	26	25	49
0	74 ± 1	3.70	0.10	0.09	4.190	2.1361	26	25	49

compressive stresses increased when the bias voltage is superior to -15 V (Fig. 12) and can reach values superior to -5000 GPa. For a number of coatings with such high values, the generation of microcracks was detected by top-view SEM observations. According to texture orientation measurements, the growth mechanism of the coating is also modified by applying a bias voltage. The increase of the (220) peak intensity can indicate that a second type of fiber is growing simultaneously with the other fibres and this situation can generate high compressive stresses in the coating. The E-modulus is slightly decreasing when the bias voltage is increasing, but the hardness level is almost stable and not really different for each of these coatings was observed.

### 3.2. Mechanical properties of HiPIMS TiAlN coatings by comparison with CAE

#### 3.2.1. Hardness and E-modulus

It is now understood that the enhanced hardness (H) is not the single important property of the hard coatings [38]. For many applications the toughness/resistance to plastic deformation,  $H^3/E^2$  ratio and the elastic strain prior to the plastic deformation, H/E is more important than its extremely high hardness. The influence of elasticity in combination with hardness is considered as a reliable indicator of the wear resistance [39]. Thus, higher H/E ratios of a coating will be an indication of the coating ability to resist to mechanical degradation and failure in tribo-contact events, because the contact area will remain elastic at higher stresses during external impacts. Also, a high value of the  $H^3/E^2$  ratio could be related to the increased ability of the coating to absorb energy during deformation up to fracture. From state of the art, it is now considered that a challenging H/E ratio around 0.1 needs to be fulfilled in order to reach a high wear resistance. Concerning the TiAlN coatings synthesized

during this work, all coatings deposited by the HiPIMS process have relatively high and constant hardness. Furthermore, depending on the processing conditions, it is possible to generate different levels of in-situ compressive stresses and also, of Young moduli (E). All these data are summarized in the Fig. 13 where the mechanical properties  $H^3/E^2$  and H/E of the produced TiAlN coatings are calculated as a function of the internal in-situ compressive stresses. All generated coatings have values approaching the 0.1 H/E ratio, whatever is the stress level.

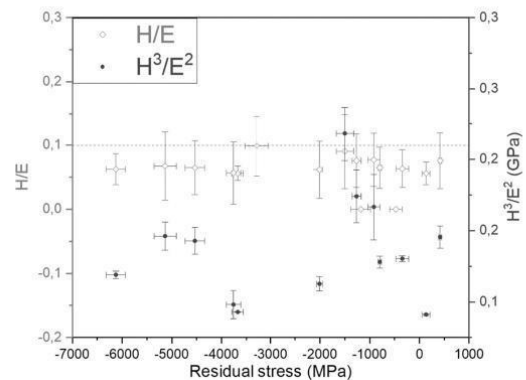


Fig. 13. The TiAlN HiPIMS coating's residual stresses and its relation with the mechanical properties  $H^3/E^2$  and H/E.

**Table 6**  
The chemical compositions of the coatings deposited on the tribo-discs, the lattice parameters of the cubic structure for the different coatings, the FWHM of the (422) peak and the crystallite size as well as the residual stress values, the coating hardness ( $H_{IT}$ ) and the E-modulus ( $E_T$ ) with the wear test related result and roughness profile.

Mode	Lattice $a_0$ Å	FWHM determined on (422) (°)			Composition (at.%)			Residual stress (MPa)	Hardness ( $H_{IT}$ ) GPa	E-modulus (GPa)	Diameter of the damage circle on the steel ball µm	Roughness surface ( $R_a$ ) µm	wear track width µm	Roughness wear track ( $R_a$ ) µm
		Al	Ti	N	Al	Ti	N							
TiAlN-CAE1	4.1663	1.961	22	29	49	-472 ±127	30.7±0.8	528.353	2890	0.141	1170	0.150		
TiAlN-CAE2	4.1762	2.2265	22	28	50	-1176.8 ±200	31.4±0.7	520.713	2471	0.110	1010	0.150		
TiAlN-HPiMIS1	4.1905	1.9378	26	26	48	-1263.7 ±94	30.5±1.5	404.162	1196	0.030	960	0.181		
TiAlN-HPiMIS2	4.1988	2.6605	24	28	48	-6125.1 ±191	30.7±1.3	493.873	1217	0.058	1680	0.214		

3.2.2. Wear resistance

In order to clarify the conjugated effect of the coating technology and its generated stress levels in the coatings' mechanical properties, their wear and abrasion resistance were measured in a way to investigate the possible correlations between those properties and their behaviour during machining processing. One of the main results of the ball-on-disc tribological tests is the friction coefficient, which is not only directly related to friction force occurring between the two sliding bodies but also indicates how well the bodies react to mutual contact. The test at room temperature was done on four  $Al_{50}Ti_{50}N$  as deposited coatings deposited on WC-Co by CAE and HiPIMS. The chemical compositions of the coatings deposited on the tribo-discs, the lattice parameters of the cubic structure for the different coatings, FWHM, coating hardness and E-modulus are reported in Table 6. The surface roughness and the evolution of the friction coefficient along the wear test are plotted in Fig. 14.

The friction coefficient varied substantially from the beginning of the test up to a 20 m distance (the running-in stage) as higher wear occurred. Thereafter, the friction coefficient was stable for all samples and the two HiPIMS coatings have lower values of coefficient of friction than the two CAE coatings, respectively 0.5–0.6 and 0.7–0.8.

The wear track profile using Gaussian filter 0.25 mm, the SEM micrographs for wear track area and the EDX analysis are presented in Fig. 15. Generally, during this type of test, the contact of the static body with the rotating sample is producing damages to the coating and a wear kinetic of the coating can be recorded. In our case, the TiAlN coating is much harder than the steel ball, the wear change was only quantified by measuring the diameter of a flat disc surface generated on the ball (the material removed from the static body). During the CAE-TiAlN coating tests, a higher wear rate was generated on the steel ball (wear ball scar) than during the HiPIMS coating tests, while the wear rate between the two CAE-TiAlN even the two HiPIMS-TiAlN was quite similar independently of their level of compressive stresses. From the SEM observations on the surface of the wear track samples, it was concluded that all coatings were still stable with no damages (e.g. cohesive fracture and coating delamination) in the wear track. The EDX analysis have shown that the quantity of iron in the wear track is higher for CAE coatings than for HiPIMS coating. This last finding can be correlated to the different friction coefficient between the two types of coatings. The friction is strongly correlated to the adhesive wear and in case of the CAE coating it is linked to the higher roughness due to the highest number of particles on top of the coating.

4. Conclusions

Same hard  $Ti_{50}Al_{50}N$  coating deposited with the same composition and the same thickness by an CAE and a HiPIMS process, completed in few cases by also,  $Ti_{50}Al_{50}N$  coating deposited by dcMS have been performed. All these coatings, independently of the deposition process, have the same morphology with a very dense columnar structure, which is not affected by the substrate, silicon wafer or WC-Co and by the nature of the adhesive interlayer. However, there is a clear structural difference between the two types of coatings where the preferred orientation changes from close to (200) by CAE to (111) by HiPIMS. From all the HiPIMS deposition conditions tested during this study, the structural difference cannot be interpreted by the fact of using energetic species as both processes produced it. Furthermore, a large range of the working pressure and the bias voltage values were tested, the deposition rate as the instantaneous deposition rate during the pulse plasma time was evaluated to be close to the continuous rate during CAE deposition. To explain this structural difference, we suggest that it is in relation with a relaxation time that appears between the pulses by HiPIMS and, also as a consequence of the low deposition rate. Regarding the mechanical properties of the coating, it has been found that both CAE and HiPIMS produce TiAlN coatings with compressive stresses, the most energetic deposition conditions by HiPIMS (high peak power, low duty cycle and



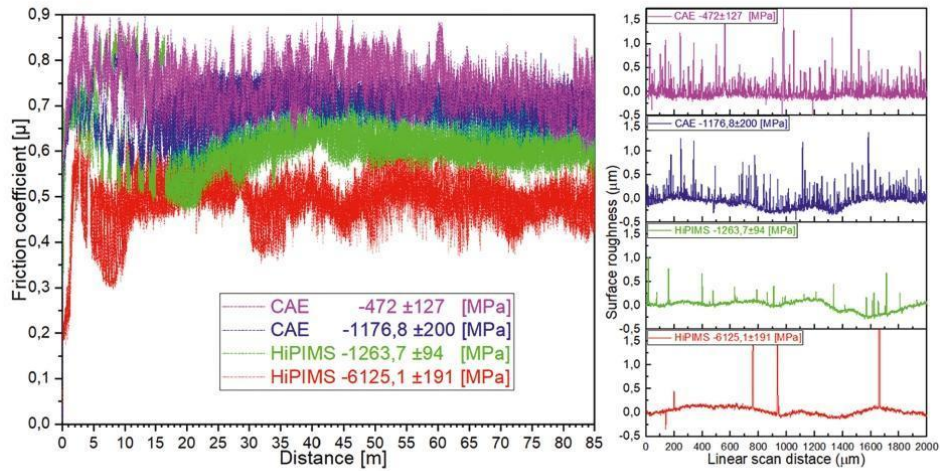


Fig. 14. The friction coefficient of different stress level of CAE and HiPIMS TiAlN coatings (left) and its relation surface roughness (right).

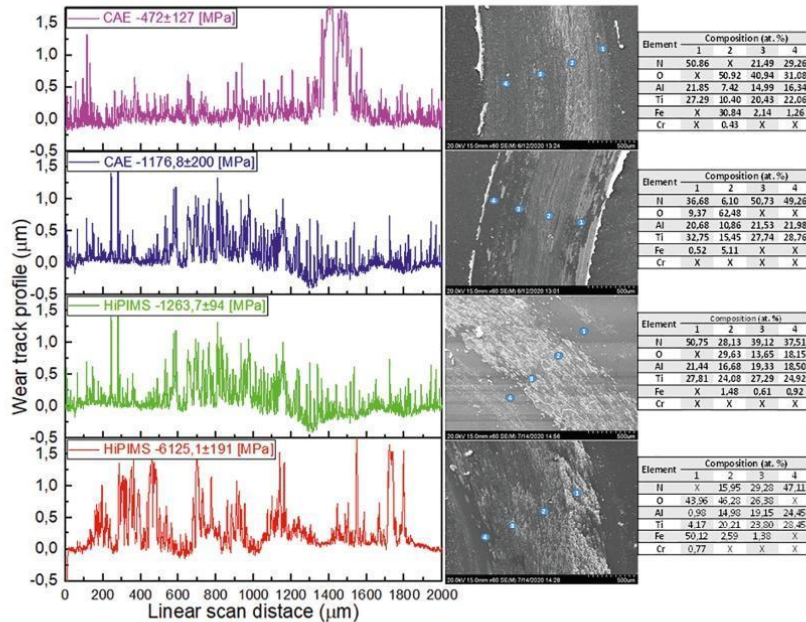


Fig. 15. The wear track profile extracted from SEM micrographs. The elemental composition of the wear track area was determined by EDX.

bias substrate) can lead to very high values sometimes superior to -5000 MPa. However, no correlation was found between the hardness values of HiPIMS coatings and their stress level, contrary to CAE coatings. Only the Young modulus is tuned by changing the HiPIMS deposition conditions, which is an advantage as it is now established that tribological coating properties are linked to the  $H/E$  and  $H^3/E^2$  ratios. Finally, ball-on-disc measurements have shown lower friction coefficients for the HiPIMS coatings by comparison with CAE process.

Supplementary data to this article can be found online at <https://doi.org/10.1016/j.surfcoat.2021.127529>.

**Abbreviations**

- HiPIMS High-Power Impulse Magnetron Sputtering
- dCMS direct-current Magnetron Sputtering
- CAE cathodic Arc evaporation

M.-R. Alhafian et al.

Surface &amp; Coatings Technology 423 (2021) 127529

FE-SEM	Field-Emission Scanning Electron Microscope
EDS	Energy Dispersive X-ray Spectrometer
TC	Texture coefficient
SAED	Selected Area Electron Diffraction patterns
HRTEM	High Resolution Transmission Electron Microscopy
FFT	Fast Fourier Transformer
R <sub>a</sub>	Roughness average

#### CRediT authorship contribution statement

M.-R. Alhafian: Conceptualization, methodology, investigation, design of experiments, writing – original draft, editing, and submission.

J.-B. Chemin: Supervision, PVD set up, process parameterization, and review.

Y. Fleming: XRD measurements validation, methodology, and review.

L. Bourgeois: Scientific discussion, mechanical properties validation, and review.

M. Penoy: Fiber texture and pole figures measurements, and investigation.

R. Useldinger: Scientific discussion

F. Soldera: Supervision, scientific discussion, and final revision.

F. Mücklich: Supervision, and scientific discussion.

P. Choquet: Conceptualization, supervision, writing – review & editing, project administration, and funding acquisition.

#### Declaration of competing interest

Mohamed Riyad ALHAFIAN reports financial support was provided by Luxembourg National Research Fund (FNR).

#### Acknowledgements

The authors thank Dr. N. Valle (LIST) and Dr. J. Ghanbaja (Institute Jean Lamour, France) for their participations to the characterizations of our samples and for valuable discussions. The financial support from the Luxembourg National Research Fund (FNR) under the CORE PPP project funding for innovation and industry partnerships (C-PPP17/MS/11622578) is gratefully acknowledged, as well as the European Doctoral Program in Advanced Materials Science and Engineering (DocMASE) for the training of the PhD student.

#### References

- Y.C. Chim, X.Z. Ding, X.T. Zeng, S. Zhang, Oxidation resistance of TiN, CrN, TiAlN and CrAlN coatings deposited by lateral rotating cathode arc, *Thin Solid Films* 517 (2009) 4845–4849, <https://doi.org/10.1016/j.tsf.2009.03.038>.
- A. Liu, J. Deng, H. Cui, Y. Chen, J. Zhao, Friction and wear properties of TiN, TiAlN, AlTiN and CrAlN PVD nitride coatings, *Int. J. Refract. Met. Hard Mater.* 31 (2012) 82–88, <https://doi.org/10.1016/j.jrmm.2011.09.010>.
- F. Hollstein, R. Wiedemann, J. Scholz, Characteristics of PVD-coatings on AZ31hp magnesium alloys, *Surf. Coatings Technol.* 162 (2003) 261–268, [https://doi.org/10.1016/S0257-8972\(02\)00671-0](https://doi.org/10.1016/S0257-8972(02)00671-0).
- G.S. Fox-Rabinovich, B.D. Beske, J.L. Endrino, S.C. Veldhuis, R. Parkinson, L. S. Shuster, M.S. Migranov, Effect of mechanical properties measured at room and elevated temperatures on the wear resistance of cutting tools with TiAlN and AlCrN coatings, *Surf. Coatings Technol.* 200 (2006) 5738–5742, <https://doi.org/10.1016/j.surfcoat.2005.08.132>.
- A. Thakur, S. Gangopadhyay, Dry machining of nickel-based super alloy as a sustainable alternative using TiN/TiAlN coated tool, *J. Clean. Prod.* 129 (2016) 256–268, <https://doi.org/10.1016/j.jclepro.2016.04.074>.
- A. Anders, A review comparing cathodic arcs and high power impulse magnetron sputtering (HiPIMS), *Surf. Coatings Technol.* 257 (2014) 308–325, <https://doi.org/10.1016/j.surfcoat.2014.08.043>.
- A.P. Ehasarian, P.E. Hovsepian, L. Hultman, U. Helmersson, Comparison of microstructure and mechanical properties of chromium nitride-based coatings deposited by high power impulse magnetron sputtering and by the combined steered cathodic arc/unbalanced magnetron technique, *Thin Solid Films* 457 (2004) 270–277, <https://doi.org/10.1016/j.tsf.2003.11.113>.
- D.A. Karpov, Cathodic arc sources and macroparticle filtering, *Surf. Coatings Technol.* 96 (1997) 22–33, [https://doi.org/10.1016/S0257-8972\(98\)80008-X](https://doi.org/10.1016/S0257-8972(98)80008-X).
- J. Vetter, J. Müller, G. Erkens, An Innovative Approach to New Hybrid Coatings Based on HiPIMS Technology: The Hi3 Process, 2012.
- V. Tiron, I.L. Velicu, O. Vasilovici, G. Popa, Optimization of deposition rate in HiPIMS by controlling the peak target current, *J. Phys. D. Appl. Phys.* 48 (2015) 495204, <https://doi.org/10.1088/0022-3727/48/49/495204>.
- C.L. Chang, S.G. Shih, P.H. Chen, W.C. Chen, C.T. Ho, W.Y. Wu, Effect of duty cycles on the deposition and characteristics of high power impulse magnetron sputtering deposited TiN thin films, *Surf. Coatings Technol.* 259 (2014) 232–237, <https://doi.org/10.1016/j.surfcoat.2014.03.011>.
- J. Alami, Z. Maric, H. Busch, F. Klein, U. Grabow, M. Kopnarski, Enhanced ionization sputtering: a concept for superior industrial coatings, *Surf. Coatings Technol.* 255 (2014) 43–51, <https://doi.org/10.1016/j.surfcoat.2013.11.040>.
- T. Shimizu, H. Komiya, Y. Teranishi, K. Morikawa, H. Nagasaka, M. Yang, Pressure dependence of (Ti, Al)N film growth on inner walls of small holes in high-power impulse magnetron sputtering, *Thin Solid Films* 624 (2017) 189–196, <https://doi.org/10.1016/j.tsf.2016.09.041>.
- A. Guillaumont, F. Lapostolle, C. Dublanche-Tixier, J.C. Oliveira, A. Billard, C. Langlade, Reactive deposition of Al-N coatings in Ar/N<sub>2</sub> atmospheres using pulsed-DC or high power impulse magnetron sputtering discharges, *Vacuum* 85 (2010) 120–125, <https://doi.org/10.1016/j.vacuum.2010.04.012>.
- HDO4054A-MS Teledyne LeCroy | Test and Measurement | DigiiKey, n.d. <https://www.digikey.lu/product-detail/en/teledyne-lecroy/HDO4054A-MS/HDO4054A-MS-ND/7200922>. (Accessed 22 January 2021).
- R.A. Baragiola, Sputtering: survey of observations and derived principles, *Philos. Trans. R. Soc. Lond. Ser. A Math. Phys. Eng. Sci.* 362 (2004) 29–53, <https://doi.org/10.1098/rsta.2003.1301>.
- Instrumented Indentation Testing (IIT): Anton Paar Wiki, n.d. <https://wiki.antonpaar.com/en/instrumented-indentation-testing-iit/>. (Accessed 22 January 2021).
- N.J.M. Carvalho, E. Zoestbergen, B.J. Kooi, J.T.M. De Hosson, Stress analysis and microstructure of PVD monolayer TiN and multilayer TiN/(Ti,Al)N coatings, *Thin Solid Films* 429 (2003) 179–189, [https://doi.org/10.1016/S0040-6090\(03\)00067-1](https://doi.org/10.1016/S0040-6090(03)00067-1).
- Tencor P-17 Stylus Profiler | 3D Profilometer | KLA, n.d. <https://www.kla-tencor.com/products/instruments/stylus-profilers/p-17>. (Accessed 22 January 2021).
- S. Sveen, J.M. Andersson, R. M'Saoubi, M. Olsson, Scratch adhesion characteristics of PVD TiAlN deposited on high speed steel, cemented carbide and PCBN substrates, *Wear* 308 (2013) 133–141, <https://doi.org/10.1016/j.wear.2013.08.025>.
- M. Tkadletz, C. Mitterer, B. Sartory, I. Letofsky-Papst, C. Czetti, C. Michotte, The effect of droplets in arc evaporated TiAlTiN hard coatings on the wear behavior, *Surf. Coatings Technol.* 257 (2014) 95–101, <https://doi.org/10.1016/j.surfcoat.2014.01.010>.
- C.V. Falub, A. Karimi, M. Ante, W. Kalss, Interdependence between stress and texture in arc evaporated Ti-Al-N thin films, *Surf. Coatings Technol.* 201 (2007) 5891–5898, <https://doi.org/10.1016/j.surfcoat.2006.10.046>.
- D. Chateigner, P. Gerni, M. Pernet, Texture analysis by the Schulz reflection method. Defocalization corrections for thin films, *J. Appl. Crystallogr.* 25 (1992) 766–769, <https://doi.org/10.1107/S0021889892006265>.
- B. Alling, P. Steneteg, C. Tholander, F. Tasnadi, I. Petrov, J.E. Greene, L. Hultman, Configurational disorder effects on adatom mobilities on Ti 1-xAl xN(001) surfaces from first principles, *Phys. Rev. B Condens. Matter Mater. Phys.* 85 (2012), 245422, <https://doi.org/10.1103/PhysRevB.85.245422>.
- G. Abadias, W.P. Leroy, S. Mahieu, D. Depla, Influence of particle and energy flux on stress and texture development in magnetron sputtered TiN films, *J. Phys. D. Appl. Phys.* 46 (2013), 055301, <https://doi.org/10.1088/0022-3727/46/5/055301>.
- K.D. Bouzakis, N. Michailidis, G. Skordaris, E. Bouzakis, D. Biermann, R. M'Saoubi, Cutting with coated tools: coating technologies, characterization methods and performance optimization, *CIRP Ann. Manuf. Technol.* 61 (2012) 703–723, <https://doi.org/10.1016/j.cirp.2012.05.006>.
- K.D. Bouzakis, S. Gerardis, G. Katirtzoglou, S. Makrimalakis, A. Bouzakis, R. Cremer, H.G. Fuss, Application in milling of coated tools with rounded cutting edges after the film deposition, *CIRP Ann. Manuf. Technol.* 58 (2009) 61–64, <https://doi.org/10.1016/j.cirp.2009.03.103>.
- B. Denkena, B. Breidenstein, Residual stress distribution in PVD-coated carbide cutting tools - origin of cohesive damage, *Tribol. Ind.* 34 (2012) 158–165, <https://doi.org/10.15488/1407>.
- G. Greczynski, J. Lu, J. Jensen, S. Bolz, W. Kölker, C. Schiffers, O. Lemmer, J. E. Greene, L. Hultman, A review of metal-ion-flux-controlled growth of metastable TiAlN by HiPIMS/DCMS co-sputtering, *Surf. Coatings Technol.* 257 (2014) 15–25, <https://doi.org/10.1016/j.surfcoat.2014.01.055>.
- K. Sarakinos, J. Alami, P.M. Karimi, D. Severin, M. Wuttig, The role of backscattered energetic atoms in film growth in reactive magnetron sputtering of chromium nitride, *J. Phys. D. Appl. Phys.* 40 (2007) 778–785, <https://doi.org/10.1088/0022-3727/40/3/014>.
- A. Hecimovic, High Power Impulse Magnetron Sputtering (HiPIMS): Fundamental Plasma Studies and Material Synthesis, 2009.
- Ç. Eda, B. Baloukas, O. Zabeida, J.E. Klemberg-Sapieha, L. Martinu, Mechanical and thermoelastic characteristics of optical thin films deposited by dual ion beam sputtering, *Appl. Opt.* 48 (2009) 4536–4544, <https://doi.org/10.1364/AO.48.004536>.
- G. Greczynski, J. Lu, M. Johansson, J. Jensen, I. Petrov, J.E. Greene, L. Hultman, Selection of metal ion irradiation for controlling Ti 1-xAl xN alloy growth via hybrid HiPIMS/magnetron co-sputtering, *Vacuum* 86 (2012) 1036–1040, <https://doi.org/10.1016/j.vacuum.2011.10.027>.

- [34] I. Petrov, P.B. Barna, L. Hultman, J.E. Greene, Microstructural evolution during film growth, *J. Vac. Sci. Technol. A Vac. Surf. Film.* 21 (2003) S117–S128, <https://doi.org/10.1116/1.1601610>.
- [35] K. Sarakinos, J. Alami, M. Wuttig, Process characteristics and film properties upon growth of TiO<sub>x</sub> films by high power pulsed magnetron sputtering, *J. Phys. D: Appl. Phys.* 40 (2007) 2108–2114, <https://doi.org/10.1088/0022-3727/40/7/037>.
- [36] A.P. Ehasarian, A. Hecimovic, J. Winter, T. De Los Arcos, R. New, V. Schulz-Von Der Gathen, M. Böke, Plasma self-organisation in high power impulse magnetron sputtering discharges, in: *IOP Conf. Ser. Mater. Sci. Eng.*, IOP Publishing, 2012, 012012, <https://doi.org/10.1088/1757-899X/39/1/012012>.
- [37] D. Lundin, M. Cada, Z. Hubička, Ionization of sputtered Ti, Al, and C coupled with plasma characterization in HiPIMS, *Plasma Sources Sci. Technol.* 24 (2015), 035018, <https://doi.org/10.1088/0963-0252/24/3/035018>.
- [38] A. Leyland, A. Matthews, On the significance of the H/E ratio in wear control: a nanocomposite coating approach to optimised tribological behaviour, *Wear*. 246 (2000) 1–11, [https://doi.org/10.1016/S0043-1648\(00\)00488-9](https://doi.org/10.1016/S0043-1648(00)00488-9).
- [39] V.P. Pasko, Red sprite discharges in the atmosphere at high altitude: the molecular physics and the similarity with laboratory discharges, in: *Plasma Sources Sci. Technol.*, IOP Publishing, 2007, p. S13, <https://doi.org/10.1088/0963-0252/16/1/S02>.
- [40] K. Sarakinos, J. Alami, S. Konstantinidis, High power pulsed magnetron sputtering: a review on scientific and engineering state of the art, *Surf. Coatings Technol.* 204 (2010) 1661–1684, <https://doi.org/10.1016/j.surfcoat.2009.11.013>.
- [41] E. Lecoq, J. Guillot, D. Duda, J.B. Chemin, P. Choquet, Elaboration of a wide range of TiO<sub>2</sub> micro/nanostructures by high power impulse inverted cylindrical magnetron sputtering, *J. Phys. D: Appl. Phys.* 47 (2014), 195201, <https://doi.org/10.1088/0022-3727/47/19/195201>.
- [42] H. Elmkhah, A. Abdollah-zadeh, F. Mahboubi, A.R.S. Rouhaghdam, A. Fattah-alhosseini, Correlation between the duty cycle and the surface characteristics for the nanostructured titanium aluminum nitride coating deposited by pulsed-DC PACVD technique, *J. Alloys Compd.* 711 (2017) 530–540, <https://doi.org/10.1016/j.jallcom.2017.03.120>.
- [43] L. Zauner, P. Ertelthaler, T. Wojcik, H. Bolvardi, S. Kolozsvári, P.H. Mayrhofer, H. Riedl, Reactive HiPIMS deposition of Ti-Al-N: influence of the deposition parameters on the cubic to hexagonal phase transition, *Surf. Coatings Technol.* 382 (2020), 125007, <https://doi.org/10.1016/j.surfcoat.2019.125007>.
- [44] B. Liang Meng, Dissertation, Comparison of High Power Impulse Magnetron Sputtering and Modulated Pulsed Power Sputtering for Interconnect Metallization, <https://www.ideals.illinois.edu/handle/2142/45348>, 2013. (Accessed 25 June 2021).
- [45] T. Schenk, C.M. Fancher, M.H. Park, C. Richter, C. Künne, A. Kersch, J.L. Jones, T. Mikolajick, U. Schroeder, On the origin of the large remanent polarization in La: HfO<sub>2</sub>, *Adv. Electron. Mater.* 5 (2019), 1900303, <https://doi.org/10.1002/aelm.201900303>.
- [46] M.E. Fitzpatrick, A.T. Fry, P. Holdway, F.A. Kandil, J. Shackleton, L. Suominen, Determination of Residual Stresses by X-ray Diffraction, 2005.
- [47] U. Weizel, J. Ligot, P. Lamparter, A.C. Vermeulen, E.J. Mittemeijer, Stress analysis of polycrystalline thin films and surface regions by X-ray diffraction, *J. Appl. Crystallogr.* 38 (2005) 1–29, <https://doi.org/10.1107/S0021889804029516>.
- [48] R. Machunze, A.P. Ehasarian, F.D. Tichelaar, G.C.A.M. Janssen, Stress and texture in HiPIMS TiN thin films, *Thin Solid Films* 518 (2009) 1561–1565, <https://doi.org/10.1016/j.tsf.2009.09.069>.
- [49] N. Nikolić, V. Maksimović, G. Branković, P. Živković, M. Pavlović, Correlation between crystal orientation and morphology of electrolytically produced powder particles: analysis of the limiting cases, *Zast. Mater.* 59 (2018) 256–264, <https://doi.org/10.5937/zasmat1802256n>.
- [50] H. Elmkhah, T.F. Zhang, A. Abdollah-zadeh, K.H. Kim, F. Mahboubi, Surface characteristics for the Ti[formula presented]Al[formula presented]N coatings deposited by high power impulse magnetron sputtering technique at the different bias voltages, *J. Alloys Compd.* 688 (2016) 820–827, <https://doi.org/10.1016/j.jallcom.2016.07.013>.

## A. Supplementary information:

Fig. 9-A shows the target current waveforms and illustrates the increase during the peak power, which is observed with the decrease of the respective duty cycle and how it leads to an increase of both the target voltage and the target current during the on-time. In other words, because of the increase of the target voltage, the peak current value decreases when lowering the duty cycle. For low duty cycle 2.5%, the current rises faster than duty cycle 5.5% until the end of the pulse and reach higher peak power.

Fig. 9b & 9c show the ionized fraction of the sputtered species, where a high ionization rate of metal and gas species can be achieved by reducing the pulse duration under the same pulse frequency [40]. In comparison with the dcMS, the advantage of this higher ionization rate in HiPIMS deposition leads to better film properties. It is therefore important to describe what happens in the discharge when varying the duty cycle for clearer perception. Firstly, a mix of nitrogen ( $N_2$ ) gas and argon (Ar) gas were present in the chamber before the plasma ignition. Following the voltage pulse, the ionization of the gaseous species occurs. The initial current rise is mainly governed by the  $Ar^+$  induced secondary emission electron coefficient since argon is the dominant species in this initial condition. Then, after this ignition, a preferential sputtering of nitrogen will lead to a progressive increase of atomic nitrogen close to the target. This nitrogen population can, in turn, be ionized and back attracted to the target, hence contributing to the total ionic current. Hence, more secondary electrons were produced. These generated electrons contribute to the total current and can ionize and dissociate more nitrogen following a gain in energy in the cathodic sheath. A cascade effect can thus occur explaining the faster target current rises during the pulse observed for the lowest duty cycle 2.5%. While for 5.5% duty cycles, peak power values were decreased. It means that electron densities are lower and results in reduced ionization of argon and nitrogen. These observations could also explain the decrease of nitrogen needed to reach the poisoned mode when the duty cycle was lowered. In dcMS condition, the target is continuously sputtered, while in pulsed mode nitrogen can react on the target surface also during the off-time, which is longer for the lowest duty cycles [41- 43]. Meng, L., et al. has reported, that the peak target current in HiPIMS plasma is strongly related to the flux of the ionized species and to the fraction of metal ions to the number of total ions [44]. Thus, by reducing the pulse duration, higher ion flux irradiation of the substrate and a higher ionization rate of Ti and Al ions can be expected.

## B. Supplementary information:

### B 1 Stress measurement:

The stress in the coating surface can be probed by measuring the strain free d-spacing as a function of the angle  $\psi$  between the surface normal and the diffraction plane normal using the  $\sin^2\psi$  method. According to Wetzal et al. [47], the stress tensor of samples presenting such a rotationally symmetric stress state has non-zero components with the following value:

$$\langle\sigma_{11}\rangle = \langle\sigma_{22}\rangle = \langle\sigma_{||}^S\rangle \quad \text{Eq. (1)}$$

As the out of plane stress is zero but the out of plane strain is not, the elastic strain  $\varepsilon_{\psi}^{\text{hkl}}$  measured by x-ray diffraction can be obtained from the following equation [47]:

$$\varepsilon_{\psi}^{\text{hkl}} = (2S_1^{\text{hkl}} + \frac{1}{2} S_2^{\text{hkl}} \sin^2\psi) \langle\sigma_{||}^S\rangle \quad \text{Eq. (2)}$$

where:  $S_1^{\text{hkl}}$  and  $S_2^{\text{hkl}}$  are the elastic constants related to a given (hkl) reflection.

$\langle\sigma_{||}^S\rangle$  is the average equal-biaxial internal in-plane stress in the film.

A plot of  $\varepsilon_{\psi}^{\text{hkl}}$  with respect to  $\sin^2\psi$  will give rise to a straight line whose slope can be used to obtain the stress  $\langle\sigma_{||}^S\rangle$  from given that  $\varepsilon_{\psi}^{\text{hkl}} = (d_{\psi}^{\text{hkl}} - d_0^{\text{hkl}})/d_0^{\text{hkl}}$  and that  $S_1^{\text{hkl}}$  and  $S_2^{\text{hkl}}$  are related to Young's modulus  $E$  and the Poisson ratio  $\nu$ , the above equation can be rewritten as:

$$(d_{\psi}^{\text{hkl}} - d_0^{\text{hkl}})/d_0^{\text{hkl}} = [((1+\nu)/E)_{(\text{hkl})} \sin^2\psi - 2\nu/E_{(\text{hkl})}] \langle\sigma_{||}^S\rangle \quad \text{Eq. (3)}$$

Taking the strain-free lattice spacing of the {hkl} planes  $d_0^{\text{hkl}}$  from the reference pattern, and making use of the fact that the cubic lattice parameter  $a^{\text{hkl}}$  is related to  $d^{\text{hkl}}$ , Eq. (3) can be simplified further [48]:

$$(a_{\psi}^{\text{hkl}} - a_0^{\text{hkl}})/a_0^{\text{hkl}} = [((1+\nu)/E)_{(\text{hkl})} \sin^2\psi - 2\nu/E_{(\text{hkl})}] \langle\sigma_{||}^S\rangle \quad \text{Eq. (4)}$$

Using the X Pert Stress software, the stress was automatically obtained from the slope  $m$  of the fitted straight line for the (200) plane.

## B 2 Texture coefficient:

Structural studies were focused on the three preferentially oriented peaks. The measured intensity values were observed in LC-XRD and compared with the standard Pdf data card 04-015-2554 for the chemical formula of  $Ti_{0.45}Al_{0.55}N$ . For obtaining the quantities information concerning the preferential crystalline orientation, Texture Coefficient (TC) along (111), (200) and (220) planes were calculated according to Eq. (5) [49, 50]:

$$TC_{hkl} = R_{hkl} / R_{hkl}^s \quad \text{Eq. (5)}$$

where:

$$\text{the recorded reflections } R_{hkl} = (I_{hkl} / \sum I_{hkl}) \times 100 \quad \text{Eq. (6)}$$

$$\text{the standard reflections } R_{hkl}^s = (I_{hkl}^0 / \sum I_{hkl}^0) \times 100 \quad \text{Eq. (7)}$$

$I_{hkl}$  is the measured relative intensity of a plane (hkl) and  $I_{hkl}^0$  the standard intensity of the plane (hkl) taken from the Pdf data.

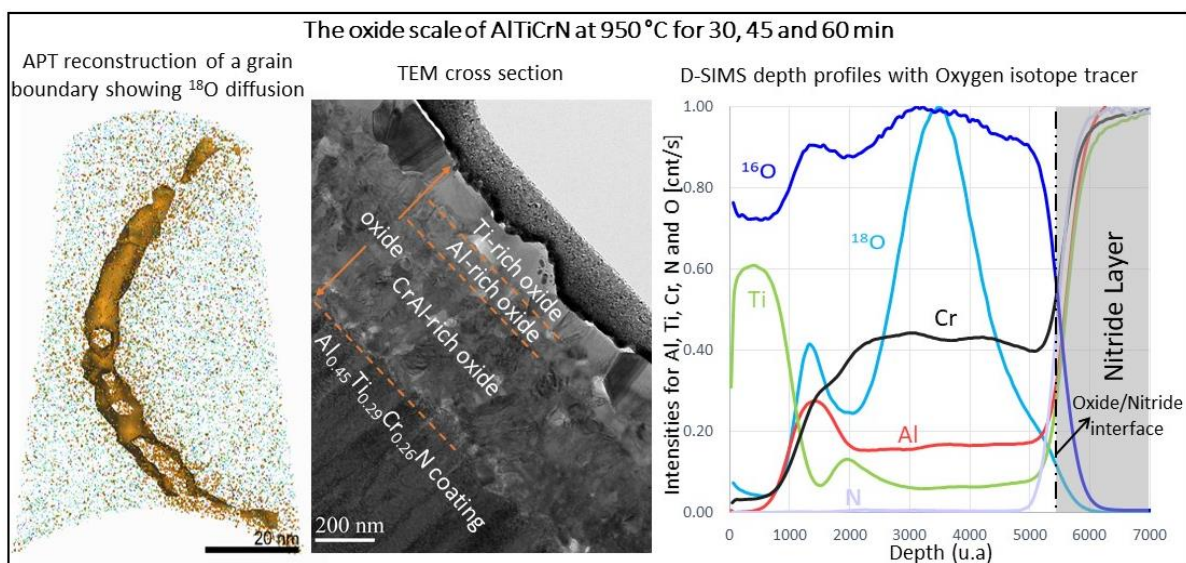
A sample with randomly oriented crystallite presents  $TC_{hkl} = 1$ , while the larger value, the larger abundance of crystallites oriented at the (hkl) direction. The higher value of texture coefficient indicates the preferred orientation of the films along that diffraction plane. This means that the increase in preferred orientation is associated with an increased number of grains along that plane.



## 7.2 Paper II

## Study of the oxidation mechanism at high temperature of nanofiber textured AlTiCrN coatings produced by physical vapor deposition using high-resolution characterization techniques

M-R. Alhafian, J-B. Chemin, N. Valle, B.El Adib, M.Penoy, L. Bourgeois, J.Ghanbaja, J. Barrirero, F. Soldera, F. Mücklich and P. Choquet







Contents lists available at ScienceDirect

Corrosion Science

journal homepage: [www.elsevier.com/locate/corsci](http://www.elsevier.com/locate/corsci)

## Study of the oxidation mechanism at high temperature of nanofiber textured AlTiCrN coatings produced by physical vapor deposition using high-resolution characterization techniques

M.-R. Alhafian<sup>a,\*</sup>, J.-B. Chemin<sup>a</sup>, N. Valle<sup>a</sup>, B. El Adib<sup>a</sup>, M. Penoy<sup>b</sup>, L. Bourgeois<sup>b</sup>, J. Ghanbaja<sup>c</sup>, J. Barrirero<sup>d</sup>, F. Soldera<sup>d</sup>, F. Mücklich<sup>d</sup>, P. Choquet<sup>a,\*</sup>

<sup>a</sup> Luxembourg Institute of Science and Technology, 41 rue du Brill, L-4422 Belvaux, Luxembourg

<sup>b</sup> Ceratizit Luxembourg S.à.r.l., 101 route de Holzen, L-8232 Mamer, Luxembourg

<sup>c</sup> University of Lorraine, CNRS, Inst Jean Lamour, UMR7198, F-54011 Nancy, France

<sup>d</sup> Saarland University, Campus D3.3, Saarbrücken 66123, Germany

### ARTICLE INFO

#### Keywords:

High-Power Impulse Magnetron Sputtering (HiPIMS)  
Aluminium-titanium-chromiumnitride (AlTiCrN) coatings  
Oxidation resistance  
Thermal stability  
Oxygen isotopic analysis

### ABSTRACT

AlTiN coatings with a NaCl structure have onset point of oxidation around 850 °C. To withstand oxidation above 850 °C, we studied the influence of Cr addition on the structure, mechanical properties and oxidation resistance of different AlTiCrN coatings. The structural evolution during the annealing of the AlTiCrN coating was revealing that all coatings kept the NaCl structure up to 950 °C. The oxidized coatings shown that the addition of Cr promoted the formation of a TiO<sub>2</sub> layer over a gradient CrAl<sub>2</sub>O<sub>3</sub> layer. This last layer is very rich in aluminum under the TiO<sub>2</sub> layer and richer in chromium at the nitride-oxide interphase.

### 1. Introduction

Increasing the efficiency of cutting tools working in a dry machining environment has become an urgent necessity, not only because of its cost-effectiveness but also because of the detrimental impact of metal-working-fluids on the environment. However, the heat generated during machining causes plastic deformation of the workpiece. Therefore, the surface protection of high-speed cutting tools by coatings with high thermal stability and oxidation resistance are subjects of research [1–9].

Physical Vapor Deposition (PVD) is one of the most preferred techniques used to perform surface protection on cutting tools due to its environment-friendliness and its low process temperature deposition [10]. The latest development in the PVD technology is the High-Power Impulse Magnetron Sputtering (HiPIMS) system which possesses the ability during the pulse to generate high density of sputtered ionized species and consequently, to produce dense protective coatings and

more homogeneous thicknesses on complex substrates with potential for high-aspect-ratio trench filling applications [11]. Furthermore, Reactive High-Power Impulse Magnetron Sputtering (R-HiPIMS) is now considered as an alternative to the Arc-evaporation process for the deposition of new generations of hard and multifunctional coatings. Zauner et al. have published the interest of HiPIMS to tune the parameters in a way of optimizing ratio and energy of Ti<sup>IV</sup> and Al<sup>III</sup> ions to stabilize a preferred cubic structure [12]. More recently, the authors are reported a work were using powder sintering Ti-Al composite targets with a R-HiPIMS deposition system and choosing the right discharge parameters allows to produce TiAlN with structural and mechanical properties similar to Arc-evaporation with better tribological properties [13]. Also, it was also demonstrated that the use of a hybrid HiPIMS/DCMS co-sputtering configuration can offer the possibility of a much higher kinetic solid-solubility limit for adding element in the cubic face structure by a well choice of the HiPIMS composition target and this for DCMS [14].

**Abbreviations:** Hybrid HiPIMS, Hybrid High-Power Impulse Magnetron Sputtering; dcMS, direct-current Magnetron Sputtering; FE-SEM, Field Emission Scanning Electron Microscopy; EDS, Energy Dispersive X-ray Spectroscopy; TEM, Transmission Electron Microscopy; SAED, Selected Area Electron Diffraction; HRTEM, High Resolution Transmission Electron Microscopy; APT, Atom Probe Tomography; D-SIMS, Dynamic Secondary Ion Mass Spectrometry.

\* Corresponding authors.

E-mail addresses: [mohamed.alhafian@list.lu](mailto:mohamed.alhafian@list.lu), [r.alhafian@gmail.com](mailto:r.alhafian@gmail.com) (M.-R. Alhafian), [patrick.choquet@list.lu](mailto:patrick.choquet@list.lu) (P. Choquet).

<sup>1</sup> ORCID: 0000-0003-0305-3952

<sup>2</sup> ORCID: 0000-0001-8696-5812

<https://doi.org/10.1016/j.corsci.2022.110226>

Received 22 November 2021; Received in revised form 3 March 2022; Accepted 4 March 2022

Available online 23 March 2022

0010-938X/© 2022 Elsevier Ltd. All rights reserved.

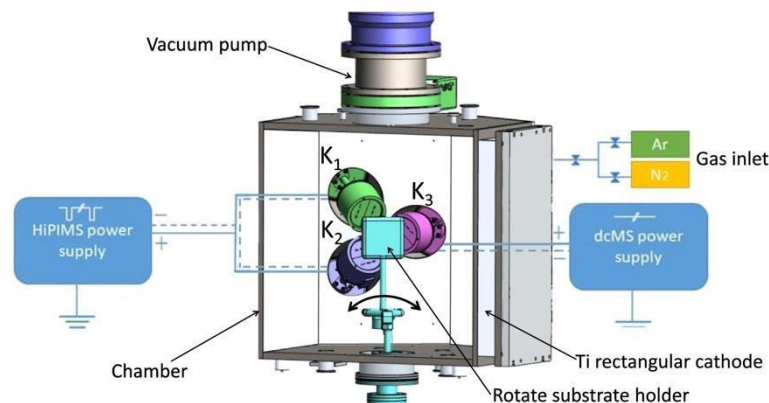


Fig. 1. Schematic drawing of the hybrid dcMS/HiPIMS co-sputtering system with the cathode magnetron connections and the sample holder rotation,  $K_{1,2,3}$  are the circular sputtering cathodes used for studied coatings and the Ti rectangular cathode used for interlayer deposition.

The thermal stability of the coated cutting tool is extremely important since its cutting edge is exposed to an elevated temperature during the working processes. TiN and CrN binary systems have been widely used as protective coatings for cutting tools. However, they are not oxidation resistant above 500 °C and 600 °C, respectively [15]. An improvement of the thermal stability up to 850 °C was achieved by the addition of another alloying element such as Al or Cr to the binary nitride coatings [16–19]. According to our recent studies, particularly in the case of AlTiN HiPIMS coatings, if good surface finishing and mechanical properties were achieved, the oxidation resistance is still limited and the elaboration of AlTiN coatings containing another oxidative protective element, for example by HiPIMS process, needs to be studied [13]. Besides that, it is well known that AlCrN coatings have higher oxidation resistance than AlTiN [20]. Therefore, a new coating combining advantages of AlTiN and AlCrN, was proposed here to improve the thermal performances at temperature higher than 850 °C. Effectively, AlTiCrN coating displays enhanced oxidation resistance, and its performance can also be optimized with the Al/Ti ratio. Several research works have demonstrated that the mechanical properties and the oxidation resistance increase with higher Al content as long as a cubic crystal structure can be maintained [20–23]. Also, other published works have introduced that the addition of chromium can combine the excellent mechanical properties of TiAlN with highest tribological properties (CrN). In 2017, Yu X. Xu et al. reported published data on single-phase cubic coatings in the TiN-AlN-CrN quasi-ternary phase diagram and they more particularly studied the thermal properties at 900 °C of two coatings  $Ti_{0.18}Al_{0.35}Cr_{0.47}N$  and  $Ti_{0.26}Al_{0.48}Cr_{0.26}N$ . They have shown that the addition of chromium has increased the thermal stability resistance with increasing Cr content, and both have excellent oxidation resistance [24]. Also, Danek et al. studied the oxidation resistance of AlTiCrN coatings at 900 °C and they have reported the benefit of Cr in delaying the diffusion of Ti to the surface. They explained the improvement in oxidation resistance by the growing of an inner protective amorphous layer of Al-Cr-O or a crystalline  $Cr(Al)_2O_3$  layer according to Cr content [25]. Donohue et al. studied the oxidation performance of  $Al_{0.53}Ti_{0.44}Cr_{0.03}N$  coating and they reported the onset oxidation temperature to 920 °C [26], which is the proposed temperature during dry machining. However, it still lacks a detailed characterization of the oxide layer to understand the mechanisms involved in oxidation process.

In this paper, high quality hard AlTiCrN coatings were developed by using a hybrid HiPIMS system. The effects of the aluminum/titanium ratio and chromium content on the high-temperature performances of these quaternary nitride hard coatings were evaluated. Scanning

Electron Microscopy (SEM) and X-Ray Diffraction (XRD) analysis were used for detailed investigations of the coating morphology, structure and phase stability after high-temperature oxidation tests. Furthermore, to determine more accurately the growth mechanisms of the oxide layers at 950 °C, characterization observations by Transmission Electron Microscopy (TEM) of each oxide layer were carried out. Additionally, isotopic ( $^{18}O_2$  and  $^{16}O_2$ ) labeled oxidation experiments were designed to determine the anionic and cationic diffusion mechanisms that control the oxide growth of each oxide layer. The subsequent oxide layers were investigated by Dynamic Secondary Ion Mass Spectrometry (D-SIMS), completed by Atom Probe Tomography (APT) mappings. Thanks to this complete knowledge of the oxide layer and understanding of its growing mechanism, an optimization of the Cr and of the ratio Ti/Al is suggested.

## 2. Experimental procedure

### 2.1. Coating deposition

The different  $Al_xTi_yCr_{1-(x+y)}N$  coatings were deposited on mirror-polished silicon wafers with a crystal orientation of  $100 \pm 0.5^\circ$  and also on polished cemented tungsten carbide plane disc with chemical composition of Co = 5.8 wt% and (Ti Ta Nb)C = 7.4 wt%. Prior to deposition, both substrates were cleaned in an ultrasonic bath using ethanol for ten minutes. The coatings were carried out by hybrid HiPIMS technologies into a PVD coater machine equipped with one Ti rectangular cathode with a surface of 500 cm<sup>2</sup> for deposition of the TiN interlayer and three 4-in circulars cathodes  $K_1$ ,  $K_2$  and  $K_3$  used for the elaboration of the different hard nitride coatings. The circular cathodes are placed at an angle of 30°, 30° and 45° from the substrate respectively, with respect to the same distance of 120 mm from the substrate holder. To avoid a coating composition variation and to ensure a uniform thickness of the coating, the deposit runs in a dynamic mode where the substrate speed was 5 rpm with 70° rotation. A schematic drawing of the configuration for the targets and the deposition system is shown in Fig. 1.

The chamber was first pumped down to  $10^{-6}$  mbar and the substrate holder was preheated to 450 °C. Following the evacuation and pre-heating step, the samples were activated with an Ar ion bombardment using three microwaves antenna to generate the active plasma. Furthermore, in order to avoid any contaminants in the coatings (e.g., O), the targets were first pre-sputtered during 10 min. An approximative 0.5 μm-thick TiN interlayer was deposited by dcMS to improve the coating adhesion. During the deposition time, 22 sccm of  $N_2$  flow and 50



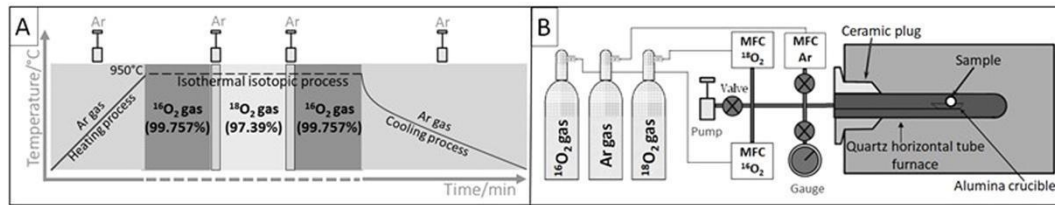


Fig. 2. Schematic drawing of isotopic oxidation experiments (A), furnace system (B).

scm of argon were injected, yielding a working pressure of 5  $\mu\text{bar}$ . These flows were determined via a target poisoning study by investigating the variation of the target voltage as a function of the reactive gas flow, to allow sputtering in the compound mode and to reach stoichiometric nitride coatings.

Two targets ( $K_1$  and  $K_2$ ) with the three sequentially compounds of  $\text{Ti}_{50}\text{Al}_{50}$  at%,  $\text{Ti}_{45}\text{Al}_{55}$  at% or  $\text{Ti}_{40}\text{Al}_{60}$  at% were used and one more target ( $K_3$ ) of  $\text{Cr}_{100}$  at% have been run during this study. The power on the targets was applied by using two generators. The targets ( $K_1$  and  $K_2$ ) were connected to a HiPIMS generator using a duty cycle of 3.5% with a pulse length of 2000  $\mu\text{sec}$ , at a pulse repetition of 500 Hz with an average power of 3200 W (target power density of 18.6  $\text{W}/\text{cm}^2$ ) and a peak voltage of - 480 V. The target ( $K_3$ ) was connected to a dcMS generator, different deposition average powers were used to study the effect of the Cr content on the coating properties. Taking into account preliminary results, not reported in this article, the hybrid TiAl-HiPIMS/Cr-dcMS co-sputtering configuration was chosen as only this one, gives the possibility to reach coating hardness of 30 GPa and internal compressive stresses higher than - 1000 MPa. A continuous substrate bias voltage was kept constant at  $-35 \pm 5$  V for all deposition conditions. The thicknesses and deposition rates of the coatings were in the range of 3.0–3.5  $\mu\text{m}$  and 0.8–1.0  $\mu\text{m}/\text{h}$ , respectively.

## 2.2. Characterizations

The determination of the elemental composition of the coatings and their microstructure were carried out by using a Field Emission Scanning Electron Microscope FE-SEM (Hitachi SU-70) equipped with an Oxford X-Max<sup>N</sup> 20  $\text{mm}^2$  Energy-Dispersive X-ray Spectroscopy (EDS) detector [27]. The as-deposited and oxidized coatings on Si wafer substrates were used for SEM and TEM observations to define the coating growth morphology, the thickness of the oxidized layers, the grain size and the crystal structures. TEM investigations were carried out using a JEM-ARM 200F Cold FEG TEM/STEM (JEOL) operating at 200 kV and equipped with a spherical aberration (Cs) probe and image. The point resolution was 0.12 nm in TEM mode and 0.078 nm in STEM mode.

The texture analyses were performed on a PANalytical Empyrean XRD operating in Bragg-Brentano (BB) geometry in point focus configuration using a  $\text{Cu K}\alpha$  radiation at 45 kV and 40 mA. The residual stress measurements and the stress-free lattice  $a_0$  were performed using the classical single  $\{hkl\} \sin^2\psi$  method on the (200) reflection plane of the  $\text{Ti}_{0.45}\text{Al}_{0.55}\text{N}$  phase [13,28,29]. Grazing Incidence X-ray Diffraction (GI-XRD) measurements were performed for phase identification of as-deposited and oxidized samples at a grazing angle of  $2^\circ$  with a Bruker D8 Discover diffractometer in parallel beam configuration. For the nitride coating phases, the diffractograms were recorded at room temperature on as-deposited coatings and also, after an annealing stage. The Full Width at Half Maxima (FWHM) were calculated on the (422) reflection peak measured in GI-XRD with an incident angle  $\omega$  fixed to  $2^\circ$ , and the crystallite size was calculated using Scherrer's equation. In order to track the generation of the different oxide phases, an oxidation of the coatings in air was performed in-situ the X-ray diffractometer and diffraction patterns were recorded from room temperature to 950  $^\circ\text{C}$ , using the DHS-1100 hot stage furnace from Anton Paar. The heating rate condition was set to 1  $^\circ\text{C}$  per second and the cooling was assisted using a flow of compressed air. Before each XRD measurement, the temperature of the DHS-1100 hot stage furnace was held constant for 1 min. Furthermore, three measurements were performed at 950  $^\circ\text{C}$ . The first one was done immediately after reaching this maximal temperature and the second and third ones were started after 1 h and 2 h of heating at 950  $^\circ\text{C}$ , respectively.

The determination of the surface instrumented hardness ( $H_{IT}$ ) and the instrumented elastic modulus ( $E_{IT}$ ) at room temperature were measured by a nano-indentation equipment from Anton Paar-CSM NHT3 with a Berkovich diamond tip [30]. The applied load was 20 mN leading to a penetration depth of  $\approx 0.2 \mu\text{m}$  in a  $4 \times 5$  indentation matrix and the Poisson ratio  $\nu$  was assumed to be 0.18 [31].

For a better understanding of the different diffusion mechanisms, which control the oxidation kinetics, isotopic oxidation experiments were carried out with coatings deposited on Si wafer. The oxidation experiments consist of successive steps done in different atmospheres containing either mainly  $^{16}\text{O}_2$  (99.757%  $^{16}\text{O}_2$ , 0.205%  $^{18}\text{O}_2$ , 0.038%

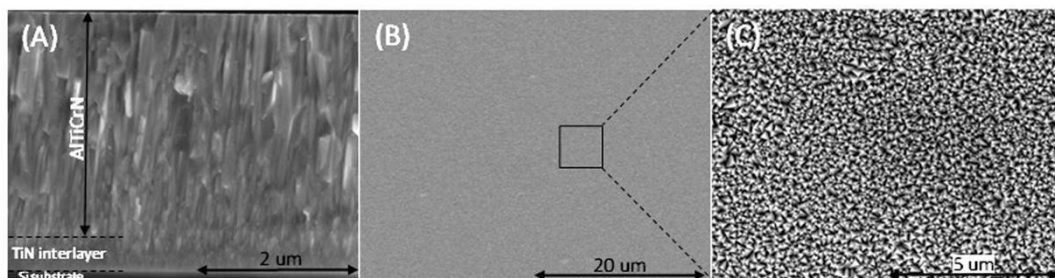


Fig. 3. The cross-section (A), the top-view images (B) and (C) of as-deposited  $\text{Al}_{0.42}\text{Ti}_{0.32}\text{Cr}_{0.26}\text{N}$  coating on Si wafer substrates, present the TiN bonding layer, the micro-columnar structure, and the pyramidal tips of columns.

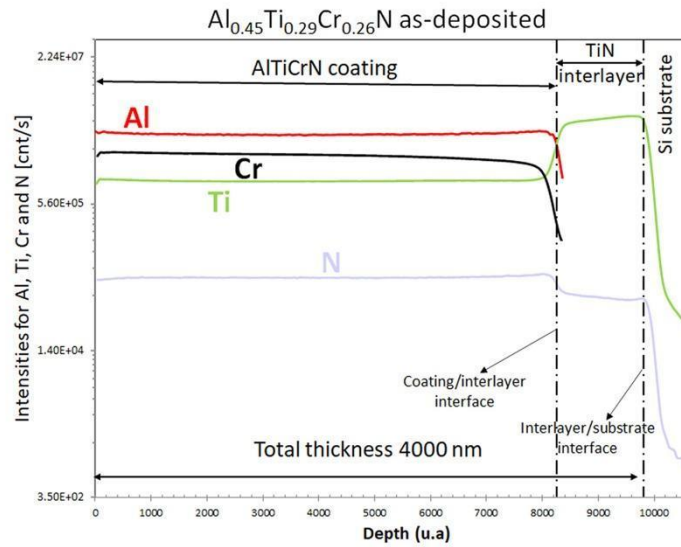


Fig. 4. D-SIMS depth profile for as-deposited  $\text{Al}_{0.45}\text{Ti}_{0.29}\text{Cr}_{0.26}\text{N}$  shows a homogeneous distribution of coatings elements, the TiN interlayer, and the Si substrate (Y-axis is in logarithmic scale).

$^{17}\text{O}_2$  or  $^{18}\text{O}_2$  (EurisoTop, 97.39%  $^{18}\text{O}_2$ , 2.12%  $^{16}\text{O}_2$ ) and the hot furnace was a Nabetherm equipment. For purposes of simplification, the isotopic sequence will be referred to  $^{16}\text{O}_2$  or  $^{18}\text{O}_2$  depending on the most abundant isotope present in gas. Different isotopic oxidation stages were undertaken with successive oxidations in  $^{16}\text{O}_2$  or  $^{18}\text{O}_2$ : (1)  $^{16}\text{O}_2$  for 15 or 30 min, (2)  $^{18}\text{O}_2$  for 15 min and (3)  $^{16}\text{O}_2$  for 15 or 30 min and consequently, the total oxidation durations were 30, 45 or 60 min for all cases. The experimental setup for the oxidation procedure is presented in Fig. 2. After these oxidation periods, elemental depth profiling was conducted via dynamic secondary ion mass spectrometry using a CAMECA SC-Ultra instrument in positive ion mode, with a  $\text{Cs}^+$  ion

bombardment. The impact energy was 2.0 keV. The total acquisition time were carried out in a range from 15 to 60 min, commensurate with the oxide thickness to be analysed. For APT analyses, samples were prepared in a dual-beam focused ion beam/scanning electron microscopy workstation (FIB/SEM) Helios NanoLab 600™ (FEI), following the standard lift-out preparation detailed in [32]. A final cleaning step at 2 kV was performed to minimize Ga damage during the thinning of the specimens. Laser pulsed APT was performed using a LEAP™ 3000XR (CAMECA) at a repetition rate of 200 kHz, at a temperature of about 50–60 K, a pressure lower than  $1.33 \times 10^{-8}$  Pa, and laser pulse energies of 0.5–0.7 nJ. The evaporation rate of the specimen was 5 atoms per

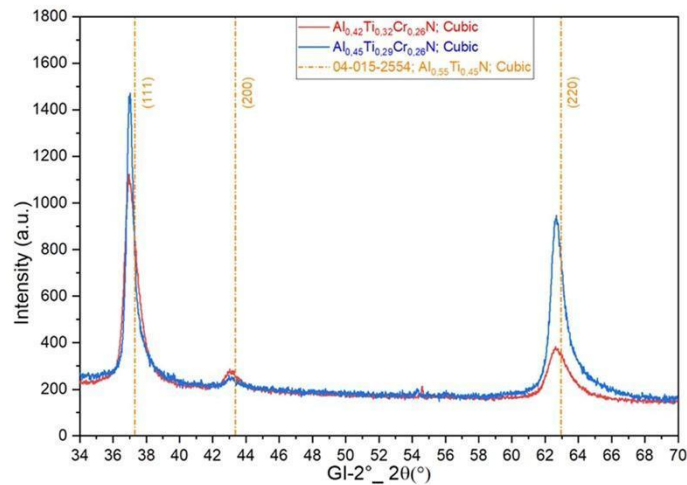


Fig. 5. The GI-XRD spectra at  $2^\circ$  of 0-20 for two as-deposited  $\text{Al}_{0.42}\text{Ti}_{0.32}\text{Cr}_{0.26}\text{N}$  and  $\text{Al}_{0.45}\text{Ti}_{0.29}\text{Cr}_{0.26}\text{N}$  coatings with the three main texture orientation. The vertical line indicates the standard position of the c- $\text{Al}_{0.55}\text{Ti}_{0.45}\text{N}$  corresponding to PDF card number 04-015-2554.



**Table 1**  
Characterization of samples coated with two different Ti/Al ratios of AlTiCrN produced by hybrid HIPIMS. For calculation, the Poisson ratio was set to 0.18.

PVD technology	Target coatings	Texture coefficient			Lattice a <sub>0</sub> Å	FWHM determined on (422) °	Grain size nm	Residual stress MPa	Phase	Composition at%				Hardness (H <sub>IT</sub> )		E-modulus GPa
		(111)	(200)	(220)						Al	Ti	Cr	N	GPa	GPa	
Hybrid HIPIMS	TiAl45/55 Al <sub>0.42</sub> Ti <sub>0.32</sub> Cr <sub>0.26</sub> N	2.35	0.31	1.05	4.189	3.3517	5.78	-4089 ± 341	cfc	21.7	16	13.5	48.8	32.1 ± 0.7	499 ± 13	
	TiAl40/60 Al <sub>0.45</sub> Ti <sub>0.29</sub> Cr <sub>0.26</sub> N	3.47	0.19	0.14	4.189	3.4691	5.58	-4923 ± 109	cfc	23.3	14.8	13.4	48.5	32.9 ± 1.2	514 ± 13	

1000 pulses. Data reconstruction was carried out with the software package IVAST<sup>TM</sup>3.6.14 using voltage mode with an evaporation field of 35 V/nm, k-factor of 4 and image compression factor of 1.5.

### 3. Results and discussion

#### 3.1. Properties of as-deposited coatings

The morphology of the Al<sub>0.42</sub>Ti<sub>0.32</sub>Cr<sub>0.26</sub>N and Al<sub>0.45</sub>Ti<sub>0.29</sub>Cr<sub>0.26</sub>N coatings was observed by SEM, Fig. 3. It can be observed the initial stages of the film growth where a micro-columnar structure TiN interlayer with around ≈0.5 μm thickness, followed by a AlTiCrN film with a micro-columnar structure extending from the initial formation with slightly enlarging the micro-columns as the growth ran its course (Fig. 3a). A good bonding between the film and substrate was estimated since no gaps were detected in the film-substrate interface. It can be clearly seen in the top-view micrographs that the coating has uniform surface without macro particle defects and with pyramidal tips of columns (Fig. 3b & c). Fig. 4 shows the D-SIMS depth profiles of as-deposited Al<sub>0.45</sub>Ti<sub>0.29</sub>Cr<sub>0.26</sub>N where the elemental data of all metallic elements and nitrogen from the coating surface to the substrate were measured. The depth profiles highlight the deposition of homogeneous deposition of AlTiCrN coating followed with a TiN interlayer and then the Si substrate. The 0-2θ of GI-XRD at 2° patterns of as-deposited Al<sub>0.42</sub>Ti<sub>0.32</sub>Cr<sub>0.26</sub>N and Al<sub>0.45</sub>Ti<sub>0.29</sub>Cr<sub>0.26</sub>N coatings are shown in Fig. 5. These coatings exhibit the typical peaks of a single-phase cubic structure with a (111) preferred crystallographic orientation and at least two more visible reflections (200) and (220) also reported in Table 1. An evaluation of the residual stresses has been carried out on these two different coatings. The values of compressive stresses range from -4000 MPa to -5000 MPa, with the highest value reported for the lower Ti/Al ratio. By comparison with other values reported in the literature, these can be considered as high. Based on other measurements done in a previous comparative studies, this high stress evaluation could be linked to the WC-Co hard substrate used and to the choice of the coating Young's modulus and Poisson ratio, details of the stress measurements have been already reported in the Supplementary information of reference [13] The instrumented hardness (H<sub>IT</sub>) of the AlTiCrN coatings was measured for both coatings to be ≈32–33 GPa, and the elastic modulus was determined to be ≈500 GPa.

#### 3.2. Stability of the nitride layer up to 950 °C

The evolution with time and temperature of the oxide as well as the stability of the single-phase cubic structure for the Al<sub>0.42</sub>Ti<sub>0.32</sub>Cr<sub>0.26</sub>N coated sample was followed between 30 °C and 950 °C and the XRD patterns are reported in Fig. 6. The 0-2θ measurements performed on this coating show a shift to high angle during the heating stage for peak (111) from 37.09° at 30 °C to 37.25° at 650 °C. A possible hypothesis of this shift can be associated with the stress-reducing phenomena during the temperature rises. Stress relaxation or recovery would be due to the rearrangement of defects and not due to a recrystallization mechanism, since there has no change in texture associated. After reaching this temperature of 650 °C and after, up to 950 °C, no more shift for this (111) peak was recorded. During the 3-hour holding at 950 °C, there is a relative peak signal decrease and a new shift to lower angles which can be explained by the growth of the oxide scale on top of the nitride coating and the detection of a new peak associated with the Al<sub>x</sub>Cr<sub>y</sub>O<sub>3</sub> rhombohedral phase generation.

Fig. 7 shows TEM micrographs of the non-oxidized part of the Al<sub>0.45</sub>Ti<sub>0.29</sub>Cr<sub>0.26</sub>N coating after 1-hour holding at 950 °C. No segregation, precipitation or coarsening are observed, even at the coating-substrate interface (Fig. 7A). Selected area electron diffraction patterns (SAED) show the three structural regions of the sample starting from the single-crystalline Si substrate followed by the poly-crystalline structures for both, the TiN interlayer and AlTiCrN coating. Based on

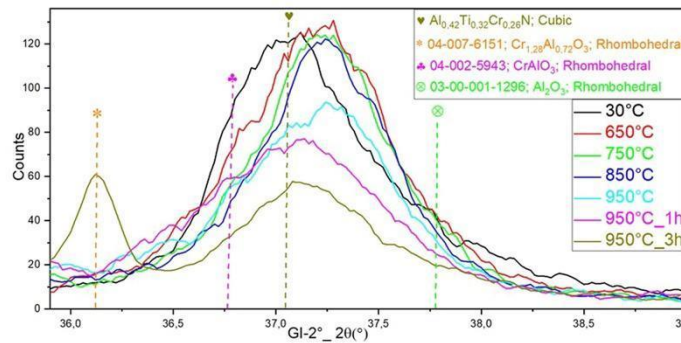


Fig. 6. The evolution of (111) peak of  $\text{Al}_{0.42}\text{Ti}_{0.32}\text{Cr}_{0.26}\text{N}$  coating oxidized in air at temperatures ranging from 30 °C to 950 °C.

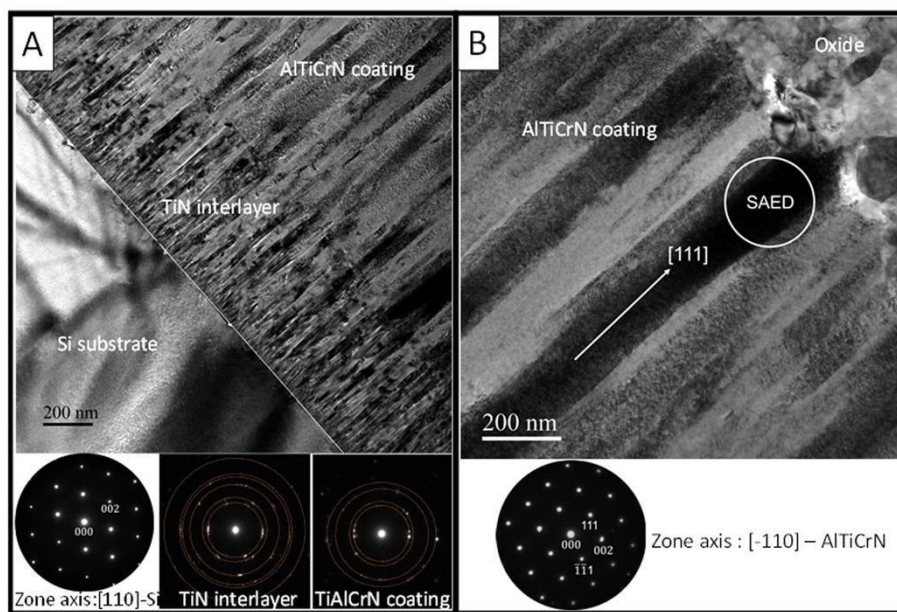


Fig. 7. TEM micrograph and SAED pattern focused on the non-oxidized part of the coating  $\text{Al}_{0.45}\text{Ti}_{0.29}\text{Cr}_{0.26}\text{N}$  at 950 °C for 1 h (A) internal part of the coating with the interface with the Si substrate. (B) external part of the coating.

the electron diffraction analyses done and summarized here by the presentation of one typical pattern (Fig. 7B), a possible spinodal decomposition and further precipitation of h-AlN at 950 °C after an annealing duration of 30 min was not detected with this coating composition. Other previous works [25,33] have reported for similar AlTiCrN coating compositions, structural evolutions as a function of time at 900 °C from XRD diffraction measurements. They described the broadening and the shift to higher angles of fcc diffraction peaks but they were not able to correlate this diagram change to the spinodal decomposition or to the generation of new peaks linked to the oxidation of the film. This new result by electron diffraction analyses can indicate that these previous XRD pattern evolutions were not driven by structural modification of the AlTiCrN coating. TEM investigations at high resolution, not reported in the paper, found that the size of the coating's column size at 950 °C has grown compared to as-deposited and it is

between 65 and 85 nm at the upper zone and around 10 nm for the interlayer.

### 3.3. Oxidation study up to 950 °C

#### 3.3.1. Description of the oxide layers

On the evolution of the GI-XRD reflection patterns when increasing temperature up to 950 °C (Fig. 6), the tetragonal  $\text{TiO}_2$ -rutile phase is identified from 700 °C with a lattice spacing of  $a = 4.61 \text{ \AA}$  and  $c = 2.98 \text{ \AA}$  corresponding to PDF card number 01-089-6975 and 04-005-4661. For the rhombohedral  $\text{CrAlO}_3$  phase, this one is detected at higher temperature, around 800 °C, with a lattice spacing of  $a = b = 4.88 \text{ \AA}$  and  $c = 13.32 \text{ \AA}$  corresponding to PDF card number 04-002-5943 and 04-007-6151. As different lattice parameters can be reported for this phase, depending on the ratio of Al/Cr, here, it is in



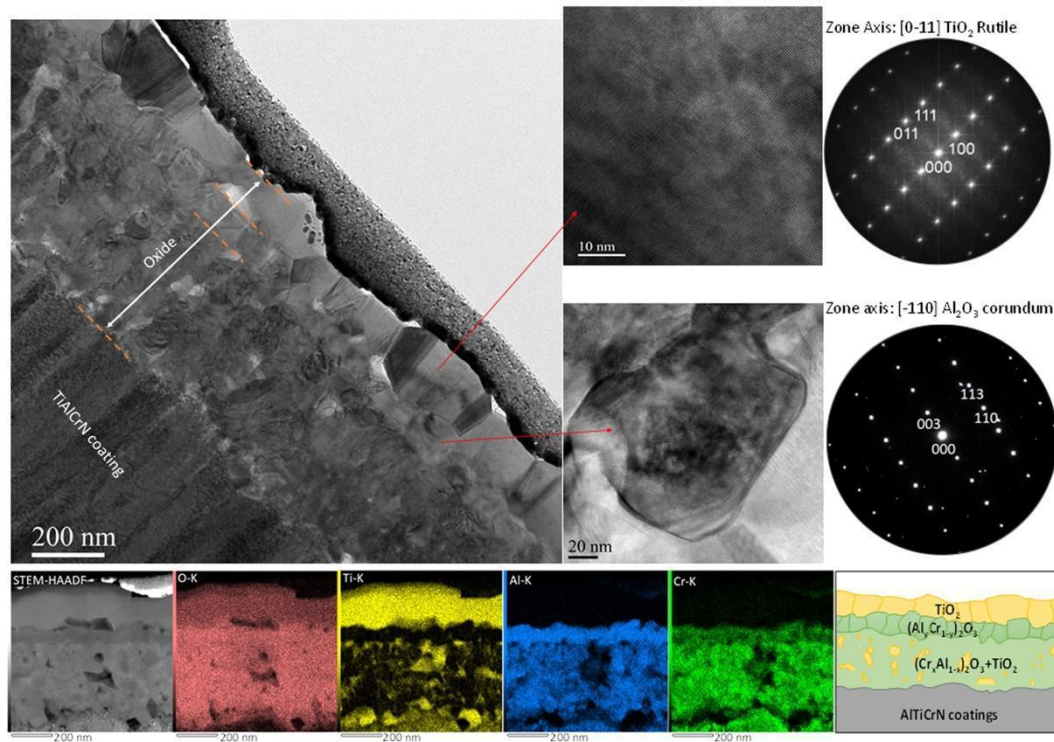


**Fig. 8.** shows an overview TEM micrograph of  $\text{Al}_{0.45}\text{Ti}_{0.29}\text{Cr}_{0.26}\text{N}$  coating oxidized in air at  $950\text{ }^\circ\text{C}$  for 30 min. The lattice resolved diffraction contrast of  $\text{TiO}_2$  and  $\text{Al}_2\text{O}_3$  along the  $[0-11]$  and  $[-110]$  zone axis, respectively and corresponding selected area electron diffraction (SAED). STEM-HAADF and EDX color coded maps of oxidation regions presenting the contrast of O (red), Ti (yellow), Al (blue) and Cr (green) as well as the schematic drawing of oxidation regions deduced from results presented in Fig. 8 and Fig. 9.

good agreement with these introduced by Bondioli et al. [34]. At  $950\text{ }^\circ\text{C}$ , the first evidence of a  $\text{Al}_2\text{O}_3$  phase corresponding to PDF card number 00-001-1296 was detected. The absence of reflection of this last oxide phase up to  $950\text{ }^\circ\text{C}$  will be discussed later. Fig. 8 presents TEM micrographs of the cross-section of  $\text{Al}_{0.45}\text{Ti}_{0.29}\text{Cr}_{0.26}\text{N}$  coating at  $950\text{ }^\circ\text{C}$  after 30 min of oxidation. The oxide scale presents a total thickness of about  $610 \pm 25\text{ nm}$ . The elemental distribution of these oxide area is depicted by the colored EDX maps. From the outermost to the internal oxidized area, the oxide is made of a very rich titanium oxide region, followed by an aluminum-chromium based oxide whose thicker internal layer contain Ti oxide rich islands. The two high-magnification TEM images reveal two types of grains in its outer region. Their respective electron diffraction patterns indicate that the largest grains ( $125\text{--}230\text{ nm}$ ) at the external surface and rich in titanium, have a rutile structure whereas the other grains ( $40\text{--}90\text{ nm}$ ) just below are rich in aluminum and have a rhombohedral  $\text{Al}_2\text{O}_3$  corundum structure. Much more fine oxide grains have also been observed for the more internal aluminum-chromium mixed oxide, with a size around  $10\text{--}20\text{ nm}$ . Inside the thickness of this aluminum-rich oxide region, the D-SIMS analyses have shown that the chromium concentration is decreasing from its inner zone to its outer zone (Fig. 10, the region between a and b). The thicknesses of each oxide region at  $950\text{ }^\circ\text{C}$  and after 30 min are  $\approx 160 \pm 15$ ,  $\approx 90 \pm 5$  and  $\approx 385 \pm 25\text{ nm}$ , respectively. For this aluminum-chromium oxide region, the EDX analyses gave an average oxide stoichiometry for the biggest grains,  $\text{Al}_{1.5}\text{Cr}_{0.5}\text{O}_3$  and for the smallest grains,  $\text{Al}_{1.0}\text{Cr}_{1.0}\text{O}_3$ . It has also to be reported that other titanium-oxide grains with smaller size were

detected in the mixed chromium-aluminum-oxide region (Fig. 8). Since the titanium is not miscible in the mixed  $(\text{Al}_x\text{Cr}_y)_2\text{O}_3$ , it makes the formation of islands with  $\text{TiO}_2$  grains with larger grain size by comparison with these of the mixed Al-Cr oxide matrix.

Fig. 9 shows a BF-TEM image of the inner mixed chromium-aluminum-oxide region  $(\text{Cr}_x\text{Al}_{1-x})_2\text{O}_3$  and the corresponding selected area diffraction patterns obtained along  $[100]$  and  $[\bar{1}\bar{1}0]$  zone axes. The crystal lattice parameters vary slightly depending on the Cr amount in the oxides  $(\text{Cr}_x\text{Al}_{1-x})_2\text{O}_3$  with different lattices as it is reported in Pearson's crystal data [35]. Some of the lattice parameters found and associated to oxide stoichiometry are:  $a = b = 0.477\text{ nm}$ ,  $c = 1.302\text{ nm}$  for  $\text{Al}_{1.896}\text{Cr}_{0.104}\text{O}_3$ ,  $a = b = 0.476\text{ nm}$ ,  $c = 1.298\text{ nm}$  for  $\text{Al}_{1.68}\text{Cr}_{0.32}\text{O}_3$  and  $a = b = 0.492\text{ nm}$ ,  $c = 1.346\text{ nm}$  for  $\text{Al}_{0.72}\text{Cr}_{1.28}\text{O}_3$ .

### 3.3.2. Growth mechanism of the oxide layers

Several factors generally affect the formation and growth of the oxides, such as the properties of the metal oxides, partial pressure of reaction gas and also, the presence of defects in the crystal structure of the oxides. Concerning the growth kinetic, it is in general controlled by diffusion phenomena. D-SIMS depth profiles of the oxidized  $\text{Al}_{0.45}\text{Ti}_{0.29}\text{Cr}_{0.26}\text{N}$  coating at  $950\text{ }^\circ\text{C}$  for various durations and different gas sequences between  $^{16}\text{O}_2$  and  $^{18}\text{O}_2$  were carried out to go deeper in the understanding of the oxide growth mechanism (Fig. 10). The different layers observed on TEM images are also clearly visible on D-SIMS profiles, i.e. from the surface to the interface with the nitride: the Ti oxide, the Cr-Al oxide with an outer zone rich in aluminum. From the

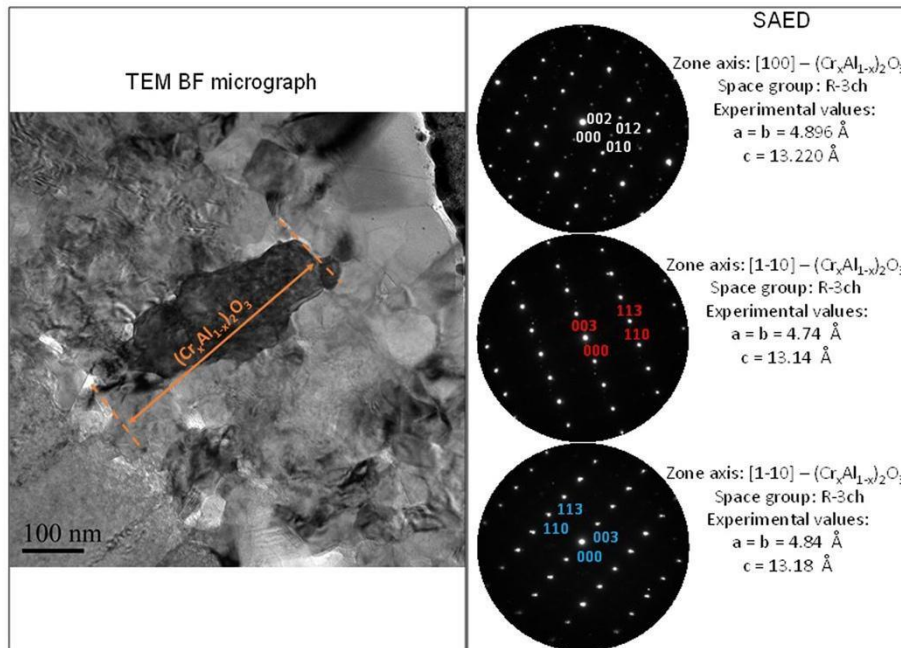


Fig. 9. The lattice resolved diffraction contrast of TEM analysis of  $Al_{0.45}Ti_{0.29}Cr_{0.26}N$  coating after oxidized at  $950\text{ }^{\circ}C$  for 30 min focusing on  $(Cr_xAl_{1-x})_2O_3$  region aligned along the three-zone axis.

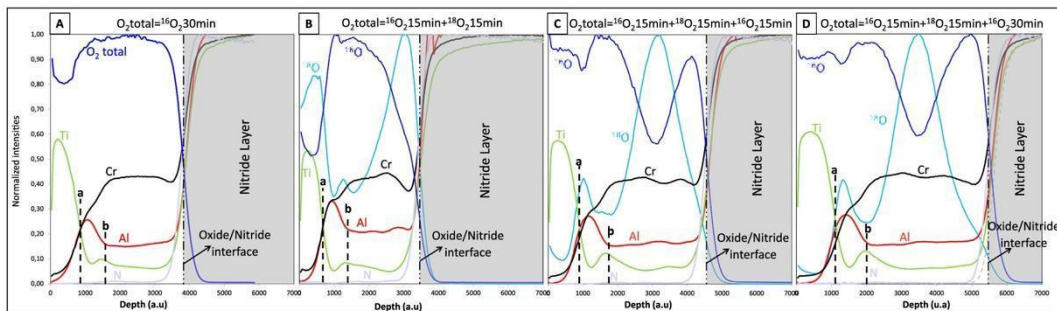


Fig. 10. O, Al, Ti, Cr and N D-SIMS depth profiles for  $Al_{0.45}Ti_{0.29}Cr_{0.26}N$  oxidized coating at  $950\text{ }^{\circ}C$  using different isotopic oxidation sequences: (a) 30 min of  $^{16}O_2$ , (b) 15 min of  $^{16}O_2$  and 15 min of  $^{18}O_2$ , (c) 15 min of  $^{16}O_2$  15 min of  $^{18}O_2$  and 15 min of  $^{16}O_2$ , and (d) 15 min of  $^{16}O_2$  15 min of  $^{18}O_2$  and 30 min of  $^{16}O_2$ . The dashed vertical lines (a and b) delimit the different layer of the oxide scale.

determination of the different positions of these layer interfaces with time, reported on the different SIMS profiles on the Fig. 10 by the dashed lines a and b, we have followed their thickness evolutions. Considering that the sputtering rate for each oxide layer which constituted the oxide scale is the same, we can observe that each oxide continues to grow during the all-oxidation period. From this statement, it can be reported that the total oxide thickness growth mechanism is the result of a continuous oxidation process for each oxide layer. Thanks to the multi-gas stage oxidation experiments, it has been possible to show relevant information about the oxidation growth mechanism on this AlTiCrN coating at  $950\text{ }^{\circ}C$ . For that, it is now discussed the evolution of the oxygen isotopic profile after different total oxidation times presented in

Fig. 10B, C and D in comparison with the oxide layer generated after 30 min without any artificial enrichment in  $^{18}O_2$  (Fig. 10A). For the last three coatings, a first oxidation period was carried out under  $^{16}O_2$  ( $^{16}O$  and  $^{18}O$  in proportion fixed by the natural abundances) during 15 min to grow a first oxide layer covering all the coating surface. Then, the oxidation continues for additional 15 min under  $O_2$  mainly composed by  $^{18}O_2$  (97.39%). For the last two oxidized coatings (Fig. 10C and D), another  $^{16}O_2$  oxidation period was added during 15 and 30 min, respectively. Thanks to a normalization step of the different depth profiles, it can be seen in Fig. 10B, after 30 min of oxidation time, that the  $^{18}O$  profile shows two main peak intensities and one more with a smaller intensity. Taking into account the TEM oxide scale



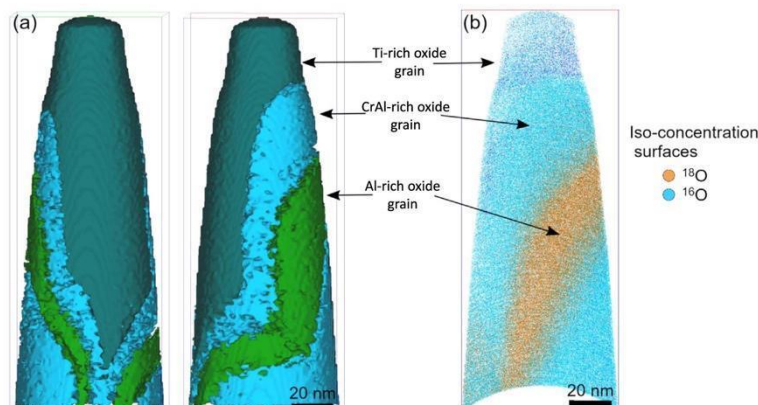


Fig. 11. APT reconstruction showing the three different types of oxide grains formed on the oxidized coating at 950 °C. (a) Two views of the same reconstruction rotate 90 degrees. (b) Highlight of the oxygen isotopes distribution with  $^{18}\text{O}$  primarily found in the Al-rich oxide grain and  $^{16}\text{O}$  primarily in CrAl- and Ti-rich oxide grains. The mass-to-charge-state ratio, reported in Supplementary material 5.A.

investigations and the evolution of Ti, Al, and Cr SIMS intensities, the localization of these peaks can be associated to the different layers. The first high intensity  $^{18}\text{O}$  peak is located on the top oxide surface and it follows the titanium profile (first  $^{18}\text{O}$  peak), while the two other high intensity peaks are located in the second oxide layer. One specific peak just below the aluminum-rich outer region (second  $^{18}\text{O}$  peak) coincides with a small Ti peak after 30 min of oxidation and the other one (third  $^{18}\text{O}$  peak) is present at the interface with the remaining nitride layer. The presence of  $^{18}\text{O}$  in the outer titanium layer indicates the contribution to the outward cation diffusion during the oxide growth and this mechanism can control the formation of the rutile  $\text{TiO}_2$  oxide layer. The enrichment of  $^{18}\text{O}$  at the nitride/oxide interface indicates the contribution of the inward diffusion of oxygen in the transport processes. After longer oxidation periods, i.e., 15 and 30 min under  $^{16}\text{O}_2$ , outward cation diffusion with titanium and inward anionic diffusion with oxygen continue (Fig. 10C and D) and lead to a thicker  $\text{TiO}_2$  layer and an increase of Ti content on the other side of the Al rich oxide. As the oxidation continues, the intensity of the first  $^{18}\text{O}$  peak drastically decreases whereas the second one totally disappears. The third  $^{18}\text{O}$  peak remains present until the end of the experiment. In regards, to this statement and considering that the chromium intensity profile is decreasing from its internal interface at the mixed chromium-aluminum oxide interface to titanium oxide interface, it can be proposed the following hypothesis to explain the existing of this aluminum-rich oxide region. If we consider that the external titanium oxide is not a complete barrier for oxygen molecule diffusion, a relatively high oxygen pressure can be present at the interface between the mixed chromium-aluminum oxide and the titanium oxide, chromium volatile oxide species can be produced, and this statement can follow to a chromium depletion zone and the formation of very high aluminum oxide layer just below the titanium oxide scale. It is known that, during the oxidation of metal alloy rich in chromium, at high temperature, around 1000 °C and higher, two reactions can occur: firstly, a chromium-rich oxide scale formation and secondly, the chromium species volatilization from this layer where many reactions are possible depending on the oxidation atmospheres and the oxygen vapor pressures. Different Cr species volatilization reactions in  $\text{O}_2$  are reported in the literature depending of the oxygen partial pressure and temperature:  $\text{CrO}_3$ ,  $\text{CrO}_2$ ,  $\text{CrO}$  and  $\text{Cr}$  [36–38]. Hilpert et al. [39] have modeled thermodynamics data using Chemsage program to thermodynamically study the formation of Cr volatile species in dry and humid air. The main species volatilized are  $\text{CrO}_3$  and  $\text{CrO}_2(\text{OH})_2$  respectively. Now, to confirm the anionic and cationic

Table 2  
Composition of the three different types of oxide grains measured by APT.

	Ti-rich oxide grain	Al-rich oxide grain	CrAl-rich oxide grain
Al	2.2 ± 0.1	42.4 ± 0.1	29.2 ± 0.1
Ti	39.2 ± 0.1	–	0.1 ± 0.1
Cr	3.4 ± 0.1	3.3 ± 0.1	12.7 ± 0.1
$^{16}\text{O}_2$	54.8 ± 0.1	13.5 ± 0.1	56.0 ± 0.1
$^{18}\text{O}_2$	0.4 ± 0.1	40.9 ± 0.1	2.1 ± 0.1
$^{16}\text{O}_2 + ^{18}\text{O}_2$	55.2 ± 0.1	54.4 ± 0.1	58.1 ± 0.1

diffusion mechanisms which could control the oxide growth, APT analysis was performed in the oxide layer of an oxidizing coating after a cycle with 15 min under  $^{16}\text{O}_2 + 15$  min under  $^{18}\text{O}_2 + 15$  min under  $^{16}\text{O}_2$  at 950 °C. The specimens were prepared to carry out the analysis in the mixed chromium-aluminum oxide layer (Fig. 11) (further detailed information in Supplementary material 5.A). At the volume size of around one hundred cubic nanometers, it is possible to see that there is some heterogeneous composition of this oxide scale which can correspond to three different type of oxide grains: one more rich in aluminum, one mixed aluminum-chromium and the third one, in titanium (Table 2). More in detail, the two mixed aluminum-chromium grains show no Ti content and this analysis is in good agreement with the TEM observations. Additionally, it confirms that this oxide layer partly contains  $\text{TiO}_2$  grains. Also, it can be reported that the main concentration in  $^{18}\text{O}_2$  is detected into the alumina rich grain, which can be associated to the fact that this grain is generated in a second time with the depletion of chromium replaced by oxygen. This observation confirms the SIMS profile analyses in this oxide scale where a regular decrease of the chromium content from the inner to the outer zone is reported. APT was also used to provide concentration profiles across grain boundaries. Fig. 12 shows three grain boundaries between the mixed oxide grains enriched in  $^{18}\text{O}$  and Ti. This grain boundary segregation depicts the outward diffusion of titanium from the mixed oxide for the growth of the  $\text{TiO}_2$  top oxide layer and the inward oxygen diffusion to drive the oxidation kinetic of this coating at the interface between the oxide and the nitride phase.

### 3.3.3. Influence of the Ti/Al ratio and the Cr content on the oxide growth kinetics for the TiAlCrN coatings

The optimization of the Al/Ti ratio was realized by using two other target configurations  $\text{Ti}_{45}/\text{Al}_{55}$ , and  $\text{Ti}_{40}/\text{Al}_{60}$  with one Cr target to

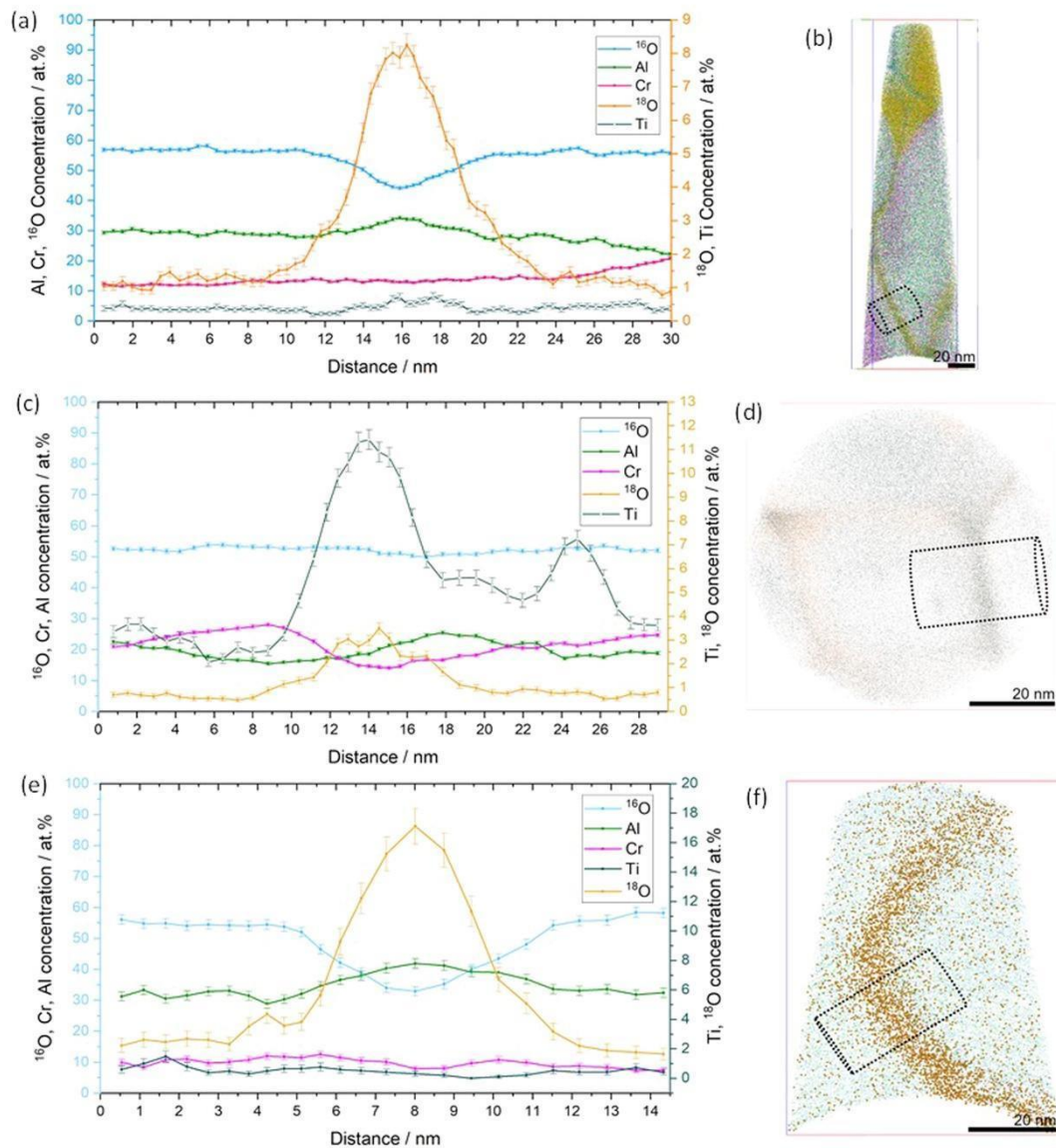


**Fig. 12.** Grain boundary segregation at three different reconstructions in  $(\text{CrAl})_2\text{O}_3$ . (a) Concentration profile across the boundary highlighted in (b) showing segregation of  $^{18}\text{O}$ . (c) Concentration profile showing Ti and  $^{18}\text{O}$  segregation at the boundary shown in (d). (d) Top view of a reconstruction showing grain boundaries. (e) Concentration profile showing  $^{18}\text{O}$  grain boundary segregation in the region marked in (f).

deposit  $\text{Al}_{0.44}\text{Ti}_{0.33}\text{Cr}_{0.23}\text{N}$  and  $\text{Al}_{0.47}\text{Ti}_{0.32}\text{Cr}_{0.21}\text{N}$  coating, respectively. D-SIMS depth profiles were then carried out on the oxidized coatings and reported in Fig. 13. The difference in composition do not change the layers that composed the oxide but the coatings have different oxidation kinetics as depicted by the different SIMS sputtering time needed to go through the whole oxide thickness. So, the total oxide thickness is smaller for the coating containing the lower Ti/Al<sub>(40/60)</sub> ratio (Fig. 13b). If we can clearly say that the increase of the aluminum content in the

nitride coating decreases its oxidation kinetics at 950 °C, it is not possible to associate this results to one particular oxide layer and also, to a different for the composition of chromium-aluminum oxide layer as the Cr/Al ratio are almost the same for both oxidized coatings (Fig. 13a and b). The normalized D-SIMS profiles for  $\text{Al}_{0.45}\text{Ti}_{0.29}\text{Cr}_{0.26}\text{N}$  and  $\text{Al}_{0.54}\text{Ti}_{0.34}\text{Cr}_{0.12}\text{N}$  oxidized coatings on Fig. 13d and c show the impact of Cr content addition in the TiAlCrN coatings studied. The evolution of the two oxidized regions present similar trend of intensity profile.



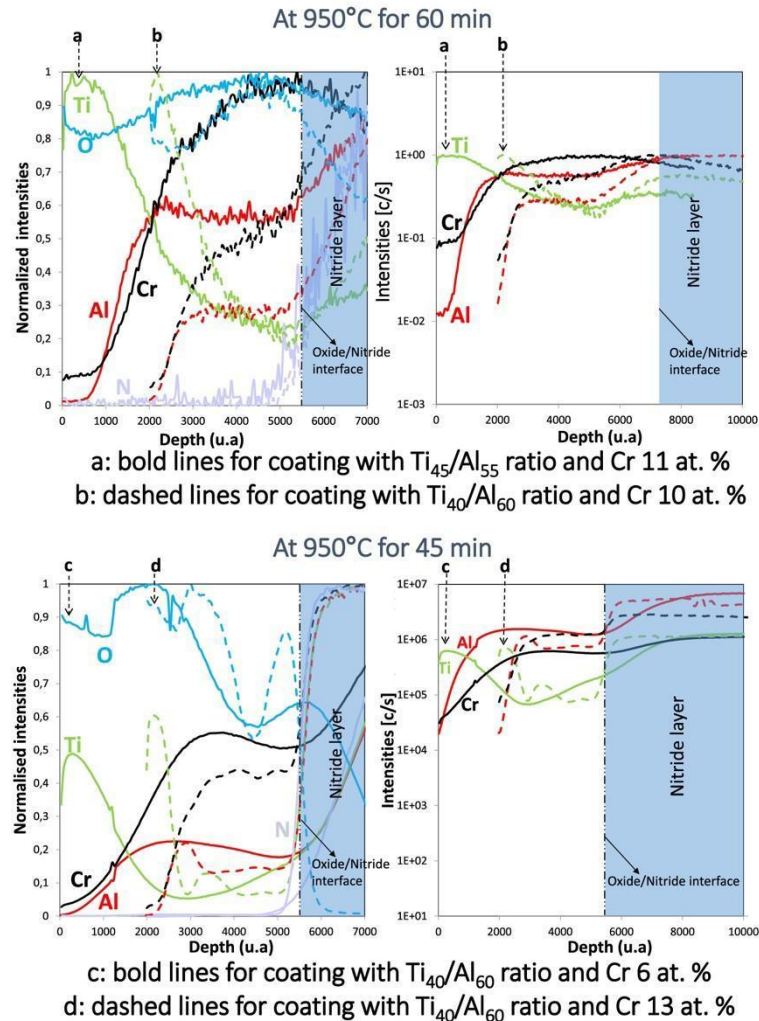


**Fig. 13.** D-SIMS depth profiles of  $\text{Al}_{0.44}\text{Ti}_{0.33}\text{Cr}_{0.23}\text{N}$  and  $\text{Al}_{0.47}\text{Ti}_{0.32}\text{Cr}_{0.21}\text{N}$  oxidized at 950 °C for 60 min (top left: normalized intensities and top right: intensities in c/s) and  $\text{Al}_{0.45}\text{Ti}_{0.29}\text{Cr}_{0.26}\text{N}$  and  $\text{Al}_{0.54}\text{Ti}_{0.34}\text{Cr}_{0.12}\text{N}$  oxidized at 950 °C for 45 min (at the bottom left: normalized intensities and at the bottom right: intensities in c/s).

However, the thickness of both Ti oxide and Al-rich oxide decreases with a higher addition of Cr content in the coating as well as the thickness of the mixed CrAl-oxide. The intensities recorded for the Cr and Al elements can indicate that the level of chromium increases in the mixed Cr-Al oxide when its content is higher in the coating (Fig. 13d). It is clear that Cr addition increases the oxidation resistance of the AlTiN coatings.

#### 4. Conclusions

TiAlCrN coatings have been synthesized by codeposition with a hybrid process using dcMS and HiPIMS to investigate the structural phase stability of AlTiCrN coatings and to determine the growth oxidation mechanism at high temperature, 950 °C. As-deposited AlTiCrN coating shows a micro-columnar structure without macro particle defects and with typical single-phase cubic structure and a main

orientation, (111). The mechanical measurements at the coating surface show that Cr content can stabilize the hardness and the elastic modulus independently of the Al/Ti ratio with an elastic modulus of  $\approx 500$  GPa and the hardness in the range of 33 GPa. The AlTiCrN coating keep the single-phase cubic structure up to 950 °C without any segregation, precipitation, or coarsening. The oxidation growth of the coating was followed between 30 °C and 950 °C by XRD. The tetragonal  $\text{TiO}_2$ -rutile phase is identified at 700 °C and the rhombohedral  $(\text{Cr}_x\text{Al}_y)_2\text{O}_3$  phase detected at 800 °C. Furthermore, at 950 °C, the first evidence of a  $\text{Al}_2\text{O}_3$  phase was detected. Transmission electron microscopy cross-section observations after an isothermal oxidation at 950 °C, have shown that the gradient  $(\text{Cr}_x\text{Al}_y)_2\text{O}_3$  layer is very rich in aluminum under the  $\text{TiO}_2$  layer and richer in chromium at the nitride-oxide interphase, the presence of Cr decreasing the oxide grain size. Depth oxide profile analyses by Secondary Ion Mass Spectrometry, completed by Atom Probe

Tomography were also performed on these oxidized coatings after different sequential steps of  $^{18}\text{O}_2$  with  $^{16}\text{O}_2$  at 950 °C. From all these collected data, hypothesis are proposed where the oxidation mechanism is controlled by the cationic diffusion of oxygen to the oxide-coating interface and by the anionic grain-boundary diffusion of titanium at the external surface as well as because of a higher oxygen pressure generated by the inward diffusion of this species at the grain boundaries, chromium volatile species can be produced. Thanks to APT results in the mixed aluminum-chromium oxide scale, grain boundary segregations are depicted and can confirm an outward diffusion of titanium for the development of the  $\text{TiO}_2$  top oxide layer and an inward oxygen diffusion to drive the oxidation kinetic of this coating at the interface between the oxide and the nitride. At the end, a complementary study where the influence of the Al/Ti ratio and the Cr content on the oxidation and thermal resistances at 950 °C for these AlTiCrN nitride alloy coatings is adding.

#### CRediT authorship contribution statement

**M.-R. Alhafian:** Conceptualization, Methodology, Investigation, Design of experiments, Writing – original draft, Writing – review, editing & submission. **J.-B. Chemin:** PVD set up, and review. **N. Valle:** SIMS measurements, Isotopic oxidation, Scientific discussion, Writing – review and editing. **B. El Adib:** SIMS measurements, Isotopic oxidation, and Scientific discussion. **M. Penoy:** Fiber texture and Stress measurements validation. **L. Bourgeois:** Scientific discussion, Mechanical properties Validation, and review. **J. Ghanbaja:** TEM analysis, and Scientific discussion. **J. Barrirero:** APT sample preparation, Reconstruction and analysis, Scientific discussion, and review. **F. Soldera:** Scientific discussion, and Final revision. **F. Mücklich:** Scientific discussion. **P. Choquet:** Conceptualization, Investigation, Supervision, Writing – review & editing, Project administration, and Funding acquisition.

#### Declaration of Competing Interest

The authors declare that they have no known competing financial interests or personal relationships that could have appeared to influence the work reported in this paper.

#### Data availability

The raw/processed data required to reproduce these findings cannot be shared at this time as the data also forms part of an ongoing study.

#### Acknowledgment

The authors acknowledge discussions with Dr. Y. Fleming (Luxembourg Institute of Science and Technology) for their analysis and contributions relating to XRD-diffraction results. The authors acknowledge S. Migot and Dr. H. Kabbara (Institute Jean Lamour, France) for the preparation of FIB-lamellae. The authors gratefully acknowledge the funding support that was received from the Luxembourg National Research Fund (FNR) under the CORE PPP project, NANOPIMS, funding for innovation and industry partnerships (C-PPP17/MS/11622578). The authors are also thankful to PULSATEC project and the European Doctoral Program in Advanced Materials Science and Engineering (DocMASE).

#### Appendix A. Supporting information

Supplementary data associated with this article can be found in the online version at doi:10.1016/j.corsci.2022.110226.

#### References

- [1] Wolf-Dieter Münz, Titanium aluminum nitride films: A new alternative to TiN coatings. *J. Vac. Sci. Technol. A: Vac. Surf., Films* 4 (6) (1986) 2717–2725.
- [2] Siegfried Hofmann, A.John Hermann, Selective oxidation and chemical state of Al and Ti in (Ti, Al) N coatings. *Surf. Interface Anal.* 12 (6) (1988) 329–333.
- [3] D. McIntyre, et al., Oxidation of metastable single-phase polycrystalline TiO. 5AlO. 5N films: Kinetics and mechanisms. *J. Appl. Phys.* 67 (3) (1990) 1542–1553.
- [4] Chung Wan Kim, Kwang Ho Kim, Anti-oxidation properties of TiAlN film prepared by plasma-assisted chemical vapor deposition and roles of Al. *Thin Solid Films* 307 (1–2) (1997) 113–119.
- [5] Yahya Dogu, Ersan Aslan, Necip Camucu, A numerical model to determine temperature distribution in orthogonal metal cutting. *J. Mater. Process. Technol.* 171 (1) (2006) 1–9.
- [6] O. Knotek, M. Böhmer, Tw Leyendecker, On structure and properties of sputtered Ti and Al based hard compound films. *J. Vac. Sci. Technol. A: Vac. Surf. Films* 4 (6) (1986) 2695–2700.
- [7] T. Leyendecker, et al., The development of the PVD coating TiAlN as a commercial coating for cutting tools. *Surf. Coat. Technol.* 48 (2) (1991) 175–178.
- [8] T. Nojit, P. Visuttipitukul, K. Taweepup, Thermal oxidation resistance of quaternary TiAlCrN coatings prepared with cathodic arc evaporation. *J. Aust. Ceram. Soc.* 574 (57) (2021) 1209–1218, <https://doi.org/10.1007/s41779-021-00617-X>.
- [9] A. Hemmati, J. Paiva, S.C. Veldhuis, Thermal stability and machining performance of arc evaporated Ti1-xAlxN hard PVD coatings with x=0.5–0.73 ratios using an integrative approach. *Materialia* 17 (2021), 101132, <https://doi.org/10.1016/j.mtl.2021.101132>.
- [10] Atul P. Kulkarni, G.Joshi Girish, G.Sargade Vikas, Dry turning of AISI 304 austenitic stainless steel using AlTiCrN coated insert produced by HPPMS technique. *Procedia Eng.* 64 (2013) 737–746.
- [11] V. Kouznetsov, K. Macák, J.M. Schneider, U. Helmersson, I. Petrov, A novel pulsed magnetron sputter technique utilizing very high target power densities. *Surf. Coat. Technol.* 122 (1999) 290–293.
- [12] L. Zauner, P. Ertelthaler, T. Wojcik, H. Bolvardi, S. Kolozsvári, P.H. Mayrhofer, H. Riedl, Reactive HiPIMS deposition of Ti-Al-N: influence of the deposition parameters on the cubic to hexagonal phase transition. *Surf. Coat. Technol.* 382 (2020), 125007.
- [13] M.-R. Alhafian, J.-B. Chemin, Y. Fleming, L. Bourgeois, M. Penoy, R. Useldinger, F. Soldera, F. Mücklich, P. Choquet, Comparison on the structural, mechanical and tribological properties of TiAlN coatings deposited by HiPIMS and cathodic arc evaporation. *Surf. Coat. Technol.* 423 (2021), 127529, <https://doi.org/10.1016/j.surfcoat.2021.127529>.
- [14] G. Greczynski, J. Lu, M. Johansson, J. Jensen, I. Petrov, J.E. Greene, L. Hultman, Selection of metal ion irradiation for controlling Ti1-xAlxN alloy growth via hybrid HiPIMS/magnetron co-sputtering. *Vacuum* 86 (2012) 1036–1040.
- [15] Xing-Zhao Ding, X.T. Zeng, Structural, mechanical and tribological properties of CrAlN coatings deposited by reactive unbalanced magnetron sputtering. *Surf. Coat. Technol.* 200 (5–6) (2005) 1372–1376.
- [16] Huddedar, S., et al. Microstructure and mechanical properties of AlTiCrN, AlCrN coatings deposited by cathodic arc evaporation (PVD) technique. In: *Proceedings of the 21st International Conference on Processing and Fabrication of Advanced Materials*. Vol. 1. 2012.
- [17] Harish C. Barshilia, et al., Nanolayered multilayer coatings of CrN/CrAlN prepared by reactive DC magnetron sputtering. *Appl. Surf. Sci.* 253 (11) (2007) 5076–5083.
- [18] A. Hörling, L. Hultman, M. Odén, J. Sjölen, L. Karlsson, Mechanical properties and machining performance of Ti1-xAlxN-coated cutting tools. *Surf. Coat. Technol.* 191 (2–3) (2005) 384–392.
- [19] D.-F. Li, The effects of aluminium composition on the mechanical properties of reactivity sputtered TiAlN films. *J. Mater. Sci.* 33 (8) (1998) 2137–2145.
- [20] Herbert Willmann, et al., Hardness evolution of Al-Cr-N coatings under thermal load. *J. Mater. Res.* 23 (11) (2008) 2880–2885.
- [21] K. Yamamoto, et al., Properties of (Ti, Cr, Al) N coatings with high Al content deposited by new plasma enhanced arc-cathode. *Surf. Coat. Technol.* 174 (2003) 620–626.
- [22] Rikard Forsén, et al., Effects of Ti alloying of AlCrN coatings on thermal stability and oxidation resistance. *Thin Solid Films* 534 (2013) 394–402.
- [23] Yuxiang Xu, et al., Influence of Ti on the mechanical properties, thermal stability and oxidation resistance of Al-Cr-N coatings. *Vacuum* 120 (2015) 127–131.
- [24] Y.X. Xu, H. Riedl, D. Holec, L. Chen, Y. Du, P.H. Mayrhofer, Thermal stability and oxidation resistance of sputtered TiAlCrN hard coatings. *Surf. Coat. Technol.* 324 (2017) 48–56.
- [25] M. Danek, et al., Influence of Cr additions on the structure and oxidation resistance of multilayered TiAlCrN films. *Surf. Coat. Technol.* 313 (2017) 158–167.
- [26] L.A. Donohue, et al., Microstructure and oxidation-resistance of Ti1-x-y-zAlxCrYzN layers grown by combined steered-arc/unbalanced-magnetron-sputter deposition. *Surf. Coat. Technol.* 94 (1997) 226–231.
- [27] Raúl A. Baragiola, Sputtering: survey of observations and derived principles. *Philos. Trans. R. Soc. Lond. Ser. A: Math., Phys. Eng. Sci.* 362 (1814) (2003) 29–53.
- [28] U. Wetzel, J. Ligot, P. Lamparter, A.C. Vermeulen, E.J. Mittemeijer, Stress analysis of polycrystalline thin films and surface regions by X-ray diffraction. *J. Appl. Crystallogr.* 38 (2005) 1–29 (ISSN 0021-8898).
- [29] [https://web.stanford.edu/group/glam/xlab/MatSci162\\_172/LectureNotes/06\\_Stress&Texture.pdf](https://web.stanford.edu/group/glam/xlab/MatSci162_172/LectureNotes/06_Stress&Texture.pdf)
- [30] <https://wiki.anton-paar.com/en/instrumented-indentation-testing-ii/>
- [31] Edzo Zoestbergen, X-Ray Analysis of Protective Coatings, Rijksuniversiteit te Groningen, 2000.

---

M.-R. Alhafian et al.

*Corrosion Science* 201 (2022) 110226

- [32] K. Thompson, D. Lawrence, D.J. Larson, J.D. Olson, T.F. Kelly, B. Gorman, In situ site-specific specimen preparation for atom probe tomography, *Ultramicroscopy* 107 (2007) 131–139, <https://doi.org/10.1016/j.ultramic.2006.06.008>.
- [33] Yin-Yu Chang, Chia-Yuan Hsiao, High temperature oxidation resistance of multicomponent Cr–Ti–Al–Si–N coatings, *Surf. Coat. Technol.* 204 (6–7) (2009) 992–996.
- [34] Federica Bondioli, et al., Reaction mechanism in alumina/chromia (Al<sub>2</sub>O<sub>3</sub>–Cr<sub>2</sub>O<sub>3</sub>) solid solutions obtained by coprecipitation, *J. Am. Ceram. Soc.* 83 (8) (2000) 2036–2040.
- [35] [https://www.asminternational.org/search/-/journal\\_content/56/10192/6382084/DATABASE](https://www.asminternational.org/search/-/journal_content/56/10192/6382084/DATABASE)
- [36] M. Stanislawski, et al., Chromium vaporization from high-temperature alloys. I. Chromia-forming steels and the influence of outer oxide layers, *J. Electrochem. Soc.* 154 (4) (2007) A295.
- [37] H. Kurokawa, C. Jacobson, L. Dejonghe, S. Visco, Chromium vaporization of bare and of coated iron–chromium alloys at 1073 K, *Solid State Ion.* 178 (3–4) (2007) 287–296.
- [38] C. Collins, J. Lucas, T.L. Buchanan, M. Kopezyk, a Kayani, P.E. Gannon, M. C. Deibert, R.J. Smith, D.S. Choi, V.I. Gorokhovskiy, Chromium volatility of coated and uncoated steel interconnects for SOFCs, *Surf. Coat. Technol.* 201 (7) (2006) 4467–4470.
- [39] W. Wongpromrat, Étude de la sublimation du chrome lors de l'oxydation haute température de l'alliage AISI 441 et recherche de solutions de protection (Doctoral dissertation), King Mongkut's Institute of Technology Ladkrabang, 2015.



## A Supplementary material about APT

### A 1 APT sample preparation

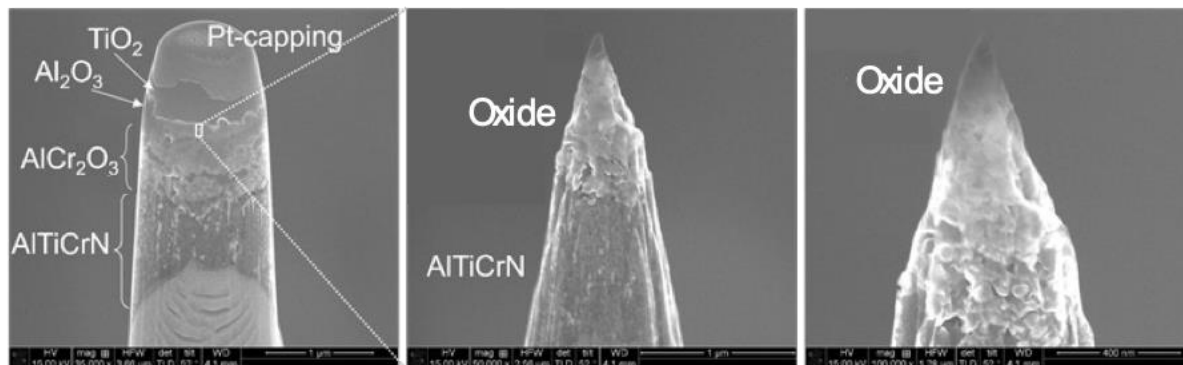


Fig. 14 A: APT specimens were prepared by the lift out technique, and thinned to get the transition region between  $\text{TiO}_2$ ,  $\text{Al}_2\text{O}_3$  and  $(\text{AlCr})_2\text{O}_3$  at the first 100 – 200 nm of the tip. The specimens were thinned with a large shank angle to avoid thermal tails in the mass spectrum.

### A 2 Determination of compositions by APT

The sample analysed by APT in this study is composed of  $\text{Ti}_2\text{O}$ ,  $\text{Al}_2\text{O}_3$  and  $(\text{AlCr})_2\text{O}_3$  oxides. The mass-spectrum for the complete reconstructions contain a large number of peaks and several overlaps (see Table I). Peak overlaps are normally solved by the implementation of a peak deconvolution algorithm in IVAS software. However, in this case the oxidation was performed with isotopic sequence artificially enriched in  $^{18}\text{O}_2$  isotope, that changes the natural abundance ratios not only of the oxygen peaks in the mass spectrum, but also of evaporated compound ions involving oxygen. For this reason, the use of the peak deconvolution algorithm was not possible.

Instead of that, to minimize peak overlaps, the regions involving each of the three oxides were separately exported and analysed. Most of the overlaps were solved in this way. Figure 15 shows an example of the mass spectra for each oxide region. The overlap of  $^{18}\text{O}^+$  and  $\text{H}_2^{16}\text{O}^+$ , which appears as a contaminant, was disregarded since water molecules appear in general in small amounts in comparison with the oxygen isotope studied (**REF: ASCHAUER 2021**). The overlap at 16 [Da] between  $^{16}\text{O}^+$  and  $\text{Ti}^{3+}$  only played a role in the Ti-rich oxide and even in this region most of the Ti evaporated as  $\text{Ti}^{+2}$  and  $\text{TiO}^+$ . Figure 15(B) confirms that  $\text{Ti}^{+3}$  isotope-peaks at 15.3 [Da] and 15.6 [Da] barely pass over the

background line. Considering the aforementioned shortcomings in the implementation of a peak-deconvolution algorithm, the APT analysis in the present work focuses on the objective of differentiating the oxide regions and identifying / assigning the different oxygen isotopes to the oxide layers. Table II shows the APT compositional quantification of each oxide showing that  $^{16}\text{O}$  is primarily present in Ti- and Cr-rich regions, while  $^{18}\text{O}$  is mostly found in the Al-oxide. A deviation of the overall compositions of about 2-5% cannot be excluded.

Table I: Peaks' assignment and overlaps

Mass-to-charge ratios [Da]						
8	$^{16}\text{O}^{++}$			43	$\text{Al}^{16}\text{O}^+$	$\text{Al}_2^{16}\text{O}_2^{++}$
9	$\text{Al}^{+++}$			43.5	$\text{Al}_2\text{O}_2^{++}$	$\text{CrO}_2^{++}$
13.5	$\text{Al}^{++}$			44	$\text{AlO}^+$	
16	$^{16}\text{O}^+$			44.5	$\text{AlO}^+$	$\text{Al}_2\text{O}_2^{++}$
17	$^{17}\text{O}^+$	$\text{OH}^+$		45	$\text{Al}^{18}\text{O}^+$	$\text{Al}_2^{18}\text{O}_2^{++}$
18	$^{18}\text{O}^+$			52	$\text{Cr}^+$	
21.5	$\text{Al}^{16}\text{O}^{++}$			59	$\text{Al}^{16}\text{O}_2^+$	
22	$\text{AlO}^{++}$			60	$\text{AlO}_2^+$	
22.5	$\text{Al}^{18}\text{O}^{++}$			61	$\text{AlO}_2^+$	
23	$\text{Ti}^{++}$			62	$\text{TiO}^+$	
23.3	$\text{Al}_2^{16}\text{O}^{+++}$			63	$\text{TiO}^+$	$\text{Al}^{18}\text{O}_2^+$
23.5	$\text{Ti}^{++}$			64	$\text{TiO}^+$	
24	$\text{Al}_2^{18}\text{O}^{+++}$	$\text{Ti}^{++}$		65	$\text{TiO}^+$	
24.5	$\text{Ti}^{++}$			66	$\text{CrO}^+$	$\text{TiO}^+$
25	$\text{Cr}^{++}$	$\text{Ti}^{++}$		68	$\text{CrO}^+$	
26	$\text{Cr}^{++}$			69	$\text{CrO}^+$	
26.5	$\text{Cr}^{++}$			70	$\text{Al}_2\text{O}^+$	$\text{CrO}^+$
27	$\text{Al}^+$	$\text{Cr}^{++}$		71	$\text{Al}_2\text{O}^+$	
28.6	$\text{Al}_2^{16}\text{O}_2^{+++}$			78	$\text{TiO}_2^+$	
29.3	$\text{Al}_2\text{O}_2^{+++}$			79	$\text{TiO}_2^+$	
30	$\text{Al}_2^{18}\text{O}_2^{+++}$			80	$\text{TiO}_2^+$	
31	$\text{TiO}^{++}$			81	$\text{TiO}_2^+$	
31.5	$\text{TiO}^{++}$			82	$\text{CrO}_2^+$	$\text{TiO}_2^+$
32	$^{16}\text{O}_2^+$	$\text{TiO}^{++}$		84	$\text{CrO}_2^+$	
32.5	$\text{TiO}^{++}$			85	$\text{CrO}_2^+$	
33	$\text{CrO}^{++}$	$\text{TiO}^{++}$		86	$\text{Al}_2\text{O}_2^+$	$\text{CrO}_2^+$
33.5	$\text{TiO}^{++}$			87	$\text{Al}_2\text{O}_2^+$	
34	$\text{CrO}^{++}$			88	$\text{Al}_2\text{O}_2^+$	
34.5	$\text{CrO}^{++}$			96	$\text{TiO}_3^+$	



35	$\text{Al}_2^{16}\text{O}^{++}$	$\text{CrO}^{++}$	98	$\text{CrO}_3^+$	
35.5	$\text{Al}_2^{16}\text{O}^{++}$		100	$\text{CrO}_3^+$	
36	$^{18}\text{O}_2^+$	$\text{Al}_2^{18}\text{O}^{++}$	101	$\text{CrO}_3^+$	
41	$\text{CrO}_2^{++}$		102	$\text{Al}_2\text{O}_3^+$	$\text{CrO}_3^+$
42	$\text{CrO}_2^{++}$		103	$\text{Al}_2\text{O}_3^+$	
42.5	$\text{CrO}_2^{++}$		104	$\text{Al}_2\text{O}_3^+$	

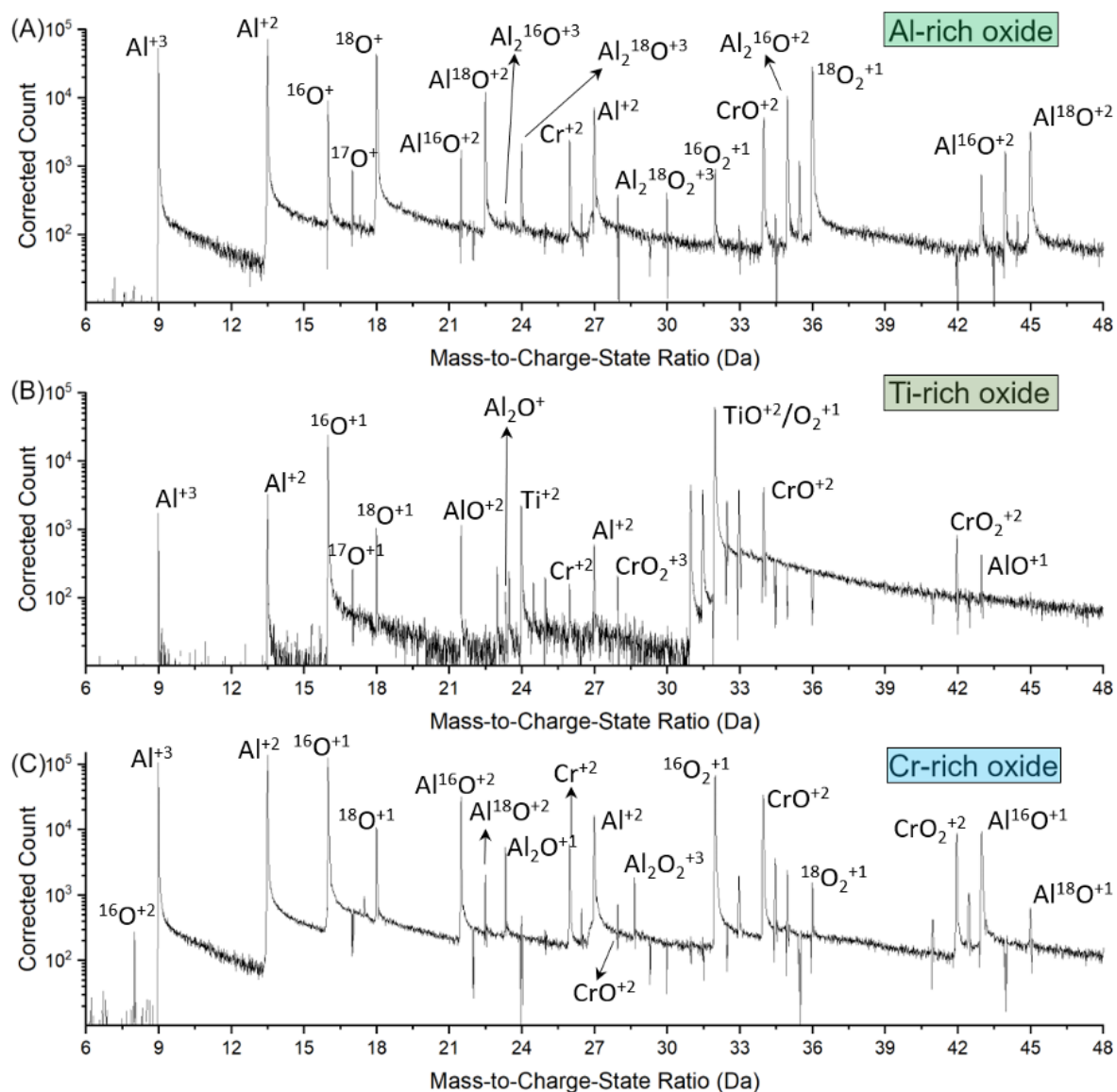


Fig. 15: Mass spectra of the three oxide regions separately. A zoom in of the Spectra between 6 and 48 Da is shown to highlight the difference between the spectra in the region with the highest number of peaks.

Table II: Composition of the three oxide regions by APT.

	Ti	Al	Cr	$^{16}\text{O}$	$^{18}\text{O}$	$^{16}\text{O}+^{18}\text{O}$
$\text{Al}_2\text{O}_3$	--	42.4	3.3	13.5	40.9	54.4
$\text{Ti}_2\text{O}$	39.2	2.2	3.4	54.8	0.4	55.2
$(\text{Al,Cr})_2\text{O}_3$	0.1	29.2	12.7	56.0	2.1	58.1

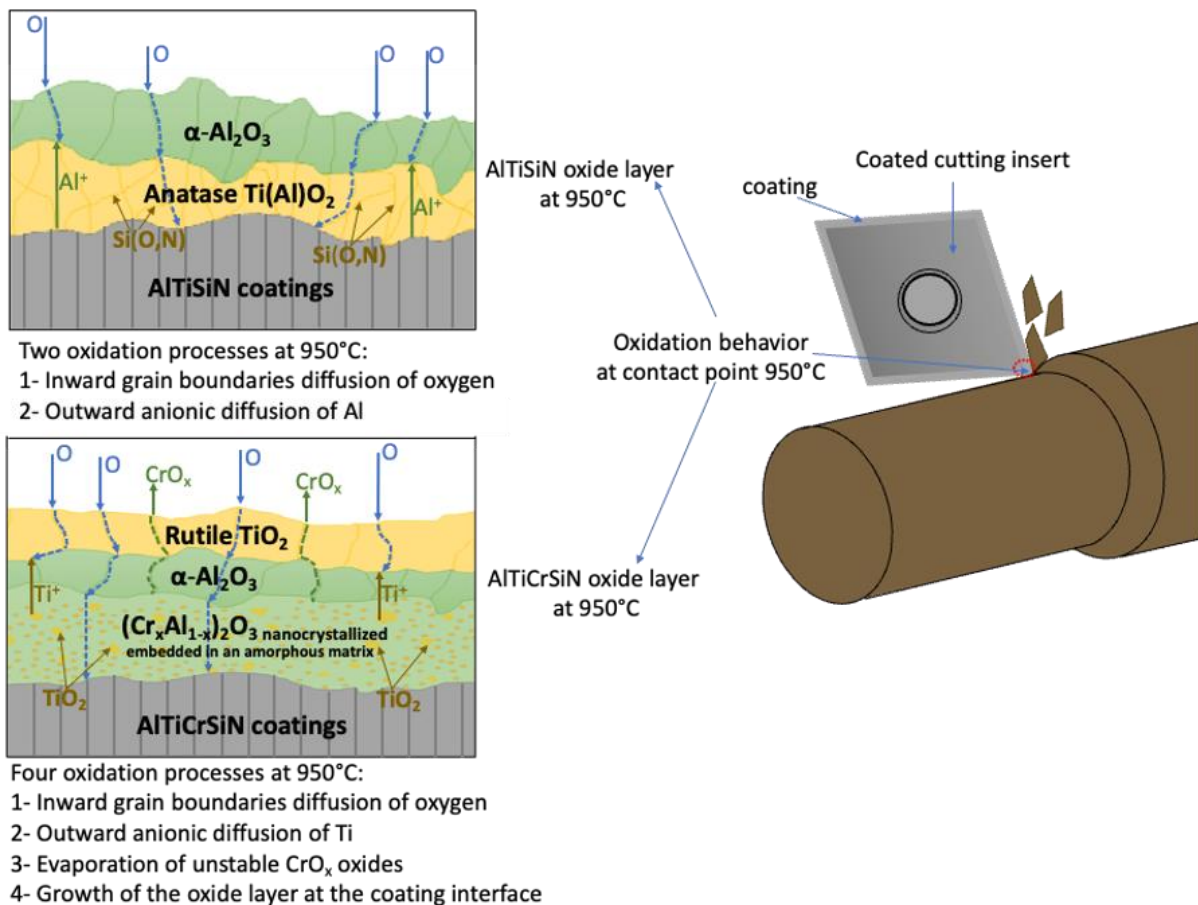


## 7.3 Paper III.

## Influence of Si addition on the phase structure and oxidation behavior of PVD AlTiN and AlTiCrN coatings using high-resolution characterization techniques

Author(s):

M-R. Alhafian, N. Valle, J-B. Chemin, L. Bourgeois, M. Penoy, R. Useldinger, J. Ghanbaja, F. Mücklich, and P. Choquet





Contents lists available at ScienceDirect

Journal of Alloys and Compounds

journal homepage: [www.elsevier.com/locate/jalcom](http://www.elsevier.com/locate/jalcom)

## Influence of Si addition on the phase structure and oxidation behavior of PVD AlTiN and AlTiCrN coatings using high-resolution characterization techniques

M.-R. Alhafian<sup>a,\*</sup>, N. Valle<sup>a</sup>, J.-B. Chemin<sup>a</sup>, L. Bourgeois<sup>b</sup>, M. Penoy<sup>b</sup>, R. Useldinger<sup>b</sup>, J. Ghanbaja<sup>c</sup>, F. Mücklich<sup>d</sup>, P. Choquet<sup>a,\*</sup>

<sup>a</sup> Luxembourg Institute of Science and Technology, 41 rue du Brill, L-4422 Belvaux, Luxembourg

<sup>b</sup> Ceratizit Luxembourg S.à.r.l., 101 route de Holzen, L-8232 Mamer, Luxembourg

<sup>c</sup> Univ Lorraine, CNRS, Inst Jean Lamour, UMR7198, F-54011 Nancy, France

<sup>d</sup> Saarland University, Chair of Functional Materials, Campus D3.3, Saarbrücken 66123, Germany

### ARTICLE INFO

#### Keywords:

AlTiSiN - AlTiCrSiN PVD coatings  
Micromechanical properties  
O<sup>18</sup> isotopic oxidation labelling  
Transmission Electron Microscopy (TEM)  
Dynamic-Secondary Ion Mass Spectrometry (D-SIMS)  
Atom Probe Tomography (APT)

### ABSTRACT

The influence of Si concentrations on AlTiN and AlTiCrN coatings deposited by PVD has been investigated by using high-resolution characterization techniques: TEM, Dynamic SIMS, Atom Probe Tomography (APT) analyses and nano hardness measurements. First, investigations focus on crystallographic phase stability, microstructural observations and micromechanical studies to understand the effect of the Si addition on these two nitride coatings. Second, the oxidation mechanisms and the kinetics of oxide growth at 950 °C for various durations are examined. Results indicate that the addition of Si introduces high compressive stresses in both coating groups, reaching values in the range of – 6 GPa. However, the behavior of Si content differs for AlTiN coatings with and without chromium. In AlTiSiN coatings, increasing Si addition leads to reduce residual stresses, while no significant change is observed for AlTiCrSiN coatings. This stress evolution is associated with a decrease in crystallinity density of the TiAlN coatings due to Si addition, but this structural phenomenon is not observed when Si is added to the quaternary metallic coatings TiAlCrN. Si content also influences the nanohardness, but the variation among coating is not substantial, with values around 34 +/– 2 GPa, and an elastic-modulus around 443 +/– 40 GPa. Regarding oxidation resistance at 950 °C, the addition of Si in AlTiN coating results in the formation of an external alumina oxide layer and beneath it, a nanometer sized TiO<sub>2</sub> anatase crystallites layer. After the growth of this bi-layer oxide scale, the inward cationic diffusion of the oxygen is very significantly reduced, and it can explain its high oxidation resistance. In contrast, for AlTiCrSiN coatings, the oxide scale morphology is different, consisting of a pure TiO<sub>2</sub> rutile outer layer, followed by an Al-rich oxide and a mixed oxide region of (AlCr)<sub>2</sub>O<sub>3</sub> with small islands of TiO<sub>2</sub>. The growth of this last oxide scale shows a regular increase over time, primarily driven by inward oxygen diffusion at the nitride coating interface.

### 1. Introduction

The need of continuous performance increases of hard nitride coatings for industrial tool applications still demands further

improvements of their mechanical properties and oxidation resistance, particularly in the field of dry high-speed cutting technology. For example, the surface temperatures of TiAlN cutting tools during dry turning tests for the machining of stainless-steel pieces were measured

**Abbreviations:** HIPIMS, High-Power Impulse Magnetron Sputtering; dcMS, direct-current Magnetron Sputtering; FE-SEM, Field-Emission Scanning Electron Microscope; EDS, Energy Dispersive X-ray Spectrometer; TEM, Transmission Electron Microscopy; SAED, Selected Area Electron Diffraction patterns; HRTEM, High Resolution Transmission Electron Microscopy; APT, Atom Probe Tomography; D-SIMS, Dynamic Secondary Ion Mass Spectrometry.

\* Correspondence to: Luxembourg Institute of Science and Technology (LIST), Maison des Matériaux, 5 Avenue des Hauts-Fourneaux, 4362 Esch-Sur-Alzette, Luxembourg.

E-mail addresses: [r.alhafian@gmail.com](mailto:r.alhafian@gmail.com) (M.-R. Alhafian), [patrick.choquet@list.lu](mailto:patrick.choquet@list.lu) (P. Choquet).

<sup>1</sup> ORCID: 0000-0003-0305-3952

<sup>2</sup> ORCID: 0000-0001-8696-5812

<https://doi.org/10.1016/j.jalcom.2023.171800>

Received 29 May 2023; Received in revised form 28 July 2023; Accepted 16 August 2023

Available online 29 August 2023

0925-8388/© 2023 Elsevier B.V. All rights reserved.



between 700 and 1100 °C for the following cutting parameters: cutting speed between 90 and 250 m/min, depth of the cut 0.25 mm and feed rate 0.20 mm/rev [1]. When the coated cutting tools are subjected to these elevated temperatures, an increase of its oxidation and wear resistance is required for enhancing the lifetime of these cutting and forming tools [2–5]. One of the most successful ways for improving the oxidation resistance in the titanium nitride-based coatings is to alloy TiN with different elements, such as Al, Cr, and Si (systems TiAlN, TiCrN, TiSiN [6–9]). TiAlN is now a widely used coating for high-speed machining applications. Aluminum alloying shows an efficient improvement behavior against oxidation by forming a protective  $\alpha$ -Al<sub>2</sub>O<sub>3</sub> outer-layer and a porous TiO<sub>2</sub> sub-layer at 850 °C [10]. However, there is maximum Al content to conserve the cubic structure for TiAlN coatings. In the literature, the reported limit for conserving the structure for a Ti<sub>1-x</sub>Al<sub>x</sub>N composition is when x is equal or below 0.67 [11]. Higher x values lead to a degradation of the coating's mechanical properties due to the loss of the cubic structure [10]. However, it is also known that the oxidation degradation process for Ti<sub>1-x</sub>Al<sub>x</sub>N with x = 0.67 occurs already at 850 °C in air. This is a rather low value, considering the current working surface temperatures for dry high-speed cutting tools (up to 950 °C). Chromium is also a metallic element which can improve the oxidation resistance of titanium nitride coatings. The protective behavior for TiCrN coating was recorded at 850 °C by forming Cr<sub>2</sub>O<sub>3</sub> and TiO<sub>2</sub> oxide layers [12]. Moreover, the addition of Cr can also improve the oxidation resistance and the tribological performances of ternary cubic TiAlN alloy coatings. Different publications have already reported the thermal and oxidation properties of TiAlCrN coatings at temperature up to 950 °C [13–15]. According to our recent studies, particularly in the case of AlTiCrN coatings, it is worthwhile to note that the oxidation resistance in AlTiCrN coatings depends on both the Al/Ti or Cr/Ti alloying ratios [16]. Also, a further increase of the Al or Cr content can also lead to the dissociation of the solid solution cubic structure to a mix with cubic and hexagonal structure [17,18]. Consequently, to achieve optimal performance at high temperatures, precise control of the Al and Cr contents in TiAlCrN coatings is essential. Tribological tests have demonstrated that the composition of TiAlCrN coatings needs to be adjusted for each machining test, considering the heat-resistance of the working material. The addition of a fourth metallic element to the composition of titanium nitride coating can be a way for further improving the high temperature performances of these titanium nitride coatings.

Silicon proves to be an interesting alloying element to increase the oxidation resistance and the mechanical properties [19]. Previously published works have reported significantly better oxidation resistance of Si-containing coatings compared to the ones without Si [20–22]. For example, TiSiN coatings show a nano-composite structure, consisting of TiN nano-crystallites embedded in a thin amorphous SiN<sub>x</sub> matrix at the grain boundaries. During the oxidation, a SiO<sub>2</sub> layer is formed, which limits the diffusion of oxygen and increases the oxidation resistance [23–25]. Recently, the TiAlSiN nano-composite coatings have attracted a lot of interest from the scientific community because of its low thermal conductivity and its excellent oxidation resistance [26,27]. In the TiAlSiN coating structure, Al atoms substitute the Ti atoms in the TiN lattice and Si atoms are present with nitride atoms by incorporation either as a substitutional solid solution into TiAlN lattice or via the formation of a separate amorphous Si<sub>3</sub>N<sub>4</sub> phase surrounding a nano-crystalline TiAlN. Besides, a number of papers have demonstrated the benefit of Si addition to TiAlN coatings for a good oxidation resistance, thermal stability and mechanical properties.

Until now, very limited works have been dedicated to study the high temperature behavior of AlTiCrSiN coatings. For instance, Bobzin, K., et al. studied the thermal and mechanical loads of (TiAlCrSi)N and (TiAlCrSi)ON during milling tests. They reported a fine crystalline morphology with a cubic structure for both coatings and good oxidation resistance up to 900 °C. The nitride coating showed an increase of tool life by 10% compared to the oxynitride coating. These observations are

attributed to the high aluminum/titanium ratio (1.35) in (TiAlCrSi)N coating [28]. Huang, J., et al. reported the oxidation resistance for CrTiAlSiN Arc coatings at 900 °C in air for 2 h, where the TiO<sub>2</sub> region followed by a mixed Al<sub>2</sub>O<sub>3</sub> and Cr<sub>2</sub>O<sub>3</sub> regions were formed. They assumed that the titanium top surface oxide was formed by outward cationic diffusion through the cracks, which is observed in the mixed oxide regions [29]. However, to the best knowledge of the authors, the optimization of the AlTiCrSiN coating composition produced by High Power Impulse Magnetron Sputtering (HiPIMS) to increase their high temperature performance at 950 °C has not yet been adequately studied to date.

Therefore, this paper compares the effects of Si addition on both AlTiN and AlTiCrN coatings in their as-deposited state at 450 °C and describes the coating stability and thermal behavior at 950 °C over different durations. Both titanium nitride-based coatings were synthesized by using a co-deposition system where HiPIMS is used to deposit the Ti, Al and Cr elements and direct current Magnetron Sputtering (dcMS) process to tune the Si content. X-Ray Diffraction (XRD) analysis and Scanning Electron Microscopy (SEM) observations were used to detail the influence of different silicon contents on the coating's structure and morphology. The hardness and the E-modulus of films were measured by a nano-indentation test. The corresponding effect of Si addition on the oxidation resistance at 950 °C and the morphology of the oxide layers were also revealed by High-Resolution Transmission Electron Microscopy (HR-TEM). Moreover, Dynamic-Secondary Ion Mass Spectrometry (D-SIMS) and Atom Probe Tomography (APT) were used to further identify the growth mechanisms of the oxide layers at 950 °C using sequence steps of <sup>16</sup>O<sub>2</sub> and the isotope <sup>18</sup>O<sub>2</sub> gas with different durations.

## 2. Experimental methods

All AlTiSiN and AlTiCrSiN coatings with different Si contents were deposited onto mechanically polished WC–Co (carbide) plane disc with chemical composition of Co = 5.8 wt% and (Ti Ta Nb)C = 7.4 wt%, they were used as coated substrates for the hardness, E-modulus and the stress measurements. The same coatings were also deposited onto mirror-polished silicon wafers with crystal orientation of 100 ± 0.5° and 1 mm thickness. These coated substrates were used for thermal testing and analytical characterizations. Prior to the deposition, all substrates were ultrasonically cleaned using an ethanol bath for five minutes.

The coatings were carried out by dcMS and HiPIMS technologies in a PVD coating machine comprising three circular cathodes C<sub>1</sub>, C<sub>2</sub> and C<sub>3</sub>, each of which having a diameter of four inches. In addition, one more Ti rectangular cathode with a surface of 500 cm<sup>2</sup> was used for the deposition of a TiN interlayer. The cathode to substrate distance was 120 mm. To avoid a variation in coating composition and to ensure a uniform coating thickness, the deposition was initiated by switching left and right the substrate holder positioned in front of the cathodes with a moving speed of 5 rpm and for 70°. A schematic diagram of the dcMS and HiPIMS coating system is shown in Fig. 1.

The deposition procedure was as follows. After loading the samples, the vacuum chamber was evacuated to a base pressure of 10<sup>-6</sup> mbar and then, the substrate holder was preheated to 450 °C. The substrate temperature was controlled by a calibrated thermocouple directly mounted behind the sample's holder. Following these two steps, the substrates were subjected to plasma etching with Ar ion bombardment using three microwave antennas and a DC bias of – 200 V for 30 min to remove any surface contaminants and do an activation of the substrates. Furthermore, in order to avoid any oxidation contaminants in the coatings coming from the targets, they were sputter cleaned for 10 min. Before coating, a mixture of 50 sccm high purity argon (99.999%) and 22 sccm nitrogen (99.999%) gas were injected, producing a working pressure of 5 × 10<sup>-3</sup> mbar. This nitrogen (N<sub>2</sub>) gas flow was determined via a target poisoning study by investigating the variation of the target voltage as a function of the total gas mixture flow rates, to allow sputtering in the

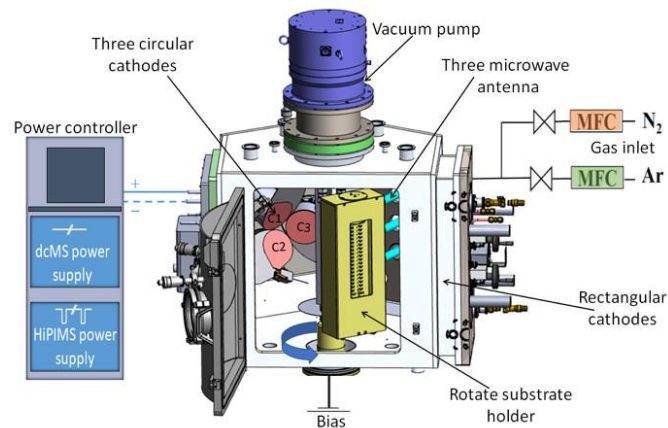


Fig. 1. Schematic view of the co-sputtering PVD coater machine.

compound mode and to reach stoichiometric nitride coatings [30]. The deposition process began when the substrates were in front of the Ti rectangular target, where the deposition of a 0.5  $\mu\text{m}$ -thick TiN interlayer was carried out in dcMS mode. This interlayer is used to improve the coating adhesion.

Two Ti based target compositions were afterwards sequentially used to elaborate the TiAl alloy nitride coatings:  $\text{Ti}_{50}\text{Al}_{50}$  at% and  $\text{Al}_{48}\text{Ti}_{30}\text{Cr}_{22}$  at% (reported in the target position  $C_1$  and  $C_2$  on the Fig. 1). An additional  $\text{Si}_{100}$  at% target ( $C_3$ ) for the production of the Si-doped coatings was used to carry out a co-deposition process. The power on the target was applied by using two types of generator: 1) a HiPIMS generator operated on the  $C_1$  and  $C_2$  targets with a duty cycle of 3.5% and a pulse length of 2000  $\mu\text{s}$ , at a repetition frequency of 500 Hz and an average power of 3200 W (target power density of 18.6  $\text{W}/\text{cm}^2$  and voltage of  $-480$  V) and 2) a dcMS power generator operated on the Si target, whose current was adjusted to reach different Si contents. During the deposition step, a bias voltage of  $-35 \pm 5$  V was applied on the substrate holder. The thicknesses and deposition rates of the coatings were estimated over a series of deposition and they were in the range of 3.0–3.6  $\mu\text{m}$  and 0.8–1.0  $\mu\text{m}/\text{h}$ , respectively. The samples were cooled down to less than 100  $^\circ\text{C}$  before venting the coating chamber.

The composition, the morphology and thickness of as-deposited coatings were investigated by Field-Emission Electron Microscopy (FE-SEM; Hitachi SU-70) coupled to an Oxford X-Max<sup>N</sup> 20  $\text{mm}^2$  Energy-Dispersive X-ray Spectrometer (EDS; Oxford Instruments). The structure, texture, residual stresses and the stress-free lattice  $a_0$  measurements were performed by X-ray diffraction on a PANalytical Empyrean XRD operated in Bragg-Brentano geometry in point focus configuration using a  $\text{Cu K}\alpha$  radiation at 45 kV and 40 mA. The calculation of the texture coefficient (TC) for the three main presenting peaks (111), (200) and (220) for all sample compounds is outlined in detail elsewhere [30]. The residual stress measurements were carried out using the single  $\{hkl\} \sin^2\psi$  method on the (200) reflection plane of the TiAlN phase assuming a Poisson ratio  $\nu$  of 0.250 [31] and using an elastic-modulus  $E_{\text{it}}$  determined during the nano-indentation measurements. More details of measurements are described elsewhere [30]. The Full Width at Half Maximum (FWHM) for the (422) diffraction peak of the fcc phase (located at  $2\theta = 129^\circ$ , depending on coating composition) for all measurements was determined in Grazing Incidence-XRD (GI-XRD). Complementary structural investigations of the as-deposited coatings were also carried out with a Bruker D8 Discover diffractometer equipped with a  $\text{Cu K}\alpha$  anode operated at 40 kV and 40 mA in grazing incidence mode. All GI-XRD measurements were performed with a fixed incidence angle

$\omega$  is  $2^\circ$ . A number of GI-XRD measurements were also performed on the coatings after oxidation tests by X'Pert Pro XRD equipped with a PIXcel3D detector and a  $\text{Cu K}\alpha$  anode operated at 45 kV and 40 mA. For the measurements performed on the Bruker D8 Discover as well as the PANalytical X'Pert Pro, the instruments were in line focus configuration with a parallel mirror mounted on the primary optics and a parallel plate collimator mounted in front of the detector.

The nano-indentation tests were carried out at room temperature of  $22 \pm 2^\circ\text{C}$  to estimate the hardness of the coatings and its elastic modulus using Anton Paar-CSM NHT3 instrument with a Berkovich diamond indenter [32]. Before indentation, the samples were observed under an optical microscope and a suitable area was chosen. Maximum indentation depth was determined to be less than 1/10 of the film thickness, thus excluding the effect of the substrate deformation. For each film, the nanoindentation tests were repeated for more than 20 times with a loading speed of 20  $\text{mN}/\text{s}$ . Thus, the values reported herein represent the average of these values.

Isotopic oxidations of AlTiSiN and AlTiCrSiN films were carried out in a Nabertherm 50/250/12 horizontal fused-silica tube furnace. The coated samples were inserted into the furnace on fused-silica boats and the temperature of the samples was monitored using a chromel-alumel thermocouple attached to the underside of the boat directly behind the substrate. Oxidation experiments were carried out at  $950 \pm 5^\circ\text{C}$  for different times ranging from 16 min up to 64 min. The oxidation atmosphere was controlled using a two-step approach. Firstly, a  $^{16}\text{O}_2$  gas with (99.757% purity) was employed for 16 min, followed by second step utilizing  $^{18}\text{O}_2$  gas with (97.39% purity) for 9 min. Subsequently, several sequences of  $^{16}\text{O}_2$  gas were introduced each lasting between 0 and 24 min. Further details of the oxidation experiments are covered elsewhere [16].

Cross-sectional thin foils were prepared for Transmission Electron Microscopy (TEM) investigations using a SEM coupled with a focused ion beam (Helios NanoLab 600i, Thermo Fisher). The microstructure of the films and crystal phase identification were investigated by TEM. These investigations were carried out using a JEOL JEM-ARM 200 F (Cold FEG) TEM operating at 200 kV and equipped with a spherical aberration probe and image and with a point resolution of 0.12 nm in TEM mode and 0.078 nm in STEM mode. The chemical depth profiles were conducted via dynamic secondary ion mass spectrometry (D-SIMS) in a CAMECA SC-Ultra instrument in positive ion mode, using  $\text{Cs}^+$  primary-ion beam with an impact energy of 2.0 keV and acquisition time range from 16 to 64 min, commensurate with the oxide thickness, which analyzed. The different elements of interest were measured as  $\text{MCS}_x^+$  (M



= Al, Ti, Cr, Si, O or N and  $x = 1$  or  $2$ ) cluster ions.

APT samples were prepared in a dual-beam focused ion beam/scanning electron microscopy workstation (FIB/SEM) Helios NanoLab 600™ (FEI). Laser Pulsed APT was performed using a local electrode atom probe in a LEAP™ 3000XR (CAMECA) at a repetition rate of 200 kHz, with a sample ground temperature of 60 K, a pressure lower than  $1.33 \times 10^{-8}$  Pa, and a laser pulse energy of 0.5 nJ. The evaporation rate was 5 atoms per 1000 pulses. Data reconstruction was carried out with the software package IVAS™3.6.14 using the voltage evolution curve. The evaporation field was estimated from the mass spectrum using Kingham curves to be 40 V/nm. All specimens were reconstructed with an image compression factor of 1.65 and a k-factor between 3.3 and 4.1 individually for each tip due to the variation in shank angle between tips [33].

### 3. Results and discussion

#### 3.1. Properties for as-deposited coatings

The EDX chemical compositions analysis in Table 1 indicate that all coatings are stoichiometric (Al-Ti-Cr-Si)N. The cross-section SEM images of the AlTiSiN and AlTiCrSiN coatings have been performed for each Si content studied (not reported in this article) and all coatings have a dense structure with fine fibrous columns. By comparison with previous works focused on AlTiCrN coatings elaborated in the same conditions [16], the addition of Si resulted in the refinement of the columns. The average of the column's width was determined to be about 50 nm and about 100 nm with and without addition of Si, respectively. Furthermore, the observations of the coating microstructure become less defined with Si content above 3 at% for both coatings. This last observation will be discussed in more details with TEM and XRD results.

Fig. 2 shows the D-SIMS depth profiles of both  $\text{Al}_{52}\text{Ti}_{45}\text{Si}_{2.6}\text{N}$ , and  $\text{Al}_{46}\text{Ti}_{28}\text{Cr}_{23}\text{Si}_{2.6}\text{N}$  as-deposited. The depth profiles highlight the formation of AlTiSiN coating (Fig. 2A), and AlTiCrSiN coating (Fig. 2B) with a uniform concentration of each element, followed by a TiN bounding interlayer with a thickness of 500 nm and then the Si substrate, respectively.

The GI-XRD diffraction spectra of all as-deposited coatings are shown in Fig. 3 for the two groups of coatings AlTiSiN (Fig. 3A) and AlTiCrSiN (Fig. 3B). The  $\text{Al}_x\text{Ti}_{1-x}\text{Si}_y\text{N}$  coatings with a Si content ranging from  $y = 1.4$ – $6.4$ , exhibit the typical peaks of a single cubic phase structure characterized with the (111), (200) and (220) reflection peaks. Associated to the increase of the Si content in the TiAlN coatings, a slight decrease of the total number of counts for these 3 peaks can be reported, indicating a less crystallized structure of the coating. When the Si

content is increased,  $y = 6.4$ , a broadened diffraction signal was observed within the angle range of  $34$ – $36^\circ$ , indicating the presence of wurtzite AlN and suggesting the initiation of a transition from a B1 cubic structure to a B4 hexagonal structure. For the highest Si content,  $y = 10$ , the coating is not more crystallized, or it can contain only nano-crystallized grains. This last point will be later discussed with the TEM analyses. The AlTiCrSiN as-deposited coatings have also a cubic structure and with a silicon content below 3 at%, the highest intensity peaks correspond to (111) reflection plane. Additionally, another reflection peak corresponding to the (220) plane is observed. For the highest Si content,  $y = 10$ , (200) reflection plane is predominant in the grazing incidence spectrum.

For the coatings containing Si and Cr, the presence of any peak within the angle range of  $34$ – $36^\circ$  is not visible, even when the Si content increases. This structural phenomenon can be correlated to the values ratio of  $\text{Al}/(\text{Al}+\text{Ti}+\text{Cr})$  which is different between the two coatings. With a similar Si content, this ratio for AlTiCrSiN coatings is lower than for AlTiSiN, 0.47 and 0.53, respectively. Due to this lowest ratio, the cubic structure of AlTiCrSiN exhibits improved stability compared to AlTiSiN coatings with a similar Si content, as shown in Fig. 3B. Additionally, even with the highest Si content ( $y = 10$ ), the peak of the cubic phase structure, (200) remains clearly visible for AlTiCrSiN. This statement can be correlated with other parameters in relation with the structural properties of the coatings (Table 1). It was observed that for the  $\text{Al}_{50}\text{Ti}_{43}\text{Si}_{6.4}\text{N}$  coatings, the lattice parameter  $a_0$  and FWHM are  $a_0 = 4.23 \text{ \AA}$  and  $\text{FWHM} = 5.92^\circ$ . In the other hand, for the AlTiCrSiN coatings, the lattice-parameter  $a_0$  and FWHM slightly decrease with an increase of the Si content: for  $\text{Al}_{46}\text{Ti}_{28}\text{Cr}_{23}\text{Si}_{2.6}\text{N}$ ,  $a_0 = 4.21 \text{ \AA}$  and  $\text{FWHM} = 4.26^\circ$  and for  $\text{Al}_{45}\text{Ti}_{26}\text{Cr}_{23}\text{Si}_{5.7}\text{N}$ ,  $a_0 = 4.19 \text{ \AA}$  and  $\text{FWHM} = 3.17^\circ$ . From these different results, it can be proposed that in the case of the AlTiN coatings, the introduction of Si induce an increase of the crystalline cell and a decrease of the grain size and the opposite effect appears for the AlTiCrN coatings. This result could explain why it has been observed that Si addition has a retardant effect of the amorphization mechanism when chromium is present in the coating composition.

The different measurements of the internal mechanical properties for each coating (residual stresses, nanohardness and Young Modulus) are reported in Table 1. It can be shown that high compressive stresses (values superior to  $-6$  GPa) can be recorded with the addition of silicon for both coating groups. However, a Si content superior to 1 at% into these aluminum and titanium nitride coatings does not have the same behavior if the AlTiN coatings contain the chromium. For the AlTiSiN coatings (Fig. 4), the increase of the Si addition causes a decrease of the residual stresses in contrast to AlTiCrSiN, for which an increase of Si content does not modify this mechanical property. Considering the

**Table 1**

Characteristics of the samples studied: EDX composition (at%), stress free lattice spacing  $a_0$  (Å) and Full Width at Half Maxima (FWHM) determined from XRD on (422) reflection plane, instrumented values of the hardness, Young's modulus,  $H_{IT}/E_{IT}$ ,  $H_{IT}^2/E_{IT}^2$  and stress values. As well as the structure of all (Al-Ti-Si-Cr)N as-deposited coatings on WC-Co substrate. B1: cubic structure. B4: hexagonal structure. These data are determined from Theta 2theta spectra which are not here presented.

Coating	Composition (at%)					Lattice $a_0$ (Å)	FWHM determined on (422) ( $^\circ$ )	Stress (MPa)	$H_{IT}$ (GPa)	$E_{IT}$ (GPa)	$H_{IT}^2/E_{IT}^2$	$H_{IT}^3/E_{IT}^3$	structure
	Al	Ti	Cr	Si	N								
$\text{Al}_{62}\text{Ti}_{37}\text{Si}_{1.4}\text{N}$	31.4	18.6	X	0.7	49.3	4.213	3.4280	-6626 $\pm 577$	34.9 $\pm 0.9$	396 $\pm 15$	0.088	0.270	B1
$\text{Al}_{52}\text{Ti}_{45}\text{Si}_{2.6}\text{N}$	26	22.6	X	1.3	50.1	4.228	4.5582	-7447 $\pm 304$	34.7 $\pm 0.4$	494 $\pm 80$	0.070	0.171	B1
$\text{Al}_{50}\text{Ti}_{43}\text{Si}_{6.4}\text{N}$	25	21.7	X	3.2	50.1	4.231	5.9200	-2335 $\pm 260$	31.8 $\pm 0.6$	444 $\pm 12$	0.071	0.162	B1
$\text{Al}_{48}\text{Ti}_{41}\text{Si}_{10}\text{N}$	23.8	20.8	X	5.1	50.3	4.242	Peak too small	+955 $\pm 83$	X	X	X	X	B1+B4
$\text{Al}_{46}\text{Ti}_{28}\text{Cr}_{23}\text{Si}_{2.6}\text{N}$	22.8	13.6	11.4	1.3	50.9	4.212	4.2591	-6330 $\pm 233$	32.5 $\pm 0.7$	445 $\pm 12$	0.073	0.173	B1
$\text{Al}_{46}\text{Ti}_{27}\text{Cr}_{23}\text{Si}_{4.1}\text{N}$	22.4	13.3	11.5	2	50.8	4.211	3.7992	-6307 $\pm 119$	32.9 $\pm 0.5$	405 $\pm 7$	0.081	0.217	B1
$\text{Al}_{45}\text{Ti}_{26}\text{Cr}_{23}\text{Si}_{5.7}\text{N}$	22.3	13	11.1	2.8	50.8	4.192	3.1696	-6320 $\pm 313$	34.7 $\pm 0.6$	512 $\pm 14$	0.067	0.159	B1
$\text{Al}_{45}\text{Ti}_{26}\text{Cr}_{22}\text{Si}_{10}\text{N}$	21	12.7	10.7	5	50.6	4.184	Superposition with WC	-5806 $\pm 389$	31.3 $\pm 0.5$	400 $\pm 6$	0.078	0.190	B1



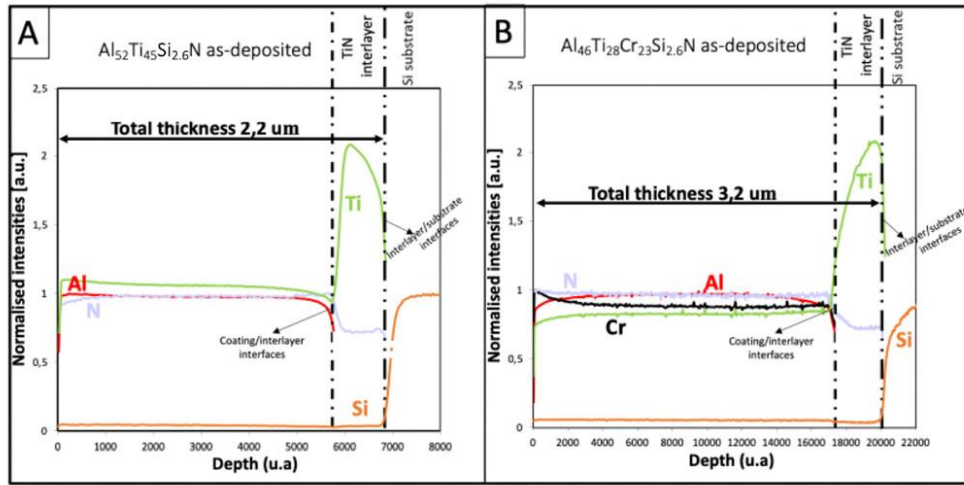


Fig. 2. D-SIMS depth profiles for as-deposited coatings (A)  $\text{Al}_{52}\text{Ti}_{45}\text{Si}_{2.6}\text{N}$  and (B)  $\text{Al}_{46}\text{Ti}_{28}\text{Cr}_{23}\text{Si}_{2.6}\text{N}$  showing the distribution of elements through the whole coating, the TiN interlayer, and the Si substrate.

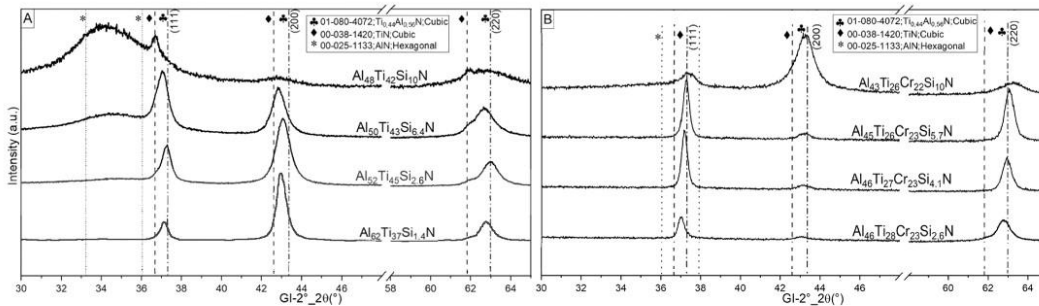


Fig. 3. Grazing incident X-ray diffraction profiles of the (A)  $(\text{Al-Ti-Si})\text{N}$  and (B)  $(\text{Al-Ti-Cr-Si})\text{N}$  as-deposited coatings on Si wafers.

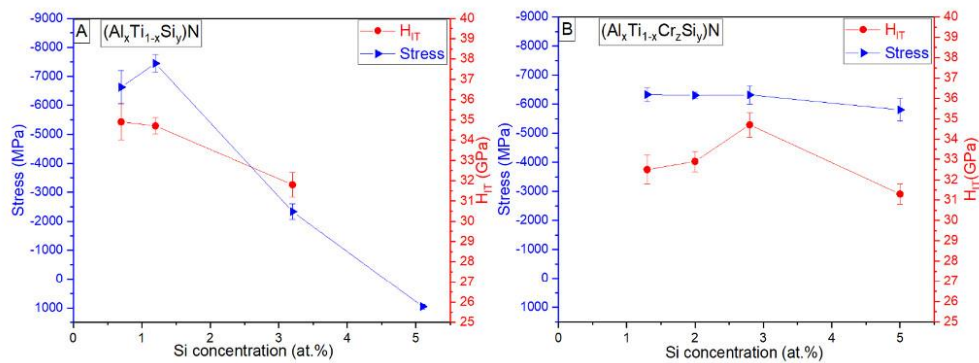


Fig. 4. Evolution of the residual stress (left scale) and the instrumented hardness ( $H_{IT}$ ) (right scale) of (A) the  $(\text{Al-Ti-Si})\text{N}$  and (B) the  $(\text{Al-Ti-Cr-Si})\text{N}$  coatings with the silicon content.

comments reported from the XRD analyses on these different coatings, we can propose that the decrease of the residual stresses for the TiAlSiN coatings can be associated to the formation of wurtzite phase and to a reduction of its crystallinity density with the Si addition. This structural phenomenon is not visible when the Si addition is associated to the quaternary metallic coatings, TiAlCrN. It is seen in Fig. 4 that the hardness is also influenced by the Si content. The evolutions of the values can be correlated with these reported for the compressive residual stresses of these two groups of nitride coatings, the highest hardness measurement was about  $34 \pm 2$  GPa, and the average values of instrumented elastic-modulus was determined to be about  $443 \pm 40$  GPa.

### 3.2. Oxidized coatings at 950 °C

In this section, oxidation behavior at high temperature of the  $\text{Al}_{52}\text{Ti}_{45}\text{Si}_{2.6}\text{N}$  and  $\text{Al}_{46}\text{Ti}_{28}\text{Cr}_{23}\text{Si}_{2.6}\text{N}$  coatings will be discussed. As described in a previous section, both coatings have been deposited in the same coater equipment and with the same process conditions. Furthermore, these coatings exhibit identical cubic structures, Si content, and mechanical properties, specifically in terms of toughness and resistance to plastic deformation, as indicated by a  $H^3/E^2$  ratio of 0.17. Consequently, the authors consider that this offers an optimal situation to completely explore the effect of Si addition during oxidation and to see if there is a synergetic effect when the aluminum-titanium-silicon nitride coating also contains chromium.

Firstly, our recent study, with a particular focus on Si-free AlTiN and AlTiCrN oxidized coatings, indicated that the AlTiN coating, despite possessing a comparable Al/Ti ratio, exhibits insufficient oxidation resistance when subjected to temperatures of 950 °C. Indeed, at this temperature, we can observe that the coating undergoes a complete oxidation which could be explained by the formation of a porous rutile  $\text{TiO}_2$  structure [16]. In contrast, the oxidation resistance of AlTiCrN

coatings at 950 °C, have displayed a more intricate relationship influenced by both the Al/Ti and Cr/Ti alloying ratios. In this case, the coating demonstrates partial oxidation, leading to the development of a rutile  $\text{TiO}_2$  surface layer with an  $\text{AlCr}_2\text{O}_3$  superior protective layer situated beneath it. The research shows that the microstructure of this underlayer is a main parameter in the oxidation kinetic of these AlTiCrN coatings as it defines the inward oxygen diffusion [16]. Secondly, let's discuss various aspects of the thermal behavior of the AlTiSiN and AlTiCrSiN base coatings after subjecting them to a 49 min heat treatment at 950 °C, before delving into a comprehensive study of their oxide layer and growth mechanism. The dark field and bright field TEM micrographs show cross-sections of the  $\text{Al}_{52}\text{Ti}_{45}\text{Si}_{2.6}\text{N}$  and  $\text{Al}_{46}\text{Ti}_{28}\text{Cr}_{23}\text{Si}_{2.6}\text{N}$  coating holding at 950 °C for 45 min (Fig. 5A and B). The diffraction contrast images of the nitride coating part indicate that both coatings maintain a microstructure with fine fibrous columns similar to the one just after the deposition. For the AlTiSiN coating, the fibre size is estimated between 55 and 70 nm and for the AlTiCrSiN coating between 55 and 95 nm. The selective area electron diffraction (SAED) patterns also show a structural thermal stability for the AlTiSiN or AlTiCrSiN coatings. The lattice spacing determined from SAED pattern is corresponding to the cubic structure for both coatings and the main plane orientation (111) is conserved. No indication of structural phase separation between aluminum and titanium phase has been highlighted and therefore, it can be considered that the incorporation of Si atoms into these two nitride alloys largely delays the phase separation during their use at this high temperature.

The diffraction analyses using a GI-XRD configuration have been carried out on  $\text{Al}_{52}\text{Ti}_{45}\text{Si}_{2.6}\text{N}$  and on  $\text{Al}_{46}\text{Ti}_{28}\text{Cr}_{23}\text{Si}_{2.6}\text{N}$  coatings oxidized at 950 °C and their diffraction patterns are now shown in Fig. 6. The analysis also reveals the presence of  $\alpha\text{-Al}_2\text{O}_3$  corundum phase in addition, two crystalline  $\text{TiO}_2$  phases, anatase and rutile which are all detected for the two oxidized samples. The  $\text{TiO}_2$  anatase phase is largely dominant with well-defined peaks in  $\text{Al}_{52}\text{Ti}_{45}\text{Si}_{2.6}\text{N}$  coating in contrast

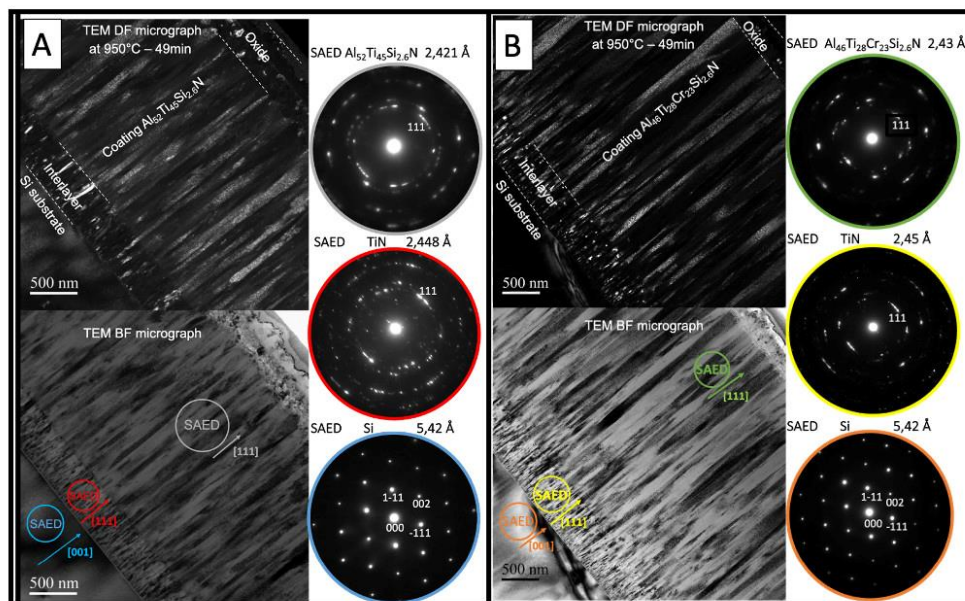


Fig. 5. Dark and bright field TEM micrographs of the cross-section of the oxidized coatings of  $\text{Al}_{52}\text{Ti}_{45}\text{Si}_{2.6}\text{N}$  and  $\text{Al}_{46}\text{Ti}_{28}\text{Cr}_{23}\text{Si}_{2.6}\text{N}$  at 950 °C for 49 min, respectively. The selected area electron diffraction (SAED) patterns for all the oxidized coatings areas.



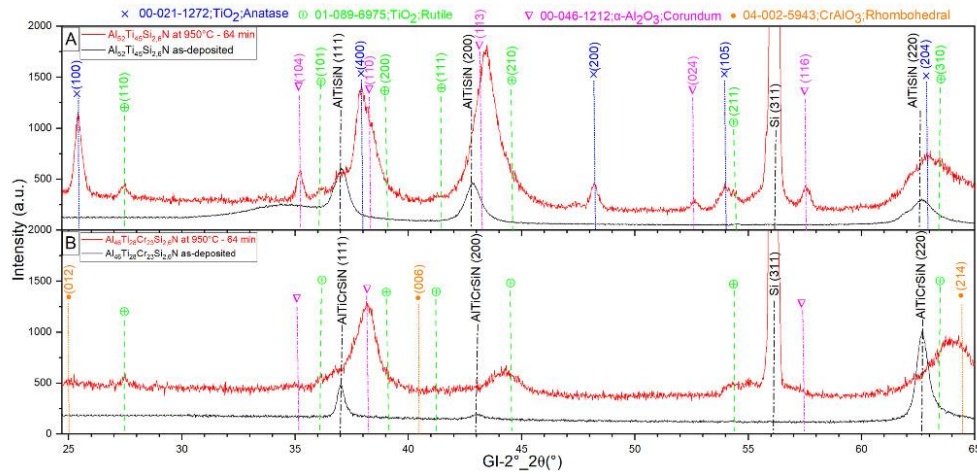


Fig. 6. Grazing incidence XRD pattern ( $\omega 2^\circ$ ) performed on the XRD XPert Pro patterns of  $\text{Al}_{46}\text{Ti}_{28}\text{Cr}_{23}\text{Si}_{26}\text{N}$  and  $\text{Al}_{52}\text{Ti}_{45}\text{Si}_{26}\text{N}$  samples heated at  $950^\circ\text{C}$  for 64 min. For structure identification, the ICDD 2021 database was used.

to the rutile phase detected in  $\text{Al}_{46}\text{Ti}_{28}\text{Cr}_{23}\text{Si}_{26}\text{N}$  coating with broad peaks. One more rhombohedral phase associated with a  $\text{CrAlO}_3$  chemical composition could also be detected for this last coating (this phase

will be later confirmed in the TEM results section). However, as both oxidized coatings exhibit a high-angle shift for the nitride peaks (111), (200), and (220), the appearance of the rhombohedral phase cannot be

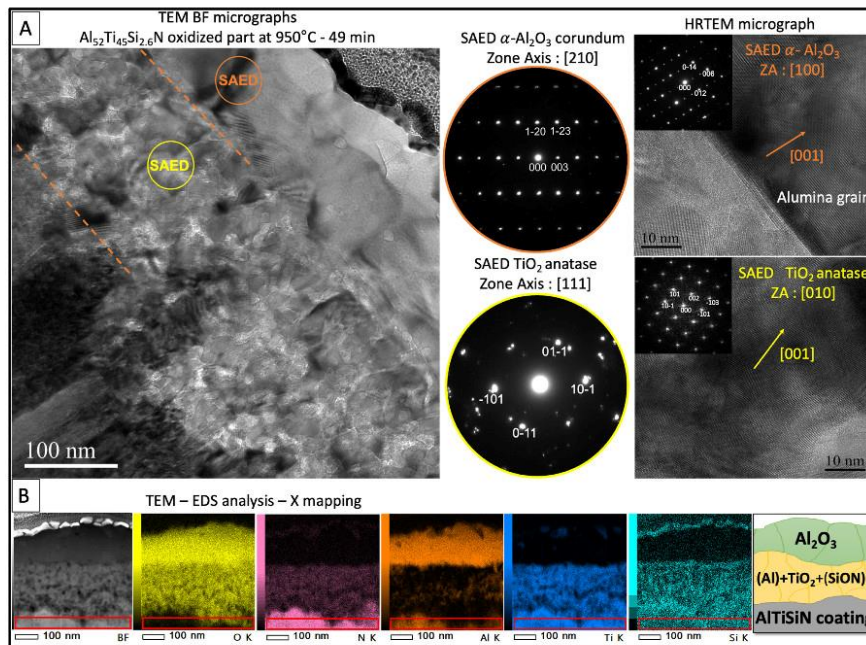


Fig. 7. TEM investigation of the oxide formed in air at  $950^\circ\text{C}$  for 49 min on  $\text{Al}_{52}\text{Ti}_{45}\text{Si}_{26}\text{N}$  coating. (A) Bright field image, lattice resolved diffraction contrast of  $\text{Al}_2\text{O}_3$  and  $\text{TiO}_2$  along the [210] and [111] zone axis, respectively and corresponding selected area electron diffraction (SAED). (B) STEM-HAADF and EDX color coded maps of oxidized regions presenting the distribution of O (yellow), N (pink), Al (orange), Ti (blue) and Si (cyan) as well as the schematic drawing of oxidized regions.

alone considered for the peak at 64.5°. This shift can also be attributed to the relaxation of stress phenomena during the temperature increase, which involves defect rearrangement rather than recrystallization, as there is no associated change in texture. The shift can be linked to the growth of the oxide scale on top of the nitride coating.

To go deeper in the presentation of the oxide layers for these two types of coatings, TEM cross-section observations and EDX mappings have been carried out. First, discussions will be dedicated to the addition of Si to AlTiN coating. Fig. 7 shows the results for the Al<sub>52</sub>Ti<sub>45</sub>Si<sub>2.6</sub>N oxidized coating. Fig. 7A clearly shows a bilayer oxide structure with an outer layer rich in aluminum, the α-Al<sub>2</sub>O<sub>3</sub> corundum with a thickness of 165 nm and an inner layer rich in titanium, TiO<sub>2</sub> anatase with a thickness of 221 nm. The presence of Si on the top of these two layers is related to Si contamination during the sample preparation. The grain sizes of Al<sub>2</sub>O<sub>3</sub> are bigger compared to TiO<sub>2</sub> with a range between 80 and 180 nm and 20 – 40 nm, respectively. Furthermore, the EDS mapping analysis (Fig. 7B) show the distribution of Al, Ti, Si, N and O in the oxide layer and easily define the interface between these two layers. The elemental mapping also reports that Si and N are detected in the inner oxide layer, the presence of these two elements can indicate that other phases rich in silicon like Si<sub>3</sub>N<sub>4</sub> (with also SiO<sub>2</sub>) may be present in the titanium oxide scale. EDS local analyses have been performed in the titanium-rich oxide scale and small amounts of Si, N and Al are found. The presence of these two elements, Si and N could indicate that the inner TiO<sub>2</sub> oxide layer growth by internal oxygen diffusion. This state will now be considered during the presentation of the results of the elementary depth profiles into the different oxide layers.

D-SIMS depth profiles of the Al<sub>52</sub>Ti<sub>45</sub>Si<sub>2.6</sub>N oxidized at 950 °C under sequential atmosphere containing <sup>16</sup>O<sub>2</sub> and <sup>18</sup>O<sub>2</sub> isotopes after different durations in the range of 16–49 min are shown in Fig. 8. This elemental analysis confirms that the oxide scale is structured with two layers, a top oxide layer rich in Al (region 1) and an inner layer rich in Ti (region 2). The depth profiles (Fig. A-D) reported in real count intensities show that region 1 mainly consists of alumina and at a low level whereas region 2, mainly consists of titanium oxide. Also, the two chemical elements, Si

and N, are part of the inner titanium-rich oxide layer. Silicone and Nitrogen present a similar behavior with a bump near the interface between region 1 and region 2. Considering that diffusion of silicon and titanium into alumina is difficult, this observation can confirm that this titanium oxide inner scale has grown mainly by an internal oxygen diffusion where the partial pressure of oxygen controls the selective oxidation of the different metallic elements.

During the 16–49 min period of D-SIMS analysis, it was observed that the sputtering time for oxide layers, which directly depends on oxide thickness, showed only a very slight increase. This statement indicates that a dense and compact oxide layer is developed during the first period of 16 min and then, the growth of this protective layer can largely reduce the oxygen diffusion at the oxide-nitride interface and consequently blocks the oxide growth mechanism. By comparison, the authors have already reported that the same AlTiN coating with a similar Al/Ti ratio, but without Si has poor oxidation resistance at this high temperature of 950 °C [16]. Additional insight data of the diffusion mechanism into the oxide layer can be now obtained by analyzing the isotopic profiles of oxygen for different oxidation durations (Fig. 8A''–D''). On the Fig. 8B'', the coating was oxidized during 25 min with a first period of 16 min under <sup>16</sup>O<sub>2</sub> (Fig. 8A'', 16 min) and a second one of 9 min, under <sup>18</sup>O<sub>2</sub>. With these sequential oxidation conditions, the highest <sup>18</sup>O normalized signal is observed at the external surface. For a longer oxidation duration (Fig. 8C'', 36 min) with an adding oxidation period of 11 min under an <sup>16</sup>O<sub>2</sub> atmosphere, the <sup>18</sup>O profile is still mainly visible at the external surface and it presents a second bump at the interface between the two oxides. For longer oxidation duration (Fig. 8D'', 49 min), with an additional oxidation period of 24 min under an <sup>16</sup>O<sub>2</sub> atmosphere, the <sup>18</sup>O depth profile is very similar to the oxidation duration of 36 min. The detection of <sup>18</sup>O at the external surface clearly indicates a very low external growth of the oxide scale, the bump at the alumina and titanium oxide interface can be associated to the formation of new oxide grains in this region. Finally, the absence of a high concentration of <sup>18</sup>O at the oxide-nitride interface can be correlated to a very weak internal oxidation mechanism. All these reaction mechanisms

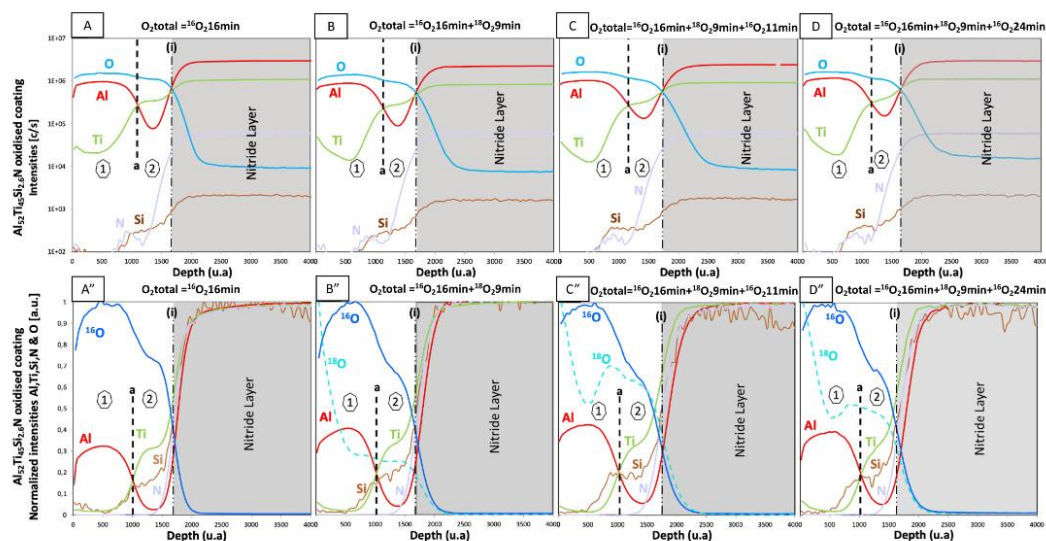


Fig. 8. D-SIMS depth profiles of Al<sub>52</sub>Ti<sub>45</sub>Si<sub>2.6</sub>N oxidized at 950 °C using different durations of <sup>16</sup>O<sub>2</sub> and <sup>18</sup>O<sub>2</sub>. (A) to (D): Raw SIMS intensities. The O profiles correspond to total oxygen (<sup>16</sup>O and <sup>18</sup>O). (A'') to (D'') Normalised SIMS intensities for the element of interest and the two oxygen isotopes. The dashed line (a) indicates the position of the interface between the two oxide regions 1 and 2. The dashed line (i) indicates the position of the interface between the nitride and the oxide.



can confirm that the internal oxygen diffusion in the inner anatase TiO<sub>2</sub> layer is very slow and consequently, the growth oxidation mechanism at the nitride-oxide interface is blocked. The most probable hypothesis is that it is possible to correlate this statement with the presence of Si and also N in this internal oxide layer (Fig. 7B), it can be suggested that a silicon nitride or silicon oxide phase surrounding the titanium oxide grains can delay the inner oxygen diffusion and foster the bulk oxide diffusion of Al and Ti which is a low kinetic process.

To summarize during the oxidation process at 950 °C, a double oxide layer Al<sub>2</sub>O<sub>3</sub>/TiO<sub>2</sub> grows on the surface of the AlTiSiN coating. The description of this oxide scale stack is similar to those already described for AlTiN coatings oxidized at lower temperature of 800 °C, [34]. However, the authors have observed during this study that AlTiN coatings without a Si addition do not show an oxidation resistance above 800 °C mostly because of the quality of the oxide scales. They reported a relatively large quantity of porosities in the titanium oxide layer. In this study, at this high temperature of 950 °C, the high oxidation resistance of AlTiSiN coatings is associated to the growth of a dense Al<sub>2</sub>O<sub>3</sub> protective oxide, which with time will limit the oxide growth kinetic and it can act as an oxygen diffusion barrier against an internal oxidation phenomena [4,34]. D-SIMS results clearly show that an Al<sub>2</sub>O<sub>3</sub> growth on

the external oxide surface of the AlTiN coatings containing Si. However, due to limited oxygen inward diffusion, the growth of the TiO<sub>2</sub> layer on the same coating ceases after a certain time. This last phenomenon can be associated to the fact that a thermal stability of the TiO<sub>2</sub> oxide scale has been reported with the detection of the anatase structure at this high temperature. It can be proposed that the presence of Si (and N) in the TiO<sub>2</sub> layer region, delay the oxygen diffusion at the oxide/nitride interface. With this situation, it minimizes the oxygen partial pressure at the grain boundaries and consequently delay the anatase-rutile transformation. In previous works, the authors [35] and another research group, Rafaja et al. [36] have claimed the formation of SiO<sub>x</sub> phase at the oxide grain boundaries. This process can follow to a core-shell around TiO<sub>2</sub> grains and it can contribute to hindering the oxygen diffusion. Also, in this work it has been determined that the TiO<sub>2</sub> grains can contain a certain content of Al ≈ 3–5 at%. Interestingly, this 'doping' phenomenon could contribute to stabilizing the anatase structure of TiO<sub>2</sub> even at high temperatures.

A synergistical effect when Cr and Si are added to AlTiN coating will now be discussed. TEM micrographs of the cross-section of the Al<sub>46</sub>Ti<sub>28</sub>Cr<sub>23</sub>Si<sub>2.6</sub>N oxidized coating at 950 °C are shown in Fig. 9. These observations indicate that the oxide scale also shows a multilayer

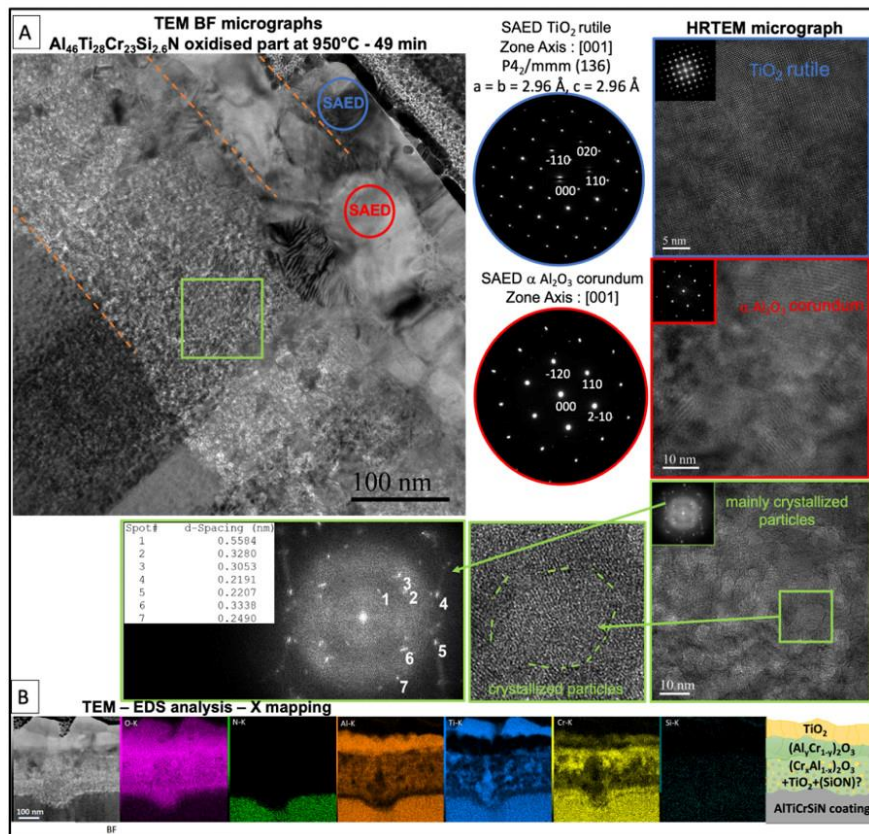


Fig. 9. TEM micrograph of Al<sub>46</sub>Ti<sub>28</sub>Cr<sub>23</sub>Si<sub>2.6</sub>N coating oxidized in air at 950 °C for 49 min (A) The lattice resolved diffraction contrast of TiO<sub>2</sub> and Al<sub>2</sub>O<sub>3</sub> along the [0-11] and [-110] zone axis, respectively and corresponding selected area electron diffraction (SAED). (B) STEM-HAADF and EDX color coded maps of oxidation regions presenting the contrast of O (magenta), N (green), Al (orange), Ti (blue), Cr (yellow) and Si (cyan) as well as the schematic drawing of oxidation regions (B).

structure, but this time, with three oxide regions: a Titanium layer at the outermost part, underneath an alumina-rich oxide layer, and below a mixed layer with chromium-aluminum-oxide and titanium-oxide grains. This description of the oxide scale has already been reported by the authors during the presentation of the oxidation behavior, also at 950 °C, of different AlTiCrN coatings containing different Cr contents but without Si addition [16]. After an oxidation duration of 49 min (Fig. 9A), the TiO<sub>2</sub>-rich scale nearer to the surface is identified as a rutile phase with a thickness of 43 nm, followed by an  $\alpha$ -Al<sub>2</sub>O<sub>3</sub> corundum scale with a thickness of 97 nm and then a mixed oxide region (Al-Cr-Ti-O) with a higher thickness of 229 nm at the interface with the unoxidized coatings. By comparing the Cr and Al mapping across this mixed oxide layer, an increase of Cr content from the nitride-oxide interface to the outward direction is visible, whereas the Al content shows a uniform distribution on top. Dark field TEM observations show that this internal oxide region is partially crystallized with particle grains size of  $\approx$  5 nm surrounded with an amorphous area. Electron diffraction analyses have then determined that this mixed oxide region contains nano-sized or sub-nanosized CrAlO<sub>3</sub> grains mixed with TiO<sub>2</sub> rutile grains. Different interplanar distances  $d_{hkl}$  (3.28 Å, 2.49 Å and 2.20 Å) corresponding to crystallites present in the third oxide region have been determined. It could correspond to TiO<sub>2</sub>-rutile with tetragonal crystal system (unit cell:  $a = b = 4.611$  Å,  $c = 2.982$  Å) and considering the reference pattern JCPDS 00-021-1276 where the interplanar distances  $d_{110}$ ,  $d_{101}$  and  $d_{111}$  correspond to 3.247 Å, 2.487 Å and 2.188 Å, respectively. This last description of the third oxide region is different from the inner oxide region reported by the authors in previous works of the oxidized AlTiCrN coatings without Si elaborated in the same conditions, whose oxide scale was totally constituted of small, crystallized grains [16]. To investigate the impact of Si addition on the crystallinity of this inner oxide scale (region 3), an Al<sub>46</sub>Ti<sub>28</sub>Cr<sub>23</sub>Si<sub>2.6</sub>N oxidized coating at 950 °C during 49 min has been analyzed by Atom Probe Tomography. Fig. 10 shows an APT reconstruction of a small oxide volume in the upper zone of the oxide region 3, close to the interface between the Cr-Al mixed oxide scale and the alumina-rich scale with two views rotated by 90°. Three iso-concentration surfaces I, II and III for the same reconstruction highlight three distinct oxide nanograin regions, namely Cr-rich (I- pink region), Ti-rich (II- dark blue region), and Al-rich (III- green region) determined by a higher concentration of 20 at%. However, none of these regions show a significant concentration of Si. To complete this investigation, 5 nm slice cuts across the reconstruction has been established. In APT Fig. 11, it is reported a rectangular blue zone where the elemental distribution of the chemical element between the region II and III (Fig. 11A), and between the region I and II (Fig. 11B) has been

followed. However, the associated concentration profiles do not show a possible segregation of Si at these two grain boundaries.

To go deeper into the understanding of the oxide growth by determining the anionic and cationic diffusion phenomena, elemental chemical profiles have also been done in Fig. 12. D-SIMS depth profiles of the Al<sub>46</sub>Ti<sub>28</sub>Cr<sub>23</sub>Si<sub>2.6</sub>N oxidized at 950 °C under an atmosphere containing alternatively <sup>16</sup>O<sub>2</sub>-<sup>18</sup>O<sub>2</sub>-<sup>16</sup>O<sub>2</sub> for different durations (16; 25; 36 and 49 min) are now discussed. They are presented in two different ways: firstly, SIMS depth profiles with the real count intensities and the total oxygen profile (Fig. 12 A-D) and secondly, a normalized SIMS intensity depth profiles considering the <sup>16</sup>O and its isotopic <sup>18</sup>O element (Fig. 12 A''-D''). This second description is more appropriated to see the evolution of composition at the different oxide scale interfaces. These D-SIMS depth profiles of the Al<sub>46</sub>Ti<sub>28</sub>Cr<sub>23</sub>Si<sub>2.6</sub>N oxidized coating is in good agreement with the TEM description of the oxide scale as the three different regions are clearly visible with large chemical elementary variations corresponding to the three different identified oxide layers. On the top surface, called region 1, the Ti and O signals are the highest signal elements. Below this first oxide scale, in region 2, the Al signal is dominant, the Ti and Si signals are low. The maximum Cr signal is detected in the third oxide layer, region 3, where Al and Ti are also relevant elements. The N and Si elements are also detected in this inner oxide layer with their signals decreasing from the coating interface to the external zone of this layer. The presence of dash-lines b, and c on the figure are corresponding to the interfaces between the three oxide regions and the last dash-lines (i) between the oxide and nitride regions.

As this sputtering time during the SIMS analysis can be correlated qualitatively to the thickness of the oxides, comparisons were done between the AlTiSiN and the AlTiCrSiN coatings. Fig. 13 shows the time evolutions to sputter the oxide scale grown at 950 °C for these two coatings as a function of the square root oxidation time. It is visible that the slopes of the kinetic rate are different and for the Al<sub>52</sub>Ti<sub>45</sub>Si<sub>2.6</sub>N, this one is lower, indicating the Al<sub>52</sub>Ti<sub>45</sub>Si<sub>2.6</sub>N alloy exhibits better oxidation resistance at 950 °C than Al<sub>46</sub>Ti<sub>28</sub>Cr<sub>23</sub>Si<sub>2.6</sub>N.

During the oxidation of the AlTiCrSiN coatings, the sputtering time of D-SIMS depth profiles to reach the oxide-coating interface shows a time evolution which indicates a continuous growth of the oxide layer. This is not the case for the AlTiSiN coatings as the sputtering time increases very slowly after 16 min. This statement can be directly correlated to the presence of this fully covered alumina layer which delays the inward diffusion of oxygen.

To go deeper in the growth of the oxide layer on the Al<sub>46</sub>Ti<sub>28</sub>Cr<sub>23</sub>Si<sub>2.6</sub>N coating, the normalized SIMS profiles reported after different durations with the successive sequences of isotopic oxidation using <sup>16</sup>O<sub>2</sub>,

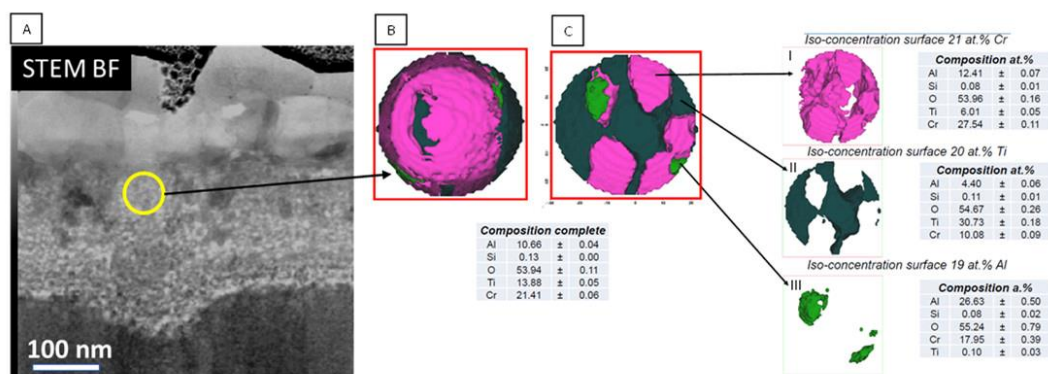


Fig. 10. The TEM-BF micrographs for Al<sub>46</sub>Ti<sub>28</sub>Cr<sub>23</sub>Si<sub>2.6</sub>N oxidized sample (A) shows the selected area for APT analysis. The front (B) and back (C) of the reconstruction APT sample and the three main Iso-concentration surfaces for the Cr-/Ti-/Al-rich regions (I, II and III).



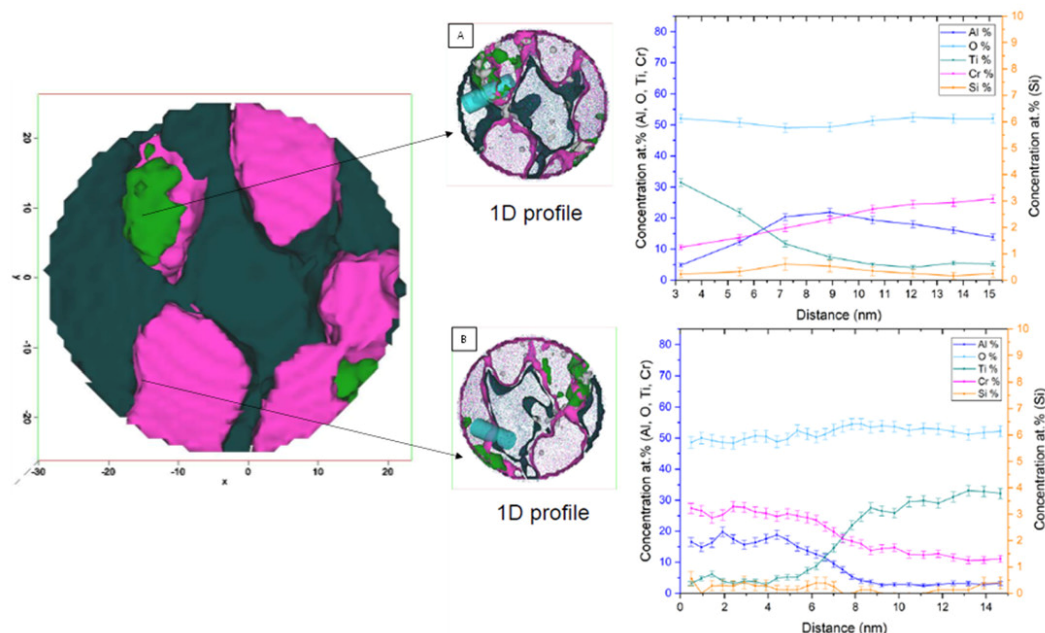


Fig. 11. Two concentration profile across the grain boundary of the three main Iso-concentration surfaces for the Cr-/ Ti-/ Al-rich regions (A) and across the grain boundary of the Iso-concentration surfaces for the Cr-/ Ti-rich regions (B) shows No segregation of Si at the boundaries.

$^{18}\text{O}_2$  and again  $^{16}\text{O}_2$  gas can now be discussed (Fig. 12A"-D"). Three bumps for the isotopic  $^{18}\text{O}$  signal can be reported and they are localized at each scale interface: region 1–2, region 2–3 and region 3-nitride coating, these interfaces can be considered as the main zone where the oxide scales are growing. Based on these data, the inward oxygen diffusion to the oxide-coating interface seems to be the main driving force and it controls the total growth of the oxide layer. It is clearly visible from the SIMS profiles when an oxidation step is done after the  $^{18}\text{O}$  period, the oxide continues to grow as the oxygen bump for the region 3 is moving inside the oxide layer after 36 and 49 min. In the same time, an anionic diffusion of Al and Ti are necessary for the development of the two external oxide layers (bumps of region 1–2 and 2–3) but from the SIMS depth profiles, it could indicate that their growth kinetics are lower.

#### 4. Conclusions

A comparison of introducing Si into AlTiN (Al/Ti ratio 1.7) and AlTiCrN (Al/Ti+Cr ratio 0.9) on the intrinsic mechanical properties and the high temperature resistance of these PVD coatings, well-known for the improvement of lifetime for cutting tools, was carried out. For these two as-deposited coatings, the introduction of Si has led to an increase of the compressive stresses and hardness levels superior to 30 GPa were recorded. Concerning the oxidation resistance of the AlTiN coating, the introduction of Si below 10 at% offers the possibility to developed a protective oxide layer at 950 °C. The metallurgical characterizations and more specifically, the TEM cross-section observations of the oxide scale and the oxygen isotopic depth profiles by SIMS, have shown that this oxide protective layer is composed of a mixed oxide, pure alumina nearer the surface and a Ti-rich near the nitride. The addition of Si leads to the formation of nanometer sized  $\text{TiO}_2$  anatase crystallites under the alumina oxide, the presence of Al into  $\text{TiO}_2$  can act a doping

phenomenon to stabilize the anatase phase. The SIMS depth profiles with time show that after the growth of this bi-layer oxide scale, the inward cationic diffusion of the oxygen is very reduced, and this explains the high oxidation resistance of these AlTiSiN coatings at 950 °C. The oxidation study for AlTiCrSiN coatings has reported a different oxide scale morphology with a pure  $\text{TiO}_2$ -rutile at the external surface, followed by an Al-rich oxide and internally, a mixed oxide region of  $(\text{AlCr})_2\text{O}_3$  with small islands of  $\text{TiO}_2$ . This inner oxide is composed of very small, crystallized oxide grains surrounded by other amorphous grains. This particular oxide scale morphology has been correlated to the detection of Si and N elements which could delay the total crystallization mechanism of this mixed oxide layer. A regular increase with time of the oxide scale has been recorded for these last oxidized coatings and the SIMS analyses have shown that their kinetic growth is mainly controlled by the inward oxygen diffusion with a major oxidation mechanism at the nitride coating interface.

#### CRedit authorship contribution statement

**M.-R. Alhafian:** Methodology, Investigation, design of experiments, draft writing, editing, and submission. **N. Valle:** SIMS measurements, scientific discussion, and review. **J.-B. Chemin:** Implementation of the PVD coatings, scientific discussion. **L. Bourgeois:** Conceptualization, scientific discussion, mechanical properties validation, and review. **M. Penoy:** DRX analysis, and scientific discussion. **R. Useldinger:** scientific discussion and review. **J. Ghanbaja:** TEM analysis, and scientific discussion. **F. Mücklich:** Scientific discussion. **P. Choquet:** Conceptualization, Investigation, Supervision, review & final writing, editing, Project administration, and Funding acquisition.

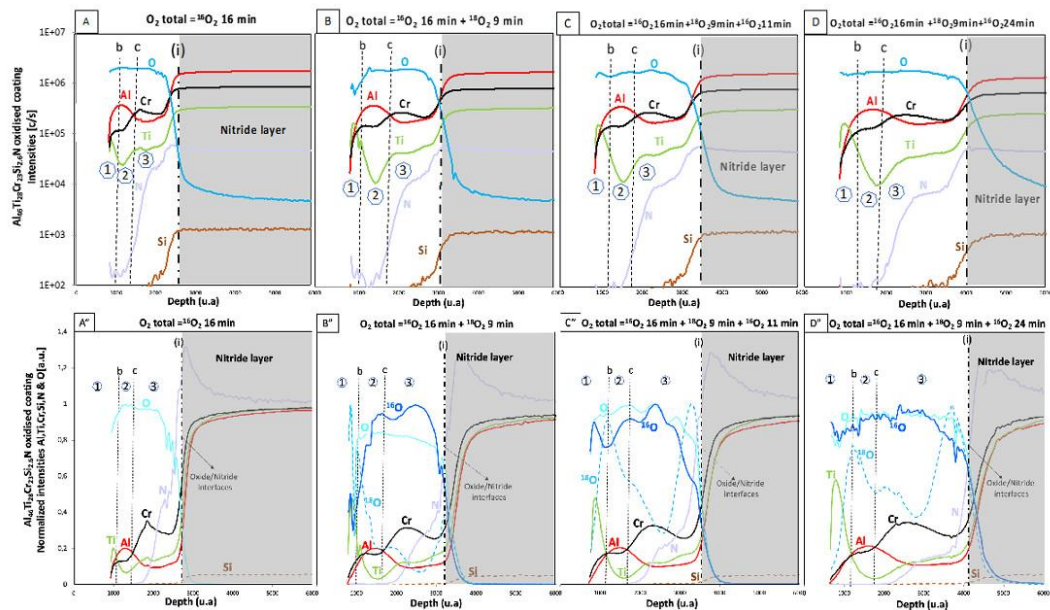


Fig. 12. D-SIMS depth profiles of  $\text{Al}_{46}\text{Ti}_{28}\text{Cr}_{23}\text{Si}_{2.6}\text{N}$  oxidized at  $950^\circ\text{C}$  using different durations of  $^{16}\text{O}_2$  and  $^{18}\text{O}_2$ . Where the normalised intensity of total  $\text{O}_2$  instead of  $^{16}\text{O}_2$  and  $^{18}\text{O}_2$  is shown. The dashed lines b, and c indicate the position of the interfaces between the oxide regions 1, 2, and 3. The dashed line (i) indicates the position of the interface between the nitride and the oxide.

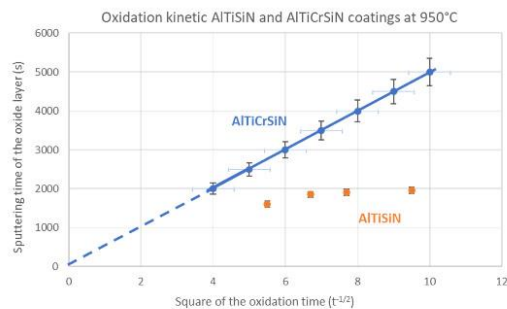


Fig. 13. Time evolutions of oxide scale growth at  $950^\circ\text{C}$  for  $\text{Al}_{46}\text{Ti}_{28}\text{Cr}_{23}\text{Si}_{2.6}\text{N}$  and  $\text{Al}_{52}\text{Ti}_{45}\text{Si}_{2.6}\text{N}$  based on D-SIMS sputtering times as a function of the square root oxidation time.

**Declaration of Competing Interest**

The authors declare the following financial interests/personal relationships which may be considered as potential competing interests: Mohamed Riyad ALHAFIAN reports financial support was provided by Luxembourg National Research Fund (FNR).

**Data Availability**

The authors do not have permission to share data.

**Acknowledgment**

The authors wish to acknowledge the financial support from the Luxembourg National Research Fund (FNR) under the NANOPIMS and HI3M projects funded by the call for innovation and industry partnerships (C-PPP17/MS/11622578 and BRIDGES2020/MS/15381200), as well as the European Doctoral Program in Advanced Materials Science and Engineering (DocMASE) for their collaboration during the PULSA-TEC project. We are very thankful to Dr. H. Kabbara and S Migot (Institute Jean Lamour, France) for the TEM sample preparation. We also thank B. El Adib for his work on SIMS measurements and oxidation experiments with oxygen isotopic tracers, Dr. Y. Fleming for the exchanges on the XRD measurements (Luxembourg Institute of Science and Technology, Luxembourg) and Dr. F. Soldera and J. Barrirero (Saarland University, Germany) for the APT sample preparation, measurement, reconstruction and analysis.

**References**

- [1] L. Tu, S. Tian, F. Xu, X. Wang, C. Xu, B. He, W. Zhang, Cutting performance of cubic boron nitride-coated tools in dry turning of hardened ductile iron, *J. Manuf. Process.* 56 (2020) 158–168.
- [2] D. Dudzinski, A. Devillez, A. Moufki, D. Larrouquiere, V. Zerrouki, J. Vigneau, A review of developments towards dry and high speed machining of Inconel 718 alloy, *Int. J. Mach. Tools Manuf.* 44 (2004) 439–456.
- [3] A. Höling, L. Hultman, M. Odén, J. Sjölen, L. Karlsson, Mechanical properties and machining performance of Ti1-xAlxN-coated cutting tools, *Surf. Coat. Technol.* 191 (2005) 384–392.
- [4] D. McIntyre, J.E. Greene, G. Håkansson, J.E. Sundgren, W.D. Münz, Oxidation of metastable single-phase polycrystalline TiO. 5AlO. 5N films: Kinetics and mechanisms. *J. Appl. Phys.* 67 (3) (1990) 1542–1553, <https://doi.org/10.1063/1.345664>.
- [5] J. Zhang, Z. Liu, C. Xu, J. Du, G. Su, P. Zhang, X. Meng, Modeling and prediction of cutting temperature in the machining of H13 hard steel of multi-layer coated cutting tools, *Int. J. Adv. Manuf. Technol.* 2021 (2021), 11511–11537.



- [6] O. Banakh, P.E. Schmid, R. Sanjinés, F. Lévy, High-temperature oxidation resistance of Cr<sub>1-x</sub>Al<sub>x</sub>N thin films deposited by reactive magnetron sputtering, *Surf. Coat. Technol.* 163–164 (2003) 57–61.
- [7] L. He, L. Chen, Y. Xu, Y. Du, Thermal stability and oxidation resistance of Cr<sub>1-x</sub>Al<sub>x</sub>N coatings with single phase cubic structure, *J. Vac. Sci. Technol. A Vac. Surf. Film.* 33 (2015), 061513.
- [8] A. Plink, T. Larsson, J. Sjölen, L. Karlsson, L. Hultman, Influence of Si on the microstructure of arc evaporated (Ti,Si)N thin films: evidence for cubic solid solutions and their thermal stability, *Surf. Coat. Technol.* 200 (2005) 1535–1542.
- [9] F. Pei, Y.X. Xu, L. Chen, Y. Du, H.K. Zou, Structure, mechanical properties and thermal stability of Ti<sub>1-x</sub>Si<sub>x</sub>N coatings, *Ceram. Int.* 44 (2018) 15503–15508.
- [10] S. Hofmann, H.A. Jehn, Selective oxidation and chemical state of Al and Ti in (Ti, Al)<sub>n</sub> coatings, *Surf. Interface Anal.* 12 (1988) 329–333.
- [11] Ren Qiu, et al., Atom probe tomography investigation of 3D nanoscale compositional variations in CVD TiAlN nanolamella coatings, *Surf. Coat. Technol.* 426 (2021), 127741.
- [12] D.B. Lee, Y.C. Lee, S.C. Kwon, High temperature oxidation of TiCrN coatings deposited on a steel substrate by ion plating, *Surf. Coat. Technol.* 141 (2001) 232–239.
- [13] T. Nojit, P. Visuttipitukul, K. Taweewap, Thermal oxidation resistance of quaternary TiAlCrN coatings prepared with cathodic arc evaporation, *J. Aust. Ceram. Soc.* (2021) 1–10.
- [14] X. Sui, G. Li, H. Zhou, S. Zhang, Y. Yu, Q. Wang, J. Hao, Evolution behavior of oxide scales of TiAlCrN coatings at high temperature, *Surf. Coat. Technol.* 360 (2019) 133–139.
- [15] M. Danek, F. Fernandes, A. Cavaleiro, T. Polcar, Influence of Cr additions on the structure and oxidation resistance of multilayered TiAlCrN films, *Surf. Coat. Technol.* 313 (2017) 158–167.
- [16] M.R. Alhafian, J.B. Chemin, N. Valle, B. El Adib, M. Penoy, L. Bourgeois, J. Ghanbajac, J. Barrirerod, F. Solderad, F. Mücklich, P. Choquet, Study of the oxidation mechanism at high temperature of nanofiber textured AlTiCrN coatings produced by physical vapor deposition using high-resolution characterization techniques, *Corros. Sci.* 201 (2022), 110226.
- [17] C. Paksunchai, S. Denchithareon, S. Chaiyakun, P. Limsuwan, Growth and characterization of nanostructured TiCrN films prepared by DC magnetron cosputtering, *J. Nanomater.* 2014 (2014).
- [18] R. Forsén, M. Johansson, M. Odén, N. Ghafoor, Decomposition and phase transformation in TiCrAlN thin coatings, *J. Vac. Sci. Technol. A Vac., Surf., Film.* 30 (2012), 061506.
- [19] H.C. Barshilia, M. Ghosh, Shashidhara, R. Ramakrishna, K.S. Rajam, Deposition and characterization of TiAlSiN nanocomposite coatings prepared by reactive pulsed direct current unbalanced magnetron sputtering, *Appl. Surf. Sci.* 256 (2010) 6420–6426.
- [20] C. Hu, L. Chen, Y. Lou, N. Zhao, J. Yue, Influence of Si content on the microstructure, thermal stability and oxidation resistance of TiAlSiN/CrAlN multilayers, *J. Alloy. Compd.* 855 (2021), 157441.
- [21] F. Pei, H.J. Liu, L. Chen, Y.X. Xu, Y. Du, Improved properties of TiAlN coating by combined Si-addition and multilayer architecture, *J. Alloy. Compd.* 790 (2019) 909–916.
- [22] M. Parlinska-Wojtan, A. Karimi, O. Coddet, T. Cselle, M. Morstein, Characterization of thermally treated TiAlSiN coatings by TEM and nanoindentation, *Surf. Coat. Technol.* 188–189 (2004) 344–350.
- [23] J.B. Choi, K. Cho, M.H. Lee, K.H. Kim, Effects of Si content and free Si on oxidation behavior of Ti–Si–N coating layers, *Thin Solid Films* 447–448 (2004) 365–370.
- [24] Y. Tanaka, N. Ichimiya, Y. Onishi, Y. Yamada, Structure and properties of Al–Ti–Si–N coatings prepared by the cathodic arc ion plating method for high speed cutting applications, *Surf. Coat. Technol.* 146–147 (2001) 215–221.
- [25] J.C. Oliveira, F. Fernandes, F. Ferreira, A. Cavaleiro, Tailoring the nanostructure of Ti–Si–N thin films by HIPIMS in deep oscillation magnetron sputtering (DOMS) mode, *Surf. Coat. Technol.* 264 (2015) 140–149.
- [26] Q. Ma, L. Li, Y. Xu, X. Ma, Y. Xu, H. Liu, Effect of Ti content on the microstructure and mechanical properties of TiAlSiN nanocomposite coatings, *Int. J. Refract. Met. Hard Mater.* 59 (2016) 114–120.
- [27] S. Carvalho, L. Rebouta, A. Cavaleiro, L.A. Rocha, J. Gomes, E. Alves, Microstructure and mechanical properties of nanocomposite (Ti,Si,Al)<sub>n</sub> coatings, *Thin Solid Films* 398–399 (2001) 391–396.
- [28] K. Bobzin, T. Brogelmann, N.C. Kruppe, M. Carlet, Wear behavior and thermal stability of HPPMS (al, ti, cr, si) ON (Al, ti, cr, si) n and (ti, al, cr, si) n coatings for cutting tools, *Surf. Coat. Technol.* 385 (2020), 125370.
- [29] J. Huang, S.H. Zhang, C.W. Zou, X.B. Zhang, Q.M. Wang, C.Y. Wang, Fabrication of multi-component Cr–Al–Ti–Si–N coatings by arc ion plating for high-speed machining, *Sci. Adv. Mater.* 10 (1) (2018) 1–7, <https://doi.org/10.1166/sam.2018.2850>.
- [30] M.R. Alhafian, J.B. Chemin, Y. Fleming, L. Bourgeois, M. Penoy, R. Useldinger, F. Soldera, F. Mücklich, P. Choquet, Comparison of the structural, mechanical and tribological properties of TiAlN coatings deposited by HIPIMS and cathodic arc evaporation, *Surf. Coat. Technol.* 423 (2021), 127529.
- [31] P.J. Withers, M. Preuss, A. Steuwer, J. Pang, Methods for obtaining the strain-free lattice parameter when using diffraction to determine residual stress, *J. Appl. Crystallogr.* 40 (5) (2007) 891–904, <https://doi.org/10.1107/S0021889807030269>.
- [32] Reference to a website: Anton Paar, Instrumented indentation testing (<https://wiki.anton-paar.com/en/instrumented-indentation-testing-ii/>).
- [33] S.M. Reddy, D.W. Saxe, W.D. Rickard, D. Fougereuse, S.D. Montalvo, R. Verberne, A. Van Riessen, Atom probe tomography: development and application to the geosciences, *Geostand. Geoanal. Res.* 44 (1) (2020) 5–50.
- [34] A. Joshi, H.S. Hu, Oxidation behavior of titanium-aluminum nitrides, *Surf. Coat. Technol.* 76 (1995) 499–507.
- [35] R. Aninat, N. Valle, J.-B. Chemin, D. Duda, C. Michotte, M. Penoy, L. Bourgeois, P. Choquet, Addition of Ta and Y in a hard Ti–Al–N PVD coating: Individual and conjugated effect on the oxidation and wear properties, *Corros. Sci.* 156 (2019) 171–180.
- [36] D. Rafaja, C. Wüstefeld, M. Dopita, M. Růžicka, V. Klemm, G. Schreiber, D. Heger, M. Šima, Internal structure of clusters of partially coherent nanocrystallites in Cr–Al–N and Cr–Al–Si–N coatings, *Surf. Coat. Technol.* 201 (24) (2007) 9476–9484.



## 8 Perspectives and outlook

This thesis represents the first systematic work related to the investigation and implementation of the high power pulsed technology in the (LIST) laboratory. It is focused mainly on characterization of the HiPIMS coatings discharges operated in the various working gas compositions and pressures. However, this work also reports on the fabrication and characterization of the model metal nitride coatings in a great variety of conditions. Such a systematic study established a solid background for further directions of research. Based on the results obtained in this thesis, the perspectives and suggestions of possible research trends that could follow this work will be presented in this chapter.

- The work conditions of this type of coating required both good mechanical properties and oxidation stability at elevated temperature. It would be interesting to complement this study by the diagnostics of multilayer coatings where one layer responds to mechanical properties and the other to the oxidation stability needed. e.g. the possible engineering of multi-layered TiAlN/AlTiCrN, TiAlN/TiAlSiN or TiAlCrN/TiAlCrSiN coatings for the optimisation of resistance to plastic deformation and hot wear resistance. It is assumed that a better thermal insulation, commonly found for high-Al coatings. In addition, the layer thickness, the adhesion, the internal stresses between the layers and the crack propagation are such investigations that would enable a better understanding of multilayer structure effects.

In fact, the monolayer coating leads to crack propagation rapidly to the substrate. Some expectation from multi-layering coatings:

- Reduction of potentially overlapping influences of different coating layers helps relax stresses at interfaces, ultimately minimizing the total stress level of the coatings.
- Layer thickness is simply required to be constant to avoid any significant micro- or nanostructural influence on the coating's performance. This hold true even for chemically identical multi-layering structures. This means that multilayer coatings fail in a laminar manner.
- Delaying the occurrence of indentation induced large cracks, as can be deduced from higher values of the fracture toughness and the critical load for cracking.

- Nanostructured layers prevent crack propagation where the micro-cracks develop mainly in the vicinity of the top surface and, in turn, the interfaces between layers can substantially change the direction of the initial crack when it penetrates deep into the coating, hence overall retarding coating crack formation.

- Different researchers have pointed to the super-lattice concept [143 - 145], which could be one of the evolutions of multilayer coatings. It is based on the deposition of a layered structure of two materials with the growth of a single crystal structure where interfaces between the layers would provide energy barriers to the motion of dislocations, where a single layer thickness is in the size of the lattice parameter of the coated material. It generally shows very good mechanical properties different from normal multilayer coatings.

We recommend further research on nanocomposite monolayer or nano-layer TiAlSiN to improve the oxidation resistance and mechanical properties of this coating.

## 9 Appendix

In order to achieve the maximum benefit of the experiments and investigations done during this study, this chapter will introduce some modification, which is used in the thesis to prepare the samples or modify some parameters that have not been published since it is not in the focus consideration of the study or it needs deeper investigation later by other researchers.

### 9.1 Stoichiometric curve

To stabilise the deposition conditions of both sputtering processes HiPIMS and dcMS in the full-reactive target mode, implemented feedback control of the gas flow was done based on the monitoring of the reactive gas partial pressure, the cathode voltage and optical emission spectra from the discharge particles (Figure 9.1).

At higher pressures, the mean free path of the electron is short. The electrons do not gain enough energy from the electric field to ionise the gas atoms or molecules due to their frequent collisions with the gas molecules. Therefore, cathode voltage increases as the pressure increases, whereas at lower pressures, the ionisation process is ineffective due to the low electron-neutral collision probability.

The relation between the cathode voltage and the current for the discharge particles can be classified as follows:

- First, when a voltage is applied, the discharge current is very small. This current consists of contributions from various external sources such as cosmic radiation generating free electrons and ions.
- Second, when the voltage has become large enough to collect all these charged particles, this current remains nearly constant with increased voltage.
- Third, when the voltage is further increased, the charged particles eventually obtain enough energy to produce more charged particles through collisions with the working gas atoms or by a bombardment of the electrodes leading to a generation of secondary electrons. As more

charged particles are created, the current increases while the voltage is limited by the output impedance of the power supply and remains roughly constant.



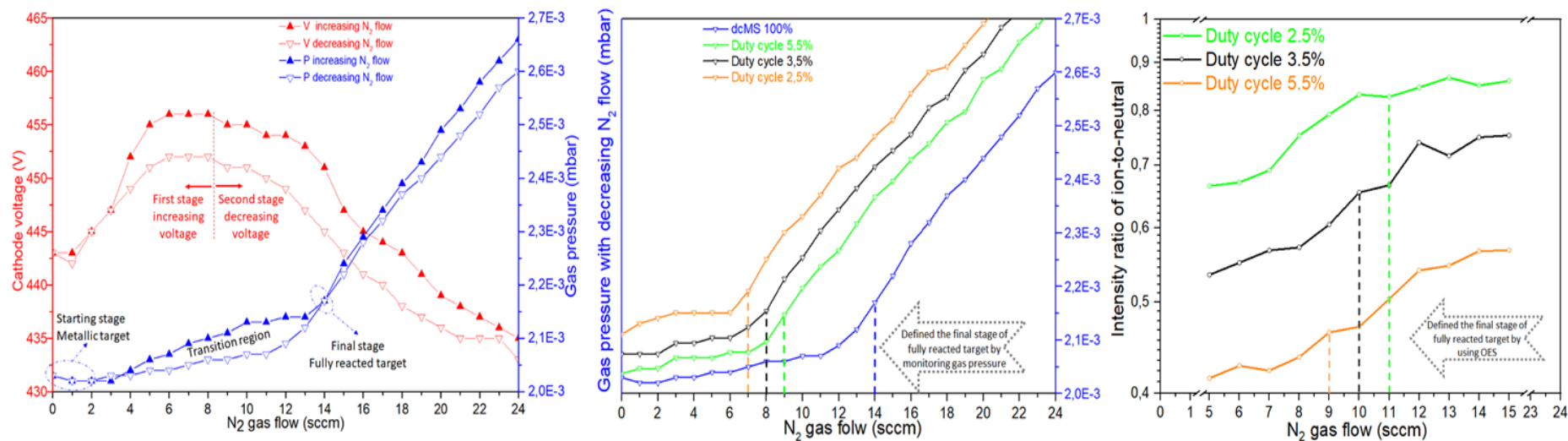


Fig. 9.1 Hysteresis curves for the reactive sputtering discharge of dcMS above TiAl cathode in N<sub>2</sub>/Ar mixture. The transition region between the metallic and poisoned target, the two-stage of cathode charge are highlighted (left). The full reactive mode (poisoning) target by dcMS requires a higher amount of N<sub>2</sub> flow than HiPIMS for same applied power density, as well as increasing duty cycles, increase the required N<sub>2</sub> flow for poisoning (middle). Using Optical emission spectrum to define the required N<sub>2</sub> flow for poisoning target is more precise than using gas pressure (right).

The determination of the N<sub>2</sub> flow by OES is more reliable for the different duty cycle more using gas pressure, as figure 9.1 describes. The best condition inside the chamber during the coating has been chosen by using OES for ion/neutral ratio in order to form stoichiometric coatings. At this condition, no more reactive gas can be absorbed neither on the substrate nor on the chamber walls subsequently. When the gas starts to react on the target surface and supply its materials, the compound formation rate on the target rises with increasing the gas supplied. Therefore the voltage decreases. As a result, the partial pressure of the unused reactive vapours in the chamber (the total pressure) increases. This further intensified coating formation rate on the cathode until its full coverage. The transition in the target composition from the metallic to the poisoned regime is also reflected by an abrupt drop in the voltage, due to the rise in secondary electron intensity. A further rise in N<sub>2</sub> is followed by a linear growth of pressure while voltage stays constant.

Conversion of the target back from the poisoned to the metallic state occurs at a lower value of N<sub>2</sub> flow, because of the lower voltage for the formed oxide layer. Thus, both curves for voltage and pressure follow different pathways with increasing and decreasing N<sub>2</sub> flow. This phenomenon is known as hysteresis and presents a challenge for the deposition of compound coatings. In order to prepare a stoichiometric coating at a viable deposition rate, one has to operate the discharge at a certain critical value of the reactive gas flow that is at the edge of the transition towards the poisoned target state.

## 9.2 Energetics of adhesion

Adhesion is defined as the interaction between the closely contiguous surfaces, e.g. a film and substrate where the two surfaces are held together by valence forces. Film adhesion to the substrate is certainly the first attribute a film must possess before any of its other properties can be further successfully exploited.

Adhesion problem of coatings on Si substrate by HiPIMS has been shown for all coating conditions, as opposed to dcMS coatings. Coatings on the WC-Co substrate exhibit better coating adhesion than on Si for the same coating's condition (see figure 9.2) since substrates with increased roughness offer better adhesion.

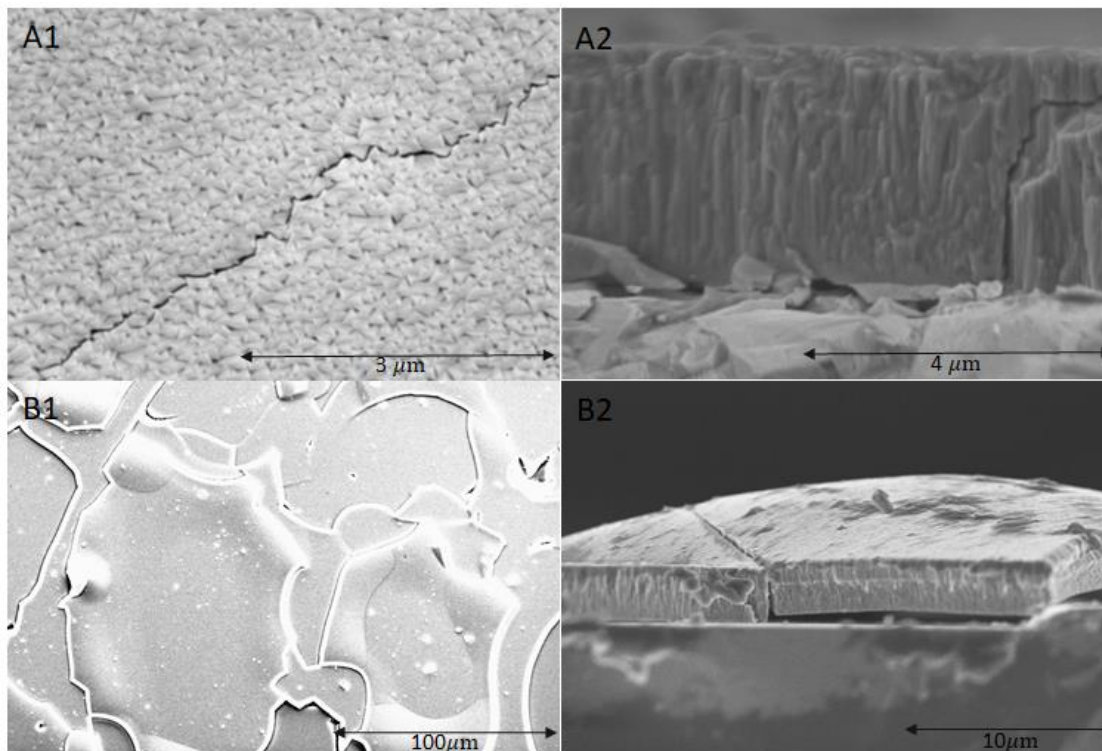


Fig. 9.2 Top-view image of the crack propagation on the coating's surface on WC-Co substrate (A1). The cross-section image of the vertical and branching crack propagation between the coating columns on WC-Co substrate (A2). Top-view image of the scales coatings formed on Si substrate resulting from weakly adhesion (B1) and cross-section (B2).

Bad adhesion, delamination and visible cracks on the surface induced by internal stresses are presented in the figure above. In dealing with these difficult subject, different approaches were used to improve the adhesion, chief among these approaches are the following.

### 9.2.1 Plasma ion etching

Substrate pre-treatment (plasma etching) is defined as the removal of material from the surface via plasma processes [17] which was carried out in our study by using stable microwave antennas discharge with low output power (150 W) and (Ar = 50 sccm) to have stable pressure in the chamber of  $0.85 \mu\text{bar}$  at  $450 \text{ }^\circ\text{C}$ . The noble gas argon formed ions; the etching effect is based on the knocking out of atoms or molecules from the substrate by the kinetic energy of the electrons accelerated in the electric field. By applying a negative bias voltage to the substrate the kinetic energy of the ions can be used by accelerating the ions in

the electric field and using them to bombard the substrate. By bombardment with ions, the substrate molecules are put into an excited state that makes them more reactive. Hence, the etching rate is considerably increased. However, plasma etching is only carried out in low-pressure because a longer treatment duration is necessary to achieve noticeable etching effects. Figure 9.3 presented four different approaches of etching with different bias voltage duration.

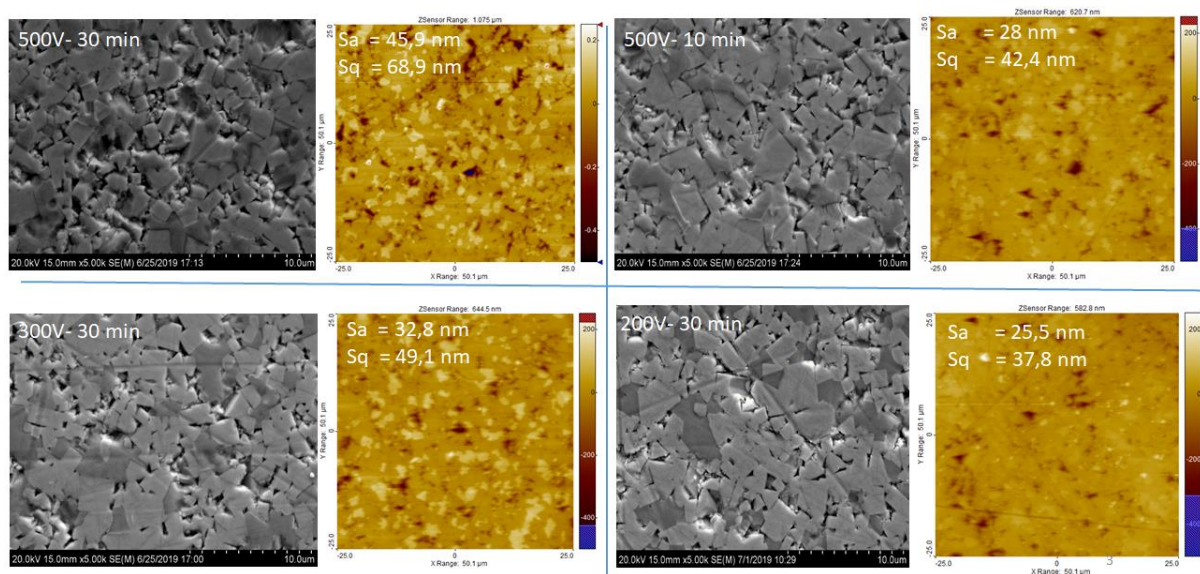


Fig. 9.3 Top-view images in the scanning electron microscope (SEM) and the 3D Maps view by Atomic Force Microscopy (AFM) for the WC-Co substrates after different biases exposure time.

Where Sq and Sa are Root mean square height and arithmetical mean height, respectively.

Etching the surface of the cemented tungsten carbide was used in order to sputter-clean the surface oxides and other impurities prior to film deposition. A rough surface with gaps and cavities is observed in the figure above; this is attributable to the duplication of the microstructure etching of WC-Co where cavities are in relation to strong cobalt binder etching. In other words, the cobalt is softer than tungsten and since bias is applied to the substrate is increasing the energy of argon ions impact in the plasma, the strong ionic impact will damage mainly the cobalt and remove it, while it will let the tungsten carbide that formed grains with cavities between them.

### 9.2.2 An intermediate layer

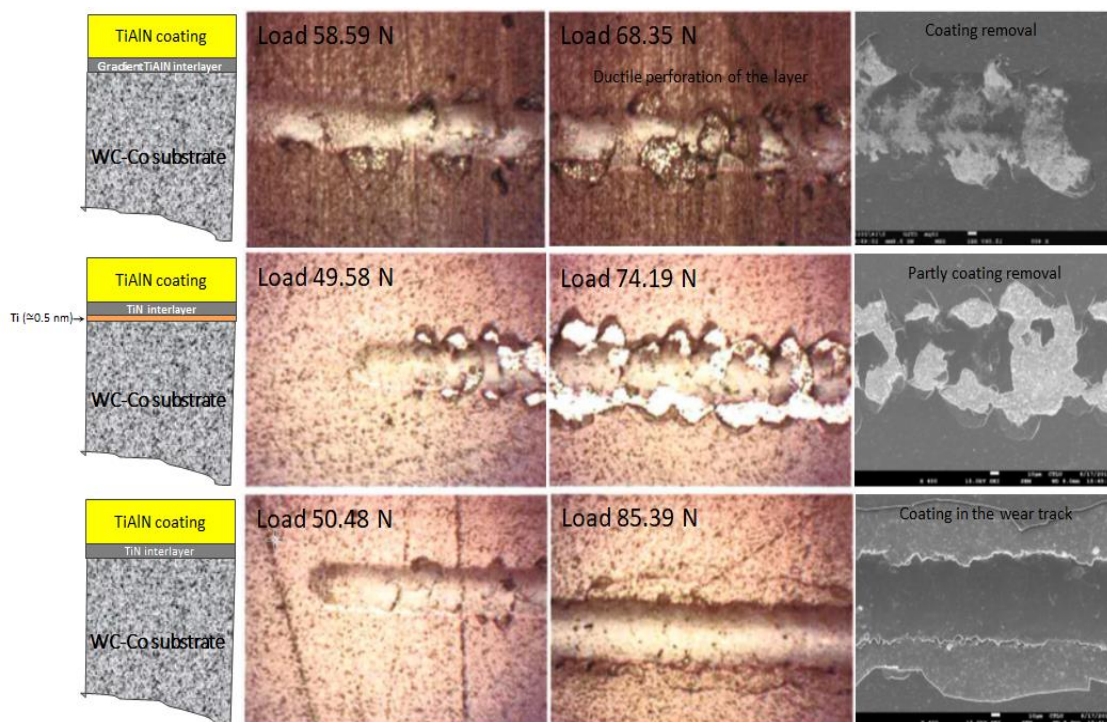
In order to achieve an efficient substrate-film, the interface must be tailored because it plays an important role in the ability of the coating to have good adherence to the substrate and



transfer load without delamination. Furthermore, the high hardness of the substrate is supposed to be not negatively affected by coatings, which is ensured by the interlayer. Clearly, a detailed understanding of this interface is essential to better predict the behavior of the macro-system.

Even though the nature of bonding and the microscopic details of the electronic and chemical interactions at the film-substrate interface is of critical importance to adhesion, the primary focus of this study is to view the effect of adhesion on film quality, durability, and environmental stability. To achieve this, a mechanical scratch test was used to measure the force or energy required to separate the film from the substrate.

The coatings were scratched according to ISO 20502 standard [146] by applying an increasing force from 50 N to 100 N to diamond stylus with a rate of increasing force of 10 N/min and an indenter traverse speed of 10 mm/min to promote adhesive and/or cohesive failure of the coating-substrate system. Failure events were detected by direct microscopic observation of the scratch. Figure 9.4 shows three types of interlayers which were deposited by dcMS with around ( $\approx 0.5 \mu\text{m}$ ) thickness to improve the coating adhesion. The study covered: TiN interlayer, TiAl interlayer with a gradient content of N in order to pass from metallic to nitride coatings and Ti interlayer around ( $\approx 0.5 \text{ nm}$ ) thickness followed by TiN.



---

Fig. 9.4 Schematic representation of TiAlN coating with the different intermediate layers, the binocular images of scratch test track at starting and near ending test, as well as the electron microscopy images of near ending test.

The critical forces where failure events start to appear is not only dependent on the coating adhesion strength but also on other parameters, which are directly related to the test itself (e.g. the rate of increasing force, traverse speed and diamond-tip wear). Others are related to the coating-substrate system (e.g. the roughness of coating and their substrate, inter-diffusion effects, internal film stresses, interfacial impurities, imperfect contact). This critical force is a combination of elastic-plastic indentation stresses, frictional stresses and the residual internal stress present in the coating.

Clearly the coating with gradient TiAlN interlayer under a weak transversal load is systematically entirely removed from the substrate of what is called continuous ductile perforation of the coating. Whereas the TiN interlayer had improved the adherence of the coating-substrate system and transferred load without delamination.

### 9.3 Impact of substrate temperature

Set of films were studied under the same deposition conditions at 300 °C, 400 °C and 450 °C substrate temperature (Figure 9.5). Generally, heating the substrates during the deposition process is used to increase the energy flux towards the forming film, where the mobility of the film-forming species (adatoms) is impacted by substrate temperature, higher temperature leads to higher adatoms. Consequently, enhanced surface diffusion may contribute to the desired film densification. Many researchers reported that an increase in substrate temperature leads to an increase in surface mobility of atoms, leading to the accommodation of atoms in special lattice positions with lower energy. Thus, increasing substrate temperature plays an important role in increasing crystallinity, growing the size of grains forming films, which strengthening preferred crystallographic orientation, as well as it leads to the rougher film surface [147 - 149].

Nevertheless, there is no noticeable change in the coating structure and content, as well as in the grain size or surface roughness since the temperature range is small. In contrast, an



improvement of the deposition rate from 85 to 100 nm/min was achieved at a higher temperature.

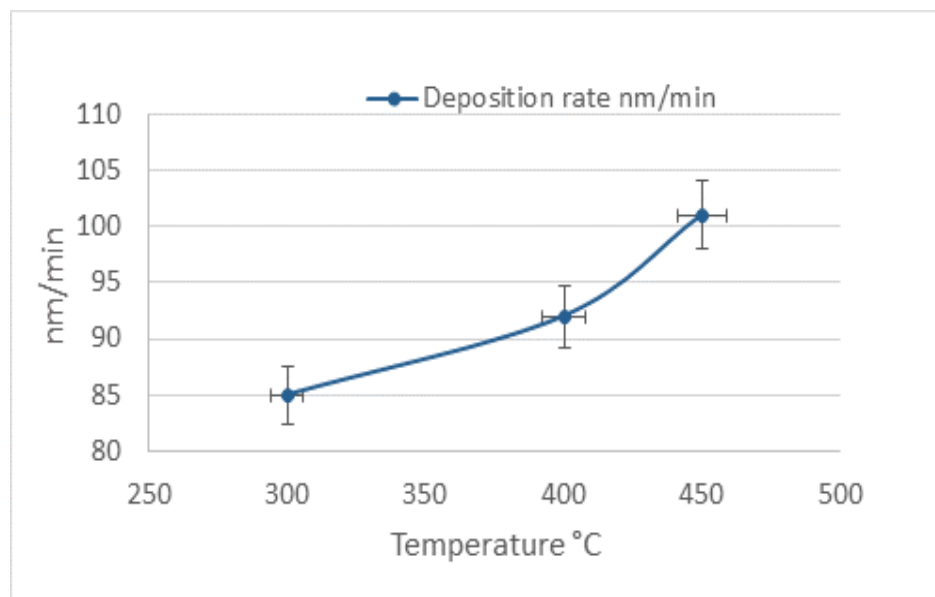


Fig. 9.5 The change of deposition rate at different substrate temperatures.

## 9.4 Coatings thermal response

### 9.4.1 Isotherm and temperature sweep tests by TGA

The study of oxidative behavior of coated alumina spacers was started by using two types of TGA analysis. First, Temperature sweep tests under an inert atmosphere during the heating from room temperature to 1100 °C on the average of 5 K/min using O<sub>2</sub> 40 ml/min synchronisation (Figure 9.6). Second, isotherm tests at 900 °C and 950 °C for 13 and 2 hours, respectively (Figure 9.7).

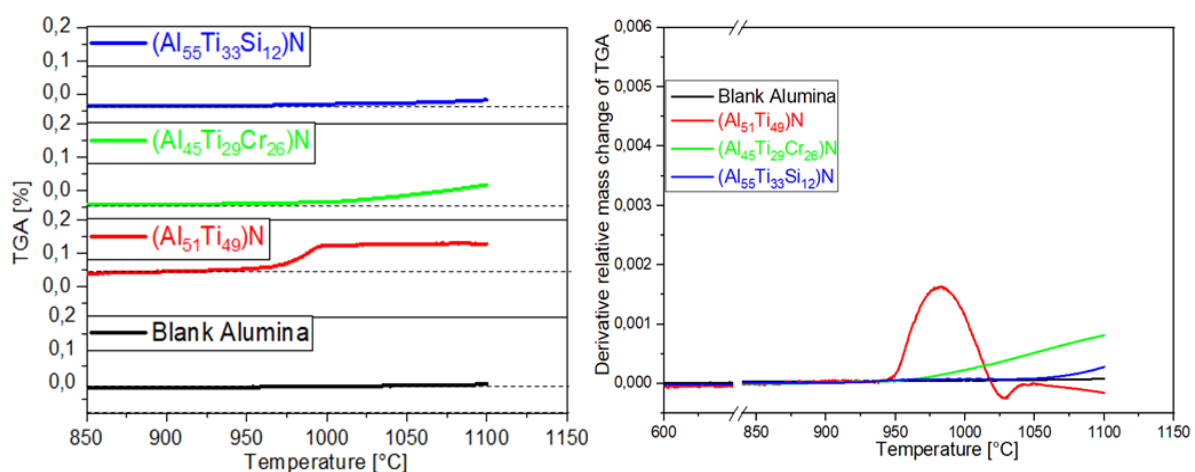


Fig. 9.6 In-situ measurements of the mass change of one uncoated blank alumina as a reference signal and three coated one by  $\text{Al}_{51}\text{Ti}_{49}\text{N}$ ,  $\text{Al}_{45}\text{Ti}_{29}\text{Cr}_{26}\text{N}$  and  $\text{Al}_{55}\text{Ti}_{33}\text{Si}_{12}\text{N}$  during heating from room temperature until 1100 °C (left), and the derivative relative mass change of its (right).

Figure 9.6 (left) shows that the mass of the reference blank alumina (used as baseline) is constant until 1100 °C, which is the critical temperature of the TGA equipment. This temperature was the highest temperature that could be reached in the thermogravimetric used in this work. The mass of  $\text{Al}_{51}\text{Ti}_{49}\text{N}$  coated sample is approximately constant up to ~950 °C, followed with a slight increase in mass change for 50 °C indicative of onset oxidation and followed by a mass plateau. The mass of  $\text{Al}_{45}\text{Ti}_{29}\text{Cr}_{26}\text{N}$  coated sample is constant up to ~1000 °C followed by a remarkable increase in mass change indicative of onset oxidation. On the other hand, the mass of  $\text{Al}_{55}\text{Ti}_{33}\text{Si}_{12}\text{N}$  is almost constant up to ~1050 °C.

The derivative relative mass change of these four samples was plotted in figure 9.6 (right) to precisely define the onset of oxidation temperature, where 950 °C was the defined temperature for  $\text{Al}_{51}\text{Ti}_{49}\text{N}$  and  $\text{Al}_{45}\text{Ti}_{29}\text{Cr}_{26}\text{N}$  with different increase of mass ratio. The sample without Cr content has an accelerated mass increase. The mass start increases at 1050 °C for  $\text{Al}_{55}\text{Ti}_{33}\text{Si}_{12}\text{N}$  with a different amount of mass increase than the sample without Si content.

For a better understanding of this behavior of Cr and Si addition to TiAlN coatings, isothermal reactions were plotted in figure 9.7. TGA curves of  $\text{Al}_{51}\text{Ti}_{49}\text{N}$  and  $\text{Al}_{37}\text{Ti}_{36}\text{Cr}_{27}\text{N}$  were presented with similar behavior of weight increase ratio at 900 °C after 2 hours of heating where the change of initial weight is faster for the sample without Cr content. At a high temperature of 950 °C, the  $\text{Al}_{51}\text{Ti}_{35}\text{Si}_{14}\text{N}$  presents a slower increase of initial weight change compared with  $\text{Al}_{43}\text{Ti}_{31}\text{Cr}_{26}\text{N}$  presenting different oxidation kinetics.

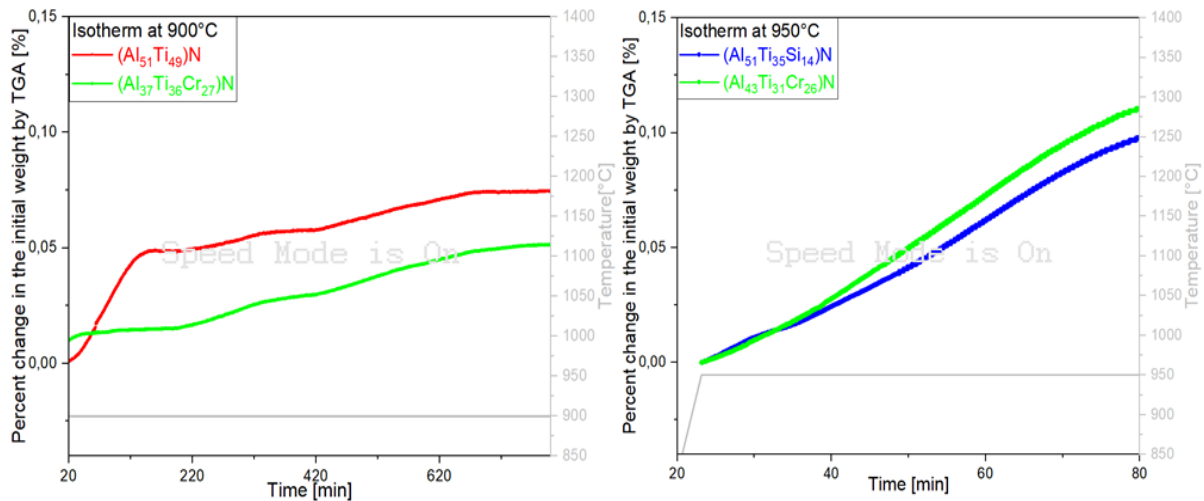


Fig. 9.7 In-situ measurements of the weight change of  $\text{Al}_{51}\text{Ti}_{49}\text{N}$ ,  $\text{Al}_{37}\text{Ti}_{36}\text{Cr}_{27}\text{N}$  at  $900\text{ }^{\circ}\text{C}$  (left) and  $\text{Al}_{51}\text{Ti}_{35}\text{Si}_{14}\text{N}$ ,  $\text{Al}_{43}\text{Ti}_{31}\text{Cr}_{26}\text{N}$  at  $950\text{ }^{\circ}\text{C}$  (right).

Since the coating is very thin  $3.5\mu\text{m}$  in comparison to the substrate, a spacer from  $\text{Al}_2\text{O}_3$ , ( $\varnothing 8 \times 0.6\text{ mm}$ ) was used. The signal from the substrate completely dominates the measuring signal of the coating since they were measured together. Unfortunately, repeating these experiments has not improved the observation of oxidation mechanisms. Nevertheless, it clarified that the onsets of oxidation of the coated sample with  $\text{TiAlN}$  and  $\text{TiAlCrN}$  are quite similar where the kinetic growth of oxidation was demoted by Cr addition to the coatings. The Si addition to the coatings plays another role in that it enhances the onset oxidation about  $\sim 100\text{ }^{\circ}\text{C}$  than the coating without Si addition.

In order to measure the thermal response of the coating, the substrate has to be removed. In fact, this is very tough work. Forsèn et al. recommended the preparation of TGA samples and the measurement up to  $1400\text{ }^{\circ}\text{C}$  by doing a very thick coating  $\sim 10\mu\text{m}$  onto Fe foils thereafter mechanically grinded and subsequently dissolved in hydrochloric acid  $\text{HCl}(37\%)$ . The remaining coating was filtered, cleaned with acetone and crushed. The result is a powder sample ready for thermal analysis [1]. Considering the maximum instrument's temperature for METTLER TGA 2 SF in our laboratory, which has the limitation of  $1100\text{ }^{\circ}\text{C}$ , no further experiments were planned.

#### 9.4.2 Study Ti/Al ratio effect by SIMS

The influence of the Ti/Al content on the oxidation behavior of three different (Ti,Al)N coatings alloys was studied by D-SIMS after annealing for 1 hour at  $1000\text{ }^{\circ}\text{C}$  in a Nabertherm

50/250/12 tube furnace. The samples  $\text{Al}_{37}\text{Ti}_{35}\text{Cr}_{28}\text{N}$ ,  $\text{Al}_{43}\text{Ti}_{33}\text{Cr}_{24}\text{N}$  and  $\text{Al}_{48}\text{Ti}_{30}\text{Cr}_{22}\text{N}$  were coated under the same condition by three different ratios of Al/Ti targets 50/50, 55/45, 60/40 and same Cr target, respectively. The alumina substrates were used during the deposit and later annealed, as stated above. Figure 9.8 shows the SIMS analyses of the oxidation part of the coatings. The data indicates inward  $\text{O}_2$  diffusion and accelerated outward Ti-diffusion, while Al significantly slows down both mechanisms, leading to much thinner oxides with higher Al coatings content. Furthermore, the shift to higher oxidation thickness was observed when decreasing the Al content in the Al/Ti target ratio.

In all coatings, the oxidized part can be divided in two regions: a Ti-rich region and AlCr-rich region. Furthermore, Ti shows a plateau in his region followed by a drastic decrease of Ti intensity to the second region. This indicates a pure  $\text{TiO}_2$  layer on the top of the oxidized part of the coatings followed by the  $\text{Al}(\text{Cr})_2\text{O}_3$  oxide region.

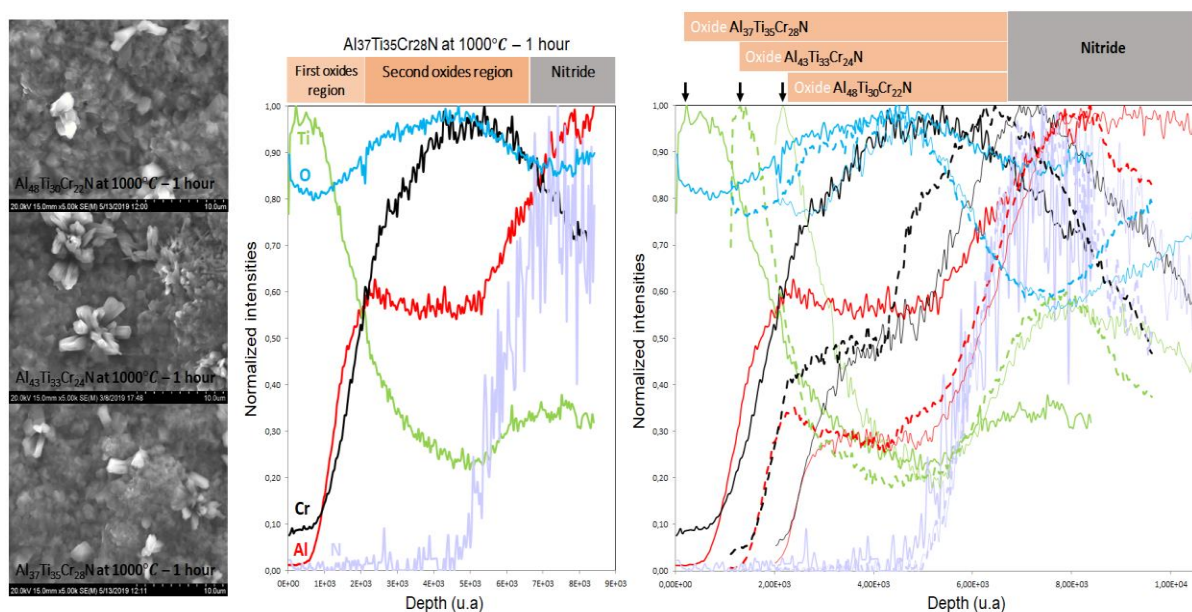


Fig. 9.8 SEM Top-view image of the oxide crystal growth on the  $\text{Al}_{37}\text{Ti}_{35}\text{Cr}_{28}\text{N}$ ,  $\text{Al}_{43}\text{Ti}_{33}\text{Cr}_{24}\text{N}$  and  $\text{Al}_{48}\text{Ti}_{30}\text{Cr}_{22}\text{N}$ . SIMS analysis of the oxidized samples  $\text{Al}_{37}\text{Ti}_{35}\text{Cr}_{28}\text{N}$  presenting the two oxides regions, as well as the comparative SIMS analysis of the oxidation part of the three coatings using the N intensity as a baseline.

All coatings were corresponding to the formation of the same oxide layer and displayed a grain-like and needle-like structure after the oxidation test at 1000 °C for an hour as the SEM images show.

The sensitivity of the SIMS analysis was affected by the topography of the Alumina substrate. The roughness of this substrate made the focused primary ion beam impacted by the surroundings ejected secondary ions (e.g. the beam affected not only from the focusing point but also from the nearest mountain). The high annealing temperature affects these results because the Ti diffuses vastly to the oxidation surface, and that makes the oxidation mechanism not easy to detect. The higher is the Al content, the lower is the oxidation kinetics of the coatings. To better understand the effect of Al/Ti ratio on the oxidation, the experiments were repeated at 950 °C for the coatings on smoother substrates (for more details see the paper II).

---

## 10 References

1. Forsén, Rikard. Mechanical properties and thermal stability of reactive arc evaporated Ti-Cr-Al-N coatings. Diss. Linköping University Electronic Press, 2012.
2. Benítez, Isabella Citlalli Schramm. Defect-engineered (Ti, Al) N thin films. Vol. 1878. Linköping University Electronic Press, 2017.
3. Norrby, Niklas, et al. "Pressure and temperature effects on the decomposition of arc evaporated Ti<sub>0.6</sub>Al<sub>0.4</sub>N coatings in continuous turning." *Surface and Coatings Technology* 209 (2012): 203-207.
4. Jehn, H. A., et al. "Characterization of PVD (Ti, Cr) N<sub>x</sub> hard coatings." *Surface and Coatings Technology* 50.1 (1991): 45-52
5. Grove, William Robert. "VII. On the electro-chemical polarity of gases." *Philosophical Transactions of the Royal Society of London* 142 (1852): 87-101
6. Edison, Thomas A. "Process of coating phonograph-records." U.S. Patent No. 713,863. 18 Nov. 1902
7. Kouznetsov, Vladimir, et al. "A novel pulsed magnetron sputter technique utilizing very high target power densities." *Surface and coatings technology* 122.2-3 (1999): 290-293.
8. Vlček, J., et al. "Ion flux characteristics in high-power pulsed magnetron sputtering discharges." *EPL (Europhysics Letters)* 77.4 (2007): 45002.
9. Sarakinos, Kostas, Jones Alami, and Stéphanos Konstantinidis. "High power pulsed magnetron sputtering: A review on scientific and engineering state of the art." *Surface and Coatings Technology* 204.11 (2010): 1661-1684.
10. Anders, André. "Discharge physics of high power impulse magnetron sputtering." *Surface and Coatings Technology* 205 (2011): S1-S9.
11. Gudmundsson, Jon Tomas, et al. "High power impulse magnetron sputtering discharge." *Journal of Vacuum Science & Technology A: Vacuum, Surfaces, and Films* 30.3 (2012): 030801.
12. Lundin, Daniel, and Kostas Sarakinos. "An introduction to thin film processing using high-power impulse magnetron sputtering." *Journal of Materials Research* 27.5 (2012): 780-792.
13. Pasko, Victor P. "Red sprite discharges in the atmosphere at high altitude: the molecular physics and the similarity with laboratory discharges." *Plasma sources science and technology* 16.1 (2007): S13.



14. Alami, Jones, et al. "Ion-assisted physical vapor deposition for enhanced film properties on nonflat surfaces." *Journal of Vacuum Science & Technology A: Vacuum, Surfaces, and Films* 23.2 (2005): 278-280.
15. Alami, Jones, et al. "On the relationship between the peak target current and the morphology of chromium nitride thin films deposited by reactive high-power pulsed magnetron sputtering." *Journal of Physics D: Applied Physics* 42.1 (2008): 015304.
16. Hala, Matej. *Characterization of high-power impulse magnetron sputtering discharges*. Ecole Polytechnique, Montreal (Canada), 2011.
17. Ehiasarian, Arutiun P., J. G. Wen, and Ivan Petrov. "Interface microstructure engineering by high power impulse magnetron sputtering for the enhancement of adhesion." *Journal of applied physics* 101.5 (2007): 054301.
18. Poolcharuansin, Phitsanu, Bernd Liebig, and James Bradley. "Plasma parameters in a pre-ionized HiPIMS discharge operating at low pressure." *IEEE transactions on plasma science* 38.11 (2010): 3007-3015.
19. Colligon, John S. "Energetic condensation: Processes, properties, and products." *Journal of Vacuum Science & Technology A: Vacuum, Surfaces, and Films* 13.3 (1995): 1649-1657.
20. Yushkov, Georgy Yu, and André Anders. "Origin of the delayed current onset in high-power impulse magnetron sputtering." *IEEE Transactions on Plasma Science* 38.11 (2010): 3028-3034.
21. Mishra, Anurag, P. J. Kelly, and J. W. Bradley. "The evolution of the plasma potential in a HiPIMS discharge and its relationship to deposition rate." *Plasma Sources Science and Technology* 19.4 (2010): 045014.
22. Rossnagel, S. M. "Gas density reduction effects in magnetrons." *Journal of Vacuum Science & Technology A: Vacuum, Surfaces, and Films* 6.1 (1988): 19-24.
23. Posadowski, Witold M., and Zbigniew J. Radzimski. "Sustained self-sputtering using a direct current magnetron source." *Journal of Vacuum Science & Technology A: Vacuum, Surfaces, and Films* 11.6 (1993): 2980-2984.
24. Gudmundsson, J. T., et al. "On the electron energy in the high-power impulse magnetron sputtering discharge." *Journal of Applied Physics* 105.12 (2009): 123302.
25. Samuelsson, Mattias, et al. "On the film density using high power impulse magnetron sputtering." *Surface and Coatings Technology* 205.2 (2010): 591-596.
26. West, Glen, et al. "Measurements of deposition rate and substrate heating in a HiPIMS discharge." *Plasma Processes and Polymers* 6.S1 (2009): S543-S547

27. Anders, Andre. "Deposition rates of high power impulse magnetron sputtering: Physics and economics." *Journal of Vacuum Science & Technology A: Vacuum, Surfaces, and Films* 28.4 (2010): 783-790.
28. Bennett, Shannon N., et al. "Reconstructing the evolutionary origins and phylogeography of hantaviruses." *Trends in microbiology* 22.8 (2014): 473-482.
29. Ganciu-Petcu, Mihai, et al. "Pulsed magnetron sputtering deposition with preionization." U.S. Patent No. 7,927,466. 19 Apr. 2011.
30. G. Greczynski, J. Lu, M. Johansson, J. Jensen, I. Petrov, J.E. Greene, L. Hultman, Selection of metal ion irradiation for controlling Ti<sub>1-x</sub>Al<sub>x</sub>N alloy growth via hybrid HIPIMS/magnetron co-sputtering, *Vacuum*. 86 (2012) 1036–1040, <https://doi.org/10.1016/j.vacuum.2011.10.027>.
31. Q. Luo, S. Yang, K.E. Cooke, Hybrid HIPIMS and DC magnetron sputtering deposition of TiN coatings: Deposition rate, structure and tribological properties, *Surf. Coat. Technol.* 236 (2013) 13–21, <https://doi.org/10.1016/j.surfcoat.2013.07.003>.
32. N. Holtzer, O. Antonin, T. Minea, S. Marnieros, D. Bouchier, Improving HiPIMS deposition rates by hybrid RF/HiPIMS co-sputtering, and its relevance for NbSi films, *Surf. Coatings Technol.* 250 (2014) 32–36, <https://doi.org/10.1016/j.surfcoat.2014.02.007>
33. V. Stranak, S. Drache, R. Bogdanowicz, H. Wulff, A.-P. Herrendorf, Z. Hubicka, M. Cada, M. Tichy, R. Hippler, *Surf. Coat. Technol.* 206 (2012) 2801
34. V. Stranak, A.-P. Herrendorf, S. Drache, M. Cada, Z. Hubicka, M. Tichy, R. Hippler, *Appl. Phys. Lett.* 100 (2012) 141604
35. S. Konstantinidis, J.P. Dauchot, M. Ganciu, M. Hecq, *Appl. Phys. Lett.* 88 (2006) 021501
36. Hultman, Lars. "Thermal stability of nitride thin films." *Vacuum* 57.1 (2000): 1-30.
37. Raumann, Leonard, Denis Music, and Jochen M. Schneider. "Origin of the nitrogen over-and understoichiometry in Ti<sub>0.5</sub>Al<sub>0.5</sub>N thin films." *Journal of Physics: Condensed Matter* 24.15 (2012): 155401.
38. Zhang, Guojun, et al. "Microstructure and tribological properties of TiN, TiC and Ti (C, N) thin films prepared by closed-field unbalanced magnetron sputtering ion plating." *Applied Surface Science* 255.21 (2009): 8788-8793.
39. Samani, M. K., et al. "Thermal conductivity of titanium nitride/titanium aluminum nitride multilayer coatings deposited by lateral rotating cathode arc." *Thin Solid Films* 578 (2015): 133-138.

- 
40. Takadoum, J., et al. "Adhesion and wear resistance of thin hard coatings." *Journal of the European Ceramic Society* 17.15-16 (1997): 1929-1932.
  41. Münz, Wolf-Dieter. "Titanium aluminum nitride films: A new alternative to TiN coatings." *Journal of Vacuum Science & Technology A: Vacuum, Surfaces, and Films* 4.6 (1986): 2717-2725.
  42. Yoon, Seog-Young, et al. "Comparison for mechanical properties between TiN and TiAlN coating layers by AIP technique." *Journal of materials processing technology* 130 (2002): 260-265.
  43. Ikeda, Tsutomu, and Hiroshi Satoh. "Phase formation and characterization of hard coatings in the Ti Al N system prepared by the cathodic arc ion plating method." *Thin Solid Films* 195.1-2 (1991): 99-110.
  44. Chakrabarti, K., et al. "Effects of nitrogen flow rates on the growth morphology of TiAlN films prepared by an rf-reactive sputtering technique." *Thin Solid Films* 406.1-2 (2002): 159-163.
  45. Hones, P., et al. "Oxidation resistance of protective coatings studied by spectroscopic ellipsometry." *Applied Physics Letters* 76.22 (2000): 3194-3196.
  46. PalDey, S. C. D. S., and S. C. Deevi. "Single layer and multilayer wear resistant coatings of (Ti, Al) N: a review." *Materials Science and Engineering: A* 342.1-2 (2003): 58-79.
  47. N. Shulumba, O. Hellman, Z. Raza, B. Alling, J. Barrirero, F. Mücklich, et al., Lattice Vibrations Change the Solid Solubility of an Alloy at High Temperatures, *Phys. Rev. Lett.* 117 (2016) 205502.
  48. Alling, Björn, et al. "Mixing and decomposition thermodynamics of  $c\text{-Ti}_{1-x}\text{Al}_x\text{N}$  from first-principles calculations." *Physical Review B* 75.4 (2007): 045123.
  49. Zhou, Min, et al. "Phase transition and properties of Ti–Al–N thin films prepared by rf-plasma assisted magnetron sputtering." *Thin solid films* 339.1-2 (1999): 203-208.
  50. Juri, Nina. "Comparison of Ti<sub>1-x</sub>Al<sub>x</sub>N coatings deposited by reactive magnetron sputtering from powder metallurgical targets and from mosaic targets."
  51. McIntyre D, Greene JE, Hakansson G, Sundgren J-E, Mucklich W-D. *J Appl Phys* 1990;67:1542.
  52. Hökrling A, Karlsson L, Johansson MP, Hultman L. Unpublished.
  53. Hultman, L., et al. "Transmission electron microscopy studies of microstructural evolution, defect structure, and phase transitions in polycrystalline and epitaxial Ti<sub>1-x</sub>Al<sub>x</sub>N and TiN films grown by reactive magnetron sputter deposition." *Thin Solid Films* 205.2 (1991): 153-164.

- 
54. Wahlström, U., et al. "Crystal growth and microstructure of polycrystalline Ti<sub>1-x</sub>Al<sub>x</sub>N alloy films deposited by ultra-high-vacuum dual-target magnetron sputtering." *Thin Solid Films* 235.1-2 (1993): 62-70.
  55. Bobzin, K., et al. "Mechanical properties and oxidation behavior of (Al, Cr) N and (Al, Cr, Si) N coatings for cutting tools deposited by HPPMS." *Thin Solid Films* 517.3 (2008): 1251-1256.
  56. Hovsepian, P. Eh, et al. "Novel CrAlYN/CrN nanoscale multilayer PVD coatings produced by the combined High Power Impulse Magnetron Sputtering/Unbalanced Magnetron Sputtering technique for environmental protection of  $\gamma$ -TiAl alloys." *Surface and Coatings Technology* 204.16-17 (2010): 2702-2708.
  57. Liu, Shiyu, et al. "Oxidation behavior of CrAlYN coatings at elevated temperatures." *Surface and Coatings Technology* 320 (2017): 357-361.
  58. Mikula, Marián, et al. "Structural evolution of TaN-alloyed Cr–Al–Y–N coatings." *Surface and Coatings Technology* 288 (2016): 203-210.
  59. Lind, Hans, et al. "Improving thermal stability of hard coating films via a concept of multicomponent alloying." *Applied Physics Letters* 99.9 (2011): 091903.
  60. Tam, Pui Lam, et al. "Structural, mechanical, and tribological studies of Cr–Ti–Al–N coating with different chemical compositions." *Thin Solid Films* 516.16 (2008): 5725-5731.
  61. Zhou, Z. F., et al. "High temperature oxidation of CrTiAlN hard coatings prepared by unbalanced magnetron sputtering." *Thin Solid Films* 517.17 (2009): 5243-5247.
  62. Kovalev, A. I., et al. "Impact of Al and Cr alloying in TiN-based PVD coatings on cutting performance during machining of hard to cut materials." *Vacuum* 84.1 (2009): 184-187.
  63. Yamamoto, K., et al. "Properties of (Ti, Cr, Al) N coatings with high Al content deposited by new plasma enhanced arc-cathode." *Surface and Coatings Technology* 174 (2003): 620-626.
  64. Forsén, Rikard, et al. "Decomposition and phase transformation in TiCrAlN thin coatings." *Journal of Vacuum Science & Technology A: Vacuum, Surfaces, and Films* 30.6 (2012): 061506.
  65. Luo, Quanshun, et al. "Tribological investigation of TiAlCrN and TiAlN/CrN coatings grown by combined steered-arc/unbalanced magnetron deposition." *Vacuum* 53.1-2 (1999): 123-126.
  66. Ostach, Daniel Michael. "High Temperature Oxidation Behavior of (Ti, Cr, Al) N Coatings Studied by in-situ Synchrotron Radiation X-ray Powder Diffraction." (2018).

- 
67. Rachbauer, R., et al. "Effect of Hf on structure and age hardening of Ti–Al–N thin films." *Surface and Coatings Technology* 206.10 (2012): 2667-2672.
  68. Hörling, Anders, et al. "Mechanical properties and machining performance of Ti<sub>1-x</sub>Al<sub>x</sub>N-coated cutting tools." *Surface and Coatings Technology* 191.2-3 (2005): 384-392.
  69. Hörling, Anders, et al. "Thermal stability of arc evaporated high aluminum-content Ti<sub>1-x</sub>Al<sub>x</sub>N thin films." *Journal of Vacuum Science & Technology A: Vacuum, Surfaces, and Films* 20.5 (2002): 1815-1823.
  70. He, Linqing, Li Chen, and Yuxiang Xu. "Interfacial structure, mechanical properties and thermal stability of CrAlSiN/CrAlN multilayer coatings." *Materials Characterization* 125 (2017): 1-6.
  71. Siwawut, Sutham, et al. "Cutting performances and wear characteristics of WC inserts coated with TiAlSiN and CrTiAlSiN by filtered cathodic arc in dry face milling of cast iron." *The International Journal of Advanced Manufacturing Technology* 97.9 (2018): 3883-3892.
  72. Kulkarni, Atul Prabhakar, and Vikas G. Sargade. "Characterization and performance of AlTiN, AlTiCrN, TiN/TiAlN PVD coated carbide tools while turning SS 304." *Materials and Manufacturing Processes* 30.6 (2015): 748-755.
  73. Chowdhury, Shahereen, et al. "Effect of interlayer thickness on nano-multilayer coating performance during high speed dry milling of H13 tool steel." *Coatings* 9.11 (2019): 737.
  74. Zhang, Quan, et al. "Tribological properties, oxidation resistance and turning performance of AlTiN/AlCrSiN multilayer coatings by arc ion plating." *Surface and coatings technology* 356 (2018): 1-10.
  75. Kim, Sun Kyu, Pham Van Vinh, and Jae Wook Lee. "Deposition of superhard nanolayered TiCrAlSiN thin films by cathodic arc plasma deposition." *Surface and Coatings Technology* 202.22-23 (2008): 5395-5399.
  76. Chaar, A. B. B., et al. "Microstructural influence of the thermal behavior of arc deposited TiAlN coatings with high aluminum content." *Journal of Alloys and Compounds* 854 (2021): 157205.
  77. Beake, Ben D., et al. "Elevated temperature repetitive micro-scratch testing of AlCrN, TiAlN and AlTiN PVD coatings." *International Journal of Refractory Metals and Hard Materials* 69 (2017): 215-226.
  78. Vettivel, S. C., et al. "Surface characteristics and wear depth profile of the TiN, TiAlN and AlCrN coated stainless steel in dry sliding wear condition." *Surfaces and Interfaces* 6 (2017): 1-10.
  79. Jacob, A., et al. "Influences of micro-blasting as surface treatment technique on properties and performance of AlTiN coated tools." *Journal of Manufacturing Processes* 29 (2017): 407-418.

- 
80. Zhao, Fan, et al. "Tribological and mechanical properties of hardness-modulated TiAlSiN multilayer coatings fabricated by plasma immersion ion implantation and deposition." *Surface and Coatings Technology* 402 (2020): 126475.
  81. Sprute, Tobias, et al. "Influence of substrate pre-treatments on residual stresses and tribo-mechanical properties of TiAlN-based PVD coatings." *Surface and Coatings Technology* 260 (2014): 369-379.
  82. Abdoos, Majid, et al. "The influence of residual stress on the properties and performance of thick TiAlN multilayer coating during dry turning of compacted graphite iron." *Wear* 454 (2020): 203342.
  83. Comakli, Onur. "Influence of CrN, TiAlN monolayers and TiAlN/CrN multilayer ceramic films on structural, mechanical and tribological behavior of  $\beta$ -type Ti45Nb alloys." *Ceramics International* 46.6 (2020): 8185-8191.
  84. Chang, Yin-Yu, Shun-Jan Yang, and Da-Yung Wang. "Structural and mechanical properties of AlTiN/CrN coatings synthesized by a cathodic-arc deposition process." *Surface and Coatings Technology* 201.7 (2006): 4209-4214.
  85. Zha, Xuming, et al. "Correlation of the fatigue impact resistance of bilayer and nanolayered PVD coatings with their cutting performance in machining Ti6Al4V." *Ceramics International* 45.12 (2019): 14704-14717.
  86. Budzynski, P., J. Sielanko, and Z. Surowiec. "Properties and phase transition of (Ti, Al) N thin films prepared by ion beam-assisted deposition." *Intermetallics* 16.8 (2008): 987-994.
  87. Hasegawa, Hiroyuki, Ayako Kimura, and Tetsuya Suzuki. "Ti<sub>1-x</sub>Al<sub>x</sub>N, Ti<sub>1-x</sub>Zr<sub>x</sub>N and Ti<sub>1-x</sub>Cr<sub>x</sub>N films synthesized by the AIP method." *Surface and Coatings Technology* 132.1 (2000): 76-79.
  88. Hofmann, Siegfried, and Hermann A. Jehn. "Selective oxidation and chemical state of Al and Ti in (Ti, Al) N coatings." *Surface and Interface Analysis* 12.6 (1988): 329-333.
  89. Kim, Byoung-June, et al. "High temperature oxidation of (Ti 1-X Al X) N coatings made by plasma enhanced chemical vapor deposition." *Journal of Vacuum Science & Technology A: Vacuum, Surfaces, and Films* 17.1 (1999): 133-137.
  90. Ohnuma, H., et al. "Effect of aluminum concentration on friction and wear properties of titanium aluminum nitride films." *Surface and Coatings Technology* 177 (2004): 623-626.
  91. Setsuhara, Y., et al. "Phase variation and properties of (Ti, Al) N films prepared by ion beam assisted deposition." *Surface and Coatings Technology* 97.1-3 (1997): 254-258.
  92. PalDey, S. C. D. S., and S. C. Deevi. "Single layer and multilayer wear resistant coatings of (Ti, Al)N: a review." *Materials Science and Engineering: A* 342.1-2 (2003): 58-79.



- 
93. Forsén, Rikard, et al. "Nanostructuring and coherency strain in multicomponent hard coatings." *APL Materials* 2.11 (2014): 116104.
  94. Reiter, A. E., C. H. Mitterer, and B. Sartory. "Oxidation of arc-evaporated Al<sub>1-x</sub>Cr<sub>x</sub>N coatings." *Journal of Vacuum Science & Technology A: Vacuum, Surfaces, and Films* 25.4 (2007): 711-720.
  95. Forsén, Rikard. *Multicomponent Alloying for Improved Hard Coatings*. Diss. Linköping University Electronic Press, 2014.
  96. Chawla, Vikas, et al. "Oxidation behavior of nanostructured TiAlN and AlCrN thin coatings on ASTM-SA213-T-22 boiler steel." *Journal of Minerals and Materials Characterization and Engineering* 9.11 (2010): 1037.
  97. Fujita, Kazuhisa. "Research and development of oxidation, wear and corrosion resistant materials at high temperature by surface modification using ion processing." *Surface and Coatings technology* 196.1-3 (2005): 139-144.
  98. Rahman, M., et al. "1.02 Techniques for Assessing the Properties of Advanced Ceramic Materials." *Comprehensive Materials Processing* (2014): 3.
  99. Chen, Li, et al. "Thermal stability and oxidation resistance of Ti–Al–N coatings." *Surface and Coatings Technology* 206.11-12 (2012): 2954-2960.
  100. Forsén, Rikard, et al. "Effects of Ti alloying of AlCrN coatings on thermal stability and oxidation resistance." *Thin Solid Films* 534 (2013): 394-402.
  101. Cooke, K. E., et al. "Development of duplex nitrided and closed field unbalanced magnetron sputter ion plated CrTiAlN-based coatings for H13 aluminium extrusion dies." *Surface and Coatings Technology* 188 (2004): 697-702.
  102. Hsu, Cheng-Hsun, et al. "Bias effects on the tribological behavior of cathodic arc evaporated CrTiAlN coatings on AISI 304 stainless steel." *Thin Solid Films* 518.14 (2010): 3825-3829.
  103. Forsén, Rikard, Naureen Ghafoor, and Magnus Odén. "Coherency strain engineered decomposition of unstable multilayer alloys for improved thermal stability." *Journal of Applied Physics* 114.24 (2013): 244303.
  104. Lewis, D. B., et al. "Structure and stress of TiAlN/CrN superlattice coatings as a function of CrN layer thickness." *Surface and Coatings Technology* 116 (1999): 284-291.
  105. Yu, Donghai, et al. "Microstructure and properties of TiAlSiN coatings prepared by hybrid PVD technology." *Thin Solid Films* 517.17 (2009): 4950-4955.

- 
106. He, Nairu, et al. "High temperature tribological properties of TiAlSiN coatings produced by hybrid PVD technology." *Tribology International* 98 (2016): 133-143.
107. Tritremmel, Christian, et al. "Oxidation behavior of arc evaporated Al-Cr-Si-N thin films." *Journal of Vacuum Science & Technology A: Vacuum, Surfaces, and Films* 30.6 (2012): 061501.
108. Chang, Yin-Yu, et al. "High temperature oxidation resistance of CrAlSiN coatings synthesized by a cathodic arc deposition process." *Journal of Alloys and Compounds* 461.1-2 (2008): 336-341.
109. Chang, Yin-Yu, and Chia-Yuan Hsiao. "High temperature oxidation resistance of multicomponent Cr-Ti-Al-Si-N coatings." *Surface and Coatings Technology* 204.6-7 (2009): 992-996.
110. Matzke H. *Defect Diffusion Forum* 1992;83:111.
111. Lee, Dong Bok, Thuan Dinh Nguyen, and Sun Kyu Kim. "Air-oxidation of nano-multilayered CrAlSiN thin films between 800 and 1000 C." *Surface and Coatings Technology* 203.9 (2009): 1199-1204.
112. Ortner, Hugo M., et al. "The history of the technological progress of hardmetals." *International Journal of Refractory Metals and Hard Materials* 49 (2015): 3-8.
113. Weidow, Jonathan, Eva Olsson, and Hans-Olof Andrén. "Chemistry of binder phase grain boundary in WC-Co based cemented carbide." *International Journal of Refractory Metals and Hard Materials* 41 (2013): 366-369.
114. Garcia, Jose, et al. "Cemented carbide microstructures: a review." *International Journal of Refractory Metals and Hard Materials* 80 (2019): 40-68.
115. Kear, B. H., and L. E. McCandlish. "Chemical processing and properties of nanostructured WC-Co materials." *Nanostructured Materials* 3.1-6 (1993): 19-30.
116. He, Jianhong, et al. "Near-nanostructured WC-18 pct Co coatings with low amounts of non-WC carbide phase: Part I. Synthesis and characterization." *Metallurgical and Materials Transactions A* 33.1 (2002): 145-157.
117. Liu, Yourong, et al. "Near-nanostructured WC-18 pct Co coatings with low amounts of non-WC carbide phase: Part II. Hardness and resistance to sliding and abrasive wear." *Metallurgical and Materials Transactions A* 33.1 (2002): 159-164.
118. <http://www.pas.rochester.edu/~blackman/ast104/spectrum.html>

- 
119. Inkson, B. J. "Scanning electron microscopy (SEM) and transmission electron microscopy (TEM) for materials characterization." *Materials characterization using nondestructive evaluation (NDE) methods*. Woodhead Publishing, 2016. 17-43.
  120. Fultz, Brent, and James M. Howe. *Transmission electron microscopy and diffractometry of materials*. Springer Science & Business Media, 2012.
  121. CARTER, BARRY AUTOR, et al. *Transmission Electron Microscopy: A Textbook for Materials Science. Diffraction. II. Vol. 1*. Springer Science & Business Media, 1996.
  122. E. Cadel, F. Vurpillot, R. Lardé, S. Duguay, B. Deconihout, Depth resolution function of the laser assisted tomographic atom probe in the investigation of semiconductors, *J. Appl. Phys.* 106 (2009) 44908.
  123. B.Gault, M.P. Moody, F. De Geuser, D. Haley, L.T. Stephenson, S.P. Ringer, Origin of the spatial resolution in atom probe microscopy, *Appl. Phys. Lett.* 95 (2009) 34103.
  124. P.Bas, A. Bostel, B. Deconihout, D. Blavette, A general protocol for the reconstruction of 3D atom probe data, *Appl. Surf. Sci.* 87–88 (1995) 298
  125. K.Thompson, J.H. Booske, D.J. Larson, T.F. Kelly, Three-dimensional atom mapping of dopants in Si nanostructures, *Appl. Phys. Lett.* 87 (2005) 052108. <https://doi.org/10.1063/1.2005368>.
  126. Strausser, Yale, ed. *Characterization in silicon processing*. Elsevier, 2013.
  127. Zhou, Yaomin, et al. "Hardness anomaly, plastic deformation work and fretting wear properties of polycrystalline TiN/CrN multilayers." *Wear* 236.1-2 (1999): 159-164.
  128. Golovin, Yu I., et al. "The size effects in hardness of polycrystalline niobium." *Technical Physics Letters* 36.4 (2010): 369-370.
  129. Yang, Fan, et al. "Mechanical Properties of Intermetallic Compounds at Elevated Temperature by Nanoindentation." 2019 IEEE 69th Electronic Components and Technology Conference (ECTC). IEEE, 2019.
  130. Pharr, G. M., and W. C. Oliver. "Measurement of thin film mechanical properties using nanoindentation." *Mrs Bulletin* 17.7 (1992): 28-33.
  131. Baran, Ö., I. Efeoglu, and Braham Prakash. "Structural, mechanical and tribological properties of TiTaBN composite graded coatings deposited by CFUBNS technique." *International Conference: Metallurgical Coatings & Thin Films 23/04/2012-27/04/2012*. 2012.
  132. Vencl, A., A. Rac, and B. Ivković. "Investigation of abrasive wear resistance of ferrous-based coatings with scratch tester." *Tribology in industry* 29.3-4 (2007): 13-6.

- 
133. Tucci, A., J-B. Guion, and L. Esposito. "Microstructure and scratch resistance of ceramic surfaces." *Afyon Kocatepe Üniversitesi Fen Ve Mühendislik Bilimleri Dergisi* 9.3 (2008): 229-237.
134. Barbhuiya, Salim, and Ikbal Choudhury. "Characterization of Mechanical Properties and the Abrasive Wear of Thermal Spray Coatings." *Thermal Sprayed Coatings and their Tribological Performances*. IGI Global, 2015. 328-359.
135. Jehn, Hermann, Georg Reiners, and Norbert Siegel. *Charakterisierung dünner Schichten*. Beuth, 1993.
136. <https://pdf.directindustry.de/pdf-en/kla-tencor/p-7-stylus-profiler/113449-775848.html#open2029567>
137. Blau, Peter J. "Friction and wear transitions of materials." (1989).
138. Bhushan, Bharat. *Principles and applications of tribology*. John Wiley & Sons, 1999.
139. Ozimina, Dariusz, et al. "Effects of a Graphene-Enhanced Lubricant on the Performance of a Tribosystem." *DEStech Transactions on Computer Science and Engineering* fe (2019).
140. <https://www.bmeclub.ch/wp-content/uploads/2016/06/Voutat-One-Page-Summary.pdf>
141. Lin, Kwang-Lung, Ming-Yeong Hwang, and Cheng-Dau Wu. "The deposition and wear properties of cathodic arc plasma deposition TiAlN deposits." *Materials chemistry and physics* 46.1 (1996): 77-83.
142. <https://lalithvarun.blogspot.com/2013/02/what-is-thermo-gravimetric-analysis.html>
143. Mayrhofer, P. H., et al. "Calorimetric evidence for frictional self-adaptation of TiAlN/VN superlattice coatings." *Surface and Coatings Technology* 177 (2004): 341-347.
144. Sproul, William D. "Reactive sputter deposition of polycrystalline nitride and oxide superlattice coatings." *Surface and Coatings Technology* 86 (1996): 170-176.
145. Ducros, C., C. Cayron, and F. Sanchette. "Multilayered and nanolayered hard nitride thin films deposited by cathodic arc evaporation. Part 1: Deposition, morphology and microstructure." *Surface and Coatings Technology* 201.1-2 (2006): 136-142.
146. Standard, I. S. O. "18754, Fine ceramics (advanced ceramics, advanced technical ceramics)- Determination of density and apparent porosity." *International Organization for Standardization* 2018.8 (2013): 15955.
147. Ruden, Alexander, et al. "Tribology of ZrN, CrN and TiAlN thin films deposited by reactive magnetron sputtering." *Dyna* 80.178 (2013): 95-100.
148. Bao, D. X., and N. Wakiya Yao. "K. Shinozaki, N. Mizutani." *Appl. Phys. Letters* 79 (2001): 3767.

149. Jalali, Reza, et al. "The effect of Al content, substrate temperature and nitrogen flow rate on optical band gap and optical features of nanostructured TiAlN thin films prepared by reactive magnetron sputtering." *Applied Physics A* 122.11 (2016): 978.





## Curriculum Vitae

**Mohamed Riyad Alhafian**

Heiglhofstraße 86, 81377 München, Germany

[r.alhafian@gmail.com](mailto:r.alhafian@gmail.com)

0049 1791668571

## PROFILE

A highly motivated and ambitious material science with entrepreneurship attitude and strong academic background. 2 years' experience in technical project management for coating solutions in automotive business and consumer electronics in a Start-up environment. High analytical skills with focus on targets, perseverance and stress resistance. Quickly adaptable and love to work in international teams with problem-solving attitude. General creative and curious mindset in terms of different technologies in manufacturing processes.

## EDUCATION

**11/2017- 11/2021**

**Researcher PHD candidate**

Faculty of Materials Science and materials technology at Saarland University in collaboration with the Materials Research and Technology (MRT) department at Luxembourg Institute of Science and Technology (LIST)

**PhD thesis**

Growth Mechanism Study of Nanostructure Hard Nitride Coating with High-temperature Resistance Obtained by High-power Impulse Magnetron Sputtering (HiPIMS)

**10/2014 to 02/2017**

**Double Degree, Master of Science (AMASE) in Advanced Materials Science and Engineering**

University of Saarland, Germany and Luleå University of Technology, Sweden (ERASMUS Program)

**Master thesis**

Magnetics Based Measurement Technique for the Assessment of Partially Damaged Structural Steels by Using Non-Destructive Testing Methods.

**Project:**

Evaluation of the Effects of Salt on Different Molded Stainless-Steel Surfaces.

**Seminars:**

Probability of Damage Analysis and Guided Wave Simulation for Structural Health Monitoring of a Thin Aluminum Plate with Three Holes using COMSOL and SolidWorks.

**01/2011 to 06/2012**

**Diploma in Economic and Social Planning**

Economic and Social Planning Institute, Damascus, Syria

**Final project title:**

The Effect of Maintenance Systems in Small and Medium Projects.

**06/2004 to 08/2009**

**BSc in Mechanical Design Engineering**

Damascus University, Syria

**Final project title:**

Technological Analysis of Computer Numbering Control (CNC) Plasma Cutting Machine

**08/2002 to 08/2004**

**Associate Degree in Mechanical Engineering**

Applied Industries Institute in Damascus, Syria

**Final project title:**

Understanding and Designing a Three Stage Gearbox.

## List of academic publications

### Paper I

**Comparison on the structural, mechanical and tribological properties of TiAlN coatings deposited by HiPIMS and Cathodic Arc Evaporation**  
**Comparison on the structural, mechanical and tribological properties of TiAlN coatings deposited by HiPIMS and Cathodic Arc Evaporation**

Surface and Coatings Technology, 2021

### Paper II

**Study of the oxidation mechanism at high temperature of nanofiber textured AlTiCrN coatings produced by physical vapor deposition using high-resolution characterization techniques**  
**Study of the oxidation mechanism at high temperature of nanofiber textured AlTiCrN coatings produced by physical vapor deposition using high-resolution characterization techniques**

Corrosion Science, 2022

### Paper III

**Influence of Si addition on the phase structure and oxidation behavior of PVD AlTiN and AlTiCrN coatings using high-resolution characterization techniques**

Alloys and Compounds, 2023

---